A Study on Global Ocean Analysis from an Ocean Data Assimilation System and its Sensitivity to Observations and Forcing fields

Thesis · November 2015

DOI: 10.13140/RG.2.1.4459.4326

1 author:

Siva Reddy

Indian National Centre for Ocean Informati…

A Study on Global Ocean Analysis from an Ocean Data Assimilation System and its Sensitivity to Observations and Forcing fields

BY

S SIVAREDDY, M.Tech.

THESIS SUBMITTED TO THE ANDHRA UNIVERSITY FOR THE AWARD OF THE DEGREE OF DOCTOR OF PHILOSOPHY

2015

Dedicated

To my Parents, Brother and my Wife

CERTIFICATE

This is to certify that the thesis entitled ***"A Study on Global Ocean Analysis from an Ocean Data Assimilation System and its Sensitivity to Observations and Forcing fields"*** is the result of bonafide research work carried out by Mr. S. Sivareddy, M.Tech., under our guidance for the degree of Doctor of Philosophy. This thesis conforms to the standards envisaged by the regulation of the University and no part of this has previously formed the basis for the award of any other degree in any other university.

Dr. M. Ravichandran
Internal Guide,
Scientist-G & Head-MOG,
ESSO-INCOIS,
Ministry of Earth Sciences (MoES),
Hyderabad.

Prof. K. V. S. R. Prasad
External guide,
Head of the Department,
Dept. of Meteorology and Oceanography,
Andhra University,
Visakhapatnam.

DECLARATION

I do hereby declare that the thesis entitled ***"A Study on Global Ocean Analysis from an Ocean Data Assimilation System and its Sensitivity to Observations and Forcing fields"*** is a genuine record of research work carried out by me at ESSO-Indian National Centre for Ocean Information services (ESSO-INCOIS), Ministry of Earth Sciences (MoES), Hyderabad, under the supervision of Dr. M. Ravichandran, Scientist-G & Head- Modelling and Ocean Observation Group, ESSO-INCOIS, MoES and Prof. K.V.S.R. Prasad, Head of the Department, Dept. of Meteorology and Oceanography, Andhra University for the award of Ph.D. and no part of this has been submitted for the award of any degree in any other university and published elsewhere anytime before.

Hyderabad **S. Sivareddy**

Date:

ACKNOWLEDGEMENTS

At the outset I am indebtful to Dr. M Ravichandran, INCOIS for his guidance and constructive critical reviews. Directly and indirectly he has played a significant role in shaping up my career in the field of ocean modeling. I am also thankful to him for accepting to be as internal guide for me to carry out this work.

I would like to thank Prof. K. V. S. R. Prasad, Dept. of Meteorology and Oceanography, Andhra University for accepting to be as external guide. I am grateful to him for his timely help on many occasions for a smooth progress of this work.

This work is possible due to the MoU between MoES & NOAA. I sincerely thank Dr. Shailesh Nayak, Secretary, MoES for making Ocean Data Assimilation as part of the implementation agreement between INCOIS and NCEP. The encouragement and facilities provided by Dr. Satish C Shenoi, Director, INCOIS to carryout this work at INCOIS are gratefully acknowledged.

This work would not have been possible without High Performance Computing (HPC) facility. I would like to acknowledge the HPC team of INCOIS for their help in porting the model and providing me storage facilities in HPC. Special thanks to Raju Devender for making INCOIS-GODAS outputs available on the LAS of INCOIS. Computer facilities provided by CWG team of INCOIS are also highly appreciated.

This work uses various observations to evaluate the model. I take this opportunity to thank all the organizations who have made oceanographic and atmospheric data available to us on their web portals. Graphics are generated using the software FERRET and editing is done using the GIMP software. The whole thesis is written using LaTeXsoftware. All these softwares are available for free online. I would like thank developers and distributors of these softwares for providing these wonderful packages online for free of cost.

Scientific discussions with Dr. Girishkumar, INCOIS ignited many ideas some of which lead to improve this work significantly. He has been one of the potential inspirer for me. I take this opportunity to thank him for all that he has done so far. The collobaration with Dr. Dave Behringer, NCEP, USA helped me to get insights on the assimilation system. I would like thank him for his constant support.

I would like to place on record the name of my friend Venkata Ramu, Andhra University for his administrative help at Andhra University, Visakhapatnam. As major portion of the current work is carried out at INCOIS, Hyderabad, a place very far away from Andhra University, Visakhapatnam, I would have definitely struggled a lot to get the administrative things done without his help. I thank him once again for his help. I take this opportunity to thank Dr. Sikhakolli Rajesh, SAC, ISRO for providing overall idea on the construction of my thesis and also for teaching me how to use LaTeX.

Scientific discussions made with my colleagues at INCOIS, Dr. H. Rahman, Dr. Harikumar, Dr. Uday Bhaskar, Mrs. Neethhu Chacko and Dr. Sudheer Joseph enriched my knowledge in oceanography. I enjoyed joyful and healthy scientific and personal interactions with them and other colleagues of MOG. I would like to thank all of them for their moral support and joyful moments.

I take this opportunity to thank my senior professors and teachers Prof. D.V. Bhaskarrao, Prof. O.S.R.U. Bhanukumar, Prof. S.S.V.S Ramakrishna, Prof. C.V. Naidu, Prof. Gopal Reddy, Prof. Kailash Reddy and Prof. Bharathi from Department of Meteorology and Oceanography, Andhra University for instilling fundamental concepts in my mind which helped me to perform scientific analysis at ease.

I thank my dear friends Sai, Srikanth, Palu, Gavasakar, Suresh, Rajesh, Anuradha, for providing moral support and joyful moments during the course of this work. I would also like to thank my cricket team mates for providing wonderful outings and joyous moments during the course of this work which helped me to relieve me from work tensions.

I owe my achievements whatever I have attained so far and those going to attain to my family (my wife, daughter, parents, brother, and my nephew). I cannot forget the kind of support, love, and affection showered by my parents, S Venkata Swamy Reddy, S Lakshmi Kantamma, and my elder brother S Krishna Reddy on me. Their hard work and efforts to make me stand tall and firm in my life have been the constant inspiration to me. I would like to take this opportunity to thank my nephew Srikanth for providing enough motivation, indirectly, to stay responsible in my life. Unlimited and unconditional support, love and affection showered on me by my sweet wife S Krishnaveni during the course of this work will never ever be erasable from my heart and soul. Joyful moments spent with my sweetest daughter Nishita helped to overcome work tensions.

Last but not the least, I would like to thank the divine God for providing me all the strength.

PREFACE

Global ocean analysis is analyzed product of ocean parameters - such as temperature, salinity, sea level, and currents - generated using an ocean data assimilation system, where global ocean observations are employed to reduce errors in global ocean model simulations. While ocean observation alone is not self sufficient to generate ocean analysis, the model based analysis is not accurate in simulating various oceanographic features. Hence, ocean models with data assimilation are used for generating ocean analysis. They are in general dynamically consistent both in the spatial and temporal scales. Such global ocean analysis is imperative to understand the ocean dynamics and thermodynamics and to provide operational nowcasts and forecasts. At present, there are a handful of data assimilation systems available for providing ocean analysis. National Centers for Environmental Prediction (NCEP) provides 10-15 day delayed ocean analysis using Global Ocean Data Assimilation System (GODAS). The NCEP-GODAS is based on quasi-global set up of Modular Ocean Model version-3 (MOM-3) and assimilates *in-situ* temperature and synthetic salinity profiles using 3D-VAR assimilation technique. Recently, an improved version of GODAS is developed at NCEP based on global MOM-4. This system can assimilate *in-situ* temperature and salinity profiles using 3D-VAR technique. The same version of GODAS has been implemented at INCOIS (here after INCOIS-GODAS) for operational purposes with an objective to provide improved global ocean analysis. This analysis helps in providing initial conditions in coupled ocean-atmosphere model (e.g. CFS; Coupled ocean-atmosphere Forecast System) for the seasonal forecast of monsoon. It also aids in understanding of the physical and dynamical state of the ocean (temperature, salinity, currents and sea level) over a range of spatio-temporal scales.

The present study, entitled *"Global Ocean Analysis from an Ocean Data Assimilation System and its Sensitivity to Observations and Forcing fields"*, focuses on delivering research quality ocean analysis using INCOIS-GODAS by diagnosing various configurations of it. Statistical (mean, standard deviation, root mean square difference, correlation) and process based (climatologies, case studies for Indian Ocean Dipole events) measures were employed to assess the quality of ocean analysis. The impact on ocean analysis by the assimilation of observed *in-situ* temperature and synthetic salinity was examined. Later the INCOIS-GODAS was improved by incorporating observed salinity assimilation instead of synthetic salinity and also by the incorporation of monthly varying river runoff. Further, impact of different momentum flux and various time scales in relaxing the model Sea Surface Temperature (SST) by observed SST, were studied. The quality of improved global ocean analysis obtained from different configuration of INCOIS-GODAS was evaluated using independent observations and other state-of-the-art ocean data assimilation systems. Moreover, the application of INCOIS-GODAS was used to understand the impact of different ocean *in-situ* observing system by conducting Observation System Evaluation Experiments (OSEs). The thesis is organized in 8 chapters.

Chapter-1 provides a brief introduction to ocean modeling, data assimilation, and the status of global ocean *in-situ* observation networks. This chapter also discusses the motivation and the objectives of the present study with background information about earlier studies conducted in this field. **Chapter-2** provides details on the ocean model configuration, assimilation scheme, and the data used for forcing, assimilation and for evaluation and validation. This chapter also discusses the methodology followed for evaluation and validation. The impact of assimilating observed *in-situ* temperature and synthetic salinity profiles and sensitivity of the assimilation system by the momentum flux on the quality of ocean analysis is examined in **Chapter 3**. As we found improvements in ocean currents with the use of satellite based QuikSCAT gridded wind product, which is not available after November, 2009, the suitability of an ASCAT based satellite gridded wind product for INCOIS-GODAS is examined in the **Chapter-4**. The ASCAT based gridded wind product was chosen because the series of ASCAT satellite sensors are foreseen to be available up to 2022. In this chapter, the suitability was determined by evaluating the ASCAT based wind product using atmospheric winds from *in-situ* (RAMA) and satellite (QuikSCAT) measurements. Further, the suitability of momentum flux estimated from the gridded ASCAT winds in simulating currents was tested by performing various sensitivity experiments. Model simulated currents from different momentum flux forcing (satellite based ASCAT and QuikSCAT and reanalyzed winds of NCEP) were compared with respect to RAMA current measurements and Ocean Surface Current Analysis-Real time (OSCAR) currents. It is found that the quality of ASCAT based gridded winds is better than re-analyzed wind product of NCEP. Also its quality is on par with the quality of QuikSCAT winds. In order to improve the salinity analysis, we have implemented observed *in-situ* salinity profile assimilation and incorporated inter-annual monthly river runoff in INCOIS-GODAS. Improvements of ocean analysis obtained with these implementations are discussed in **chapter-5**. This chapter also provides the description of the technique, used to construct an inter-annual monthly global river discharge. This gridded inter-annual monthly river discharge data set spanning 1993-2012 can be utilized in other ocean models as well.

Inputs from chapters 3, 4 and 5 were used to adjudge a best possible configuration of INCOIS-GODAS to provide research quality ocean analysis on operational basis. The addition of the following techniques eventually provided us with an improved ocean analysis.

- Assimilation of observed *in-situ* Temperature and Salinity profiles
- Incorporation of inter-annual monthly river runoff with point source option
- Strong relaxation of model SST towards observed SSTs
- Utilization of satellite based gridded wind products as a wind forcing.

In **Chapter 6**, the ocean analysis resulted from the above configuration is then used to verify the overall skill of INCOIS-GODAS in capturing intra-seasonal and inter-annual variations of different ocean parameters in the Indian Ocean. It was found that ocean analysis from the above configuration of INCOIS-GODAS (here after improved INCOIS-GODAS) reproduces the intra-seasonal and inter-annual variations of different ocean parameters with excellent skill. In order to verify whether the quality of global ocean analysis obtained from the improved INCOIS-GODAS is at contemporary measures of research quality, an inter-comparison study was also performed in this chapter. The quality of global ocean analysis from the improved INCOIS-GODAS was verified with the global ocean re-analysis obtained from NCEP-GODAS and European Center for Medium range Weather Forecast-Ocean Reanalysis-4 (ECMWF-ORAS4). Results suggest that the quality of global ocean analysis from INCOIS-GODAS is better than NCEP-GODAS and close to the quality of global ocean re-analysis of ECMWF-ORAS4. The application of INCOIS-GODAS is exploited in **Chapter-7**, by executing different experiments to study the impact of *in-situ* ocean observing systems. This was achieved by conducting Ocean Simulation Experiments(OSE). Realizations on the quality of ocean analysis under various configurations (discussed in chapters 3 to 6) served as the backbone for the OSE study as it could decipher limitations of the model and the impact of various ocean observing systems, such as Argo, Moorings, XBTs, etc in generating global ocean analysis. The improved global ocean analysis is made available to different users for both scientific and operational purposes. Dissemination mechanisms and its detail with typical examples are reported in **Chapter-8**. This chapter also summarizes the results of the present study.

Contents

ACRONYMS

3D-VAR	3 dimensional Varaiational assimilation Scheme
ADCP	Accoustic Doppler Current Profiler
AMSRE	Advanced Microwave Scanning Radiometer Earth Observing System
ARGO	Array for Real-Time Geostrophic Oceanography
AS	Arabian Sea
ASCAT	Advanced Scatterometer
AVHRR	Advance Very High Resolution Radiometer
AVISO	Archiving, Validation and Interpretation of Satellite Oceanographic data
BL	Barrier Layer
BoB	Bay of Bengal
CFS	Climate Forecast System
CLIVAR	Climate Variability and Predictability
COARE	Coupled Ocean-Atmosphere Response Experiment
CTD	Conductivity-Temperature-Depth
DASCAT	Daily averaged ASCAT based gridded winds
ECMWF	European Centre for Medium-Range Weather Forecasts
EICC	East India Coastal Current
EIO	Equatorial Indian Ocean
EKF	Ensemble Kalman Filter
EN3V2a	Ensemble 3 Version 2a
ENSO	ElNino Southern Oscillation
EUMETSAT	European Organization for the Exploitation of Meteorological Satellites
FTP	File Transfer Protocol
GFDL	Geophysical Fluid Dynamics Laboratory
GODAS	Global Ocean Data Assimilation System
IGOA	Improved Global Ocean Analysis
IIOE	International Indian Ocean Expedition
IITM	Indian Institute of Tropical Meteorology
ILD	Isothermal Layer Depth
INCOIS	Indian National Center for Ocean Information Services
InDOOS	Indian Ocean Observing System
IO	Indian Ocean
IOD	Indian Ocean Dipole

ITF	Indonesian Through Flow
LAS	Live Access Server
MLD	Mixed Layer Depth
MoES	Ministry of Earth Sciences
MOM	Modular Ocean Model
NASA	National Aerospace and Space Administration
NCAR	National Centre for Atmospheric Research
NCEP	National Center for Environmental Prediction
NDBC	National Data Buoy Center
NetCDF	Network Common Data Format
NOAA	National Oceanic and Atmospheric Administration
NODC	National Oceanographic Data Center
OGCM	Ocean General Circulation Model
OSCAR	Ocean Surface Current Analysis Real-time
PIRATA	Prediction and Research moored Array in the ATlAntic
QC	Quality Control
QSCAT	3-day moving averaged QuikSCAT based winds
QuikSCAT	QuikScatterometer
RAMA	Research Moored Array for African-Asian-Australian Monsoon Analysis and Prediction
RMSD	Root Mean Square Difference
SEAS	South Eastern Arabian Sea
SEC	South Equatorial Current
SECC	South Equatorial Counter Current
SG	Southern Gyre
SGS	Sub-Grid Scale
SLA	Sea level Anomaly
SMC	Summer Monsoon Current
SMOS	Soil Moisture and Ocean Salinity
SSH	Sea Surface Height
SSHA	Sea Surface Height Anomaly
SSS	Sea Surface Salinity
SST	Sea Surface Temperature
STD	Standard Deviation
TAO	Tropical Atmosphere Ocean
TIO	Tropical Indian Ocean
TMI	TRMM Microwave Imager

TOGA	Tropical Ocean Global Atmosphere
TRITON	Triangle trans Ocean Buoy Network
TRMM	Tropical Rainfall Measuring Mission
UNESCO	United Nations Educational, Scientific and Cultural Organization
USGODAE	United States Global Ocean Data Assimilation Experiment
WICC	West India Coastal Current
WMC	Winter Monsoon Current
WOA	World Ocean Atlas
WOCE	World Ocean Circulation Experiment
WOD	World Ocean Database
XBT	eXpendable Bathy Thermograph

List of Tables

List of Figures

Chapter 1

Introduction

1.1 Background

Water is an important element in the earth's life system. Oceans, covering approximately 71% of the earth's surface, supplies almost all the water that falls on the land. There are many earth system processes that directly or indirectly influence the supply of this water from the ocean to the land on shorter to longer time scales. Due to large memory and huge storage (in terms of heat, carbon deposits etc.) capabilities of the ocean compared to other earth system components (such as land, atmosphere), long-term variabilities in the Earth system are largely determined by the ocean processes. ElNino and Indian Ocean Dipole (IOD) are some of the inter-annual variabilities of such phenomenon, which originates in the ocean to influence the climate in many regions of the world. In-addition to these, interaction of the atmosphere with the upper ocean at relatively shorter time scales influences the rain bearing weather systems such as monsoon. The active role of the ocean amongst/along-with all components of the earth system emphasizes the need for a descent understanding of the ocean processes. Understanding these ocean processes require sampling of the ocean at various time and spatial scales.

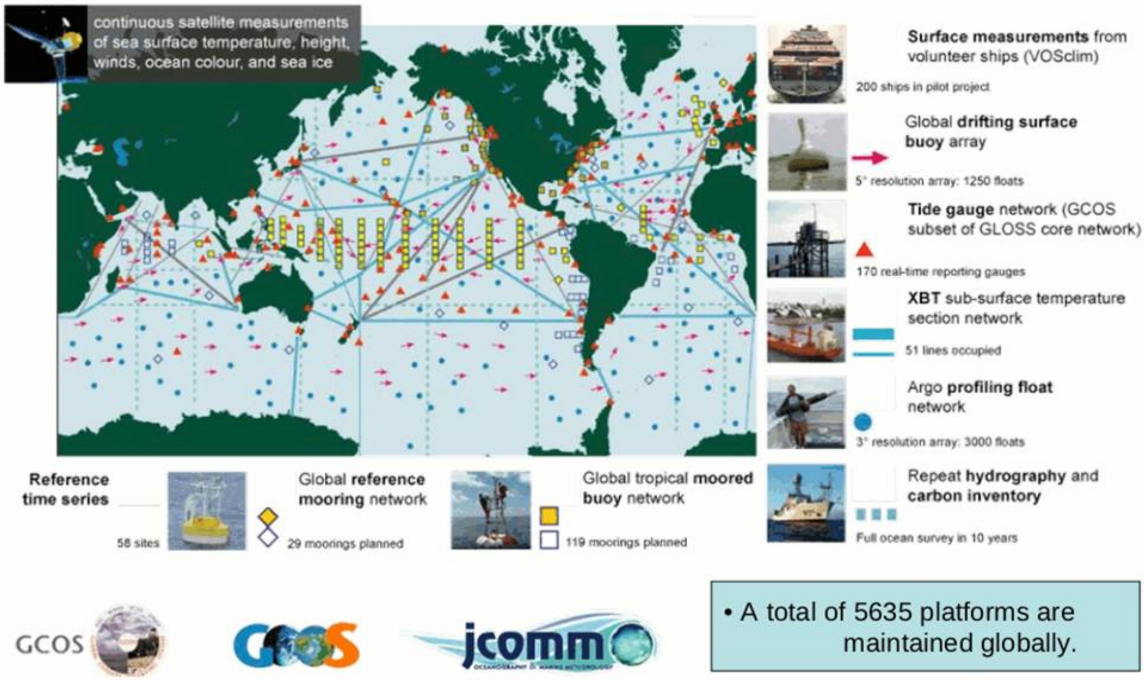

Figure 1.1: Schematic diagram showing various components of climate ocean observing systems (Source: NOAA)

1.1.1 Global Ocean Observations

Sampling the ocean can be done using both direct (*in-situ*) and remote sensing (Figure 1.1) methods. Ocean remote sensing mostly monitor the surface, whereas the direct or *in-situ* measurements are used for surface as well as subsurface. Remote sensing using artificial satellites offer spatially rich time series data. Ocean surface parameters that are estimated from satellite remote sensing include Sea Surface Temperature (SST; e.g. AVHRR, TMI, AMSR), Sea Surface Salinity (SSS; e.g. Aquarius, SMOS), Sea Surface Height Anomaly (SSHA; e.g. TOPEX/Poseidon, JASON, Saral/Altika). Major limitation of the satellite remote sensing is its inability to have depth wise sampling of the ocean. Unlike land, where the operational networks of meteorological observations placed all over the world which enabled to monitor changes in the global atmosphere, the global coverage of the subsurface observations in the ocean is largely under sampled.

In-order to understand the ocean processes in a much better way, organized

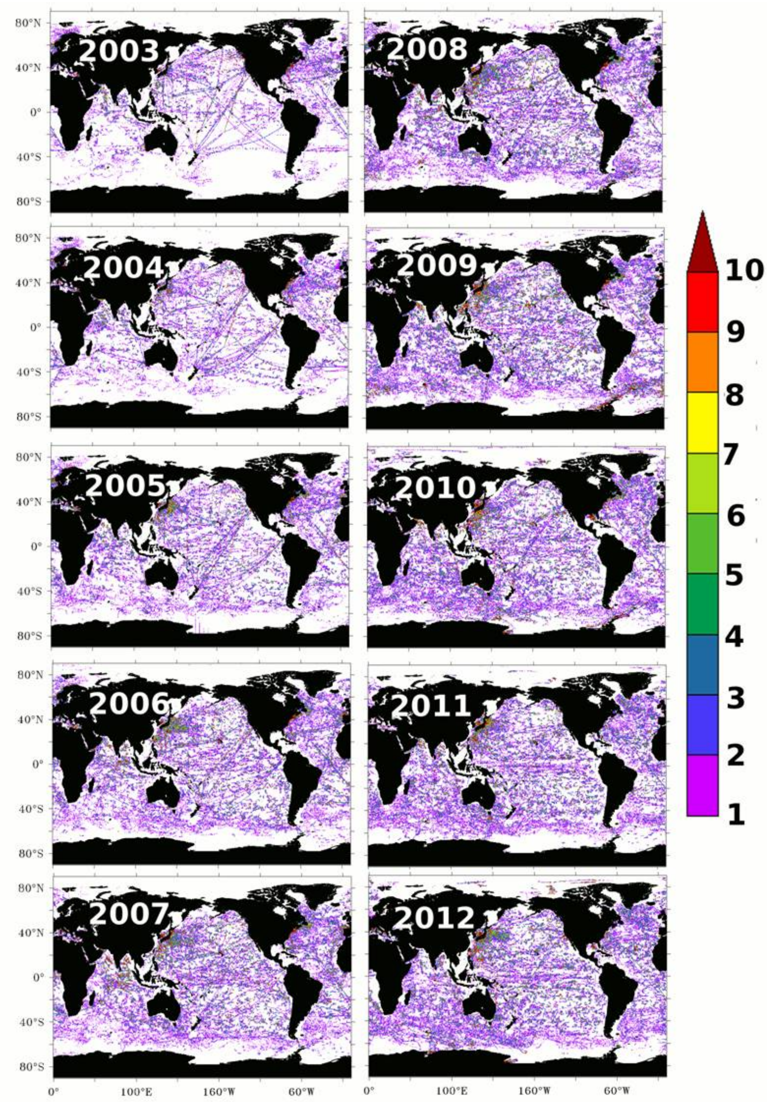

Figure 1.2: Yearwise coverage of temperature measurements from global ocean observing system. Color scale indicates the number of temperature profiles acquired in the year from the $0.5^\circ \times 0.5^\circ$ longitude-latitude grid

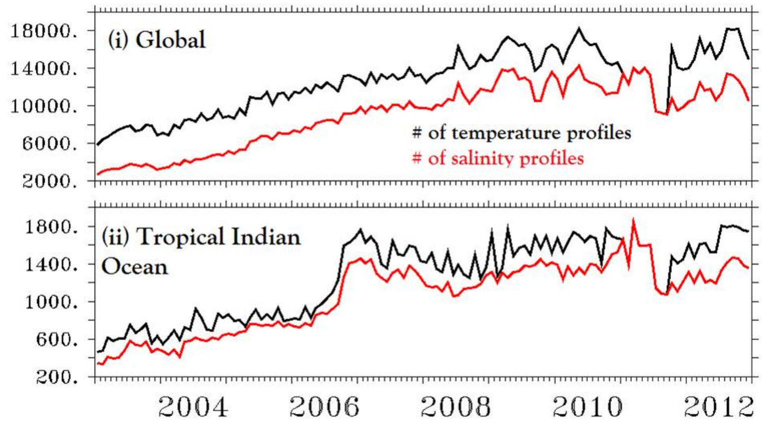

Figure 1.3: Time series of number of temperature (black) and salinity (red) profiles from GOOS illustrating the evolution of observations for (i) global and (ii) Tropical Indian Ocean ($30°E$ - $120°E$, $30°S - 30°N$)

international observational campaigns such as International Indian Ocean Expedition (IIOE), World Ocean Circulation Experiment (WOCE), Tropical Ocean Global Atmosphere (TOGA) were initiated to observe the ocean. These observational campaigns could provide temperature and salinity profiles up to deeper depths in the ocean on high vertical resolution along the ship tracks using various instruments such as Nansen bottles, eXpendable Bathy Thermographs (XBTs), Conductivity-Temperature-Depth (CTDs) as well as time series data at various locations. Even after such an effort only a few selected locations got sufficient data to allow us to study the variations in space and time; most of the world's ocean remains a very sparsely sampled. With the advent of Argo program (Freeland et al., 2010), the data sparseness is significantly reduced as can be inferred from Figure 1.2 and Figure 1.3. The figure clearly shows that ocean observations are uniformly distributed especially during the recent period. Availability of such a rich hydrographic data from the international programs enabled to discover many interesting ocean-atmospheric processes. For example, de Boyer Montégut et al. (2007) demonstrated the control of salinity on mixed layer depth in the world ocean. McPhaden et al. (2009a) studied ocean-atmosphere interactions during cyclone Nargis using Argo and tropical moorings data. Using XBT data along ship tracks Li and Dong-Xiao (2012) tried to understand the structure of thermal inversions in the south Bay of Bengal. Based on tropical mooring data Girishkumar et al. (2013) observed intra-seasonal thermocline variability in the Bay of Bengal. Though we saw huge increase in the quantity of sub-surface data during last decade (Figure 1.3), there are still some regions in the world ocean (such as poles, thermo-cline ridge, Somali current region etc.) which are largely under-sampled (figure 1.2). Besides this under-sampling, two additional limitations of the historical observational data set complicate the studies of ocean physics variability on inter-annual to decadal time scales. The first is due to changes in the observation bias resulting from the evolution of the observing system. The second limitation is due to changes in the vertical sampling of the historical temperature data set (Carton and Santorelli, 2008). These limitations demand for numerical ocean modelling.

1.1.2 Numerical Ocean Models

A "model" in the most general sense of the word, can be any kind of representation of the real world. It can be physical, like a model ship, or a theoretical construct that helps explain some phenomenon. Numerical ocean models are essentially computer codes for a system of equations governing the geophysical fluid dynamics obtained after the implementation of laws of physics such as conservation of momentum, mass, and energy for the geophysical fluids. Numerical ocean models can simulate spatial and temporal picture of the state of the ocean and also can predict how it is going to change. The basic properties predicted are temperature and salinity from the surface to the seafloor. In order to do this, models must also predict currents and changes in the surface elevation. Similarly, ocean models can also predict waves and surf, which can also be driven by winds. The Ocean General Circulation Models (OGCMs), which are of interest here simulates/predicts temperature, salinity, and sea level along with currents at various depth levels.

These OGCMs are based on a set of seven equations called as primitive equations for ocean which are described below.

Primitive equations are the fundamental equations solved by OGCMs in-order to be able to simulate ocean parameters. They are given by

$$x{-}momentum: \frac{\partial u}{\partial t}+u\frac{\partial u}{\partial x}+v\frac{\partial u}{\partial y}+w\frac{\partial u}{\partial z} = -\frac{1}{\rho_0}\frac{\partial p}{\partial x}+fv+\frac{\partial}{\partial x}\left(A\frac{\partial u}{\partial x}\right)+\frac{\partial}{\partial y}\left(A\frac{\partial u}{\partial y}\right)+\frac{\partial}{\partial z}\left(V_E\frac{\partial u}{\partial z}\right) \quad (1.1)$$

$$y{-}momentum: \frac{\partial v}{\partial t}+u\frac{\partial v}{\partial x}+v\frac{\partial v}{\partial y}+w\frac{\partial v}{\partial z} = -\frac{1}{\rho_0}\frac{\partial p}{\partial y}-fu+\frac{\partial}{\partial x}\left(A\frac{\partial v}{\partial x}\right)+\frac{\partial}{\partial y}\left(A\frac{\partial v}{\partial y}\right)+\frac{\partial}{\partial z}\left(V_E\frac{\partial v}{\partial z}\right) \quad (1.2)$$

$$z - momentum: 0 = -\frac{1}{\rho}\frac{\partial p}{\partial z} - g \quad (1.3)$$

$$continuity: \frac{\partial u}{\partial x} + \frac{\partial v}{\partial y} + \frac{\partial w}{\partial z} = 0 \quad (1.4)$$

$$Tracer(Temperature\&Salinity)Equation: \frac{\partial T}{\partial t}+u\frac{\partial T}{\partial x}+v\frac{\partial T}{\partial y}+w\frac{\partial T}{\partial z} = -A_h\left(\frac{\partial T}{\partial x}+\frac{\partial T}{\partial y}\right)-\kappa_h\frac{\partial T}{\partial z}+Q \quad (1.5)$$

$$Equation of state: \rho = \rho\left(\theta, S, p\right) \quad (1.6)$$

where x, y, and z axes are directed eastward, northward and upward, respectively. The variable t represent time and T represents tracer (either temperature or salinity). Also, θ, S, ρ, p, and g represents potential temperature, salinity, density, pressure and the gravitational acceleration respectively. In these equations reference density ρ_0 and the gravitational acceleration g are constant coefficients. The variable $f = 2\omega \sin\varphi$ is the Coriolis parameter with ω and φ representing angular velocity and latitude respectively. This Coriolis parameter is dependent on latitude. Horizontal and vertical eddy viscosity are represented by A, and V_E respectively. Similarly, A_h and κ_h in the tracer equation represent horizontal and vertical diffusion coefficients of tracer. In general these eddy viscosity and diffusion coefficients are either constants determined from empirical relations or parameterized. The parameter Q in the tracer equation (1.5)is source/sink term for the tracer.

In the above set of equations first two equations (1.1), and (1.2) represent horizontal momentum. This is obtained after implementing Boussinesq approximation (described in Appendix-A). The third equation (1.3) is traditionally called as hydrostatic equation (described in Appendix-A). This is derived by performing scale analysis on the vertical momentum equation. Equation (1.4) represent continuity equation. It is derived by using the law of conservation of mass after considering the incompressible nature of the ocean fluid. Tracer equation (1.5) represents one equation each for temperature and salinity after implementing law of conservations of energy and salt respectively. Equation of state (1.6) relates ocean density to potential temperature, salinity and pressure. Appendix-A provides extended information on how these equations are derived from basic laws of physics.

Equations (1.3), and (1.6) are diagnostic in nature to provide p, and ρ respectively using information from other equations in the set of primitive equations. Horizontal momentum equations (1.1), (1.2), and two embedded equations of (1.5) are always prognostic in nature. Equation (1.4) acts as prognostic equation for sea level when the surface of the ocean is allowed to change freely (free surface condition). The prognostic equation for sea level is derived by vertical integration of the continuity equation over the full depth of the ocean. Below is the sea level equation given for convenience

$$\frac{\partial \eta}{\partial t} = -\left(\frac{\partial u}{\partial x} + \frac{\partial v}{\partial y}\right) + q_w \tag{1.7}$$

Where η is the sea level and q_w is fresh water flux.

Ocean interacts with the atmosphere through these prognostic equations. For example, transfer of momentum is communicated via the terms associated with viscosity coefficients in the horizontal momentum equations (1.1 and 1.2). Similarly, transfer of heat and freshwater from the atmosphere and land to the ocean is done by the soure/sink terms in the tracer equation (1.5). Transfer of freshwater from the atmosphere and land to the ocean is also communicated through freshwater flux term (q_w) in the sea level equation (1.7).

In-order to implement these primitive equations in a model to provide mean-

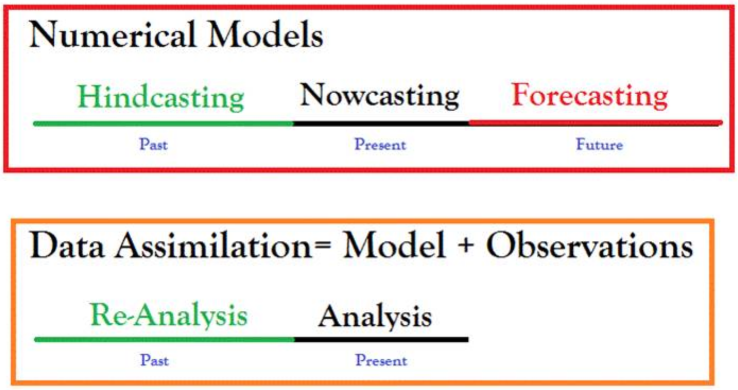

Figure 1.4: Schematic definitions of Forecast, Nowcast, Hindcast, Re-analysis and Analysis

ingful forecasts, nowcasts or hindcasts (see Figure 1.4 for the definitions), there are various other components that have to be developed and fixed with appropriate configuration. Also, there is a process to train the model using inputs from atmosphere and ocean climatologies to bring the model to the reality. Following sub-sections provide an overview on the various components in the model and on the process involved in training the model.

1.1.2.1 Horizontal and Vertical co-ordinates

All of the fore-mentioned primitive equations are expressed in Cartesian co-ordinate system (in which each point is specified uniquely in a plane by a pair of numerical co-ordinates, which are the signed distances from the point to two fixed perpendicular lines, measured in the same unit of length). However, spherical co-ordinates, which uses spherical angles in the horizontal direction and radial distances in the vertical direction, are a natural set of orthogonal curvilinear co-ordinates for representing geophysical flow (Figure 1.5). Due to its awkward coordinate singularity at North pole, which is within the Arctic ocean, most of the ocean models are typically written using angular co-ordinates that generalize the spherical angles. That is, they use general locally orthogonal co-ordinates to specify angular positions. These co-ordinates are called generalised orthogonal curvilinear co-ordinates

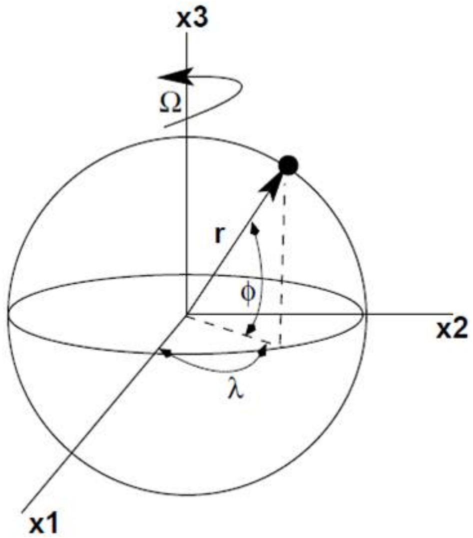

Figure 1.5: Schematic of spherical and Cartesian co-ordinates used for describing the motion of fluid parcels on rotating spherical planet. The co-ordinates are defined as $x1 = r\cos\varphi\cos\lambda$; $x2 = r\cos\varphi\sin\lambda$; $x3 = r\sin\varphi$. The co-ordinate origin is at the center of a sphere, and the rotation axis is aligned through the sphere north pole. The planet rotates with an angular velocity Ω in a direction counter clockwise when looking down from the north pole. The figure is reproduced from Chapter 3 of Griffies (2004)

(Figure 1.6).

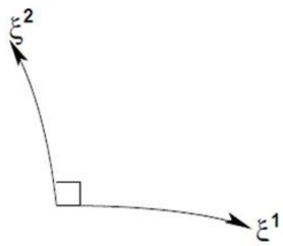

Figure 1.6: Generalized horizontal orthogonal co-ordinates of use for global ocean models. The co-ordinate lines intersect at right angles, but generally do not follow lines parallel to constant longitude or latitude. An infinitesimal horizontal region has area given by $dA = (h_1 d\zeta^1)(h_2 d\zeta^2) = dxdy$. For spherical co-ordinates $(\zeta^1, \zeta^2) = (\lambda, \varphi)$, the infinitesimal horizontal distances are $dx = (r\cos\varphi)d\lambda$ and $dy = rd\varphi$. The figure is reproduced from Chapter 3 of Griffies (2004)

Although most of the ocean model classes use the fore-mentioned generalised orthogonal curvilinear co-ordinates for representing flows in horizontal direction, each model class is distinguished from the other model class mainly based on the vertical coordinate axis. The choice of vertical coordinate represents the most fun-

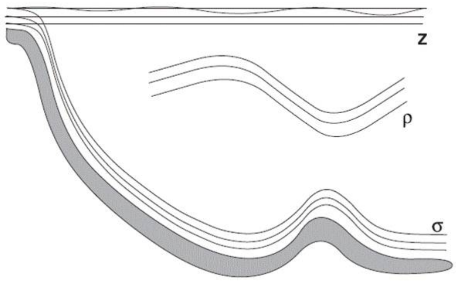

Figure 1.7: Schematic of an ocean basin illustrating the three regimes of the ocean germane to the considerations of an approximate vertical coordinate. The surface mixed layer is naturally represented using z-co-ordinates, the interior is naturally represented using isopycnal ρ co-ordinates; and the bottom boundary is naturally represented using terrain following σ co-ordinates. The figure is reproduced from Griffies et al. (2000)

damental choice that can be made when designing an ocean model. There are three fundamental vertical co-ordinates available in ocean modelling (Figure 1.7). They are (1) Depth or Z co-ordinate (2) Density or Isopycnal or ρ (rho) co-ordinate, and (3) Terrain following or σ (sigma; defined as the ratio of the pressure (p) at a given point in the ocean to the pressure at the top of the given domain (p_0); p/p_0)-coordinate. Each model class has advantages and disadvantages when simulating various flow regimes encountered in ocean modeling. For example, the depth or z-coordinate provides the simplest and most established framework for ocean climate modeling. It is well suited for situations with strong vertical/diapycnal mixing and/or low stratification, yet is cumbersome in the ocean interior and bottom. The density or ρ coordinate is less well established for climate modeling applications, but it has strong foundations in idealized configurations. It is well suited to model the observed tendency for tracer transport to be along neutral directions. The terrain following or σ (sigma)-coordinate provides a suitable framework in situations where capturing the dynamical and/or boundary layer effect associated with topography is important. It is particularly well-suited for modeling flows over the continental shelf and slope, but remains unproven in a global coupled climate modeling context. Significant advances are being made which show promise for future climate models, especially when used within a hybrid coordinate approach.

1.1.2.2 Discretization

After the mathematical and physical steps are finalized, the ocean modeler must formulate the equations of motion in a manner interpretable by computers. Such a formulation is called discretization. There are various approaches available for discretizing derivatives of the equations governing geophysical fluids. Examples include, forward, backward, centered finite difference, Runge-Kutta scheme, Adams-Bashforth scheme, Higher order schemes. The selection of a particular scheme depends on the efficiency of a scheme, for the selected spatial and temporal resolution, which in turn depends on spatial and temporal grids on which the derivatives are going to get discretized. Appendix-B provides a brief overview on spatial and temporal staggering of grids with a brief description on merits and demerits of a selected grid.

1.1.2.3 Parameterization

Models cannot simulate features and/or processes that are within the confines of a single grid box. Thus, we cannot realistically expect numerical models to resolve features at all scales, no matter how high the resolution, but the cumulative effects may still change the local ocean. As a result, a model must account for the total effect on the flow with a single number that represents friction within the grid box. The method of accounting for such effects, without directly calculating them, is called parameterization. Another way to think of parameterization is to numerically estimate the effects of a process (emulation) rather than model the process itself (simulation). There are two other main reasons for implementing parameterizatins. (1) computers are not yet powerful enough to directly treat the process of interest because the phenomena are either too small (sub-grid scale) or too complex to be mathematically simulated, and (2) some processes are often not understood well enough to be represented by an equation. Ocean models use many parameterization schemes for various reasons. Some of the most common processes that need to be parameterized in OGCMs are discussed in Appendix-C.

1.1.2.4 Training the model: Model Verification, Spinup and Inter-annual run

Once the model is built by code and configuration is fixed, it is essential to verify the model code to ensure that

- The model is programmed correctly
- The algorithms have been implemented properly
- The model does not contain errors, oversights, or bugs

Such a **verification** ensures that the specification is complete and that mistakes have not been made in implementing the model. Verification, however, does not ensure the model

- Solves an important problem
- Meets a specified set of model requirements
- Correctly reflects the workings of a real world process

The fundamental strategy of verification is the identification and quantification of errors in the computational model and its solutions. No computational model will ever be fully verified, guaranteeing 100% error-free implementation.

Next step after the model code verification is the model **spin-up**. At the start of the model spin-up, the model is initialized by using inputs from climatological values of temperature and salinity from databases with the velocity field set to zero. The model physics will spin up a velocity field in balance with the density field, even in the absence of forcing. As forcing (e.g. momentum, radaiation, fresh water fluxes) is applied, the velocity field will respond to it initially with transient flows that may not be realistic for an ocean that undergoes continuous, albeit always changing, forcing. The model is said to have finished spin-up only when it reach a state of statistical equilibrium under the applied forcing. In other words, it adjusts geostrophically to its initial state. It is usually difficult for basin-scale and global general circulation models to reach this state, as it can take hundreds of years. .

How long does it take for the ocean model to reach equilibrium?

- The deep ocean requires hundreds of years to adjust.
- The upper ocean only requires about 50 years or so.

In spin-ups of several decades (duration dictated by available resources) deep water mass properties away from strong currents or deepwater formation sites, will not evolve far from the initial state. To study upper ocean processes, such as ElNino, only the upper ocean (above the main thermocline) needs to be in equilibrium. Effectively, the spin-up time scale is the time needed for the first and second mode long Rossby waves (large-scale planetary waves) to cross the basin from east to west, affecting currents, and ultimately the watermass properties. Along the equator, the first mode baroclinic Rossby wave takes about 9 months to cross the Pacific; however the second, and higher, baroclinic modes travel slower. Hence, in the equatorial band, it takes several years for the spin-up to reach equilibrium. In the mid-latitudes, the long waves travel more slowly. It takes about 11 years for a Rossby wave to cross the Pacific. For a global ocean model, it will take several decades to achieve equilibrium in the upper ocean. It is important to understand, that an ocean model cannot be studied until this equilibrium is reached. If only the barotropic modes are considered, or the model is 2D, then the adjustment time will be much quicker, on the order of days, since the barotropic waves travel faster. It is also possible to reduce spin-up time by using data assimilation to nudge the model toward the observed state. Since SSH is the most widespread type of data coverage, this works best with barotropic models.

Also, if one is concerned only with the wind driven flows, including that arising from sea surface slopes resulting from Ekman pumping, a spin-up time on the order of days may be adequate. (Ekman pumping is the convergence or divergence of water in the Ekman layer due to spatial gradients in the Ekman transport.)

When implementing an ocean circulation model for a new domain, allowance must be made for spin-up time. This can be quite long for basin-scale models while regional models, which don't include deep ocean basins, may be spun up more quickly.

Once the model spin-up is over, it should be brought to the contemporary/real state. This is achieved by running the model further from spinup using inter-annual forcing for sufficient number of years, referred as **inter-annual run**. The model is said to have reached the contemporary/real state only when it captures the observed features realistically. In general, such a judgment is made by carrying out validation of the model outputs with respect to observations. This validation should ideally provide qualitative and quantitative view on the error that has been developed and sustained by the model during the whole process.

It should be obvious from the discussion on numerical ocean models that models develop errors in their simulations due to the uncertainty flown into it through various issues such as choice of vertical co-ordinates, model discretization, representation errors, and uncertainties in forcing and initial conditions. The errors in the model simulation, however, can be partially suppressed with data assimilation techniques by making use of observations.

1.1.3 Ocean Data Assimilation

Data assimilation is an analysis technique in which the observed information is assimilated into the model state by taking advantage of consistency constraints with laws of time evolution and physical properties (Jamet and Loisel, 2009). The data assimilation aims to provide accurate initial state for a numerical ocean forecast for instance. The optimal state of the ocean after performing data assimilation is called "analysis". The analysis generated from an assimilation system is, in principle, dynamically consistent and contain relatively less error compared to model background state.

There are two basic approaches to data assimilation: sequential assimilation, which only considers observation made in the past until the time of analysis, which is the case of real-time assimilation systems (for example, see Derber and Rosati (1989)) and non-sequential, where observation from the future can be used, for instance in a reanalysis exercise (for example Anderson et al. (1998)). Another distinction can be made between methods that are intermittent or continuous in time. In an intermittent method observations can be processed in small batches, and thus are usually technically convenient (intermittent data assimilation is used in most global operational systems, typically with a 6-h cycle performed four times a day). In a continuous method, observation batches over longer time window are considered, and the correction to the analyzed state is smooth in time, thus is physically more realistic. There are many assimilation techniques available in literature. A brief introduction on assimilation techniques that are being frequently adopted for oceanography is provided below.

Kalman Filtering: This technique is derived by Kalman in 1960. There are two steps in its sequential algorithm: (i) the forecast of the state vector and of its error variance, and (ii), the data forecast melding and error update, which include the linear combination of the dynamical forecast with the difference between the data and model predicted values for those data (i.e. data residuals). The matrix weighting these data residuals is called the Kalman gain matrix. The main advantage of the Kalman Filter is that it quantitatively generates its own error forecast and analysis. Implementation of original Kalman Filter technique is impractical for ocean applications. Due to this reason many flavours of Kalman Filters are developed, out of which Ensemble Kalman Filters, Local Ensemble Kalman Filters are mostly used in ocean and atmospheric applications.

Nudging or Newtonian Relaxation Scheme: This technique relaxes the dynamical model towards the observations. To do so, terms proportional to the difference between the data and state variables (i.e. data residuals) are added to the dynamical model. The coefficients in the relaxation can vary in time but cannot be too large to avoid model disruptions. They should be related to dynamical scales and a priori estimates of model and data errors. The nudging scheme simplifies the Kalman Filter by assigning a diagonal Kalman gain, of usually constant elements

Optimal Interpolation (OI): It is a simplification of the Kalman Filter. The data-forecast melding or analysis step is still a linear combination of the dynamical forecast with the data residuals, but in the OI scheme, the matrix weighting these residuals or gain matrix is empirically assigned. In the Kalman Filter, the gain is computed and updated internally. If the assigned OI gain is diagonal, the OI and above nudging scheme can be equivalent. However, the OI gain is usually not diagonal, but a function of empirical correlation and error matrices.

Variational Assimilation techniques (3D-VAR and 4D-VAR): All variational assimilation approaches perform a global (time-)space adjustment of the model solution to all observations and thus solve a smoothing problem. The goal is to minimize a cost function penalizing the (time-)space misfits between the data and ocean fields, with the constraints of the model equations and their parameters. In these variational schemes, the confidence on model and on observations is passed through separate matrices called model background error covariance and observational error covariance. The analysis generated from this method is sensitive to these prescribed matrices.

Each of these techniques differs in their numerical cost, their optimality, and in their suitability for real-time data assimilation (Bouttier and Courtier, 2002). Comprehensive description and discussion of the assimilation schemes can be found in Robinson and Lermusiaux (2000) and in Jamet and Loisel (2009).

1.1.4 Overview on Ocean Data Assimilation System

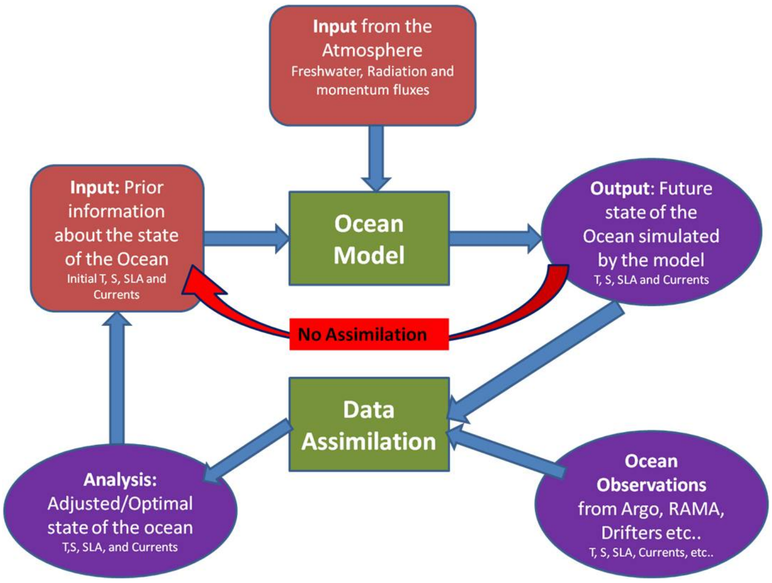

Figure 1.8: Block diagram providing an overview on ocean data assimilation system

Figure 1.8 provides an overview on ocean data assimilation system and shows various components involved in the whole system. In order to estimate the present state of the ocean, the core component of the system the "Ocean Model" need inputs from its previous run and present conditions of atmosphere at ocean surface and river runoff at river mouths. The outputs from the model are used as initial conditions for the next run in assimilation free system. If the assimilation is enabled, the assimilation schemes takes the present state of the ocean and all available/specified observations corresponding to the present state and provides ocean analysis corresponding to the present state. In general, this ocean analysis has less error compared to outputs from assimilation free run. These analysis are then used as initial conditions for the next run in assimilation enabled systems.

1.2 Motivation for setting up the Global Ocean Data Assimilation System at INCOIS

India is a country where the economy largely depends on agricultural production, which, in turn, is strongly dependent on the rainfall received over the Indian land mass during the summer monsoon months of June-September (Rajeevan and Sridhar, 2008). It is well known that the Indian summer monsoon rainfall shows large inter-annual variability both in terms of spatial distribution and intensity. A better forecast of the monsoon will aid the government in taking precautionary measures to tackle issues like deficits in food production, damage due to floods, etc. Therefore, the prediction of the inter-annual and seasonal variation of the Indian summer monsoon rainfall, particularly for the occurrence of extreme events like droughts and excessive rainfall is extremely important. However the skill of atmospheric and coupled models to predict the summer monsoon rainfall is not yet satisfactory (Gadgil and Srinivasan, 2011). For example, almost all the model predictions by the leading centers in the world using general circulation models of the atmosphere or of the coupled ocean-atmosphere system did not anticipate the large deficit in rainfall during the summer monsoon of 2009 (Nanjundiah, 2009). It is well known that the ocean SST plays a significant role in the modulation of the summer monsoon rainfall (Shenoi et al., 1999, 2002; Vecchi and Harrison, 2002; Joseph et al., 2005; Shankar et al., 2007; Francis and Gadgil, 2009). In addition, earlier modeling studies also have highlighted the significance of better oceanic initial conditions, particularly with regard to the upper ocean thermal structure, for improving the skill of climate model forecasts at the seasonal time scale (Balmaseda et al., 2009; Balmaseda and Anderson, 2009). Any inaccuracy in the upper ocean thermal structure, particularly in the SST strongly influences the atmospheric circulation in the coupled model (Balmaseda et al., 2009). In addition Balmaseda and Anderson (2009) showed that ocean initialization has a significant impact on the mean state, variability, and skill of coupled forecasts at the seasonal time scale. It is well known that, model forcing fields (surface flux products and wind products) have significant errors. These will inevitably lead to errors in the ocean model output. Data assimilation techniques are then used to improve the ocean state estimations. Hence the assimilation of ocean surface and subsurface data into an OGCM can improve the initial estimation of the ocean state, which in principle should improve the skill of seasonal forecasts.

Earlier studies reported significant improvements in the simulations of ocean state (ocean analyses) upon assimilating the hydro-graphic data (Balmaseda et al., 2007; Martin et al., 2007; Baehr et al., 2009; Smith et al., 2010). Past experience also suggests the use of synthetic salinity profiles in the assimilation along with the temperature profiles, in order to avoid problems due to the misrepresentation of density stratifications in the model and also to avoid data scarcity (Troccoli and Haines, 1999; Demirov et al., 1999; Sparnocchia et al., 1999; Maes and Behringer, 2000; De Mey and Benkiran, 2002; Troccoli et al., 2002; Haines et al., 2006) especially during pre Argo era. This approach has found to be promising over most of the regions in the global ocean except over those regions where salinity plays key role. After the advent of Argo program, uncertainties that were caused due to salinity are significantly reduced upon utilizing observed *in-situ* salinity profiles in the assimilation systems (Vidard et al., 2007; Balmaseda et al., 2007; Cazes-Boezio et al., 2008; Huang et al., 2008).

The demand for an improved global ocean analysis is high in the recent period. This is mainly because they offer dynamically consistent spatial and temporally complete products, which is an important thing for use in coupled ocean-atmospheric models and also to understand the ocean process in detail. Recent advances in ocean data assimilation and ocean observation networks enabled to reduce errors in ocean models, if any, which in turn gave confidence in building improved ocean analysis. The use of ocean data assimilation systems is increasing in the recent years. Recently, a new version of the Global Ocean Data Assimilation System (GODAS) has been developed at the National Centers for Environmental Prediction (NCEP), to increase the understanding and predictive capability of the oceans role in future climate change scenarios. This new system, which can assimilate *in-situ* temperature and salinity profiles, is part of the new Climate Forecast System-Reanalysis (CFS-R) at NCEP (Saha et al., 2010). The same CFS-R system except ocean data assimilation component is setup at Indian Institute of Tropical Meteorology (IITM), Pune under National Monsoon Mission by Ministry of Earth Sciences (MoES), Government of India to provide seasonal forecasts of monsoon. Setting up the GODAS at INCOIS (here after INCOIS-GODAS) and providing improved ocean analysis as ocean initial conditions for coupled ocean-atmospheric model at IITM, Pune improve seasonal forecasts of monsoon generated by IITM. Further, the ocean analysis products from the INCOIS-GODAS are also useful to understand dynamic & thermo-dynamic (temperature, salinity, currents and sea level) properties/phenomenon of the ocean over a range of spatio-temporal scales. These factors motivate us to setting up and operationalizing GODAS at INCOIS.

1.3 Scope and objective of the present study

The tropical Indian Ocean forms the major part of the largest warm pool on Earth, and its interaction with the atmosphere plays an important role in shaping climate on both regional and global scales. It differs from the Atlantic and Pacific in a number of climatically important ways. For example, the Asian continent drives the strongest monsoon on Earth, and the monsoonal winds generate large seasonal variations in ocean currents, many of which display annual reversals such as Somali current and the Southwest/Northeast Monsoon current south of India/Srilanka (figure 1.9 and figure 1.10 show schematic representation of ocean currents in the tropical Indian ocean during summer and winter). The tropical Indian Ocean is

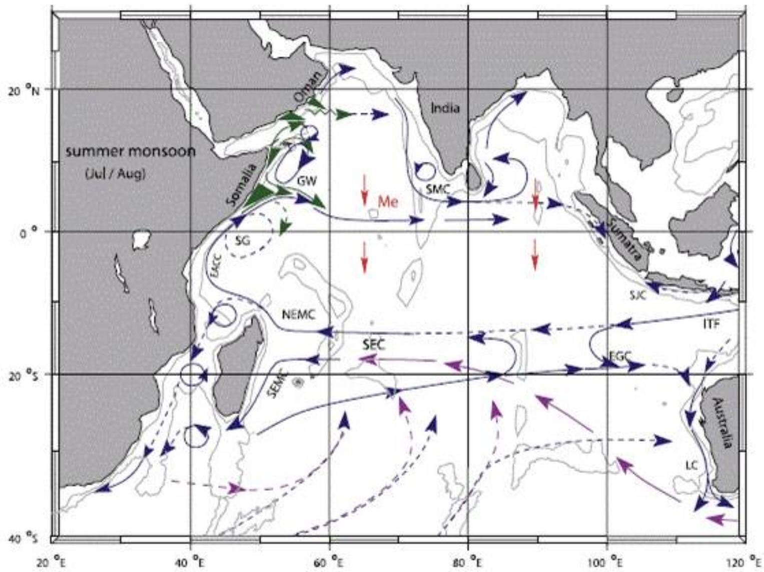

Figure 1.9: Schematic representation of identified current branches during the summer (southwest) monsoon. Current branches indicated (figure 1.10) are the South Equatorial Current (SEC), South Equatorial Countercurrent (SECC), Northeast and Southeast Madagascar Current (NEMC and SEMC), East African Coastal Current (EACC), Somali Current (SC), Southern Gyre (SG) and Great Whirl (GW) and associated upwelling wedges (green shades), Southwest and Northeast Monsoon Currents (SMC and NMC), South Java Current (SJC), East Gyral Current (EGC), and Leeuwin Current (LC). The subsurface return flow of the supergyre is shown in magenta. Depth contours shown are for 1000m and 3000m (grey). Red vectors (Me) show directions of meridional Ekman transports. ITF indicates Indonesian Throughflow. Both of the figure 1.9 and figure 1.10 figure are reproduced from Schott et al. (2009)

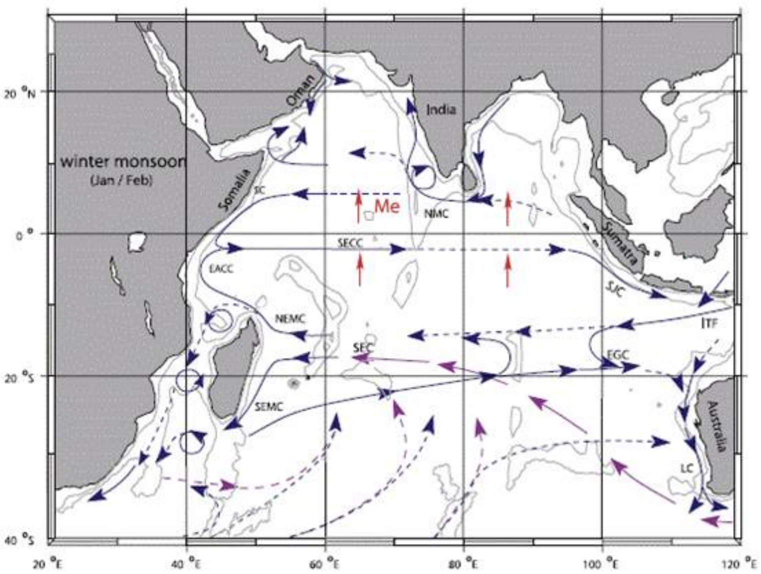

Figure 1.10: Same as figure 1.9 but for winter (northeast) monsoon

connected to South Atlantic, South Pacific and Antarctic Ocean at its southern boundary and is connected to tropical Pacific through a low-latitude exchange route, the Indonesian Throughflow (ITF). It is estimated that ITF transports approximately 10 Sv of Pacific waters into the IO, mostly within the upper ocean (< 400m). Observation (Davis, 2005; Ridgway and Dunn, 2007) and model (Speich et al., 2002, 2007) based studies indicate exchanges between the IO and other ocean takes place at intermediate depths at the southern boundary of IO as well. These processes emphasize the need for having a global model to study the tropical Indian Ocean processes.

It is well known that Indian Ocean was poorly sampled before Argo era. It resulted in the lack of deep understanding about the Indian Ocean compared to other oceans. The present study mainly focuses on delivering research quality ocean analysis for the tropical Indian Ocean by diagnosing ocean analysis fields from the assimilation system INCOIS-GODAS under various configurations. The focus on the Tropical Indian Ocean (TIO) is particularly important in the context of a well-developed **in-situ** Indian ocean observing system (IndOOS), that is being implemented by several nations in the Indian Ocean (Panel, 2006) to understand the influence of ocean dynamics in the TIO on the seasonal prediction of the monsoon. In delivering such a research quality ocean analysis, we quantify the impact of observed salinity assimilation, river runoff, importance of accurate wind products and relaxation. In the present study, we verify whether the quality of improved global ocean analysis from INCOIS-GODAS is at research quality by comparing with the global ocean analysis from other state-of-the-art ocean models. Finally, the application of INCOIS-GODAS to understand the importance of each global ocean observing system is demonstrated by carrying out a specialised set of experiments called Observation System Evaluation experiments (OSEs).

The thesis is organized in eight chapters, the present chapter being the first. The Chapter-2 provides details on the ocean model configuration, assimilation scheme, and data used for forcing, assimilation and for validation. Impact of assimilating temperature and synthetic salinity profiles with respect to assimilation-free model simulations, sensitivity of ocean analysis by different momentum forcing is examined in Chapter-3. Chapter-4 is devoted to the evaluation of ASCAT based gridded wind product using *in-situ* RAMA winds and QuikSCAT based gridded winds. Further, the suitability of momentum flux from the ASCAT product is examined by conducting sensitivity experiments using the INCOIS-GODAS. Impact of river runoff and observed salinity assimilation on the salinity analysis is discussed in Chapter-5. From the above study, a new INCOIS-GODAS configuration was set up with (1) incorporation of observed *in-situ* salinity profiles (2) incorporation of inter-annual monthly river-runoff, (3) strong SST relaxation to bring the model SST close to observations, and (4) forcing the model with satellite based winds. The ocean analysis obtained from this new configuration is then examined to demonstrate the skill of INCOIS-GODAS in capturing dominant modes of intra-seasonal and inter-annual variations in Chapter-6. The chapter also perform inter-comparison of global ocean analysis of INCOIS-GODAS with NCEP-GODAS and ECMWF-ORAS4 during the period 2004-2009. In the Chapter-7, results from OSEs are discussed to know the impact of each *in-situ* ocean observation network. Summary of the present study and data dissemination mechanisms of INCOIS-GODAS ocean analysis are provided in Chapter-8.

Chapter 2

Description of assimilation system, and Data used for the system and for validation

2.1 Configuration of the INCOIS-GODAS

The INCOIS-GODAS, configured at INCOIS, is an OGCM with an embedded ocean data assimilation scheme. The OGCM and the assimilation scheme implemented in INCOIS-GODAS are the MOM-4.0 and a 3DVAR respectively. The OGCM is a hydrostatic, primitive equation, free surface, Boussinesq ocean model with z-co-ordinates in the vertical and generalized orthogonal horizontal co-ordinates. It is fully global with an Arctic Ocean and an interactive ice model. The 3DVAR assimilation scheme, which was originally developed by Derber and Rosati (1989), assimilates both temperature and salinity. The newly configured INCOIS-GODAS is an improvement over the traditional NCEP-GODAS with respect to an extension of the model domain, an improved resolution of the model, a shorter assimilation window, different relaxation time scale (30 day) etc. The differences between INCOIS-GODAS and NCEP-GODAS are summarised in Table 2.1. Earlier ocean model sensitivity studies on model resolution (Megann and New, 2001; Hoteit

Table 2.1: Summary of differences between configurations of NCEP-GODAS and INCOIS-GODAS

	NCEP-GODAS	**INCOIS-GODAS**
OGCM	MOM3.0	MOM4.0
Domain	Quasi-Global	Fully Global - Implements Murray 1996 tripolar grid near the poles
Spatial resolution	1° in zonal and meridional. Meridional resolution is 1/3° with in 10°S-10°N	0.5° in zonal and meridional. Meridional resolution is 1/4° with in 10°S-10°N
Relaxation	Strong relaxation - 5 and 10 day for SST and SSS respectively	Weak relaxation - 30 day for both SST and SSS
Assimilation	Assimilation window of 15 days. Performs assimilation every 6hr to get analysis correction. This analysis correction is updated equally for the next few time steps	Assimilation window of 10 days. Performs assimilation every 6hr to get analysis correction. This analysis correction is updated only once

et al., 2008), relaxation (Killworth et al., 2000; Kamenkovich and Sarachik, 2004), and the assimilation window (Huang et al., 2010) have indicated that the improvements to the model such as mentioned above have the potential to enhance the quality of ocean analysis. This is one of our motivations to carry out evaluation of INCOIS-GODAS in chapter 3. The detailed explanation on the model and assimilation scheme is given in the following two sections.

2.1.1 The Ocean General Circulation Model

The OGCM in INCOIS-GODAS, the MOM-4.0 implements the tripolar grid developed by Murray (1996). Northward of $65°N$, it uses a rotated bipolar grid that places two poles over land, which eliminates the singularity in the northern ocean. Southward of $65°S$, it uses a regular latitude and longitude grid. The primitive equations are discretized on an Arakawa B-grid. The model has a uniform zonal resolution of 0.5° and a variable meridional resolution of 0.25° within 10° of the equator, which decreases exponentially from $10°S$ ($10°N$) to $30°S$ ($30°N$) to maintain a 0.5° meridional resolution polewards from $30°S$ ($30°N$). The model domain with spatial grid resolution is shown in figure 2.1. There are 40 layers in the vertical with 27 layers in the upper 400 m, and the maximum bottom depth is approximately 4.5 km. The vertical resolution is 10 m from the surface to 240 m depth and gradually increases to about 511 m in the bottom layer. The bathymetry is based on a coarsened version of the topography data by Andrew Coward and David Webb at the Southampton Oceanography Centre.

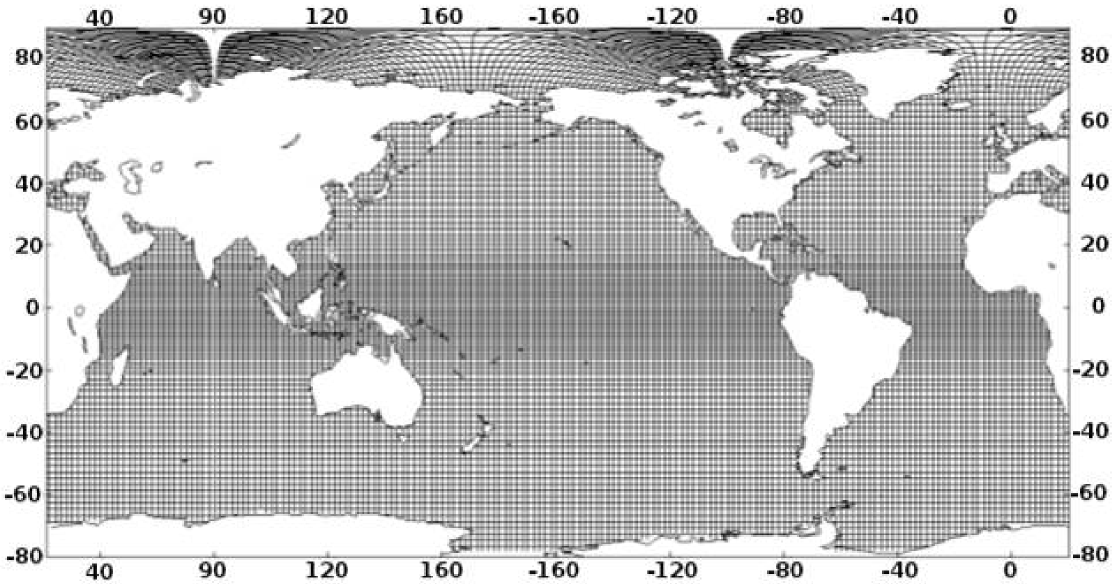

Figure 2.1: The schematic diagram of model domain and spatial grid resolution. The resolution of the grid is reduced by 4X for display. The resolution is $1/2° \times 1/2°$ increasing to $1/2° \times 1/4°$ within 10° of the equator. The grid is distorted in the Arctic.

Vertical mixing follows the non-local K-profile parameterization of Large et al. (1994). The horizontal mixing of tracers uses the iso-neutral method developed by Gent and Mcwilliams (1990) (see also Griffies et al. (1998)). The Smagorinsky viscosity scheme, with Smagorinsky isotropic viscosity coefficient set to 0.9, is used for horizontal momentum viscosity (Griffies and Hallberg, 2000). To account for background horizontal/vertical diffusivities, we used the Bryan-Lewis diffusivity model (Bryan and Lewis, 1979). The diffusivity is allowed to vary with respect to latitude, depth, and space. The expression for vertical diffusivity is

$$A_{HV}(Z) = 10^{-4}\left\{\eta + \left(\frac{\alpha}{\Pi}\right)\tan^{-1}[\beta \times 10^{-3}(Z-\mu)]\right\} \tag{2.1}$$

Where A_{HV} is vertical diffusivity, Z is depth and values of η, α, β and μ are 0.75 (0.65), 0.95 (1.15), 4.5 (4.5) and 2500 (2500) respectively above (within) the transition latitude 35°. The horizontal diffusivities are roughly $0.3 \times 10^{-4} m^2 s^{-1}$ ($1.3 \times 10^{-4} m^2 s^{-1}$) in the upper (deep) ocean. These values are time-independent.

The shortwave penetration scheme of Morel and Antoine (1994) is used to distribute incident surface radiation below the ocean surface. The amount of short wave radiation penetrating across a given depth is estimated by $Q_{pen} = 0.47 Q_{shortwave}[V_1 e^{-h1/\zeta 1} + V_2 e^{-h2/\zeta 2}]$, where $\zeta 1$ and $\zeta 2$ are the e-folding depths of long visible and short visible and ultraviolet wavelengths, and h is depth in meters. The parameters V_1, V_2, $\zeta 1$ and $\zeta 2$ are estimated from monthly chlorophyll-a climatology (mg/m^3) data. We use the SeaWiFS-based chlorophyll-a climatology (constructed from 1999 to 2001) and set the maximum depth to 100 m for the penetration of shortwave radiation. Based on the climatology used in our model, $\zeta 1$ does not exceed 3 m while $\zeta 2$ will vary between 30 m in oligotrophic waters and 4m in coastal waters. Throughout most of the ocean, the parameter V_1 is less than 0.5 and the parameter V_2 is greater than 0.5. In the present model configuration, we fix the river water insertion thickness at the boundary as 40 m. The model integration time step is 1800s and uses the two-level time stepping scheme suggested by Griffies (2004). The baroclinic and barotropic time splitting (Griffies (2004) and references there in) with respect to model integration time step are set to 1 and 80 respectively.

2.1.2 Assimilation scheme

The INCOIS-GODAS uses a 3DVAR assimilation scheme, which was originally developed by Derber and Rosati (1989). It was adopted for operational use at NCEP, where it has undergone further development to assimilate salinity profiles (Behringer and Xue, 2004; Behringer, 2007; Huang et al., 2008). The functional to be minimized is

$$I = \frac{1}{2}(T^T E^{-1} T) + \frac{1}{2}\left\{[D(T) - T_0]^T F^{-1}[D(T) - T_0]\right\} \tag{2.2}$$

where the vector T represents the correction to the first-guess prognostic tracers (temperature and salinity) computed by the model, E is the first-guess error covariance matrix, $D(T) - T_0$ represents the difference between the tracer and first guess, D is an interpolation operator that transforms the first-guess tracers from the model grid to the observation locations, and F is the observation error covariance matrix for the tracers. Temperature and salinity are treated as uncorrelated to get better simulations in regions where water mass transformation is important. In this sense, the system is univariate and E is thus block-diagonal with respect to temperature and salinity. The horizontal covariance is approximately a Gaussian that is modelled by repeated applications of a Laplacian smoother. The zonal and meridional scales of the function decrease with increasing latitude and the zonal scale is stretched with respect to the meridional scale by a factor of 2 within 10° to the equator. The zonal and meridional scales are approximately 880 km and 440 km respectively at the equator and 220 km and 220 km at $60°N$. The vertical covariance is also a Gaussian function modelled by a Laplacian smoother with a vertical scale that increases with depth as the vertical grid cell dimension; thus near the surface, the scale is approximately 10 m, while at 950 m the scale is 224 m. The estimated first-guess error variances for temperature and salinity are scaled by the square root of the local vertical gradient of the respective fields taken from previous model output, except where the vertical gradient vanishes, in which case a constant value 0.395 $(^{\circ}C)^2/m^2$, and 0.0790 $(psu)^2/m^2$ is specified. In the present study, the background error covariance matrix updated every 5th day. The background error covariance is estimated online based on the 5-day averages of temperature and salinity. For temperature, the estimated error variances are normalized to have a global maximum of 0.4 $(^{\circ}C)^2$ and a constant value of 0.12 $(^{\circ}C)^2$ in the mixed layer. The corresponding values for salinity are 0.08 $(psu)^2$ and 0.06 $(psu)^2$. These values were arrived at through a tuning process; their relatively small size is a consequence of observations being inserted multiple times over a 10-day window.

The observational errors for temperature and salinity are handled in the same way and both vary in space and time. The observational temperature variances are normalized to have a maximum value of 1.6 $(^{\circ}C)^2$ in the thermocline and a minimum of 0.8 $(^{\circ}C)^2$. The corresponding values for the observational salinity errors are 0.16 $(psu)^2$ and 0.08 $(psu)^2$. These error variance estimates are meant to include errors of representation due to variability contained in real world observations that cannot be resolved by the model.

Temperature and salinity profiles are assimilated at 6-hour intervals using all observations from the 10-day assimilation window. The more distant a profile is in time, the less weight it receives in the assimilation. This approach allows relatively sparse ocean observations to have a greater impact on the model state (Derber and Rosati, 1989; Behringer et al., 1998). In the present assimilation system, the assimilation is being done for the region $60^{\circ}S$-$60^{\circ}N$ and upto 750 m depth (30 levels).

In the present assimilation system, the SST and SSS is slowly nudged (relaxed) towards observations at each time step in the model via a Newtonian damping term in the equation of the variable

$$\frac{\partial T}{\partial t} = \beta(T_{obs} - T) \tag{2.3}$$

Where t is time and T is the variable of interest to be nudged, T_{obs} is the observation, and β is the relaxation/nudging coefficient which is constant and have units of inverse of time.

$$\beta \propto t_d^{-1} \tag{2.4}$$

In the above equations, small value of t_d implies strong nudging towards observations, conversely, large values of t_d implies lesser influence of observations. In the current system, unless specified, we use weak (t_d=30 day) relaxation for both SST and SSS. The purpose of using relaxation at the surface is to provide a constraint on the ocean at the interface with the atmosphere, and compensate for possible model drift due to errors in the surface heat and momentum fluxes.

2.2 Data sets used for INCOIS-GODAS

INCOIS-GODAS uses rich collection of data sets for forcing, relaxation and assimilation. Summary of the datasets used in the system, unless specified, as forcing fields, for assimilation, relaxation is given in 2.2. Temperature and salinity profiles collected by various ocean observations platforms such as RAMA (McPhaden et al., 2009b), TAO/ TRITON (McPhaden, 1993), PIRATA (Servain et al., 1998), moored buoys, expandable bathy thermographs (XBTs), and Argo profiling floats (Freeland et al., 2010), over the entire globe are obtained from US Global Ocean Data assimilation Experiment (USGODAE) Monterey Data Server and the National Oceanographic Data Center (NODC) World Ocean Database (WOD). The data is been merged without any duplication. Before sending temperature and salinity profiles for assimilation, these profiles are being sent for Quality checks. Quality control (QC) was performed independently using the system developed at NCEP for the near real-time version of GODAS used in operations. This QC algorithm is same as that used in Huang et al. (2008). The system checks for various flaws, for example, spikes, gaps, hooks at the top and bottom. If flaws can

Table 2.2: Source, temporal and spatial resolution and accuracy of data sets used in the model

Parameter	Data source	Spatial and temporal resolution	Reference
Sea Surface Salinity	World ocean Atlas 2001; ftp.nodc.noaa.gov	1°, Annual Climatology	Conkright et al. (2002)
Reynolds SST	ftp.emc.ncep.noaa.gov	0.25°, daily	Reynolds et al. (2007)
Gridded fields of annual climatological river runoff (Global; wide spread)	data1.gfdl.noaa.gov	1°, annual climatology	Large and Yeager (2004)
Gridded fields of River Runoff (Global)	data1.gfdl.noaa.gov	1°, Monthly; Data up to 2007. From 2008, monthly climatology is used to extend up to 2012	Dai et al. (2009)
River Runoff for Ganga and Brahmaputra	Personal communication	Monthly time series; This information is clubbed with gridded River runoff	Papa et al. (2012)
NCEP-R2 fluxes	ftp.emc.ncep.noaa.gov	≈ 2.5°, daily	Kanamitsu et al. (2002)
QuikSCAT gridded winds	apdrc.soest.hawaii.edu	Available up to 15 November, 2009. 0.25°, Daily	Wentz et al. (2001)
DASCAT gridded winds	ftp.ifremer.fr	Used as a successor of QuikSCAT (From 16th November, 2009) 0.25°, Daily	Bentamy and Fillon (2012)
Temperature and Salinity profiles	USGODAE Monterey Data Server and the NODCs World Ocean Database (WOD)	Point wise QC'd profiles	Huang et al. (2008)

be fixed (e.g spikes, hooks), the profile is retained, otherwise it is deleted. Outliers are identified and removed through comparison with 2 monthly climatologies, one based on the WOD and one based only on the Argo data set. The QC system was tuned and extensively cross-checked by visual inspection.

As part of the present study, some of the experiments use synthetic salinity for assimilation. Synthetic salinity is actually constructed based on the local climatological temperature and salinity correlation and the observed Temperature(z). So, for each Temperature(z) observation, there is a corresponding Salinity(z) = F(Temperature(z)), where F represents the local correlation.

2.3 Data and methodology used for validation

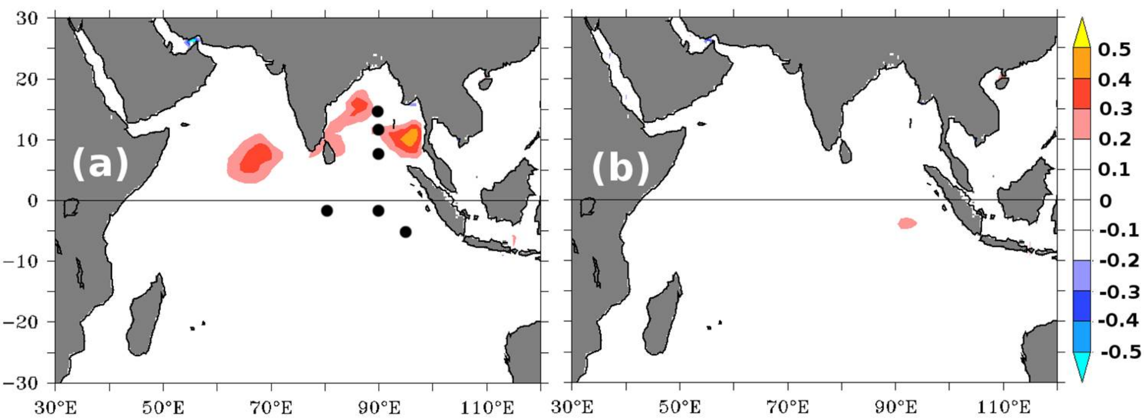

Figure 2.2: Difference in the RMSDs of salinity (psu) between the assimilation experiments where full observations are assimilated and partial observations are assimilated (full-partial). Panels (a) and (b) represents the differences pertained to *TS'* and *TS* respectively. Black circles on the panel *a* indicate the locations of temperature and salinity profiles withheld from assimilation

In order to have some independent source of temperature and salinity profiles, the profiles within 0.5° ($\approx 50km$) radius near the RAMA locations of $1.5°S\&80.5°E$, $1.5°S\&90°E$, $5°S\&95°E$, $8°N\&89°E$, $12°N\&90°E$ and $15°N\&90°E$ are not been assimilated and the locations are shown in figure 2.2. It is worth mention here that dropping profiles from these locations does not (does) affect the quality of

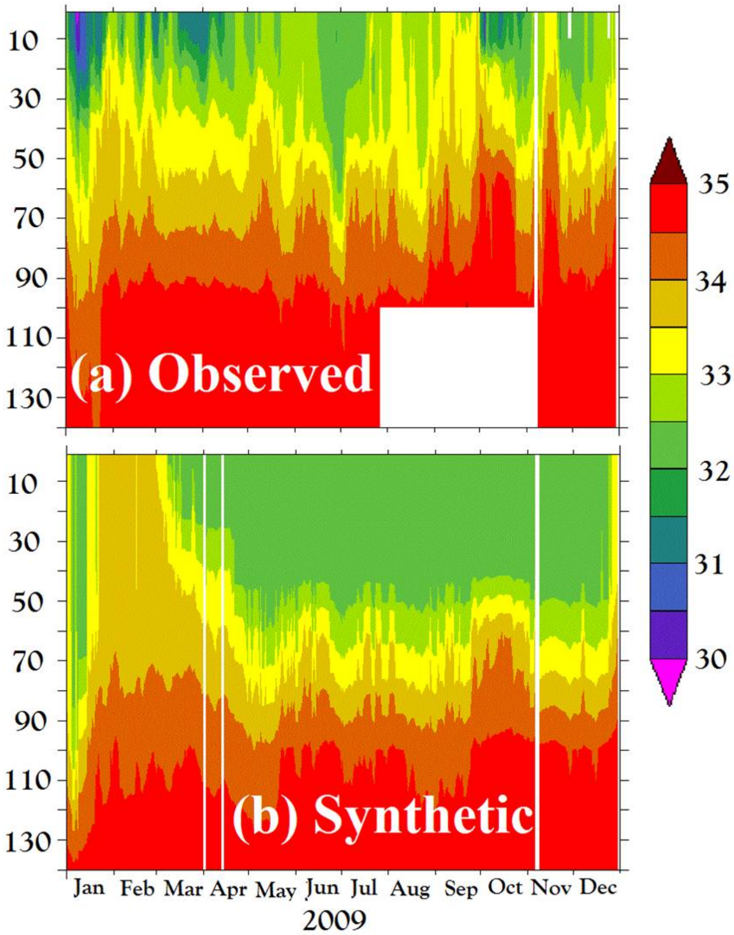

Figure 2.3: Depth-time sections of in-situ (a) observed and (b) synthetic salinity at $15°N, 90°E$

ocean analysis in the experiments where *in-situ* salinity (synthetic salinity) is used for assimilation. For example, it can be inferred from the figure 2.2 that dropping the profiles from the fore-mentioned locations improves the quality of SSS in *TS'* (figure 2.2a) significantly whereas no significant changes in the case of TS (figure 2.2b). It is found that synthetic salinity profiles, constructed from local T-S relationships, are far from real (in-situ) salinity profiles in the BoB (figure 2.3). This might be the reason behind the observed discrepancies in the quality of *TS'* in the BoB. It is worth mention here that the present study search for an improved configuration than *TS'*. The results from chapter 3 and 5 recommend observed salinity assimilation instead of synthetic salinity assimilation for an improved ocean analysis. In-fact ocean analysis from such a configuration (use of observed salinity for assimilation) is used in the present study to understand the impact of each *in-situ* ocean observation networks inversions (chapter 7). Thus it is reasonable to neglect the sensitivity of *TS'* to dropping profiles at fore-mentioned locations for assimilation.

Different types of satellite and in-situ data sets are used to validate the model output. Summary, such as source, resolution, accuracy of the data sets used for the validation is in Table 2.3. The ADCP measures currents from the sea surface down to 330 m depth at vertical intervals of 10 m. However, to avoid contamination of signals reflected at the surface as well as the limited data coverage at deeper levels, only the data between the depths of 40 m and 200 m are used in this study. The new OSCAR currents, employed in the present work, are available on $1/3° \times 1/3°$ spatial and 5-day temporal resolution. The OSCAR data processing system calculates sea surface currents from satellite altimetry (AVISO-Archiving, Validation and Interpretation of Satellite Oceanographic data), vector wind fields (QuikSCAT), as well as from sea surface temperature (Reynolds et al., 2007) using quasi-steady geostrophic, local wind-driven, and thermal wind dynamics (Dohan and Maximenko, 2010). The technique is tuned to best represent the ageostrophic motion of the 15 m drogue drifters relative to the surface wind stress. Near the equatorial regions, the new OSCAR data processing system uses a realistic shear model, based on Stommel (1960), for the Ekman component. This produces much more accurate results on the equator compared to older version of OSCAR product. Also, in the new version of OSCAR data processing system, a unique set of orthogonal polynomial basis functions, symmetric on the equator, are applied to solve the geostrophic and Ekman terms across the equatorial singularity. With these improvements, the disparity on the equator between the mean satellite-derived currents and drifter climatologies is practically eliminated in the new version of OSCAR currents (`www.oscar.noaa.gov/methodology.html`). In

Table 2.3: Source, temporal and spatial resolution and accuracy of data sets used for validation

Parameter	**Data source**	**Spatial and temporal resolution**	**Accuracy**	**Reference**
AVISO Blended Sea surface height anomaly	www.aviso.oceanobs.com	$0.33° \times 0.33°$, 7-day composite	2.5-4 cm	AVISO (2008)
TMI AMSRE SST	ftp.discover-earth.org	0.25°, daily	–	-
Reynolds SST	ftp.emc.ncep.noaa.gov	0.25°, daily	–	Reynolds et al. (2007)
Temperature and Salinity (at independent locations)	www.pmel.noaa.gov/tao	Daily time series data at 1.5, 25, 50, 75, 100, 125,150, 200, 250, 300, 500, 750 m	$\pm 0.003°C$ &$\pm 0.05psu$	McPhaden et al. (2009b)
EN3V2a - Gridded fields of temperature and salinity	www.metoffice.gov.uk	1°, Monthly	–	Ingleby and Huddleston (2007)
RAMA currents	www.pmel.noaa.gov/tao	Daily $\pm 5cms^{-1}$, $\pm 5°$	–	McPhaden et al. (2009b)
OSCAR current	www.oscar.noaa.gov	1°, 5-day	-	Bonjean and Lagerloef (2002)
ADCP current profiler	www.pmel.noaa.gov/tao	Daily	$\pm 5cms^{-1}$, $\pm 5°$	–
Aquarius based gridded Sea Surface Salinity	podaac-ftp. jpl.nasa.gov	Weekly	0.3 psu	Lagerloef et al. (2013)

general, OSCAR provides reasonably accurate ocean surface currents in off equatorial regions (Bonjean and Lagerloef, 2002). Validation and error analysis of the new version of OSCAR surface currents in the Pacific Ocean carried out by Johnson et al. (2007) and they showed that the OSCAR product provides reasonably accurate zonal surface current variability in the near-equatorial regions too. Moreover, Sikhakolli et al. (2013) has done a comprehensive evaluation of the OSCAR currents in the TIO. They have shown that the spatial patterns, including in the Equatorial region, are well captured by OSCAR currents. They have found correlations of the order 0.75 in the Equatorial region for zonal current (zonal current is dominant over meridional current in the EIO). This new OSCAR product has been used for the model validation and to address various research problems in the TIO (e.g. Joseph et al. (2012), Chakraborty et al. (2014)).

All of the data sets, which were used for model validation, were interpolated to the horizontal and vertical grids of the model. A method suggested by Sprintall and Tomczak (1992) is used to estimate mixed layer depth (MLD), isothermal layer depth (ILD), and barrier layer thickness (BLT) with deltaT set to $0.5°C$. Quantitative analysis is performed by calculating statistical parameters such as standard deviation (STD), correlation, mean difference (bias; model-observation) and root mean square difference (RMSD). All of the statistical calculations are done only during the period when both data sets are available. For ease interpretation we define December-January-February (DJF), March-April-May (MAM), June-July-August (JJA), and September-October-November (SON) as winter, spring, monsoon, and fall (post monsoon) respectively.

Chapter 3

Evaluation of the INCOIS-GODAS

3.1 Introduction

One of the important stages in building any assimilation system is to evaluate it's performance with particular emphasis on it's ability to replicate the variability on scales resolvable by the system/model. Such an evaluation determines to what extent the model is an accurate representation of the real system being modelled. The insights gained from model evaluation/validation will be useful for the improvements of the model's ability to capture realistic scenarios and for establishing the limitations of a model.

The ocean analysis products generated from operational NCEP-GODAS were validated on numerous occasions (Behringer and Xue, 2004; Behringer, 2007; Huang et al., 2008, 2010, 2012). However, there are considerable differences between NCEP-GODAS and INCOIS-GODAS (as explained in chapter 2). Further, the validation of the ocean parameters over the TIO is particularly important in the context of a well-developed *in-situ* Indian ocean observing system (IndOOS), that is being implemented by several nations in the Indian Ocean (Panel, 2006) and to understand the influence of ocean dynamics in the TIO on the seasonal prediction of the monsoon. The primary objective of this chapter is to report on the quality of the ocean analysis obtained from the INCOIS-GODAS in the TIO.

The present chapter also wants to identify problems in the assimilation system and reports the possible source of these problems. Further, this chapter examines the sensitivity of INCOIS-GODAS to momentum flux forcing and assimilation, based on the experiments carried out with different wind products: NCEP2 (Kanamitsu et al., 2002) and QuikSCAT (Wentz et al., 2001); and a free run without data assimilation (The details of the experiments are discussed in the following section). The analysis is performed for the period of January, 2004 through October, 2009. The selection of the analysis period is for the following reasons: (1) The number of *in-situ* profiles available for the assimilation in the Indian Ocean region is very sparse before 2004 and (2) The QuikSCAT mission was terminated in November, 2009. This chapter is organised as follows. Section 3.2 provides a description of the experiments carried out for this chapter. The results obtained from the validation of the ocean analyses are discussed in section 3.3. A summary of this study and recommendations are given in section 3.4.

3.2 Experiments Performed

In the first experiment, the INCOIS-GODAS is forced with NCEP2 heat, momentum and freshwater fluxes (Kanamitsu et al., 2002), and assimilates temperature and synthetic salinity and is denoted as the *TS'*. Synthetic salinity profiles are constructed from temperature observations using statistical relationships between temperature and salinity observations as explained in chapter 2. The *TS'* was performed for the period 2003 to 2009 using a restart file obtained from the assimilation system NCEP-GODAS. The NCEP2 precipitation and the annual mean value of the river runoff provided by Large and Yeager (2004) have been used for freshwater forcing. We set 40m as the river incursion thickness for mixing river runoff in the model. The turbulent fluxes of sensible and latent heats were calculated in the model using the COARE bulk algorithm (Fairall et al., 2003) with the

NCEP2 wind speed, specific humidity and air temperature, and the model SST.

High-resolution measurements by the QuikSCAT scatterometer reveal a rich diversity of persistent small-scale features in the global wind field that cannot be simulated by numerical weather prediction models (Chelton et al., 2004). Further, a number of studies have reported the superiority of the QuikSCAT wind product over the NCEP product (Agarwal et al. (2007); Kumar et al. (2012); and references therein). Earlier studies have shown that an ocean model forced with high resolution satellite derived wind fields provides a better simulation of subsurface features, SST, coastal currents and coastal upwelling processes compared to an ocean model forced with model based wind fields (Kang and Kug, 2000; Dong and Oey, 2005; Sharma et al., 2007; Agarwal et al., 2007; Jiang et al., 2008). For example, Agarwal et al. (2007) showed considerable improvements in model simulations when they were forced with QuikSCAT winds compared to NCEP winds. Considering these results, we have designed one more experiment replacing NCEP2 momentum flux with QuikSCAT momentum flux for the same period (2003-2009), denoted as the *QTS'*. In order to realize the impact of assimilation on the quality of ocean analysis, we conducted one more experiment similar to *TS'* with the assimilation disabled and it is denoted as *XA*.

3.3 Validation of INCOIS-GODAS

3.3.1 Temperature

Since the SST within the top model grid cell (5m) is relaxed to Reynold's SST with a weak 30 day time-scale, the GODAS derived SST is verified for consistency with the same Reynold's SST. It is worth mentioning here that the relaxation is so weak that model SST fields from experiments with and without relaxation are very similar. Figure 3.1 shows the seasonal evolution of the multi-year average (2004-2009) SST bias between (a) *XA* and Reynolds, and (b) *TS'* and Reynolds. Since,

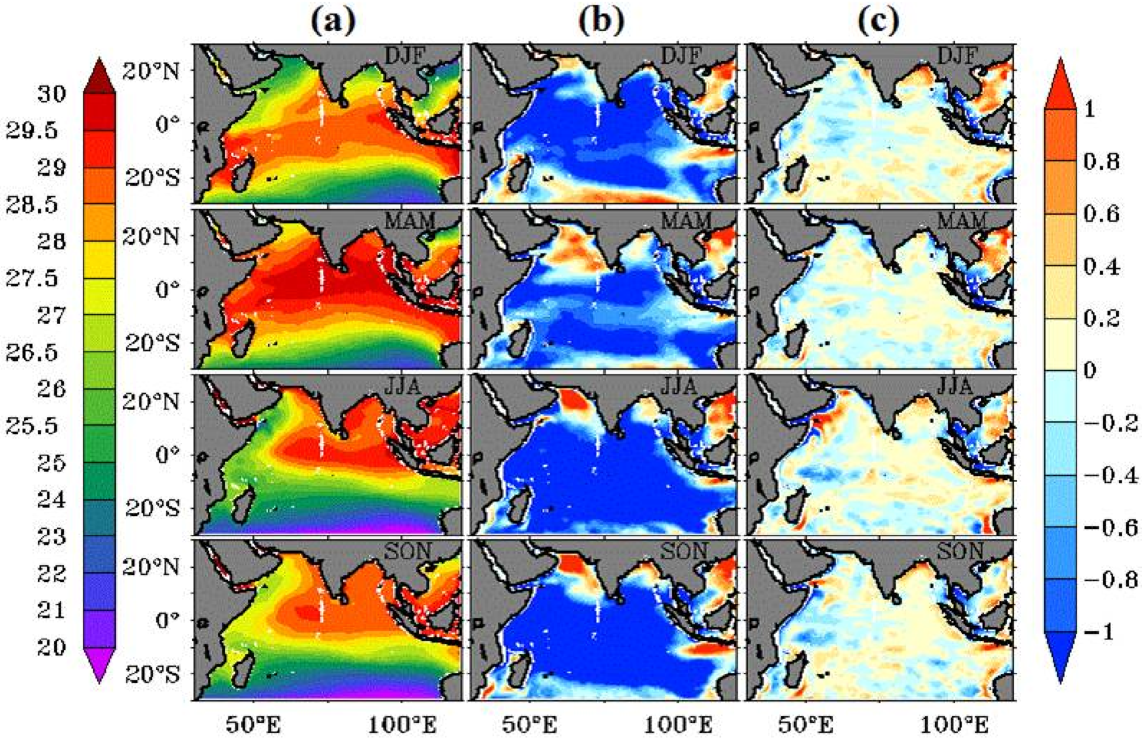

Figure 3.1: (a) Seasonal mean of observed SST (TMIAMSRE). The seasonal SST ($°C$) bias between model and observation. (b) *XA* - Observed, (c) *TS'* -Observed. In the figure, DJF, MAM, JJA, and SON represent December-January-February, March-April-May, June-July-August, and September-October-November respectively

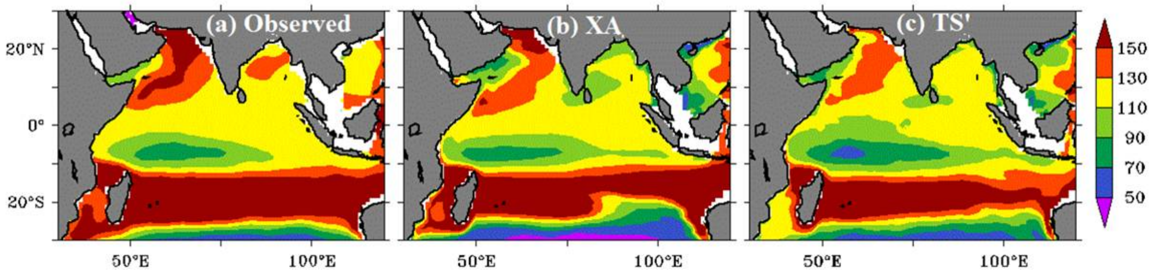

Figure 3.2: Mean depth of $20°C$ isotherm derived from (a) Observation (EN3V2a), (b) *XA*, and (c) *TS'*. Units are in *meters*

the SST field simulated by *QTS'* shows similar features as that of *TS'*, the *QTS'* is not shown here. Comparing Figures 3.1a and 3.1b, it is clear that assimilation improves the SST significantly. The improvements are larger than $1°C$ over most of the regions in the TIO. It can be observed that the model with assimilation realistically reproduces the well-known seasonal cycle in the TIO. Generally, the model with assimilation shows a very small warm bias ($0.3°C$) compared to the observations with the exception of a very few localized regions such as the head-bay, the Somalia coast and the South-Western EIO. The SST differences between the assimilation experiment and observations in these regions are relatively large and have a strong seasonal dependence. For example, SST from *TS'* in the head-bay shows a warm bias ($> 1°C$) during the winter monsoon and also during the summer monsoon. This warm bias disappears during the spring after the winter season and during the fall at the end of the summer monsoon season. The SSTs in assimilation experiments also show a warm bias ($> 1°C$) along the coasts of Somali and Oman during the summer monsoon. SSTs from all experiments show a cold bias (of around $0.5°C$) in the South West EIO region (Seychelles-Chagos thermocline ridge) during the winter. A recent study by Foltz et al. (2010) showed that the oceanic entrainment of cold thermocline water into the mixed layer due to a shallow thermocline plays an important role in modulating the mixed layer temperature in this region on a seasonal time-scale. The analysis shows that the thermocline, as simulated by assimilation experiments, is relatively shallow with respect to the Argo gridded climatology (figure 3.2). The relatively shallow thermocline in the assimilation experiments might have led to a greater entrainment of the cold thermocline water into the mixed layer, thus producing the cold bias in the assimilation experiments. The probable reasons for the discrepancies in the head bay and the Somali region are discussed in next sections. In the assimilation experiments, excluding these particular regions and time periods where there are larger biases, the overall model vs observation differences, are only $-0.2°C$

to $+0.2°C$. It is interesting to note that the correlation between the model SST and the observations is larger than 0.8 in most regions in both the *TS'* and *XA* (Figure 3.3). In the vicinity of the central EIO and along the whole west coast of India, the correlations are slightly less than $0.7°C$. However, correlations of SST with observations are relatively better in the assimilation experiments as compared to the experiment without assimilation, particularly over the central EIO. The above results indicate that weak SST relaxation, without temperature and synthetic salinity assimilation, is an inefficient way to capture the SST patterns in a realistic fashion.

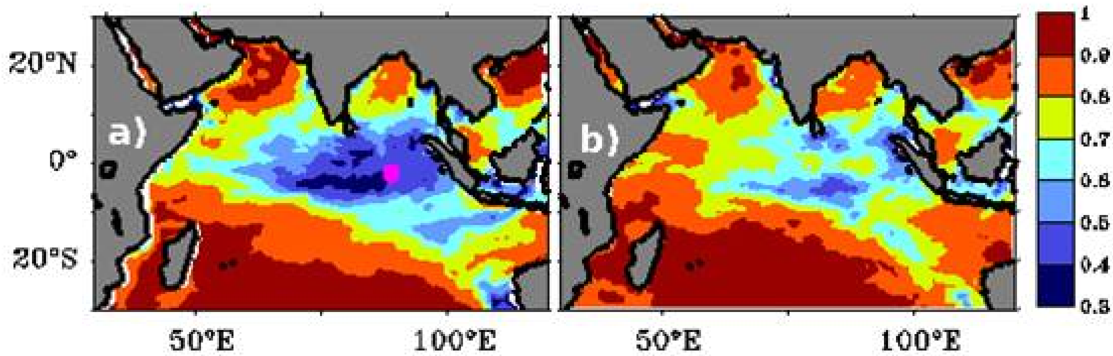

Figure 3.3: The correlation between SST obtained from (a) *XA* and Reynolds, and (b) *TS'* and Reynolds during 2004-2009

Depth wise comparison of temperature between the *XA* and *in-situ* observation (RAMA) at various independent locations suggest that the *XA* could not pick the observed temperature variations above the thermocline well and also there is a overall negative bias (Figure 3.4). However, both the assimilation experiments (*TS'* and *QTS'*) could simulate temperature structure realistically. Significant improvements are observed in both the assimilation experiments over *XA*. The improvements are especially significant between 0-150m and reach $1.5°C$ in terms of RMSD. It is interesting to observe that these improvements show seasonal dependency especially in the BoB. For example, improvements are large (by up to $2.5°C$) during monsoon and post monsoon season at $8°N \& 90°E$ location com-

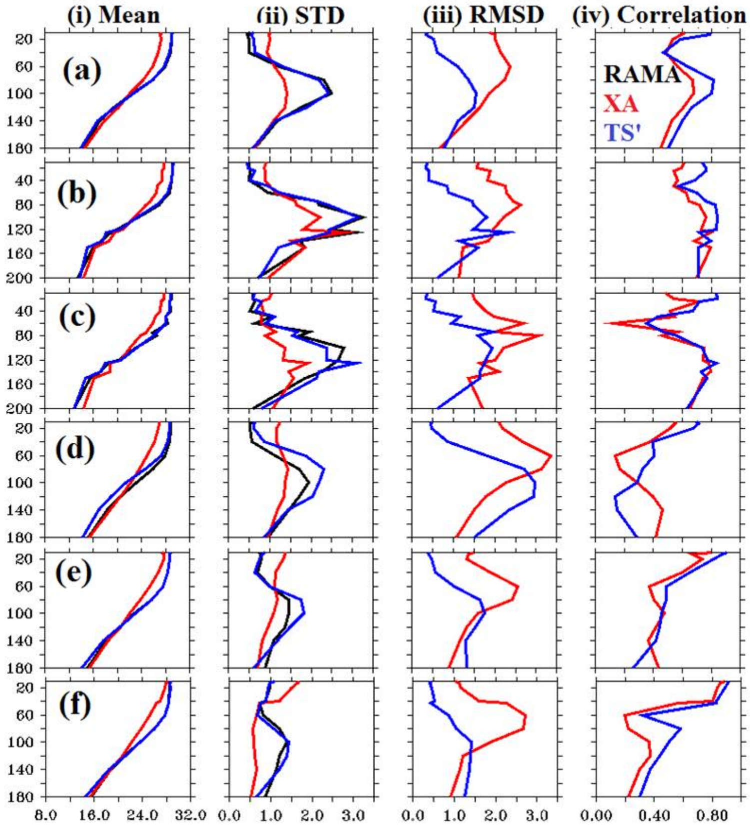

Figure 3.4: Depth-wise statistics of temperature at all independent locations. (a) $1.5°S$, $80.5°E$, (b) $1.5°S$, $90°E$, (c) $5°S$, $95°E$, (d) $8°N, 90°E$, (e) $12°N$, $90°E$, and (f) $15°N, 90°E$. Statistics include (i) Mean ($°C$), (ii) STD ($°C$), (iii) RMSD ($°C$), and (iv) correlation. RMSD and correlations are estimated between observation and model. In the figure RAMA, *XA*, and *TS'* are indicated in black, red, and blue colours respectively. Results for *QTS'* and *TS'* are almost identical thus *QTS'* not shown in the plots

pared to the other seasons (Figure 3.5). Careful analysis reveals that the quality of temperature analysis in *XA* does show significant seasonal dependencies whereas in assimilation experiments the quality of temperature analysis is relatively steady (Figure 3.5). It is noticed that RMSD's of temperature in the assimilation experiments are within the standard deviation throughout the column (0-500m) except for BoB locations. In general, RMSDs are minimum (0.2-0.75$°C$) in the upper 50m and are maximum (1-3$°C$) between 100-200m in all the assimilation experiments. Correlation exceeds 0.6 at the surface in these assimilation experiments.

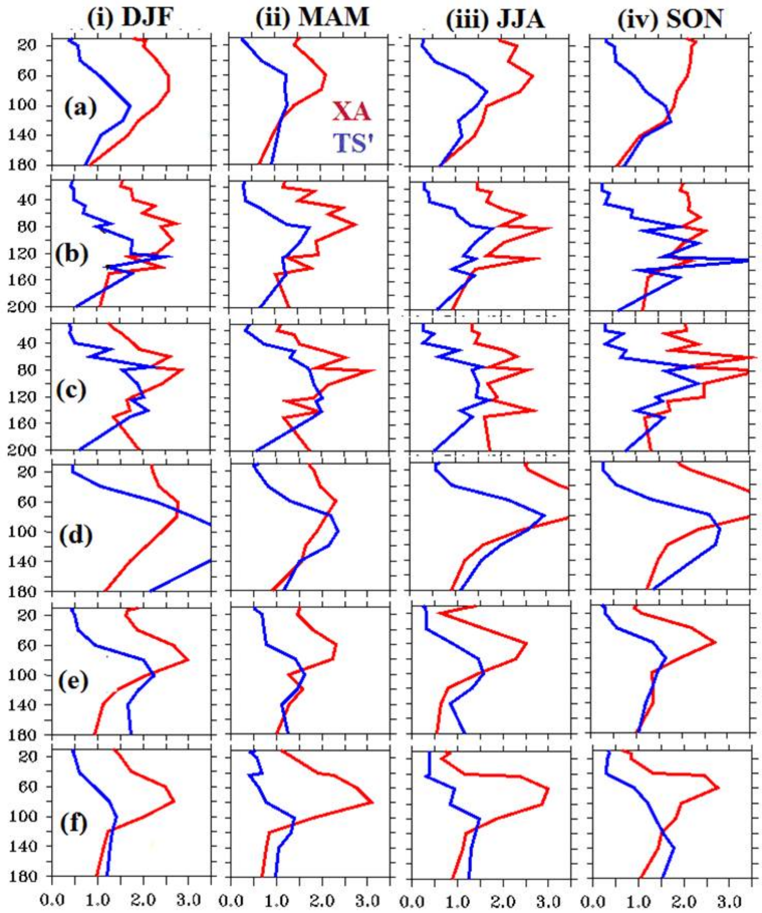

Figure 3.5: Season wise RMSD (°C) of temperature at all independent locations. (a) 1.5°S, 80.5°E, (b) 1.5°S, 90°E, (c) 5°S, 95°E, (d) 8°N, 90°E, (e) 12°N, 90°E, and (f) 15°N, 90°E. Seasons include (i) DJF (December-January-February), (ii) MAM (March-April-May), (iii) JJA (June-July-August), and (iv) SON (September-October-November). RMSD is estimated between observation and model. In the figure XA, and TS' are indicated in red, and blue colours respectively. Results for QTS' and TS' are almost identical thus not QTS' not shown in the plots.

3.3.2 Salinity

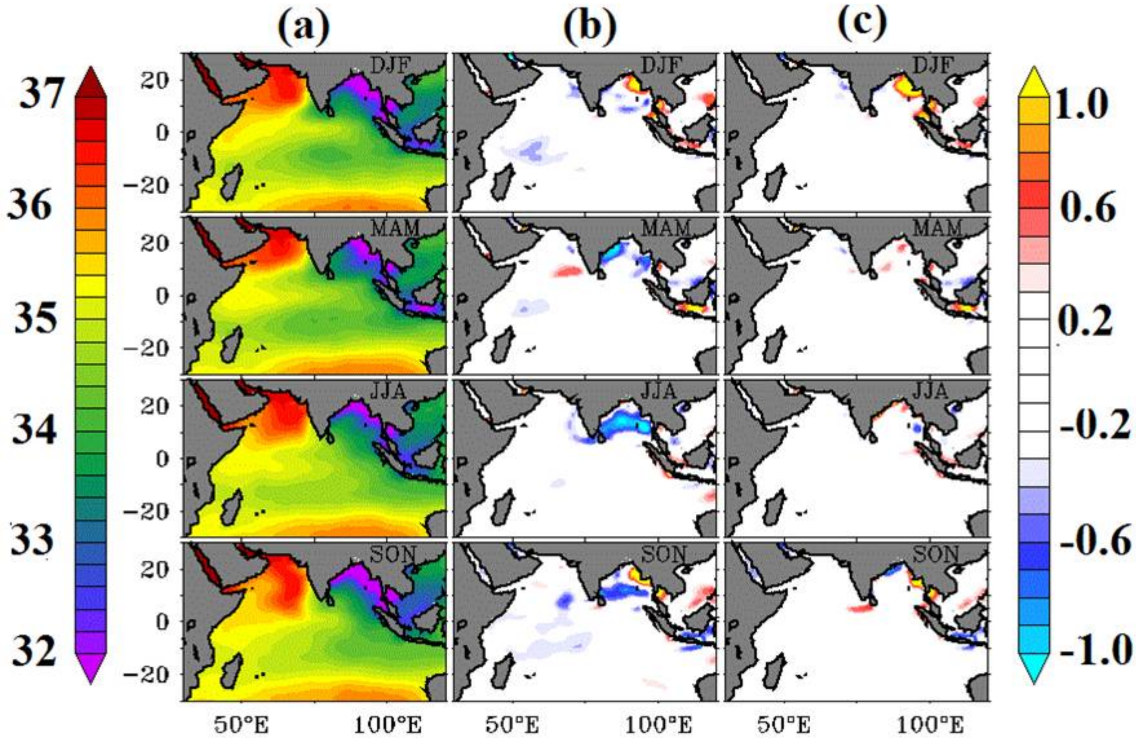

Figure 3.6: Same as figure 3.1 except for sea surface salinity. The model biases are estimated with respect to EN3V2a

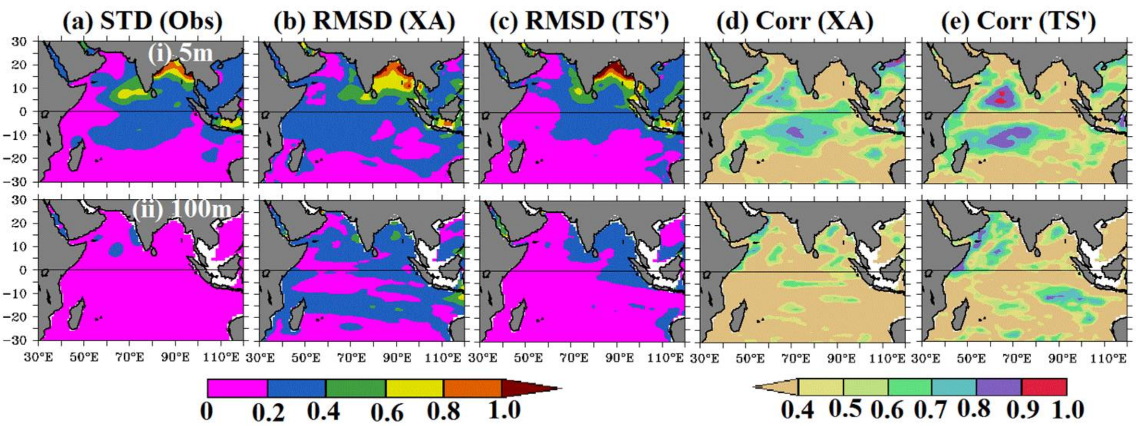

Figure 3.7: The standard deviation of SSS (psu) derived from (a) EN3V2a. RMSD (psu) and correlation between SSS of *XA* and EN3V2a, *TS'* and EN3V2a are shown in *b*,*c* and *d*,e respectively. Statistics are available for (i) surface (5m) as well as (ii) sub-surface (100m)

Figure 3.6 shows the seasonal evolution of multi-year (2004-2008) (a) average SSS derived from gridded salinity fields of EN3V2a data, and the SSS biases in each (b) *XA*, and (c) *TS'* with respect to EN3V2a. It is observed that the SSS in *TS'* and *QTS'* show similar features hence *QTS'* not shown in the figure. It is clear from figure that *XA* has a tendency to under-estimate salinities by more than 1 psu over the Bay of Bengal (BoB) especially during south west monsoon season. Large freshening anomalies are also observed over central parts of the equatorial Indian Ocean and thermocline ridge region during November and December. In contrast to the above, over-estimations are observed over the south-eastern Arabian Sea (AS) during spring. Discrepancies over most of the tropical IO are reduced upon using the temperature and synthetic salinity assimilation except over a few localized regions such as north BoB, and south-eastern AS. Improvements in SSS, in terms of RMSDs, with *TS'* over *XA* ranges from 0.2 to 0.4psu over most of the regions in the TIO (Figure 3.7). However, over few localized regions mentioned above, RMSDs are still greater than STD in *TS'* (Figure 3.7). It is observed that the spatial extent of these large RMSDs in the north BoB decreases as the depth increases and diminishes significantly at 100m (Figure 3.7). Comparing the model experiments with *in-situ* RAMA salinity confirms the above results (Figure 3.8).

Careful analysis on the discrepancies observed in the BoB indicates that these are associated with the prescription of unrealistic annual river discharge in the model and/or due to assimilation of unrealistic salinity profiles in the BoB. For example, the regions in the head Bay as seen in *XA* shows a positive bias ($> 1psu$) in the SSS during September-February and a negative bias ($< 1psu$) during March-August (Figure 3.6a and 3.6b). Earlier studies have reported that all the major rivers along the east coast of India have a pronounced annual cycle with peak discharges during August-September (Rao and Sivakumar, 2003; Papa et al., 2010) and provide greatest drop in salinity in November and December (LaViolette, 1967). The annual average of the river discharge, which has been input to the model, will provide more (less) freshwater input in to the head BoB during January-May (June-September) compared to its seasonal cycle. Further, these

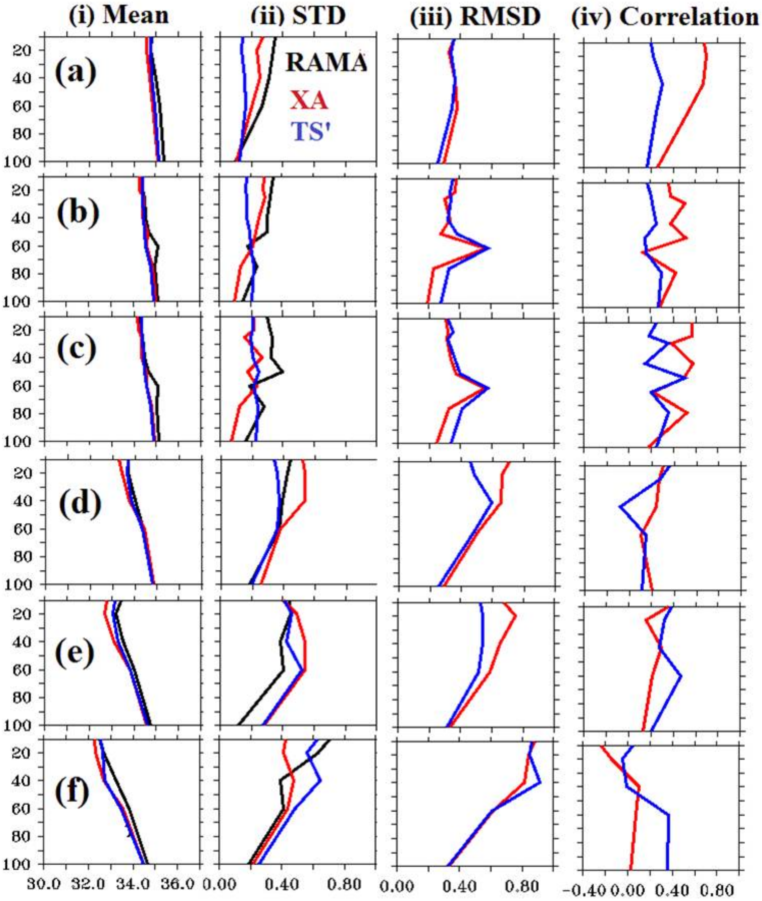

Figure 3.8: Same as Figure 3.4 except for salinity

large errors in the BoB subsequently contribute to large errors in the south-eastern AS through horizontal advection as seen in Figure 3.6a. Though prescribing unrealistic river discharge has got potential to degrade the quality of salinity field, the affect could be reduced significantly upon assimilating salinity profiles. For example, over most of the regions in the TIO, improvements in the quality of salinity are observed with *TS'* over *XA* (Figure 3.6, 3.7 and 3.8). However, in the case of head BoB during winter, the discrepancies are enhanced. It is noticed that synthetic salinity profiles are very far from real salinity profiles in north BoB especially during winter seasons (e.g. Figure 2.3). Thus the discrepancies in the head BoB observed in *TS'* might be due to combined effect of (1) unrealistic river runoff as explained earlier and (2) unrealistic synthetic salinity profiles. Earlier studies Huang et al. (2008) have shown that adding *in-situ* salinity instead of synthetic salinity to the temperature assimilation reduces errors in salinity field significantly. From the above analysis it is reasonable to speculate that inclusion of realistic river-runoff in the model would reduce errors in the salinity field especially in the head BoB. The above discussion also suggests for closing Indo-Srilankan channel in the model. Forcing ocean general circulation model with high quality precipitation product derived from satellite observations, instead of model based NCEP2, is also another option to reduce errors in salinity as suggested by the recent studies (Momin et al., 2010; Sharma et al., 2012). Some of these critical issues are solved in the chapter 5.

3.3.3 Sea surface height anomaly

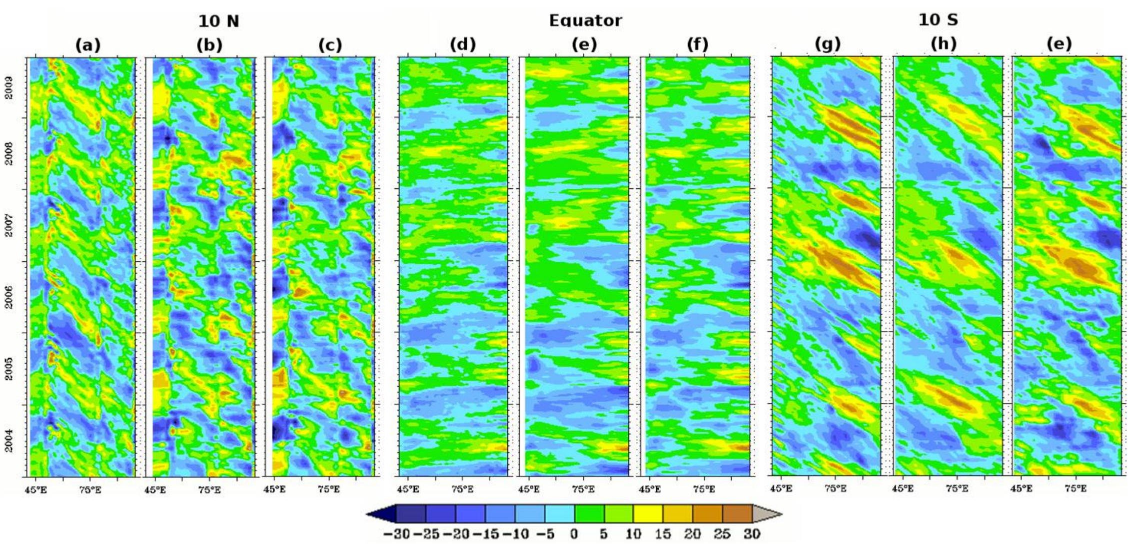

Figure 3.9: Hovmoller diagram of SSHA (cm) derived from (a) Altimeter, (b) XA, and (c) TS' along $10°N$, Eq, $10°S$ as indicated in the figure legends. Results for QTS' and TS' are almost identical thus not QTS' not shown in the plots

The TIO experiences large variations in the wind field at time scales extending from intra-seasonal to inter-annual and they have a significant influence on the vertical movement of the thermocline by local Ekman pumping and also remotely by propagating Rossby and Kelvin waves (Iskandar et al., 2005; Sakova et al., 2006; Vialard et al., 2009; Rao et al., 2010; Girishkumar et al., 2011). Both satellite and model derived SSHAs represent a first order approximation of the upper ocean thermal structure, with the SSHA mirroring the variability of the thermocline depth. It is found that all the model experiments do well at realistically capturing the signals propagating eastward along equator and westward along $10°N$ (Figure 3.9). The model without assimilation (XA), however, struggles to capture the westward propagating Rossby waves driven by Ekman pumping (Masumoto and Meyers, 1998) along $10°S$ in a realistic way (Figure 3.9). On the other hand, the SSHA from both assimilation experiments capture these signals reasonably well in terms of amplitude and phase speed with respect to the observed SSHA.

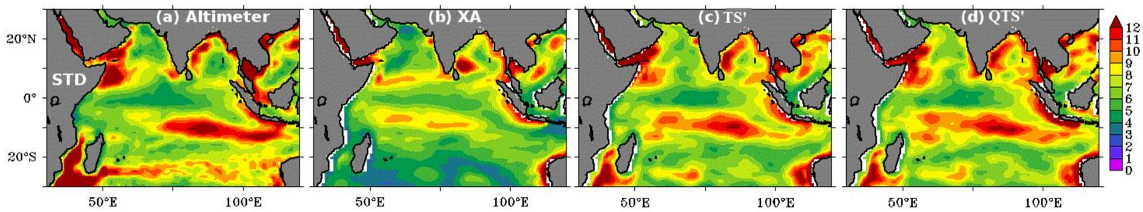

Figure 3.10: The standard deviation of SSHA (cm) derived from (a) Altimeter, (b) *XA*, (c) *TS'* and (d) *QTS'* during 2004-2009

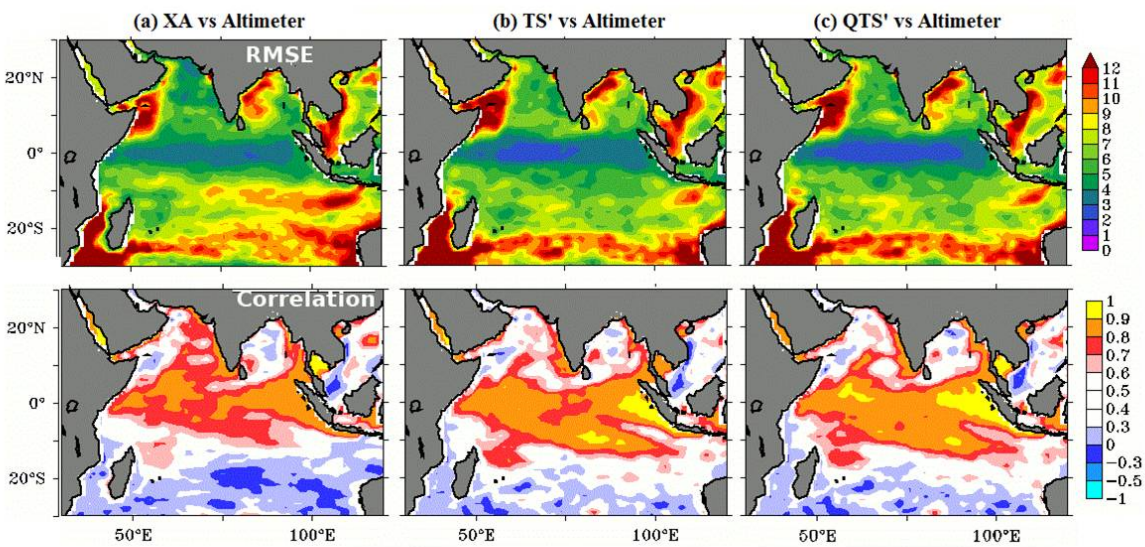

Figure 3.11: RMSD (cm, top panel) and correlation (bottom panel) between SSHA derived from the model and altimeter for (a) *XA*, (b) *TS'* and (c) *QTS'* during 2004-2009

We note that the model without assimilation (XA) has a tendency to generate large biases in SSHA patterns near the Somali region, over Bay of Bengal (BoB) and the south eastern parts of the TIO. It can be seen in Figures 3.10 and 3.11 that the errors are large wherever the variability is high. For example, the RMSD over the western BoB, Somali region and South TIO are as large as $10cm$. The assimilation of temperature and synthetic salinity appears to reduce the large errors found in *XA*, by 3-5 cm, over the regions near northwest Australia and the ITF. In general, the STD of SSHA from the model and observations match reasonably well. The RMSDs are between 2-9cm and are smaller than the STDs over most regions of the TIO in the assimilation experiments. It can be seen in the figure that discrepancies in SSHA, with respect to the RMSD and correlation, between the *TS'* and the observations are relatively small in the EIO when compared to any other region. The figure further suggests that these are reduced further by replacing NCEP2 winds with QuikSCAT winds. Assimilation, however, did not reduce the large discrepancies found in the *XA* in the region offshore of Somalia, in the western BoB and in the southern TIO. Over these regions, RMSDs and correlations are found to be greater than 12cm and less than 0.3 respectively. Earlier studies suggest that the SSHA in the BoB is significantly influenced by the presence of local freshwater (Yu, 2003; Yu and McPhaden, 2011). The relatively large SSHA discrepancies found between the model and the observations in the western BoB are likely due to an inaccurate representation of the model salinity field. It is well known that the regions offshore of Somalia and in the southern parts of the Indian Ocean are dominated by small scale eddy patterns (Schott et al. (2009) and references there in). Thus the large discrepancies in SSHAs (and in SSTs) in these regions might well be due to the inability of INCOIS-GODAS to resolve small scale eddies. At a resolution of 1/4° in the tropics, the INCOIS-GODAS is eddy-permitting, but not eddy-resolving. Even with an eddy resolving model, we would not expect to locate eddies at their correct positions owing to their chaotic nature and their sensitivity to model initial conditions as shown by Oke and Schiller (2007). Although we are assimilating *in-situ* temperature profiles, the source of these observations, the Argo array, can only provide these profiles at a nominal separation of 300 km. It is very possible for multiple eddies to remain unobserved between two Argo profiles and, thus, significant differences between the model and observed altimeter SSHA fields are a near certainty.

3.3.4 Ocean current

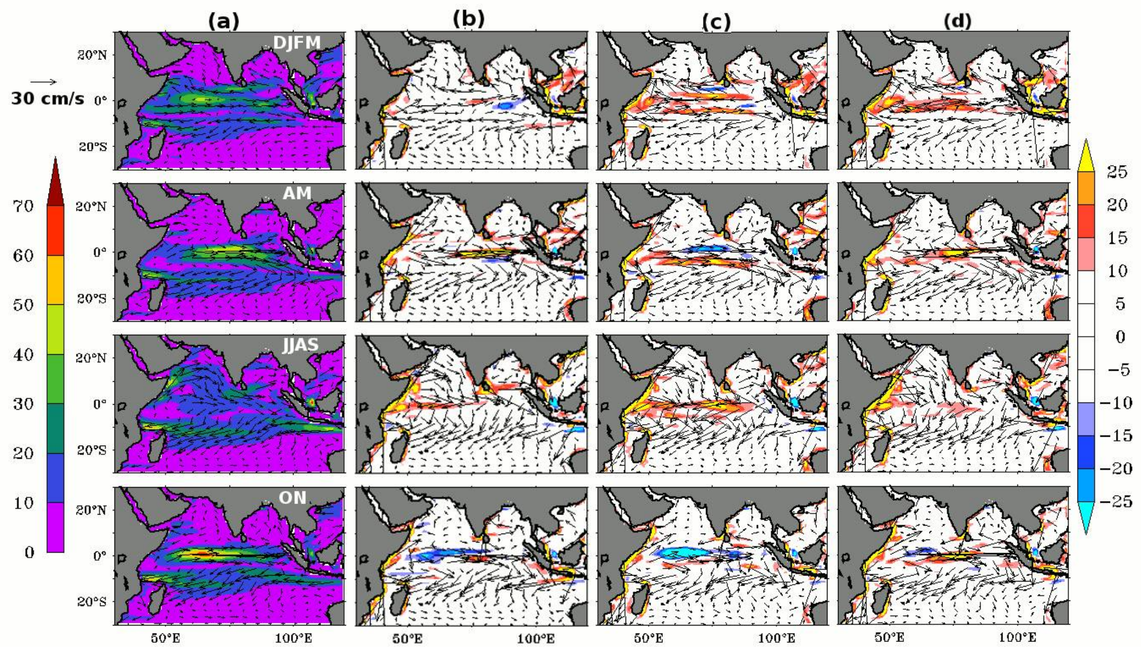

Figure 3.12: Multiyear (2004-2009) seasonal mean (DJFM, AM, JJAS and ON)) of ocean near surface current vectors (cm/s) derived from (a) OSCAR, (b) XA, (c) TS' and (d) QTS'. In the panel (a) magnitude of total current is shaded. In panels b and c, bias in XA, TS' and QTS' with respect to OSCAR total current speed is shaded

It is evident from Figure 3.12 that all of the model runs are able to capture reasonably well the seasonally reversing current systems (such as the Somali current, the North Equatorial Current, the West India Coastal current, and the East India Coastal current) as well as the permanent South Equatorial Current in the TIO (Hastenrath and Greischar (1991); Shankar et al. (2002); Schott et al. (2009) and reference therein; figure not shown). The study by Vinayachandran et al. (1999), Rao et al. (2006) showed that during the summer monsoon, the so-called Summer Monsoon Current (SMC) curves around Sri-Lanka and intrudes into the south-western Bay. The intrusion of the SMC into the south-western Bay is captured by all of the model runs.

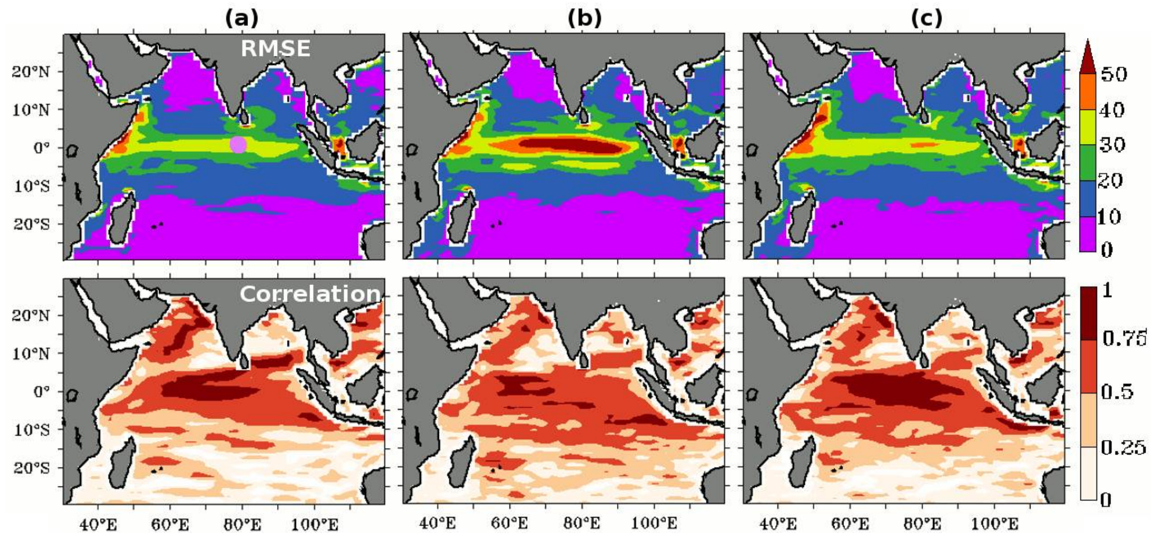

Figure 3.13: The RMSD (cm/s) (top panels) and correlation (bottom panels) between the model near surface zonal current and OSCAR for (a) XA, (b) TS' and (c) QTS' during 2004-2009. The pink circle on figure a represents the ADCP location (Equator, $80°E$

)

The eastward flowing Wyrtki Jets (Wyrtki, 1973), which develop during inter-monsoon periods (April-May and October-November) appear in the model simulations with comparable magnitudes (Figure 3.12). The TS' produces slightly weaker jets relative to the other two experiments. In general, TS' shows a westward current anomaly during the southwest monsoon season along the central part of the equator. This discrepancy, both in magnitude and direction, however, does not appear in the other two experiments (XA, QTS'). During the winter monsoon, both the assimilation experiments overestimate the strength of the equatorial currents as compared to the OSCAR currents, although the bias is less in the QTS'. All of the model runs could simulate the strong westward flowing current, observed in the OSCAR currents west of $80°E$. However, the westward currents in the assimilation experiments show an erroneous extension throughout the equatorial regime. These discrepancies over the EIO can be clearly seen in Figure 3.13. The figure shows the RMSD and correlation in the model zonal surface current obtained by comparing it with OSCAR. The figure clearly shows that the RMSD is larger in the EIO than in any other region of the TIO. It is interesting to observe that the RMSD of the zonal surface current in the *TS'* in this region is as large as $50 cm/s$ and is greater than the observed STD. Whereas, the zonal currents in the other two experiment have RMSDs between $30 - 40 cm/s$, and is less than the observed STD. These features are reflected in the correlation as well. Comparing the model zonal surface currents with the *in-situ* RAMA currents is also consistent with the above results (Figure 3.14).

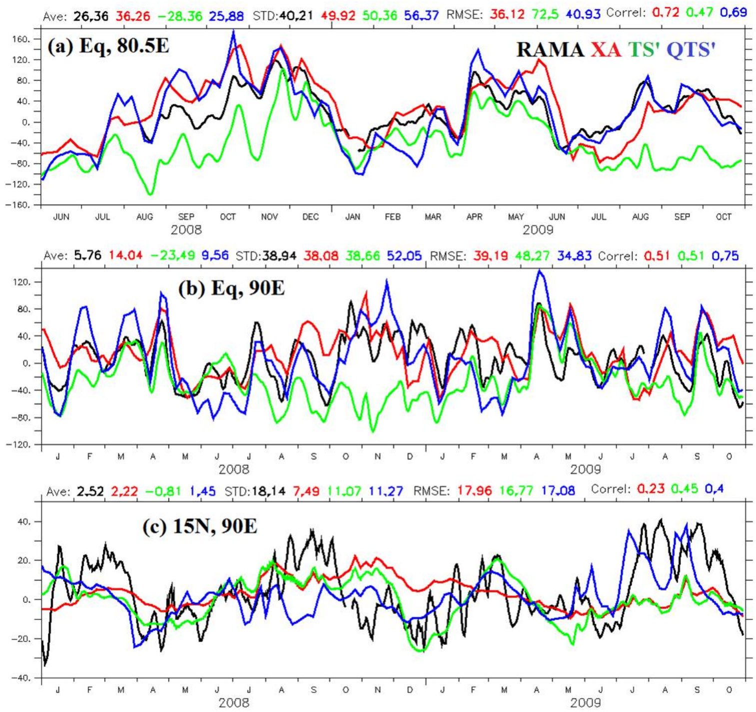

Figure 3.14: Time series of zonal surface current (cm/s) at (a) equator, $80°E$, (b) equator, $90°E$, and (c) $15°N$, $90°E$. Time series is shown for selected period to avoid showing large gaps in sampling. However, statistics shown at the top of the corresponding figures, are based on data covering 01st January, 2004 to 30th October, 2009

A comparison of the model currents with ADCP profiles reveals that the model

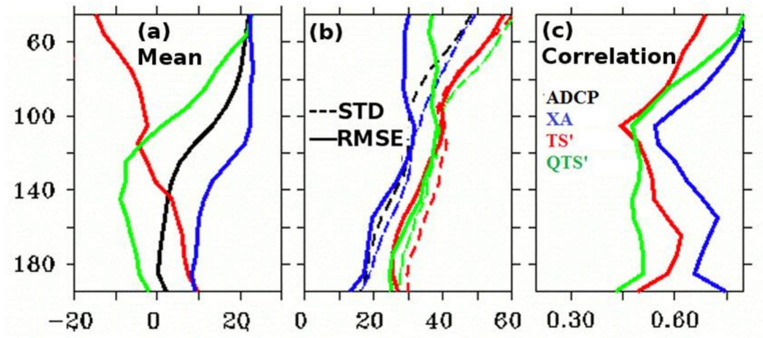

Figure 3.15: Depth-wise statistics of zonal currents at Eq, 80°E (location of RAMA buoy marked as pink circle in Figure 3.7a. (a) Mean (cm/s), (b) STD (cm/s; dashed line) and RMSD (cm/s; solid line), and (c) correlation. RMSD and correlations are estimated between observation and model. In the figure RAMA/ADCP, *XA*, *TS'*, and *QTS'* are indicated in black, blue, red, and green colors respectively

is able to reproduce the equatorial under currents (Iskandar et al., 2009) reasonably well, particularly for the *QTS'* and *XA* (Figure 3.15). Depth-wise statistics with respect to ADCP zonal currents suggest that *TS'* has large discrepancies in the surface layers compared to deeper layers (Figure 3.15). For example, the bias and RMSD in the zonal currents of the *TS'* with respect to the ADCP on the Equator at 80.5°E and between 50-100m is about 10-30 cm/s and 40-55 cm/s respectively, whereas it is 0-10 cm/s and 20-30 cm/s respectively between 150-200 m (Figure 3.15). Interestingly, these large errors in the surface layers are comparatively smaller in the other two experiments.

From the above results it is clear that the assimilation degrades the quality of the surface currents at the equator. The degradation of the equatorial currents as a consequence of the assimilation is a common feature in other assimilation systems as well (Burgers et al., 2002; Bell et al., 2004; Balmaseda et al., 2007) although it seems to be absent in 4D-Var analysis (Weaver et al., 2003; Vialard et al., 2003). As explained in Burgers et al. (2002), in shallow-water models and more complicated models, density information alone is not sufficient to specify the system completely. However, one can use the fact that the system tends to a state that is close to geostrophic balance. From potential vorticity conservation it follows that for scales large compared to the Rossby radius, the heights of the adjusted state are less affected than the rotation of the velocities, while for the small scales it is the other way round. So assimilation schemes that assimilate density information only give reasonable estimates for the velocities for the large scales, while the small scales are inherently problematic. Fortunately, in the ocean the Rossby radius is small compared to the scale of continents and ocean basins. So for many applications, density information can be sufficient for an adequate estimate of the ocean state. Close to the equator, where the Rossby radius is relatively large and the separation between the timescales of planetary waves and intertial-gravity waves is relatively small, this may require some extra care. In the present study, we thought that use of shorter time scales(every 6hr) for updating density, through the assimilation of temperature and salinity profiles, would not degrade the quality of currents at equator during the assimilation exercises. We realized from the present study that this does not provide fruitful results for equatorial currents. Burgers et al. (2002) proposed a method in which balanced updates are made for zonal velocities. Though the degradation of the surface currents introduced by the assimilation is observed to be significantly reduced by using QuikSCAT winds instead of NCEP wind forcing in the present system, it is worth to implement the scheme proposed by Burgers et al. (2002) in INCOIS-GODAS for better representation of equatorial currents in the assimilation system.

3.4 Summary and Recommendations

In this chapter, we evaluate the performance of INCOIS-GODAS in the TIO based on the experiments carried out using (1) assimilation (*TS'* and *QTS'*), in which *in-situ* temperature and synthetic salinity used, and (2) assimilation-free (*XA*) experiments. In addition, the current Chapter examines the sensitivity of the INCOIS-GODAS to different momentum forcing based on experiments carried out with different wind products: NCEP2 (*TS'*) and QuikSCAT (*QTS'*). The present study reveals that the model with assimilation could simulate most of the observed features of temperature, SSHA and currents with reasonably good accuracy in the TIO at both intra-seasonal and inter-annual time-scales.

Verifying the model SST fields with observations reveals that the model with assimilation improves SST field by $1°C$ compared to the model without assimilation. Differences between the model and observations in the two assimilation experiments are very small (about $0.2°C$) with the exception of a very few localized regions such as the head bay, the Somalia coastal zone and the south-western EIO, where the differences are relatively large ($> 0.5°C$) and have a strong seasonal dependence. The RMSD between the SSTs of the assimilation experiments and observations are smaller than $0.5°C$ in the TIO except over the few localized regions mentioned above. Significant improvements ($0.2 - 0.4psu$) are also observed in salinity analysis upon assimilation compared to without assimilation. Discrepancies in SSS, in terms of RMSDs, are less than $0.5psu$ over most of the regions in the TIO. However, discrepancies are still large in the north BoB and SEAS in TS' compared to observations. The difference in the SSHA derived from the assimilation experiments and the altimetry observations is generally less than 3 cm over most of the TIO. The RMSD between SSHA estimated from assimilation experiments and altimeter measurements are relatively small in the EIO, and relatively large in those regions affected by small scale eddies such as along the Somalia coast, in the western BoB and in the southern Indian Ocean ($> 5cm$). Comparing the quality of the ocean analyses among all of the model experiments (i.e., *XA*, *TS'* and *QTS'*) reveals that the assimilation of temperature and synthetic salinity improves the quality of the ocean analysis significantly except in the case of the equatorial current field, which is a common feature for assimilation systems. Use of satellite based QuikSCAT winds instead of model based NCEP2 winds appears to improve currents especially at equator which is in agreement with earlier studies Sengupta et al. (2007). A brief list of recommendations for the improvement of the ocean analysis from INCOIS-GODAS is described below.

1. The present configuration of INCOIS-GODAS assimilates observed temperature and synthetic salinity based on local climatological temperature and salinity correlation. The assimilation of observed salinity profiles instead of synthetic salinity profiles would improve ocean analysis significantly.

2. Current setup of INCOIS-GODAS uses NCEP2 winds. Use of satellite based wind instead of NCEP2 would improve currents significantly especially at equator.

3. Though surface current gets degraded by the assimilation of temperature and synthetic salinity the degradation has significantly reduced by using QuikSCAT winds instead of NCEP wind forcing. It is worth to implement corrective schemes, such as the one proposed by Burgers et al. (2002), in INCOIS-GODAS.

4. Use of strong SST relaxation instead of Weak relaxation might improve temperature analysis further.

5. Providing the model with realistic river discharge will further improve the ocean analysis in the head BoB.

6. The widening of the Indo-Sri Lanka channel leads to errors in the representation of currents in the model, which, in turn, contributed to errors in the salinity filed, particularly in the southeastern Arabian Sea. According to earlier studies, (Rao and Sivakumar, 1999; Kurian and Vinayachandran, 2007), this is the region where a mini warm pool forms during the spring, which plays a significant role in the progress of the monsoon and the formation of the monsoon onset vortex (Rao and Sivakumar, 1999; Shenoi et al.,

1999). A poor representation of the salinity field in this region can disrupt the thermohaline structure of model. One of the primary objectives of this ocean analysis is to provide ocean initial conditions for the coupled model, which will be used for monsoon forecasts. These forecasts are likely proven to be sensitive to the ocean heat content in the Arabian Sea. Our analysis recommends the closing of the Indo-Sri Lanka channel for a better representation of the thermohaline structure in the SEAS.

7. The analysis suggests that a higher resolution model would improve the simulation of small scale eddy activity at higher latitudes and consequently the current field.

8. It is well known that there are significant errors in the NCEP2 heat flux, which will contribute to errors in the model SST (Swain et al., 2009; McPhaden et al., 2009b). Hence forcing the model with the recently developed heat flux data, the OA flux (Yu and Weller, 2007), which have better accuracy, may provide better oceanic conditions.

Some of the above mentioned recommendations are addressed in the following chapters.

Chapter 4

Evaluation of ASCAT based gridded wind product

4.1 Introduction

OGCMs need gridded atmospheric flux products, including wind to force the ocean models. It is well known that wind stress plays a crucial role in the simulation of ocean state, especially ocean currents, in OGCMs. There are various gridded wind products available at present.These wind products can be obtained from either atmospheric model or from the satellite. Although the model based products are available for research as well as operational purposes, the quality of these products are still questionable in the tropical regions. For example, Uppala et al. (2005) have shown that Environmental Centre for Medium Range Weather Forecast Reanalysis -40 (ERA-40) has excessive precipitation and too strong Brewer-Dobson circulation in the tropical oceans. Similarly, Goswami and Sengupta (2003) have shown that National Centre for Environmental Prediction-National Centre for Atmospheric Research (NCEP-NCAR) model produces erroneous precipitation patterns due to inaccurate representation of the atmospheric convective heating over the eastern tropical Indian Ocean (IO). As suggested by Goswami and Sengupta (2003), mis-representation of precipitation patterns produces errors in the wind field. Such issues are generally less in satellite based gridded wind products. However, the quality of the satellite based products largely depends on the spatial and temporal coverage of scatterometer observations. Scatterometer observations from QuikSCAT mission have 1/4° spatial and 2 days temporal resolution. Earlier studies (Sengupta et al. (2007); and results from the previous chapter) have demonstrated the importance of using satellite blended winds instead of model based in the ocean model for better simulations of ocean parameters, mainly currents. These studies have yielded better results mainly by using QuikSCAT wind forcing. However, QuikSCAT winds are not available after November, 2009. Oceansat-II has provided scatterometer winds data during September, 2009 to February 2014. At present scatterometer winds are available only from Advance Scatterometer (ASCAT). Currently, spatially complete gridded wind products based on satellite scatterometer observations are available from limited sources to the best of our knowledge.

Bentamy and Fillon (2012) have constructed a daily averaged global gridded wind field using ASCAT winds, called DASCAT. This wind product is available online on operational basis with 2-day delay and foreseen to be available till the termination of EUMETSAT series which boards ASCAT i.e., up-to 2022. These are some important factors for use them in operational systems such as INCOIS-GODAS. However, it is important to ensure that the product is offering reasonable quality before using them in operational systems. The quality assessment of the DASCAT wind product over the world ocean based on various buoy data (NDBC, MFUK, TAO, RAMA, and PIRATA) is done by Bentamy and Fillon (2012). They also performed spatial comparison between DASCAT and a Numerical Weather Prediction model's wind product in the global ocean. However, the spatial comparison is not done, to the best of our knowledge, with the high resolution QuikSCAT based gridded wind product, which is generally considered to be the most accurate wind dataset during the last decade. Further, earlier studies Bentamy et al.

(2002) have emphasized the need for validation in the tropical Indian Ocean region due to its peculiar variabilities in the ocean-atmospheric parameters. These peculiarities include seasonal variability of wind and rainy conditions which influence the estimation of scatterometer wind and the quality of wind products are questionable.

It is clear from the above discussion that a consolidated report on the accuracy of DASCAT in the tropical Indian Ocean based on surface observations is missing. This motivate us to first compare the wind product in the tropical Indian Ocean with a widely used 3-day running mean daily QuikSCAT gridded wind (QSCAT) and the RAMA surface wind observations. After performing such a comparison for the DASCAT, the value of DASCAT for using in ocean model is evaluated based on sensitivity experiments, using INCOIS-GODAS, by carrying out using different wind forcing (NCEP-R2, QSCAT, and DASCAT). Prior demonstration of the suitability of a wind product using state of the art ocean models is important before implementing it in the operational systems since quality of winds have impact on the quality of ocean fields (Sengupta et al., 2007).

In the present chapter, analysis is carried out for the TIO during the period from 1^{st} April, 2009 to 30^{th} October, 2009. The selection of the study period is constrained by (1) the simultaneous availability of the DASCAT product, which uses 12.5 km resolution ASCAT level-2b data from 3^{rd} March, 2009 (25km resolution ASCAT level-2b data is used before this date), (2) QSCAT product, which was terminated a few days after 15^{th} November, 2009, and (3) to allow the model to adjust itself to new wind forcing (DASCAT). It is worth mentioning here that the DASCAT experiment was started from 3^{rd} March, 2009 and the initial condition for this experiment was taken from QSCAT wind based experiment. This Chapter is organized in four sections. Section 4.2 describes about model experiments conducted, and methodology followed. Results from the comparison of DASCAT wind with QSCAT and RAMA buoy measurements, and plausible causes for the differences are discussed in section 4.3. Results and discussion drawn from model experiments are also presented in section 4.3. Summary of this chapter is presented in section 4.4.

4.2 Description of Model Experiments and Methodology

In order to compare DASCAT and QSCAT wind with the *in-situ* RAMA, one has to bring RAMA to 10m height. Because, gridded winds of DASCAT and QSCAT are equivalent neutral surface winds representing the winds at 10m height, whereas, RAMA measures winds at 4m height. We use a simple approach of assuming logarithmic wind profiles so that the corrected wind speed at height z is given by

$$U(z) = U(z_m) \times \ln{(z/z_0)} \,/\, \ln{(z/z_m)} \tag{4.1}$$

where $U(z)$ is the wind speed at height z, z_0 is the roughness length, and z_m is the measurement height. This expression can be derived using a mixing length approach assuming neutral stability (Peixdto and Oort, 1992). The typical oceanic value for z_0 is $1.52 \times 10^{-4} m$ (Peixdto and Oort, 1992; Mears et al., 2001) and it is used in this study.

For the DASCAT performance assessment based on the INCOIS-GODAS, we have used observed *in-situ* salinity for the assimilation instead of synthetic salinity. It is worth mentioning here that use of observed salinity profiles in place of synthetic salinity improves the salinity as well as currents, especially in the equatorial regions corroborating the results of Huang et al. (2008). Detailed analysis on the impact of observed in-situ salinity assimilation is provided in chapter 5. Based on the above scheme, we have designed three identical experiments using INCOIS-GODAS as summarised in Table 4.1. As mentioned in the Table 4.1 the experiment *QTS* (QuikSCAT forcing) was run from 01^{st} January, 2003 to 31^{st}

Table 4.1: Summary of the experiments conducted using INCOIS-GODAS

Experiment	Momentum flux	Model run and Initial condition
QTS	QSCAT	Ran from 1^{st} January, 2003 to 31^{st} October, 2009 using initial conditions obtained from standard GODAS run
NTS	NCEP-R2	Ran from 3^{rd} March, 2009 to 31^{st} October, 2009 using initial condition from QTS experiment
DTS	DASCAT	Ran from 3^{rd} March, 2009 to 31^{st} October, 2009 using initial condition from QTS experiment
NTS_{long}	NCEP-R2	Ran from 1^{st} January, 2003 to 1^{st} January, 2009 using initial conditions obtained from NCEP-GODAS run
QTS_{short}	QSCAT	Ran from 1^{st} January, 2009 to 31^{st} May, 2009 using initial condition from NTS_{long}

October, 2009 using the initial condition from NCEP-GODAS run. Experiments NTS (NCEP-R2 forcing) and DTS (DASCAT forcing) were run from 03^{rd} March, 2009 to 31^{st} October, 2009 (DASCAT winds prepared using 12.5 km wind retrievals are available from 03^{rd} March, 2009 onwards). Ocean analysis on 02^{nd} March 2009, obtained from QTS was used as the initial condition for both the experiments NTS and DTS. Selection of the common initial condition from QSCAT forced experiment instead of NCEP-R2 forced experiment is due to the better representation of oceanic features with the QSCAT wind forcing than the NCEP-R2 wind forcing as discussed in Chapter 3.

For the present study, the evaluation is carried out using daily averaged outputs from 01^{st} April 2009 to 31^{st} October 2009, discarding the outputs of March, 2009. This analysis period is chosen after carrying out study on the model adjustment time by conducting a specialized set of experiments NTS_{long} and QTS_{short} as summarised in Table 4.1. The experiment NTS_{long} was run from 1^{st} January, 2003 to 1^{st} January 2009 using initial condition from the NCEP-GODAS run.

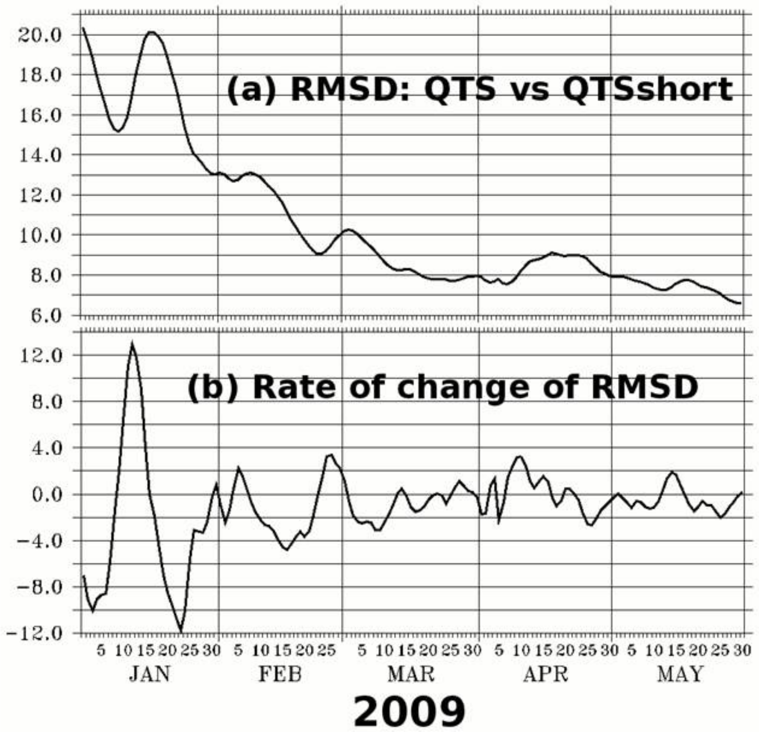

Figure 4.1: (a) Evolution of RMSD in surface current (cm/s) for the domain covering Equatorial Indian Ocean (40 ^oE-100 ^oE & 10 ^oS-10 ^oN). Rate of change of RMSD (cm/s^2) with respect to time is shown in panel b. 10-day smoothing is applied on RMSD to iron-out small changes. Number of points used for the computation of RMSD is 9600

The QTS_{short} experiment was run from 1^{st} January, 2009 to 31^{st} May 2009 using the initial condition of 1^{st} January, 2009 from NTS_{long}. Hence, comparing the surface currents, which is of main interest in the present study, from QTS (can be considered as QTS_{long}) and QTS_{short} during 1^{st} Janurary, 2009 to 31^{st} May, 2009 should tell us the model adjustment time for the surface currents. Figure 4.1a shows RMSD between surface currents from QTS and QTS_{short} in the EIO while Figure 4.1b shows rate of change of this RMSD with respect to time. The Figure 4.1 depict that RMSD reduces exponentially (Figure 4.1a) and attains low gradients in RMSD with respect to time (or rate of change of RMSD; Figure 4.1b) about a month after the start of QTS_{short}. In fact the RMSD is observed to reduce from 20 cm/s to 13 cm/s within a span of 15 days in the second half of the first month (Figure 4.1a), which indicates that the model has started stabilizing with the new wind forcing during the first month itself. The RMSD continued to decrease further in the following months but with low rate of change in RMSD. Hence for the present study, we discarded only first one month in-order to account for the model adjustment time. Using only one month for the model adjustment instead of waiting for complete equilibrium is a trade-off between the model error and effective utilization of the short common period ($\approx$ 8 months only) between QSCAT and DASCAT. It is important to understand from this trade-off that errors due to model adjustment cannot be completely discarded but the affect may be neglected when the difference in surface currents between model experiments is large enough (e.g. when the difference between the surface currents from QTS and NTS is greater than 15 cm/s (10 cm/s) during first few months (after few months) the error may be suspected due to significant contributions from differences in QSCAT and NCEP-R2 wind forcing).

In the present section, daily averaged ocean currents available from RAMA moorings (McPhaden et al., 2009b) at 10 m depth are used for comparing the model simulated current field. During the analysis period, major portion of the RAMA currents data is available over the EIO regions. We have used data from all the RAMA locations in the EIO which provided at-least 30 points for the comparison during the analysis period of 1^{st} April, 2009 to 31^{st} October, 2009. Based on this condition, we are left with only 7 RAMA locations in the EIO region to compare the model with observations. Due to the non-availability of in-situ measurements of spatial current, we have used new version of OSCAR current, prepared by Bonjean and Lagerloef (2002), to validate the model simulated current filed. In order to realize the level of accuracy of OSCAR current data in the EIO, we have performed a detailed validation of OSCAR current data in the EIO using RAMA currents (Figure 4.2). It can be inferred from the Figure 4.2 that zonal currents of OSCAR compare well with the RAMA in the Equatorial Indian Ocean; the mean bias is less than 15 cm/s; root mean square difference is less than

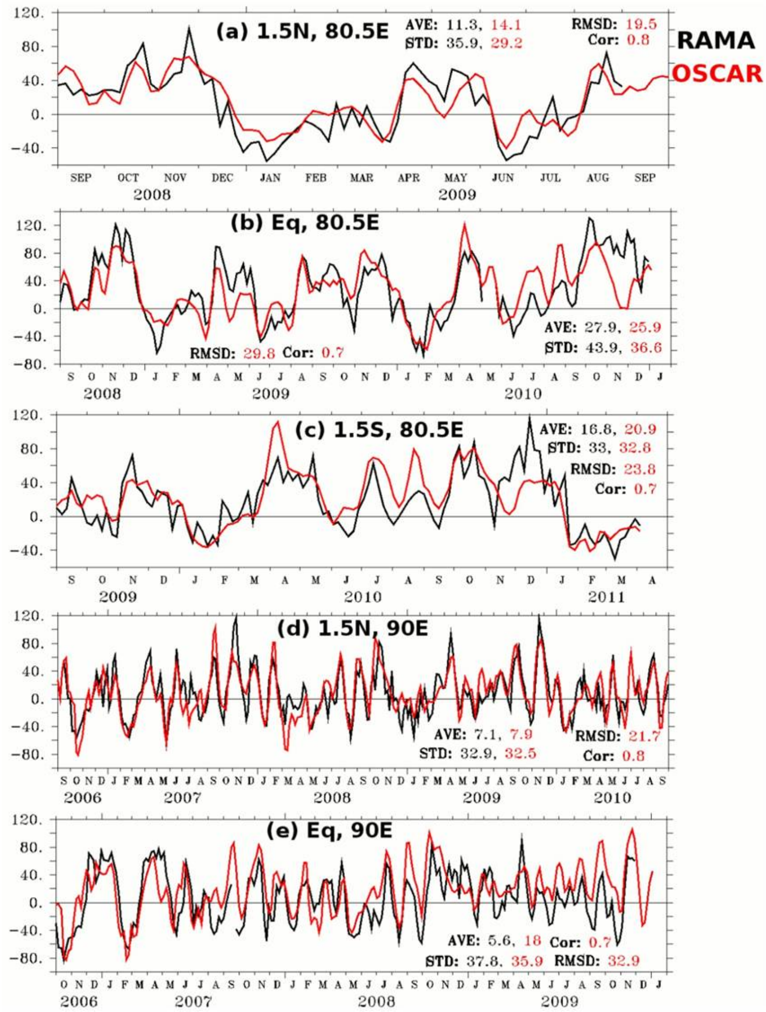

Figure 4.2: Zonal surface currents from RAMA (black) and OSCAR (red) at (a) 1.5°N, 80.5°E, (b) Eq, 80.5°E, (c) 1.5°S, 80.5°E, (d) 1.5°N, 90°E, and (e) Eq, 90°E. Statistics such as mean (AVE), Standard Deviation (STD), Root Mean Square Difference (RMSD), and Correlation are also shown in the corresponding figure. The OSCAR currents are interpolated to RAMA location and time. 5-day smoothing is applied. Statistics are computed with respect to the RAMA observations. Units are in cm/s

standard deviation; Correlation is greater than 0.7. These results are consistent with the results of Sikhakolli et al. (2013), and indicate that OSCAR current can be used as a reference for the validation of model derived current.

4.3 Evaluation of DASCAT winds

The main objective of this section is to answer the following questions (1) How accurate is the DASCAT, and (2) is it suitable for use in assimilation system, the INCOIS-GODAS. We meet the objective by performing qualitative and quantitative assessment using both observations and sensitive experiments carried out using INCOIS-GODAS. Such an assessment not only benefits the present study but also useful for the oceanographic and meteorological community to know the quality of winds from satellites.

4.3.1 Comparison of DASCAT wind vector with QSCAT wind vector

The main objective of this section is to examine the ability of DASCAT to capture large scale wind variability in the tropical Indian Ocean. In the period between 01^{st} April, 2009 to 15^{th} November, 2009 both DASCAT and QSCAT wind data are simultaneously available and it provides a unique opportunity to validate the performance of DASCAT with respect to QSCAT. The bi-monthly averages of DASCAT and QSCAT wind vectors and the difference (QSCAT-DASCAT) between wind speeds and wind vectors of these two products are shown in Figure 4.3a, 4.3b and 4.3c, respectively. Figure 4.3 clearly shows that the DASCAT accurately reproduced the location of the maxima, minima and direction of wind as seen in QSCAT products. Even though both products show strong spatial correspondence in magnitude and direction, DASCAT underestimates the mean strength of the wind by up-to 1 m/s with respect to QSCAT, except for a few

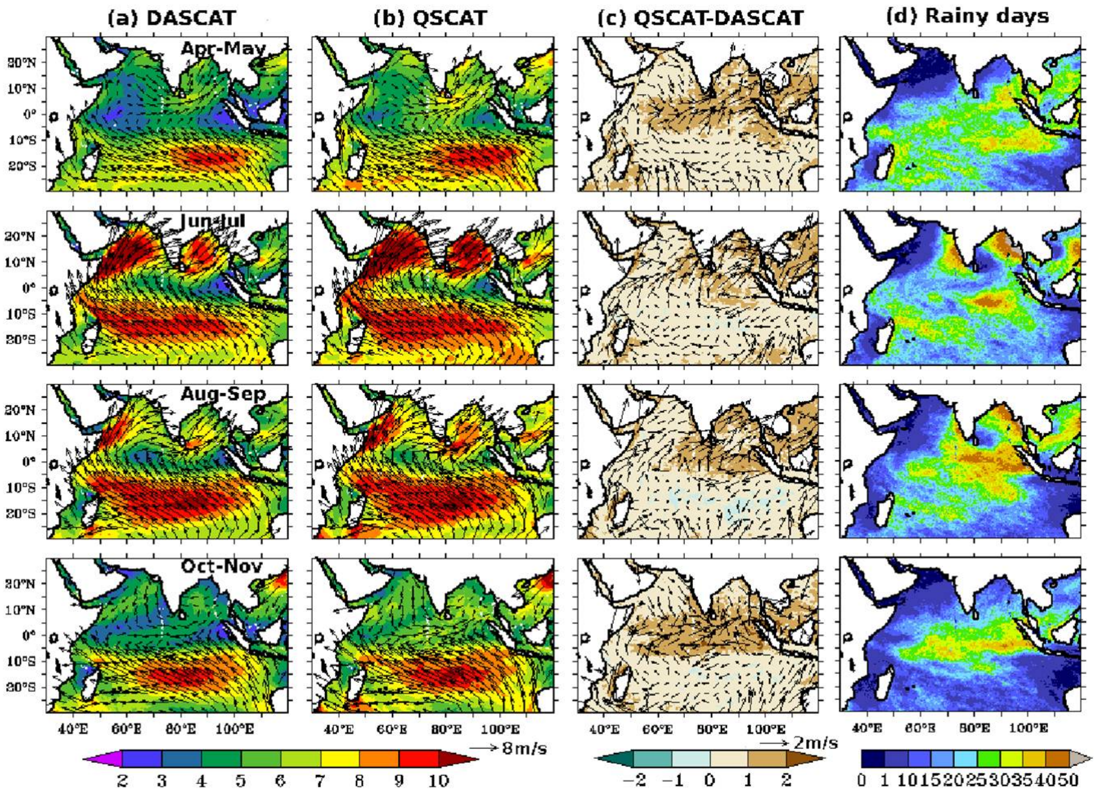

Figure 4.3: Bi-monthly (April-May, June-July, August-September and October-November) distribution of mean wind speed and wind vectors (m/s) from (a) DASCAT (b) QSCAT and (c) difference between DASCAT and QSCAT. (d) Bi-monthly distribution of the number of rainy days estimated from TRMM 3B42

localised regions in the Southern tropical Indian Ocean, where DASCAT overestimates the wind speed. However, there are certain regions, particularly in the central and eastern equatorial Indian Ocean and the Bay of Bengal, where the difference between DASCAT and QSCAT wind speed measurements are relatively large ($1 - 2.5m/s$). For example, during spring (April-May) and fall (October-November), QSCAT product shows strong westerly wind in the central and eastern equatorial Indian Ocean which was not present in DASCAT. Further, compared to QSCAT, DASCAT shows relatively weak south-westerly in the south-eastern Arabian Sea and central Bay of Bengal. The probable reason for these differences are examined in the next section.

Figure 4.4a and 4.4b shows the standard deviation of wind speed measurements

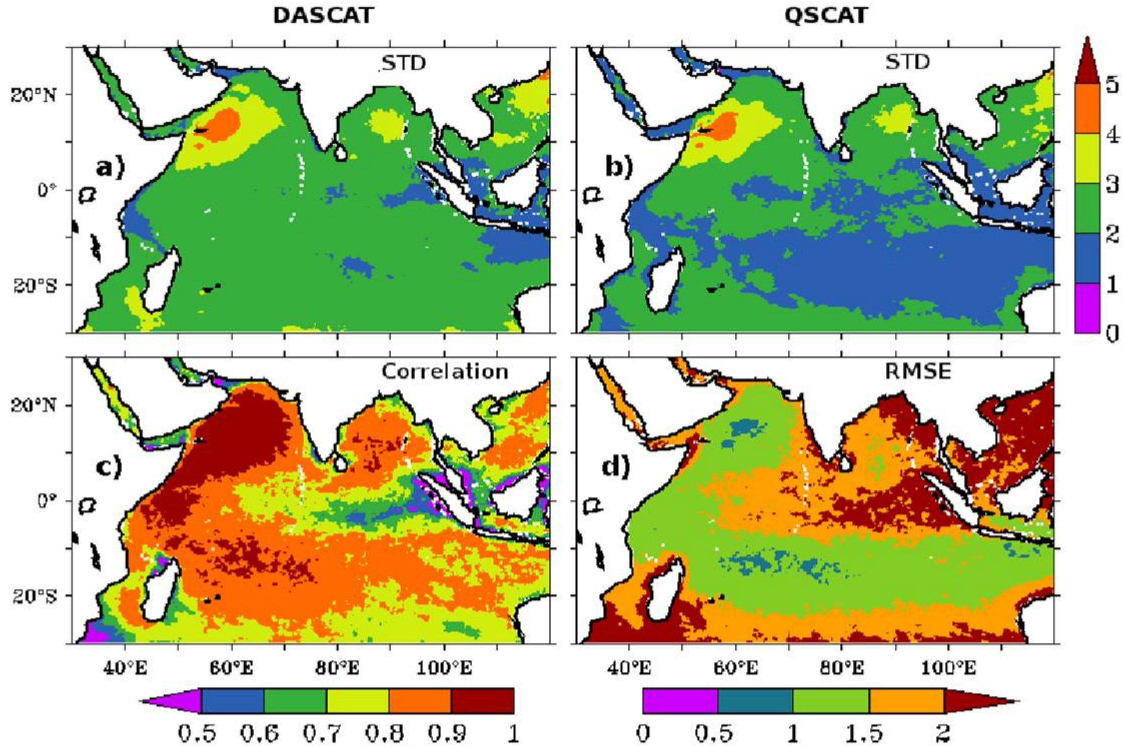

Figure 4.4: The standard deviations (m/s) of (a) DASCAT and (b) QSCAT wind speed. The (c) correlation and (d) RMSD between QSCAT and DASCAT wind products

from DASCAT and QSCAT, respectively. Figure 4.4 clearly shows that standard deviation for both winds is comparable. However, over the region south of equator, the standard deviation is much higher (by $0.5m/s$) in the DASCAT as compared to QSCAT. The correlation and RMSD between QSCAT and DASCAT wind speeds during the study period are shown in Figure 4.4c and 4.4d, respectively. The correlation is more than 0.7 over most of the region. Relatively small correlation (0.6-0.7) is observed in the regions of eastern equatorial Indian Ocean and south-eastern Arabian Sea (Figure 4.4c). The RMSD shows a value of 1.5 m/s over most of the region. However, it is higher in regions where the correlation is relatively low. Generally, RMSD is less than the standard deviation in the entire tropical Indian Ocean.

It is well known that the accuracy of scatterometer wind retrievals is affected by particular environmental conditions such as rain, low and high wind speed conditions (Quilfen et al., 2004; Satheesan et al., 2007). It is interesting to note that the wind speed underestimation in DASCAT, compared to QSCAT, is more or less stable with respect to magnitude of the wind (compare figures 4.3a, 4.3b and 4.3c). Hence, we speculate that the discrepancy between QSCAT and DASCAT may be associated with rain fall activity in that region. Figure 4.3d shows a bi-monthly distribution of the number of rainy days. The figure shows a broad geographic correspondence between the occurrences of large rainfall activity and the discrepancy between QSCAT and DASCAT measurements. It indicates that rain is a potential factor for discrepancy between QSCAT and DASCAT wind product. It is well known that difference in the C-band (employed in ASCAT) and Ku-band (employed in QuikSCAT) sensitivities to the rain lead to comparatively better estimates of wind in the former as indicated by earlier studies (Fernandez et al., 2003; Tournadre and Quilfen, 2003). It is worth mentioning here that DASCAT is constructed based on both ASCAT and ECMWF wind fields (ECMWF fields are used as an external drift in the Krigging method to construct DASCAT). However, it is not clear, which way these two factors affects the gridded DASCAT wind fields. Thus from the above discussion one cannot establish the conclusion on whether the DASCAT is a safe replacement to QSCAT or not. Hence, in the following section the QSCAT and DASCAT wind products are compared with *in-situ* wind measurement obtained from RAMA buoy in the tropical Indian Ocean.

4.3.2 Comparison of DASCAT and QSCAT wind with RAMA buoy observations

In order to understand the influence of rain and wind speed conditions based on the nature of uncertainties in QSCAT and DASCAT wind product, the *in-situ* wind data obtained from 16 RAMA buoys in the tropical Indian Ocean is used (Figure 4.5). For this analysis, QSCAT and DASCAT winds at their original grid points nearest to the location of RAMA buoy are used. Relative performance

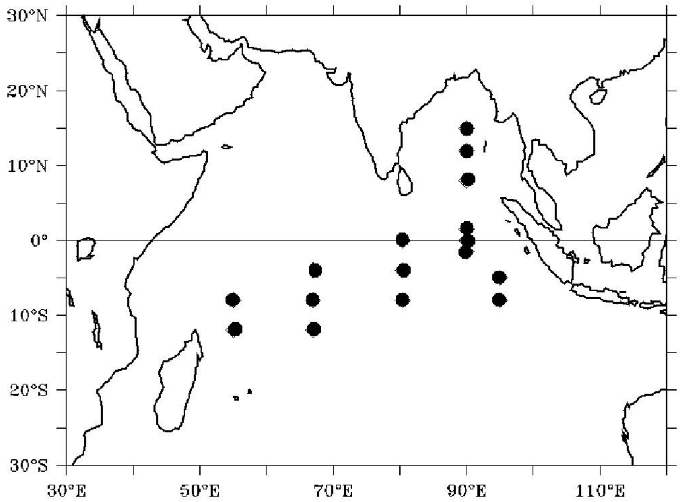

Figure 4.5: The location of RAMA buoys (filled circles) in the tropical Indian Ocean which are used for validation of QSCAT and DASCAT

Table 4.2: Summary of statistical parameter (during no-rain condition) of RAMA, QSCAT, DASCAT winds as well as of differences between buoy and scatterometer data. In the table WS, U, and V represents wind speed, zonal and meridional winds, respectively

	Average (m/s)			Standard deviation (m/s)			RMSD w.r.to RAMA (m/s)		Correlation w.r.to RAMA	
	RAMA	QSCAT	DASCAT	RAMA	QSCAT	DASCAT	QSCAT	DASCAT	QSCAT	DASCAT
RAMA wind speed $< 4m/s$ (No. of data points 235)										
WS	2.61	3.74	2.51	0.93	1.21	1.16	1.64	0.92	0.42	0.63
U	0.26	0.29	-0.17	2.00	2.79	2.14	1.87	1.09	0.74	0.88
V	0.84	1.28	0.76	1.71	2.44	1.56	1.69	1.08	0.75	0.78
RAMA wind speed $4-10m/s$ (No. of data points 764)										
WS	7.02	7.30	6.78	1.69	1.70	1.84	0.98	0.88	0.85	0.89
U	-2.11	-2.21	-2.28	5.22	5.29	4.87	1.31	1.06	0.97	0.98
V	3.86	4.17	3.79	2.36	2.47	2.45	1.35	1.13	0.85	0.89
RAMA wind speed $> 10m/s$ (No. of data points 100)										
WS	10.76	10.48	10.55	0.66	0.86	1.00	0.75	0.79	0.60	0.64
U	-0.18	-0.18	-0.57	8.44	8.03	7.74	1.23	1.18	0.99	0.99
V	6.42	6.54	6.95	1.95	1.80	1.95	1.30	1.04	0.76	0.89

of DASCAT and QSCAT wind products with respect to RAMA observation on different wind speed and rain conditions will be examined in the following two sections.

4.3.2.1 Influence of wind magnitude on DASCAT and QSCAT winds

The influence of wind magnitude on the DASCAT and QSCAT winds are investigated using RAMA buoy wind speed measurements in no-rain conditions. No-rain (rain) is defined to be the condition when TRMM rain fall shows absolute (greater than) "zero". Table 4.2 presents the statistical parameters estimated with respect to buoy wind speed ranges ($0-4m/s$, 4-10 m/s and $> 10m/s$ and are referred to as low, medium and high wind speed conditions, respectively). The standard deviation and mean of both satellite wind products are comparable with the buoy wind speed measurements in all the wind speed ranges (Table 4.2). However, standard deviation of DASCAT product shows better agreement with RAMA compared to QSCAT during low wind speed condition. The correlation is relatively low (high) during low (medium and high) wind speed conditions in both the satellite products. It is interesting to note that the correlation between RAMA and QSCAT is always lower than the correlation between RAMA and DASCAT in all the wind speed conditions. The RMSD estimated with respect to RAMA shows relatively large values for QSCAT in low wind speed conditions compared to DASCAT. Further, the RMSD, between QSCAT and RAMA, significantly improved when the wind speed increases. For instance, RMSDs between QSCAT and RAMA are varied from 1.64 to 0.98 m/s in wind speed, from 1.87 to 1.31 m/s in zonal winds, and from 1.69 to 1.35 m/s in meridional winds, when going from low to medium wind speed conditions. However, this kind of improvement is not observed with DASCAT product, since DASCAT consistently maintains low RMSD values in all wind speed conditions (Table 4.2). Further, as seen in RMSD, the correlation of buoy winds with QSCAT is always lower than DASCAT in all the wind speed conditions.

For further clarity, the RMSD between DASCAT, QSCAT and buoy for wind speed, zonal and meridional winds for each 1 m/s wind speed bin are shown in Figure 4.6. The RMSD between DASCAT and buoy shows relatively low values

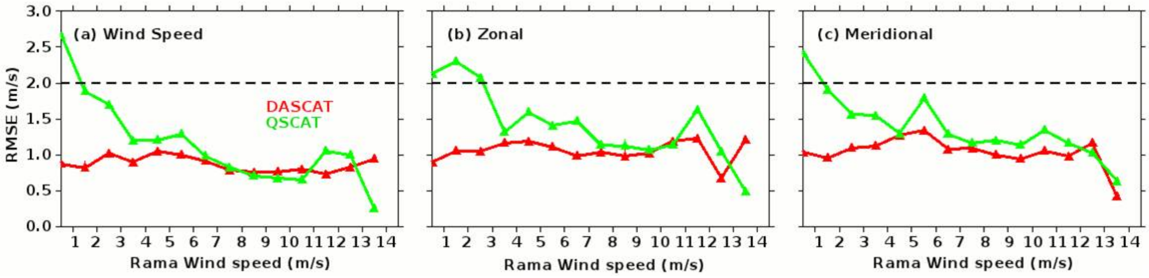

Figure 4.6: The RMSD (m/s) between DASCAT (red line) and RAMA and QSCAT (green line) and RAMA for different wind speed bins of 1 m/s interval for (a) wind speed, (b) zonal wind and (c) meridional wind. Please refer to Figure 4.8 for the number of data points used for the statistical calculation in each wind speed bin. (Note: In the figure x-axis 1 m/s indicates 0 to 1 m/s bin)

Table 4.3: Summary of the statistical analysis between RAMA and QSCAT and RAMA and DASCAT under rain and no-rain conditions. In the table WS, U, and V, represent wind speed, zonal and meridional winds, respectively

	Average (m/s)			Standard deviation (m/s)			RMSD w.r.to RAMA (m/s)		Correlation w.r.to RAMA	
	RAMA	QSCAT	DASCAT	RAMA	QSCAT	DASCAT	QSCAT	DASCAT	QSCAT	DASCAT
No-rain (No. of data points 1099)										
WS	6.42	6.83	6.21	2.7	2.41	2.76	1.14	0.88	0.92	0.95
U	-1.43	-1.49	-1.68	5.23	5.3	4.88	1.44	1.08	0.96	0.98
V	3.45	3.76	3.43	2.69	2.82	2.79	1.42	1.12	0.87	0.92
Rain (No. of data points 892)										
WS	6.53	7.68	6.46	2.85	2.5	2.87	2.07	1.25	0.8	0.9
U	-0.48	-0.53	-0.85	5.49	6.4	5.19	2.78	1.44	0.9	0.97
V	3.36	3.7	3.43	3.01	3.2	3.24	2.03	1.62	0.79	0.87

($1m/s$) in all wind speed regimes without any significant change. However, the figure clearly shows the inability of QSCAT to perform well in low wind speed conditions (Figure 4.6, green line). The RMSD goes above 2 m/s in the low wind speed conditions ($0 - 3m/s$) and gradually decreases as the wind speed increases. DASCAT consistently maintains a relatively low RMSD ($1m/s$) under all wind speed conditions when compared to QSCAT. This analysis clearly shows that QSCAT wind product has relatively poor performance in low wind speed conditions. Further, the analysis clearly depicts the better performance of DASCAT wind product in all wind speed conditions compared to QSCAT.

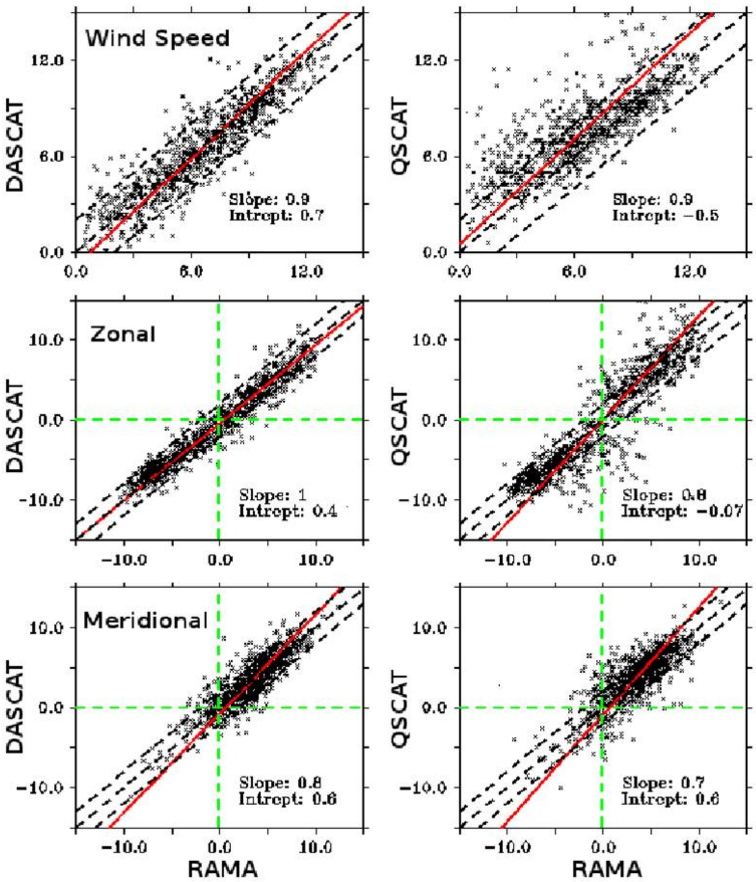

Figure 4.7: Scatterpolts between RAMA and DASCAT(left panel) and RAMA and QSCAT(right panel) for total, zonal and meridional winds (m/s) during rain events. The red line represents least squares linear fit with slope and intercept

4.3.2.2 The influence of rain on DASCAT and QSCAT winds

The influence of rain on the DASCAT and QSCAT winds is further investigated using RAMA buoy wind measurements under rain and no-rain conditions. Figure 4.7 and 4.8 show the scatter plots of QSCAT and DASCAT with respect to RAMA for wind speed (zonal and meridional) during rain and no-rain conditions respectively. The statistics of this comparison are given in Table 4.3. The analysis indicates that QSCAT has a tendency to overestimate the strength of the wind during rain and for winds of magnitude less than 5 m/s (Figure 4.7 and 4.8, Table 4.3). During no-rain conditions, both QSCAT and DASCAT have high correlation with RAMA, though the magnitude is relatively small in QSCAT (Table 4.3). During rainy conditions, both scatterometer wind products show slight decrease in the

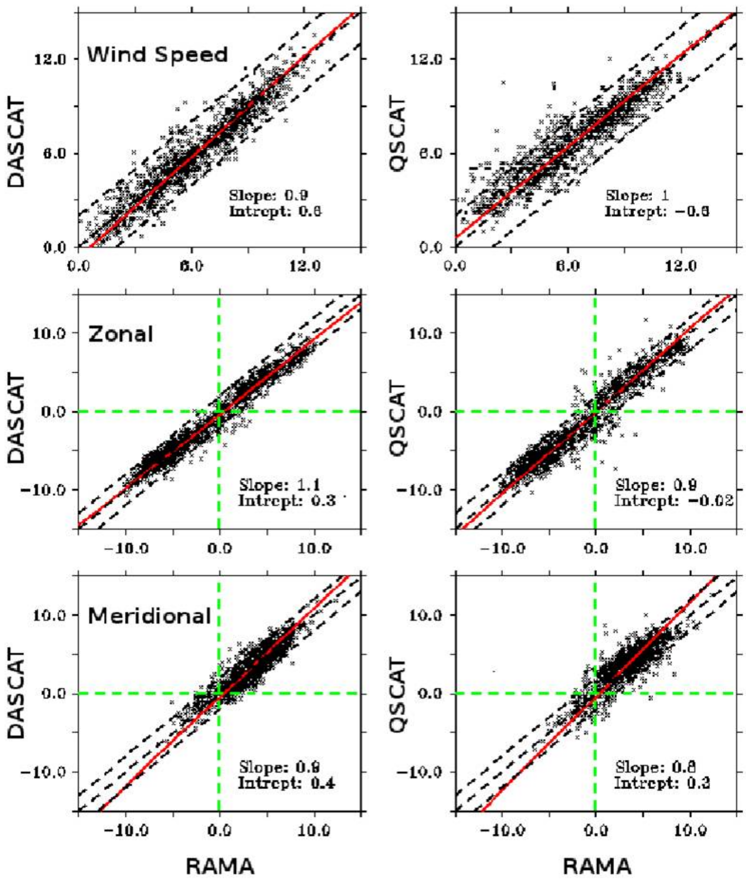

Figure 4.8: Scatterpolts between RAMA and DASCAT (left panel) and RAMA and QSCAT (right panel) for total, zonal and meridional winds (m/s) during no-rain events. The red line represents least squares linear fit with slope and intercept

correlation with RAMA buoy as expected. This might be due to the inability to rule out the uncertainties in the wind estimation caused because of the unwanted roughness at the ocean surface which is being hit by rain drops (Chelton et al., 2004). The standard deviation for both the satellite wind products is comparable with buoy wind measurements. However, during rainy days, the discrepancies in standard deviation of the wind speed measurements are relatively large in QSCAT with respect to RAMA observation. This is more evident in QSCAT zonal wind speed (Table 4.3). During no-rain conditions, the RMSD between QSCAT and RAMA (DASCAT and RAMA) is $1.25m/s$, $1.44m/s$ and $1.42m/s$ ($0.88m/s$, $1.12m/s$ and $1.12m/s$) for wind speed, zonal and meridional winds, respectively.

During rainy days, the RMSD between RAMA and both satellite wind products shows higher value as compared to the no-rain conditions. However, the difference in RMSD between rain and no-rain conditions is larger in QSCAT (both zonal and meridional wind speed) measurements as compared to DASCAT. In a nutshell, the analysis clearly depicts that DASCAT wind product shows a better performance than QSCAT, particularly in rain conditions. Further, the analysis demonstrates that gridded wind field requirement of providing wind speed with an RMSD 2 m/s is met for DASCAT in the tropical Indian Ocean.

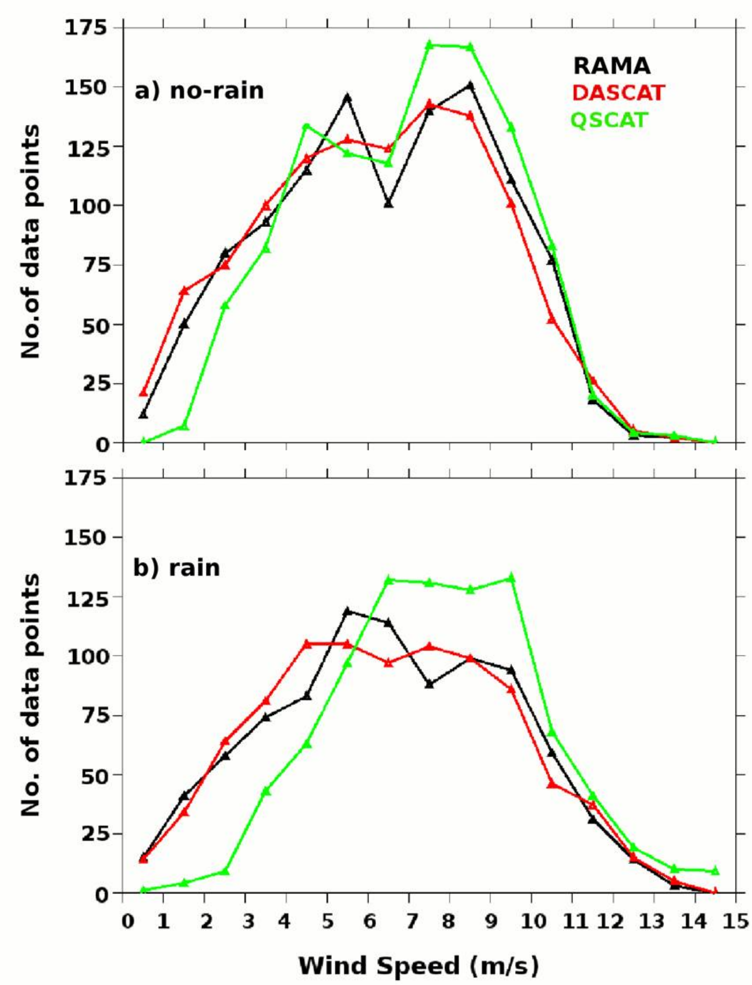

Figure 4.9: The frequency distribution of wind speed in 1 m/s bin interval from RAMA, DSCAT and QSCAT in (a) no-rain and (b) rainy conditions

The analysis from the above sections, however, does not provide combined effect of rain and different wind speed conditions on QSCAT and DASCAT products. In order to examine this, frequency distribution of wind speed (with 1 m/s bin interval) from RAMA, DASCAT and QSCAT during no-rain (Figure 4.9a) and rainy conditions (Figure 4.9b) is examined. In no-rain conditions, the frequency distribution of QSCAT and DASCAT matches well with RAMA observations (Figure 4.9a). It clearly indicates that in no-rain conditions, both QSCAT and DASCAT provide reasonably good estimation of the wind speed. In rainy conditions, QSCAT's wind speed is shifted to high wind speed, particularly when the wind magnitude is $< 10m/s$ (Figure 4.9b). This kind of discrepancy is not visible at higher wind speeds ($> 10m/s$). It indicates that rain significantly influences QSCAT wind product by inflating the estimates, particularly for winds weaker than $10m/s$. However, DASCAT measurements show a good comparison with RAMA observations even under rainy conditions. This clearly indicates the ability of DASCAT to be accurate even in rainy conditions.

The better performance of DASCAT compared to QSCAT during low wind speed and rain events may be partly associated with dependency of the wind estimation on the frequency band selection in the corresponding scatterometer instruments. In general, difference in the C-band and Ku-band sensitivities to the rain and wind lead to better estimates of wind in ASCAT than QuikSCAT during rain and low wind events as indicated by earlier studies (Fernandez et al., 2003; Tournadre and Quilfen, 2003). The higher accuracy of DASCAT in comparison with QSCAT may be partially associated with the use of ECMWF analysis fields in the Krigging method for constructing DASCAT (Bentamy and Fillon, 2012). Another possible source of the difference, when comparing daily averaged buoy winds with the same from a satellite is the difference in their sampling. Satellite data are a spatial average of instantaneous measurements, roughly equivalent to 8-10 minutes mean surface wind, while the buoy data is the temporal average of instantaneous measurements at a fixed point. So, the difference between the buoy and scatterometer wind estimation may not be due to the errors in the scatterometer measurements alone.

From the analysis it is clear that DASCAT provides reasonable accuracy in the wind field when it is compared with respect to RAMA. Though there appears to be reasonable spatial and temporal agreement between QSCAT and DASCAT wind field, the assessment on the ability of spatial and temporal variability for the DASCAT cannot be done with full confidence using direct comparisons with QSCAT and RAMA. Such an assessment, however, can be done indirectly by using ocean models. It is worth mention here that the ultimate aim of the present study is to verify the suitability of DASCAT for use in INCOIS-GODAS. The following section does this.

4.3.3 Suitability of DASCAT for use in INCOIS-GODAS

Earlier studies (Sengupta et al. (2007); Agarwal et al. (2007); in Chapter 3 of this thesis) have shown that momentum flux has significant impact on ocean current in the Indian Ocean. When INCOIS-GODAS is forced with three different momentum fluxes, noticeable differences of surface currents were found, especially in the EIO. Hence in the present section we examine the quality of simulated ocean currents from the three model experiments.

4.3.3.1 Validation of ocean surface current simulated by INCOIS-GODAS using different wind forcing

Seasonal patterns of ocean surface currents averaged for pre-monsoon (April-May), summer monsoon (June-July-August), and post-monsoon (September-October) are shown in Figure 4.10. It is worth mentioning here that the differences in surface currents between *QTS*, *DTS*, and *NTS* are not so significant in the TIO except in the EIO region (figure not shown). Notable differences are found particularly in the EIO with the three different momentum fluxes (Figure 4.10). From the figure, it is clear that both *NTS* and *DTS* show large differences in the central parts of the

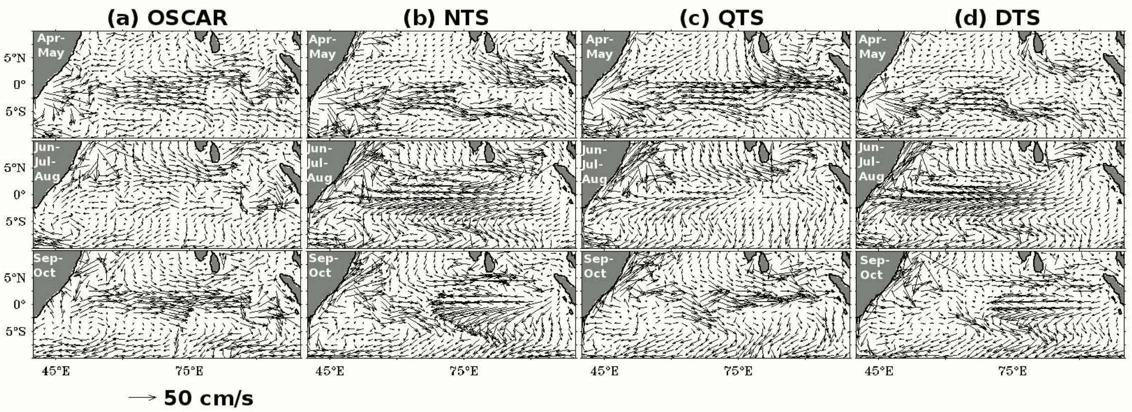

Figure 4.10: Seasonally averaged ocean surface currents (cm/s), during the year 2009, derived from (a) OSCAR, (b) *NTS*, (c) *QTS*, and (d) *DTS*. Seasons considered here are April-May (top panel), June-July-August (middle panel) and September-October (bottom panel). Upper 30 m averaged currents are represented as ocean surface currents

EIO, especially during monsoon and post-monsoon seasons. During the summer monsoon and post monsoon seasons, *OSCAR* and *QTS* show eastward current, whereas *NTS* and *DTS* show strong westward current in the central parts of the EIO region. Results from the Figure 4.10 indicate that *QTS* surface currents show reasonable agreement with OSCAR, where as *NTS* and *DTS* shows westward bias, particularly in the central parts of EIO region.

In order to enhance the confidence in the afore-mentioned results, we have compared zonal (Figure 4.11) and meridional (Figure 4.12) current from *NTS*, *QTS*, and *DTS* with in-situ current observations at all available *RAMA* buoy locations in the EIO. Figure 4.11a-4.11f (Figure 4.12a-4.12f) compares zonal (meridional) currents from the model with daily averaged 10 m zonal current observations of *RAMA* in the EIO region. In the eastern parts of the EIO (Figure 4.11e and 4.11f), the magnitude of the zonal current is weak (within 20 cm/s), except for few events which occurred during pre-monsoon and post-monsoon months as observed from RAMA. The zonal current estimates from DTS and QTS are reasonably accurate at the eastern EIO location of (1.5 °N, 90 °E; Figure 4.11e). At the (Equator, 90 °E) location, *QTS* overestimates the zonal current during pre-monsoon and post-

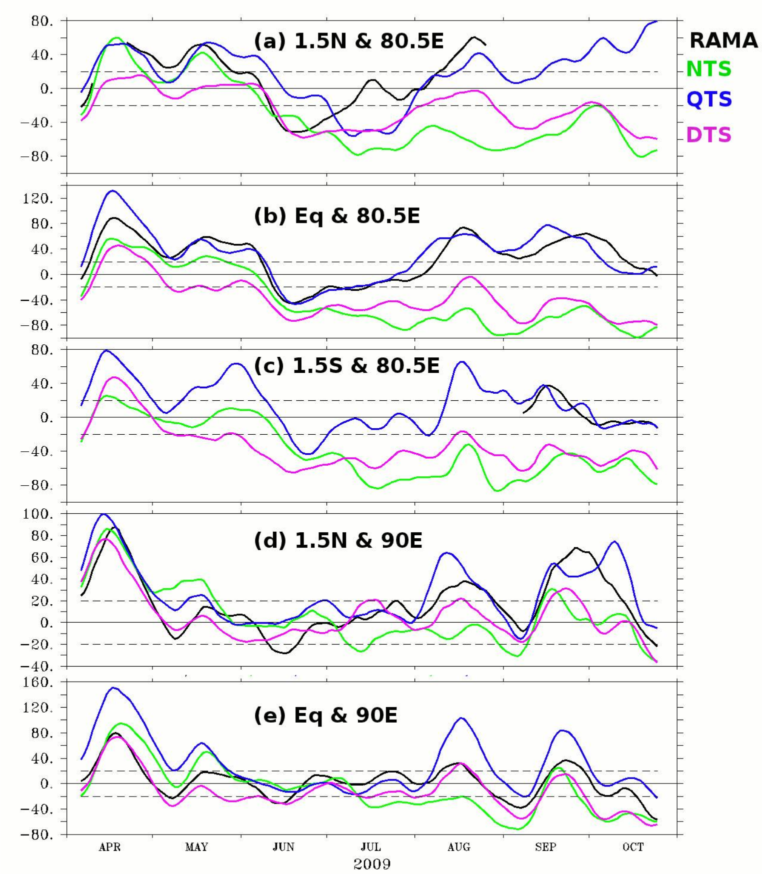

Figure 4.11: Ocean surface (30 m averaged) zonal currents from RAMA moorings (black), *NTS* (green), *QTS* (blue), and *DTS* (pink) at (a) 1.5 °N, 80.5 °E, (b) Equator, 80.5 °E , (c) 1.5 °S, 80.5 °E, (d) 4 °S, 80.5 °E (e) 1.5 °N, 90 °E, and (f) Equator, 90 °E. The model currents are interpolated to RAMA location and time. For better readability of figures all the time series have been smoothed with a 5-day running mean. Units are in cm/s

monsoon season (Figure 4.11f). Except from these localized differences, *QTS* and *DTS* appears to do fairly well in the eastern parts of the EIO region. In the central parts of the EIO (Figure 4.11a-4.11d), *QTS* follow the *RAMA* observation very closely whereas *NTS* and *DTS* have the westward bias, with *NTS* having large bias compared to *DTS*. For example, at Equator, (80.5 °E) during July-October, 2009, *QTS* and *RAMA* showed eastward current whereas *DTS* and *NTS* showed strong westward zonal current (Figure 4.11b). Performance of *QTS* is better than the other two experiments of *NTS* and *DTS* in the south-western parts of the EIO region (Figure not shown) too. Further, it can be noted from the statistics

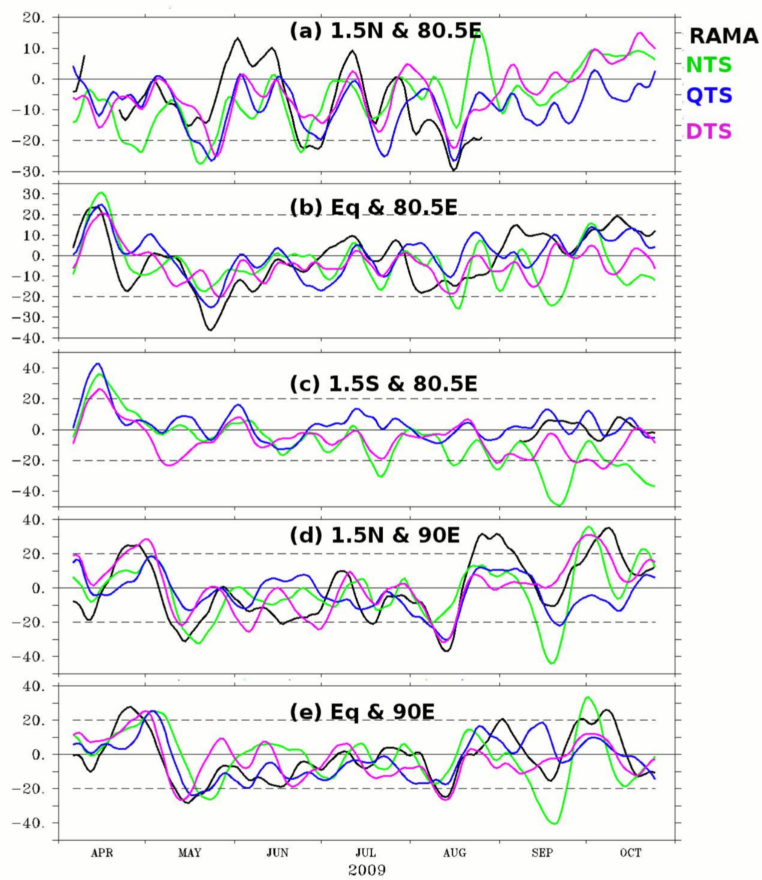

Figure 4.12: Same as Figure 4.11 except for meridional component of current.

summarized in the Table 4.4 that mean and variability of zonal currents are very well simulated by *QTS* than *NTS* and *DTS* with respect to *RAMA* observations. For instance, while the maximum observed mean bias in zonal current reaches 60 cm/s in *DTS* and *NTS*, it is less than 30 cm/s for *QTS*.

Comparisons of meridional component of surface current from *NTS*, *DTS*, and *QTS* with *RAMA* indicate that the differences between the model experiments are not large when compared to zonal component of current. This is because, at the equator, the contribution from zonal component dominante the meridional component. For example, the standard deviation (STD) of meridional component of surface currents from *RAMA* data is observed to be ranging from 4 to 18 cm/s in the EIO locations. while for the zonal component it is observed to be ranging from 15 to 35 cm/s. There are only few occasions where the magnitude

Table 4.4: Summary from the statistical comparison of surface zonal (U) and meridional (V) currents at various RAMA locations in the Equatorial Indian Ocean (EIO)

Location	**No. of points**		**Average** (cm/s)				**Standard deviation** (cm/s)				**RMSD w.r.to RAMA** (cm/s)			**Correlation w.r.to RAMA**		
			RAMA	*NTS*	*QTS*	*DTS*	*RAMA*	*NTS*	*QTS*	*DTS*	*NTS*	*QTS*	*DTS*	*NTS*	*QTS*	*DTS*
(8 ^{o}S, 55 ^{o}E)	136	U	-11.9	-29.7	-24.8	-31	17.7	8.8	15.7	5.8	27.7	24.5	26.4	-0.2	0.2	0.07
		V	-9.6	-10.5	-9.8	-8.9	10.5	6.4	7.2	6.3	12.4	8.8	8.9	-0.0	0.6	0.5
(1.5 ^{o}N, 80.5 ^{o}E)	132	U	8.9	-27.2	6.8	-20.1	32.7	38.1	33.5	23.2	51.2	27.8	34.3	0.5	0.7	0.8
		V	-7.7	-9.6	-10.2	-7.9	10.5	8.8	8	6.8	12.6	9.7	9.1	0.2	0.5	0.5
(Eq, 80.5 ^{o}E)	203	U	26	-40.4	31.6	-36.9	34.8	46.8	40.1	30.8	79.5	18.5	68.9	0.5	0.9	0.6
		V	-1.4	-4.4	0.3	-4	12.8	10.6	9.9	7.9	13.8	10.5	11.6	0.3	0.6	0.5
(1.5 ^{o}S, 80.5 ^{o}E)	48	U	5.8	-58.3	6.1	-46.7	15.9	10.7	15.5	8.2	66.2	8.6	54.2	0.3	0.8	0.5
		V	0.6	-26	2.8	-13.3	4.9	12.3	5.5	8.2	30.8	6.9	15.8	-0.6	0.2	0.4
(4 ^{o}S, 80.5 ^{o}E)	45	U	11.9	18.9	6.1	27.8	12.3	15.2	10.6	4.4	10.5	7.3	19.6	0.9	0.9	0.4
		V	-6.9	-30.6	-13.1	-23.4	4.2	10.8	4.6	11.4	26.7	6.4	19.5	-0.2	0.9	0.4
(1.5 ^{o}N, 90^{o}E)	203	U	17.4	7.3	26.9	6.3	26.8	27	27.1	22.4	27.6	18.3	19.8	0.5	0.8	0.8
		V	-0.8	-2.2	-3.1	0.6	17.8	15.2	10.6	14.9	14.5	16.5	12.3	0.6	0.4	0.7
(Eq, 90 ^{o}E)	203	U	3.8	-8.4	30.1	-12.6	25.4	39.5	44.2	29.5	31.2	38.5	20.7	0.7	0.8	0.9
		V	-2	-1.7	-2.8	-2.8	13.7	14.7	11.6	11.4	14.7	11.3	10.8	0.5	0.6	0.6

of meridional component of current crosses 20 cm/s whereas the magnitude of zonal component of current is above 20 cm/s during most of the study period. It is worthy to note that comparison of meridional surface current component from three different model experiments and observation is not so bad as can observed from Figure 4.12. For example low magnitude cross equatorial current observed from RAMA in the central (Figure 4.12a & 4.12b) and eastern parts (Figure 4.12e & 4.12f) are captured by model experiments with reasonable skill. Satellite based wind forcing experiments *QTS* and *DTS* show slightly better representation than *NTS*, which can be verified from correlation listed in Table 4.4. It can also be noted from the Table 4.4 that correlations from *DTS* with observation are better than *NTS* for meridional component.

From the above it is clear that the results from the comparisons of model simulated currents with *OSCAR* (Figure 4.10) and with *in-situ* RAMA currents are consistent with each other. The results of *QTS* and *NTS* are consistent with the results shown in Chapter-3 as well. From the above analysis, it is also clear that DASCAT and QSCAT derived surface currents are better than NCEP-R2 momentum flux, while using in INCOIS-GODAS. Comparatively less accurate representation of currents by NCEP-R2 wind forced experiment is understandable, since the quality of NCEP-R2 winds is low in the eastern parts of the TIO as discussed in Goswami and Sengupta (2003). Such errors are relatively less in the satellite blended wind products and thus offer better simulation of ocean currents in the ocean model as shown by Sengupta et al. (2007). Since the causes and impacts of discrepancies between NCEP-R2 and QSCAT in ocean models are examined in detail in the earlier studies (Sengupta et al. (2007); Agarwal et al. (2007); and also in Chapter 3), we refrain from discussing this issue in detail. Relatively less accurate representation of currents in *DTS* compared to *QTS* in the equatorial region indicates that there must be significant discrepancies between the DASCAT and QSCAT wind products. However, this result is interesting since previous two sections have shown that the performance of DASCAT is on par with the QSCAT wind. The probable reason for these discrepancies in the wind products is examined in the following section. Since the differences between the performances of model experiments are noticed at the Equator and in the zonal component of currents, the remaining part of the discussions are focused on zonal components only.

4.3.3.2 Possible factors for the less accurate representation of DASCAT forced model currents compared to QSCAT

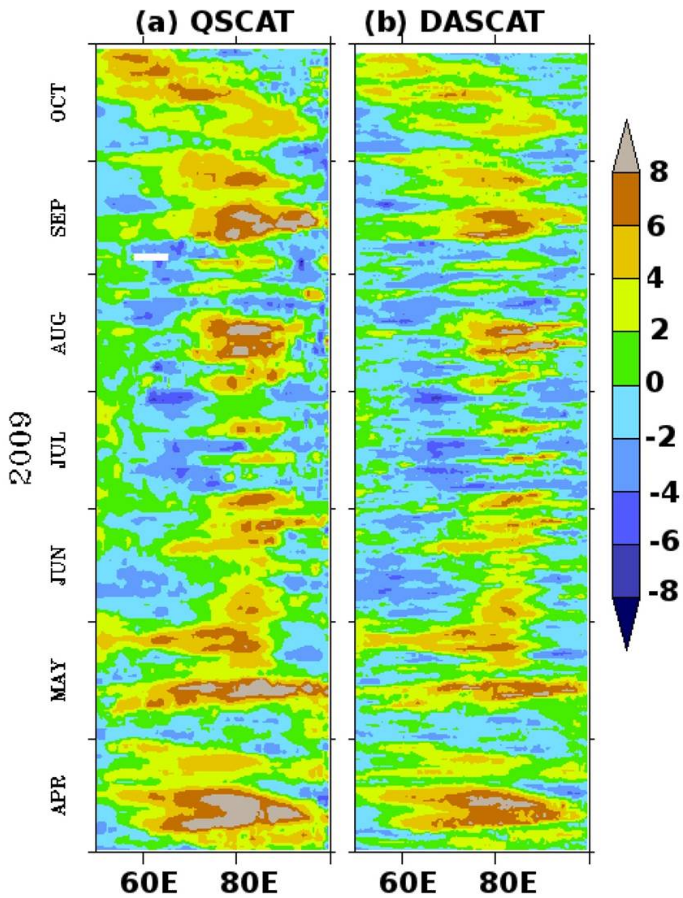

Figure 4.13: Longitude-Time sections of zonal wind speed (m/s) from (a) QSCAT and (b) DASCAT averaged for $2°S - 2°N$. Hovmoller is shown for the period 01st April, 2009 to 31st October, 2009

Figure 4.13 shows time lingitude section of zonal wind patterns along the equator from DASCAT and QSCAT during the analysis period. Occurrence of westerly wind event in intra-seasonal time scale is clearly noticeable in Figure 4.13. As suggested by Goswami and Sengupta (2003), the westerly wind bursts observed throughout the year are the responses to intra-seasonal variations of convective activity in this region. Earlier studies have shown that these intra-seasonal wind events generate intra-seasonal current variability in the EIO in the similar time scale (Senan et al., 2003). Figure 4.13 depicts that the magnitude and spatio-temporal extent of these westerly events are relatively weak in DASCAT compared to QSCAT (Figure 4.13). It is worth to mention here that DASCAT product is constructed using satellite based ASCAT wind measurements and model based European Centre for Medium-range Weather Forecasts (ECMWF) winds (Bentamy and Fillon, 2012). As reported by (Bentamy and Fillon, 2012), correlation coefficients between ASCAT and collocated DASCAT are less (0.85) at the equatorial region compared to other regions due to less coverage of ASCAT retrievals and degraded quality of ECMWF winds at the equator. Their study also showed that the high wind events ($> 12m/s$) observed from ASCAT measurements are smoothed by the objective method used to construct DASCAT. This smoothness has resulted in the underestimation of magnitude of wind in DASCAT. They also have indicated that the discrepancies are large at small scales in terms of wind amplitude. It can be observed from Table 4.2 that zonal wind variability is underestimated in DASCAT (STD; 4.88 ms^{-1} for no-rain; 7.74 ms^{-1} for high wind) compared to QSCAT (STD; 5.3 ms^{-1} for no-rain; 8.03 ms^{-1} for high wind) and RAMA (STD; 5.2 ms^{-1} for no-rain; 8.44 ms^{-1} for high wind) during rain-free and high wind events.

It can be hypothesized from the above discussion that the degradation in the quality of wind at equator in DASCAT compared to QSCAT is the source for the observed discrepancies between the zonal currents of QTS and DTS in the central parts of the EIO. However, it is not clear why the major discrepancies in the simulated current fields of DTS and QTS are observed only in central parts of the EIO. Hence, in order to further understand the differences between DTS and QTS in the simulated currents in the central parts of the EIO, we have examined zonal momentum budget in the central EIO region.

4.3.3.3 Zonal momentum budget for the Central Equatorial Indian Ocean

To perform the zonal momentum budget, the following equation from Sengupta et al. (2007) is employed.

$$\frac{\partial u}{\partial t} = -\frac{1}{\rho}\frac{\partial p}{\partial x} + \frac{\partial}{\partial z}\left(k\frac{\partial u}{\partial z}\right) + otherterms \qquad (4.2)$$

Where u,ρ,p,and k are the zonal current speed (m/s), density of sea water (kg/m^3), pressure (N/m^2), and coefficient of the vertical momentum mixing (m^2/s) respectively; Independent variables t,x,and z represent time (s), longitude (m) and depth (m) respectively. The first term on the right hand side is the Zonal Pressure Gradient (ZPG). This is obtained using model dynamic height in the upper 120 m ocean layer. The second term is the zonal wind stress term (ZWS); integration of the stress from a sufficiently deep level ($120m$) to the surface gives the following model surface boundary condition: $k(z=0)\left(\frac{\partial u}{\partial z}\right)_{z=0} = \tau_x$, where τ_x is zonal wind stress per unit mass per unit depth (m^2/s^{-2}). The $otherterms$ includes zonal, vertical and meridional advection etc. These are not considered in the present study as the zonal momentum balance at the equator is reported to be majorly between the ZPG and ZWS (Sengupta et al., 2007).

Earlier studies (Bubnov, 1994; Sengupta et al., 2007) have shown that zonal currents in the EIO region, especially eastern parts (east of $60°E$; the region where we noticed large differences between QTS and DTS), are influenced mainly by two factors, viz., ZWS and ZPG of the upper 120 m. The ZPG is westward throughout the year, except in February and March (Bubnov, 1994; Sengupta et al., 2007).

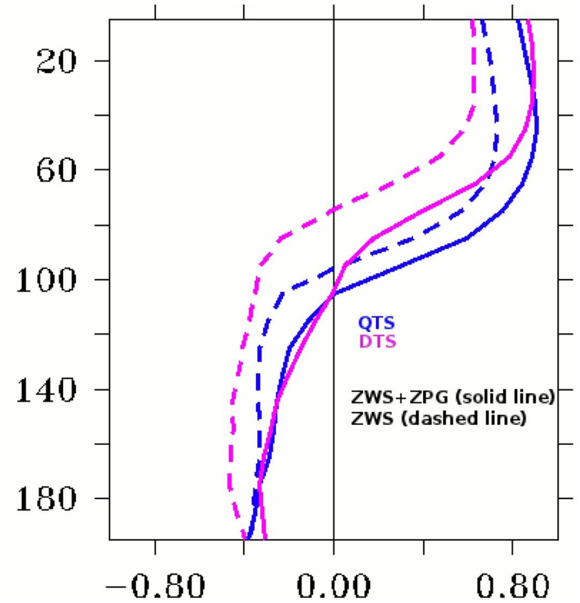

Figure 4.14: Correlation between zonal current acceleration and ZWS (dashed line), and zonal current acceleration and ZWS+ZPG (solid line). Results from the experiments corresponding to QSCAT and DASCAT forcing are shown in blue and pink color respectively. Zonal current acceleration, ZWS, and ZWS+ZPG terms are averaged for Central parts of the Equatorial Indian Ocean ($2°S$-$2°N$ and $60°E$-$90°E$; CEIO) region and smoothed by 10-days before performing correlations. The correlation greater than 0.4 is significant at 95% confidence level

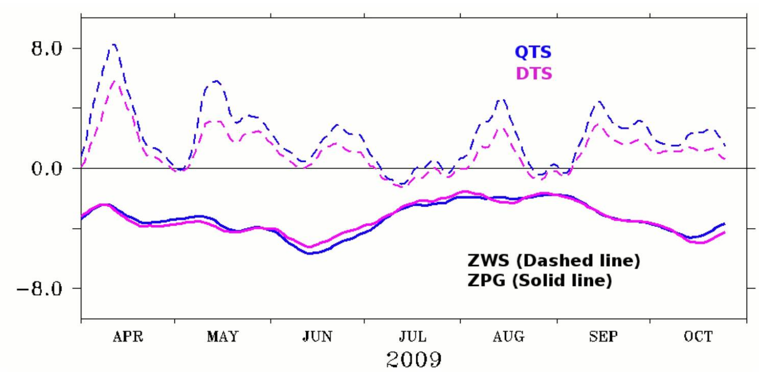

Figure 4.15: Time series of ZPG ($10^{-7}m/s^2$; thick line) and ZWS ($10^{-7}m/s^2$; dashed line) from QTS (blue) and DTS (pink) experiment. All the variables are smoothed by 10-day and averaged for the CEIO ($2°S$-$2°N$ and $60°E$-$90°E$) region before performing calculations

On intra-seasonal time scales the ZPG is largely influenced by ZWS (e.g. westerly wind bursts) via equatorial waves (Sengupta et al., 2007). In-order to understand the relative contribution of ZPG and ZWS on zonal current acceleration in the central EIO ($2°S$-$2°N$ and $60°E$-$90°E$; CEIO), we have examined the depth-wise correlation between ZWS and zonal current acceleration and ZWS+ZPG and zonal current acceleration (Figure 4.14). The correlation between ZWS and zonal current acceleration is between 0.6-0.7 in the upper 60 m layer. It indicates that around $36-49\%$ of zonal acceleration can be explained by ZWS term alone. When ZPG term is added to the ZWS term, the correlation is increased to 0.8-0.9 in the upper 60 m layer. The analysis indicates that about $70-80\%$ of zonal current variation in the CEIO can be explained by these two terms. This result is consistent with the results of Sengupta et al. (2007). It can be inferred from these results that the contribution from ZPG to total acceleration term is $28-32\%$ and is comparable to that of ZWS contribution $(36-49\%)$. Hence the remaining part of this section devotes to identify on the link between zonal current acceleration and other two terms, i.e. ZWS and ZPG. ZWS and ZPG averaged over the CEIO corresponding to QTS and DTS are shown in the Figure 4.15. From the Figure 4.15, it can be noticed that ZPG is negative (westward) throughout the analysis period corroborating the results of Bubnov (1994) and Sengupta et al. (2007). On the other hand ZWS is positive (eastward) throughout the study period. Further, the amplitude of variations in ZWS is large compared to ZPG. It is worth mentioning here that, large amplitudes of ZWS are associated with the westerly wind bursts (please compare Figure 4.13 with Figure 4.15), which typically last for 10-40 days (Sengupta et al., 2007). It can be clearly observed from the Figure 4.15 that the discrepancies in ZPG between QTS and DTS are very small compared to discrepancies in ZWS between QTS and DTS. For example, the magnitude of differences is less than $0.5 \times 10^{-7} m/s^2$ (equivalent to $0.5 m/s$ error in the surface wind) for ZPG, it reaches $3 \times 10^{-7} m/s^2$ (equivalent to $3 m/s$ error in the surface wind) for ZWS (please see Figure 4.16a). It is worth to mention here that the temperature and salinity profiles are assimilated using 3DVAR in INCOIS-GODAS. The assimilation of temperature and salinity profiles corrects the model geostrophy. Since ZPG represents the model geostrophy, it is reasonable to argue that the insignificant differences between ZPG of QTS and DTS are due to the assimilation of temperature and salinity profiles in INCOIS-GODAS. Large differences between QTS and DTS in ZWS compared to ZPG are obviously due to the discrepancies in the local wind forcing (please compare Figure 4.13 with Figure 4.15). These results indicate that the discrepancies, in the zonal current patterns of CEIO, between QTS and DTS are primarily explained by the local discrepancies (ZWS represent local effect) between DASCAT and QSCAT winds. In order to get further clarification on these results, we have analyzed the differences in budget terms between QTS and DTS.

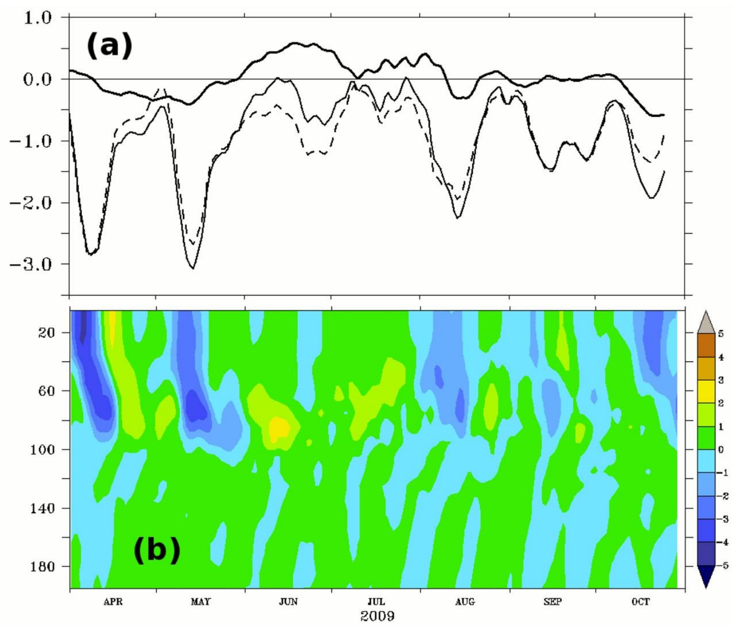

Figure 4.16: Difference between DASCAT and QSCAT (DASCAT-QSCAT) wind forced experiments in terms of differences in (a) ZWS ($10^{-7}m/s^2$; dashed line), ZPG ($10^{-7}m/s^2$;thick solid line) and ZWS+ZPG ($10^{-7}m/s^2$; thin solid line) and (b) depth-wise zonal current acceleration ($10^{-7}m/s^2$) . All the variables are smoothed by 10-day and averaged for the CEIO ($2°S$-$2°N$ and $60°E$-$90°E$) region before performing calculations

Figure 4.16 shows the difference between *QTS* and *DTS* in terms of difference in (a) ZPG (thick solid line), ZWS (thick dashed line), and ZPG+ZWS (thin solid line) along with (b) the difference between *QTS* and *DTS* in total zonal acceleration. As discussed earlier, the differences (*DTS*-*QTS*) in ZWS are larger compared to the differences in ZPG. Due to the dominance of the difference in ZWS, compared to the difference in ZPG, the difference in ZPG+ZWS shows good temporal correspondence with the difference in ZWS (Figure 4.16a). Further, the difference in ZWS (and also ZWS+ZPG) is negative throughout the study period with large differences in April, May, August, and October. Interestingly, the difference between the zonal current acceleration of *DTS* and *QTS* (*DTS*-*QTS*) also shows negative during these months with good overall temporal correspondence between the difference in ZWS (and also ZPG+ZWS) and difference in zonal current, extending up to 100m depth. This temporal correspondence confirms the fore-mentioned dominant impact of local wind differences on the discrepancies in zonal current (Figure 4.16b). From the above discussions we could find answers for the following questions.

Why the differences between *QTS* and *DTS* in the simulation of currents are exposed only in the CEIO, not in other remotely linked regions?

Why the model simulated currents of *DTS* has westward bias in the CEIO?

The answer for the first question is that the contribution from the ZPG, which represents both local and remote wind effect, is very small for the difference in current between *DTS* and *QTS*, due to the assimilation of temperature and salinity profiles in INCOIS-GODAS. The contribution from ZWS, which represents the local wind effect, is major for the differences in currents between *DTS* and *QTS* in the CEIO. The answer for the second question is that the eastward acting ZWS is less than the westward acting ZPG in the DASCAT forced model experiment.

4.4 Summary

The present study is to qualify DASCAT wind as a successor to QuikSCAT wind for use in the operational assimilation system "INCOIS-GODAS' owing to (1) the well known degraded quality of model based NCEP2 winds compared to satellite blended winds and (2) non-availability of QuikSCAT winds after November, 2009. In-order to accomplish this task, we first validate the DASCAT wind product using QSCAT and RAMA observations. Later, we verify the suitability of DASCAT, with respect to QSCAT and NCEP-R2, for use in INCOIS-GODAS. The analysis is carried out for the TIO during the period 01^{st} April, 2009 to 30^{th} October, 2009.

Comparison of DASCAT wind with QSCAT shows that even though both QSCAT and DASCAT have a strong spatial correspondence, the mean wind speed is underestimated in DASCAT (by up-to $1m/s$) with respect to QSCAT. The discrepancies between DASCAT and QSCAT winds are comparatively large over the eastern parts of north Indian Ocean (with biases and RMSDs of greater than 2 m/s and 1.5 m/s respectively). We also have found a strong spatial coherence between the number of rainy days and the differences between these two wind products. Further analysis was performed to identify the source of these discrepancies in terms of different wind speed and rain regimes using *in-situ* wind speed from the RAMA buoy. This analysis clearly shows that the accuracy of QSCAT winds show wind speed dependence and does not compare well under low wind speed conditions ($< 4m/s$). DASCAT, on the other hand, shows no significant change in accuracy with wind speed. Rainfall significantly influences the QSCAT wind product: wind speed estimates are biased high, particularly for winds weaker than $10m/s$. The DASCAT product compares well with RAMA observations even in rainy conditions.

It is found from the sensitivity experiments using assimilation system in the TIO, the INCOIS-GODAS, that the quality of ocean current analysis from the DASCAT wind forced experiment is better than NCEP-R2. Also, the quality of ocean current from the DASCAT forced experiment is on par with the QSCAT forced experiment, except in the EIO. It appears that lack of rich small scale variations in the DASCAT winds due to over smoothness leads to less accurate representation of ocean current in the upper 100m layer in these regions, especially during high wind events (e.g. wind bursts). The results further suggest that although *DTS* performance is less accurate compared to the performance of *QTS* in capturing surface currents realistically in the fore-mentioned EIO region, it is still better than *NTS*. Thus in the absence of QSCAT winds, it is a wise choice to use momentum flux derived from DASCAT instead of NCEP-R2 momentum flux, in state of the art ocean models such as INCOIS-GODAS for providing better ocean analysis or reanalysis.

Apart from finding a suitable wind product for state of the art ocean models like INCOIS-GODAS, the present study indirectly demonstrates the need for wind evaluation using state of the art ocean models. It can be argued based on the results from the present study that in the absence of enough *in-situ* observations for the wind field comparisons, the region specific issues in the gridded wind products, such as noticed in the present study, comes to lime light by testing them using state of the art ocean models. The present study also has provided valuable insights on the impact of wind errors on the ocean current analysis of assimilation systems. It is found that the impact of the wind discrepancies between DASCAT and QSCAT is majorly local and up-to 100m deep in the INCOIS-GODAS. The less impact of wind error on ocean analysis of INCOIS-GODAS is largely attributed to the correction of geostrophic field by the assimilation of temperature and salinity profiles in the INCOIS-GODAS. Since the impact of wind discrepancies is felt even in our assimilation enabled INCOIS-GODAS model, the impact is presumed to be larger in ocean forecasts. The results further suggest that although *DTS* performance is poor compared to the performance of *QTS* in capturing surface currents in the EIO region, it is still better than *NTS*. Thus in the absence of QSCAT winds, it is a wise choice to use momentum flux derived from DASCAT instead of NCEP-R2 momentum flux, in assimilation systems such as INCOIS-GODAS for generating better ocean analysis or reanalysis.

Chapter 5

Impact of river runoff and salinity profile assimilation

5.1 Introduction

Results from chapter-3 indicate that there is a lot of scope to improve ocean salinity analysis in the TIO. Accurate representation of salinity is important as it plays crucial role in the upper ocean stratification in the regions such as the Bay of Bengal (BoB). This upper ocean stratification in turn has impact on various aspects such as the intensity of storm-induced surface cooling (e.g. Sengupta et al. (2008)), influence on the amplitude of intra-seasonal variability of the Sea Surface Temperature (SST; e.g. Vinayachandran et al. (2012)) and biological productivity regimes (Prasanna Kumar et al., 2002). Salinity also has an influence on the amount of water transport from the Pacific to the Indian Ocean through Indonesian Through Flow (ITF; Murtugudde and Busalacchi (1998)). Huang et al. (2008) have shown improvements in the TIO in salinity analysis of NCEP-GODAS, which is similar to the configuration of INCOIS-GODAS, when synthetic *in-situ* salinity profile is replaced with observed *in-situ* salinity profile assimilation. The improvements in the model salinity field may also be obtained by providing realistic river runoff as reported by earlier studies (Howden and Murtugudde, 2001; Han and McCreary, 2001; Han et al., 2001; Yu and McCreary, 2004; Vinayachandran and Nanjundiah, 2009; Seo et al., 2009; Huang and Mehta, 2010; Durand et al., 2011; Akhil et al., 2014). For example, Durand et al. (2011) have shown improvements in the salinity field when they replace the monthly climatology of Ganga-Brahmaputra river runoff with inter-annual monthly Ganga-Brahmaputra river runoff in their eddy permitting ocean model. The improvements are observed mainly above $10°N$ in the BoB except during few years of anomalous river discharge, during which the improvements are observed even in west coast of India.

Although earlier studies have shown impacts of observed *in-situ* salinity assimilation (e.g. Huang et al. (2008)) on model salinity field in the TIO, unfortunately their assessments were not based on independent observations. Also, there are no comprehensive reports, to the best of our knowledge, on the spatial extent of salinity improvements with the inclusion of realistic river runoff in assimilation enabled ocean models. Motivated by these factors, in this chapter we substantiate the impact of observed *in-situ* salinity assimilation and realistic river discharge on salinity analysis of INCOIS-GODAS using a suite of satellite and *in-situ* salinity observations. In order to be able to conduct the study on the impact of river discharge a new inter-annual monthly global river discharge data set is constructed for the period 1993-2012. Detailed description on the technique used to construct this data set and also the description of the model experiments conducted using these data sets are presented in the following section. The results and discussion pertaining to evaluation and impact analysis of observed *in-situ* salinity profile assimilation and river runoff is presented in section 5.3. Section 5.4 provides summary of the present study.

5.2 Construction of inter-annual monthly River Discharge and Description of Model experiments

Flowing rivers into the ocean is an important aspect for ocean models as it influences ocean stratification which in turn affects circulation (Chamarthi et al., 2008; Durand et al., 2011) and air-sea interactions (Sengupta et al., 2008) especially at regional scales. For example, Papa et al. (2012) have shown a strong link between Ganga-Brahmaputra river discharge and upper ocean salinities in the north BoB. Durand et al. (2011), using a numerical ocean model, have shown that the inter-annual variability of Ganga-Brahmaputra river discharges has impact on sea surface salinity and also temperature in the BoB north of $10°N$ with the impact extending further to reach west coast of India in the years of anomoulous river discharge. Sengupta et al. (2006) have shown that the river discharge from Irrawady influences the salinities in the south BoB and eastern parts of the Equatorial Indian Ocean. Clearly these studies emphasize the need to have reliable estimates of inter-annual monthly river discharges especially for ocean models to provide improved salinity analysis/forecasts. Despite such an important requirement, most of the operational centers use annual or monthly climatologies of river discharge in their ocean models. This was due to the non-availability of reliable river discharge data sets. However, considerable efforts are put up recently to generate reliable estimates of the global (Dai and Trenberth, 2002; Dai et al., 2009) as well as regional (Papa et al., 2010, 2012) inter-annual monthly river discharge.

The river discharge data provided by Dai et al. (2009) is for the world's 925 largest ocean-reaching rivers. The data set is based on observed river discharge records and stream flow simulated by a land surface model (Community Land Model, version 3) forced with observed precipitation and other atmospheric forcing that are significantly correlated with the observed stream flow for most rivers.

The data set, which represents about 73% of global total runoff, accounts for all global river runoff except for Antarctic and Greenland runoff. The error in the pure observation data points is between $10 - 20\%$. The error may be large when the data gap for a river is large. The data was composed for 1948-2004. Data coverage for Indian based rivers ranges from 10-50 yrs with largest (smallest) record for Ganga and Brahmaputra (Godavari, Krishna). In order to be used as a river forcing in the ocean models, global maps of inter-annual monthly river discharge based on the Dai et al. (2009) stream flow is compiled and made available under CORE-II (Common Ocean Research Experiment-II) project. Time series of Ganga-Brahmaputra combined river discharge into the ocean, estimated using altimeter measurements and stage-discharge rating curves for the period 1993 to 2012 is provided by Fabrice Papa on personal communication. The mean error of the data is estimated to be around 17%. Information on the techniques used to construct and the error characteristics are discussed in detail by Papa et al. (2010), and Papa et al. (2012).

For the present study, we construct a data set of global maps of inter-annual monthly river discharge for the period 1993-2012, based on the fore-mentioned gridded product of CORE-II river discharge and time series of Ganga-Brahmaputra river discharge provided by Fabrian Papa. This is done primarily to utilize the constructed data set to provide improved salinity analysis from INCOIS-GODAS. Since the estimates of river discharge of Ganga-Brahmaputra in both of the datasets are highly correlated (0.9) except for some data dependent offsets, at first we use the following linear regression equation for the representative Ganga+Brahmaputra grid to be able to extend the CORE-II up to 2012.

$$Y = mX + C \tag{5.1}$$

Where Y is river discharge (expressed in $Kg/m^2/s$) from CORE-II; X is Ganga+Brahmaputra river discharge (m^3/s) provided by Papa et al. (2012); m

and C is the slope (Kg/m^5) and intercept ($Kg/m^2/s$) of the linear regression obtained from the common period i.e., 1993-2007.

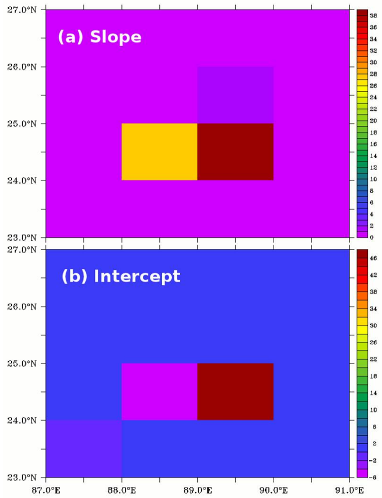

Figure 5.1: Slope (a; $10^{-9}Kg/m^5$) and intercept (b; $10^{-5}Kg/m^2/s$) in the linear regression equation obtained by comparing river discharge data from CORE-II with combined Ganga+Brahmaputra river discharge from Papa

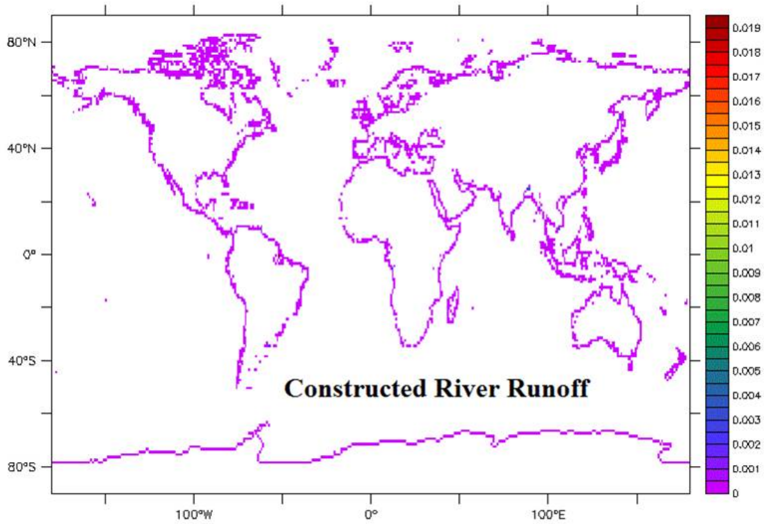

Figure 5.2: Distribution of river runoff (shaded) during August, 2009 from new dataset. Units are in $10^{-5}Kg/m^2/s$

Figure 5.1 show slope (m) and intercept (C) estimated at each grid point represented by Ganga+Brahmaputra river basin in CORE-II. We estimate Y at each of these grid points by using X (i.e. Papa et al. (2012) data) and the estimated

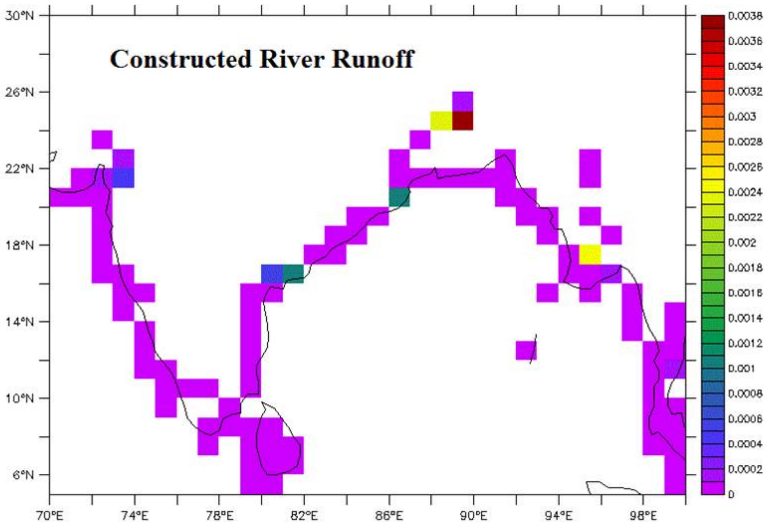

Figure 5.3: Same as 5.2 but zoomed for Indian continent

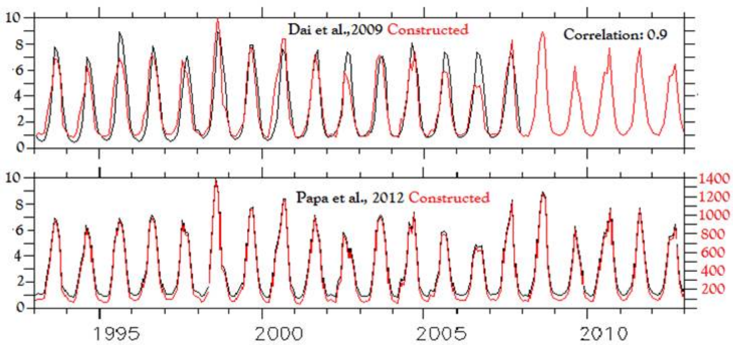

Figure 5.4: Ganga+ Brahmaputra river discharge from old (black), new (red) and Papa et al. (2012) (blue) data sets. Units for old and new data sets are $10^{-3}Kg/m^2/s$ where as for Papa et al. (2012) units are $10^2 m^3/s$. Area covering $87°E$-$91°E$ and $23°N$-$27°N$ is taken as proxy to represent Ganga+Brahmaputra river runoff from gridded products

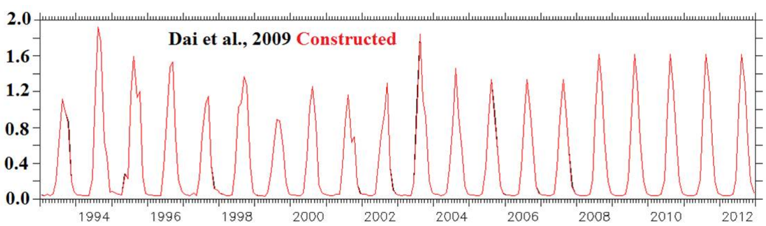

Figure 5.5: Godavarai river discharge from old (black), and new (red) data sets. Units are in $10^{-3}Kg/m^2/s$. Area covering $79°E$-$83°E$ and $15°N$-$18°N$ is taken as proxy to represent Godavari river runoff from gridded products

m and C. We note here that insertion of river discharge in each grid points based on the combined Ganga+Brahmaputra time series data may not represent the river discharge well at local grid point. However, in the present study this is not a matter of concern as these two rivers drain into ocean at very close by locations and also because we have made sure that total amount of freshwater is conserved within the specified domain of Ganga+Brahmaputra (please refer Figure 5.1 for the domain) while fitting the linear regression. For all other grid points, information from CORE-II is retained by filling the gaps during the period 2008-2012 (the extended period) with the respective monthly climatology. Hence the new gridded data set contains estimation of monthly river runoff, expressed in $Kg/m^2/s$, during the period 1993-2012 with full inter-annual variability included for Ganga+Brahmaputra region from Papa et al. (2012), and partial (only up-to 2007. From 2008, monthly climatology is used) inter-annual variability included for all other rivers from CORE-II. These features can be inferred from the figures 5.2 to 5.5. For example it can be inferred from the Figure 5.4 that new data set extends up to 2012 and differs (correlates) slightly (highly) with the old (Papa et al., 2012) data set. This small (high) mismatch (correlation) between old (Papa et al., 2012) and new data set is due to the insertion of Papa et al. (2012) data using linear regression equation at Ganga+Brahmaputra grid points in the new data set for the period 1993-2012. Successful insertion of monthly climatology to update the river runoff for 2008-2012 can be inferred from Figure 5.5.

As part of the present study, we have conducted five experiments with different river runoff data sets namely Annual climatology, monthly climatology and inter-annual monthly river discharge data sets. Table 5.1 summarizes the configuration of each of these model experiments.The first experiment, the *TS'* is the basic configuration of INCOIS-GODAS, where we assimilate observed in-situ temperature and synthetic salinity profiles. The second experiment, the *TS* differs with the *TS'* in the assimilation of salinity. The difference is the incorporation of

Table 5.1: Configuration of experiments used in the present chapter

Experiment	Profiles for Assimilation	River-Runoff	SST Relaxation	SSS Relaxation
TS'	*in-situ* observed Temperature and Synthetic salinity	Annual Climatology (Spreaded)	Weak (30 day)	Weak (30 day)
TS	*in-situ* observed Temperature and observed salinity	Annual Climatology (Spreaded)	Weak (30 day)	No Relaxation
TSP	*in-situ* observed Temperature and observed salinity	Annual Climatology (point source/No spread)	Weak (30 day)	No Relaxation
TSPM	*in-situ* observed Temperature and observed salinity	Monthly climatology (point source/No spread)	Weak (30 day)	No Relaxation
TSPI	*in-situ* observed Temperature and observed salinity	Inter-annual Monthly river runoff (point source/No spread)	Weak (30 day)	No Relaxation

observed *in-situ* salinity in *TS*. Hence the comparison of ocean analysis from *TS* and *TS'* will tell us the importance of salinity observations. Remining three experiments (*TSP*, *TSPM*, and *TSPI*) are based on newly constructed river runoff. Differences among these three experiments lies in the river runoff time series; *TSP* uses annual climatology of river runoff; *TSPM* uses monthly climatology of river runoff; *TSPI* uses inter-annual monthly river runoff. Inter-comparison of ocean analysis from these experiments should tell us the importance of river-runoff. It is worthy to note that *TSP* and *TS* are similar except that point source river runoff is implemented in *TSP* whereas pre-spreaded river runoff is used in *TS*. Hence comparison between *TSP* and *TS* should tell us the impact of pre-spreading river runoff on ocean analysis.

Since implementations of salinity assimilation and realistic river runoff are expected to have major influence on the model salinity, the present study examines the quality of salinity analysis from various experiments summarized in Table 5.1. The assessments are done based on the independent RAMA buoy and satellite based level-3 Aquarius sea surface salinity (SSS) measurements. It is worth mentioning here that the surface salinity is not relaxed to climatology in any of the model experiment except in *TS'* where a weak relaxation is used (refer Table 1 for experiment's configuration). Also, SSS from Aquarius is an independent source for evaluation of salinity analysis.

5.3 Results and Discussion

In this section, we first verify the performance of *TS* with respect to *TS'* experiment. Later, we examine the differences in the quality of salinity analysis between the experiments distinguished by the incorporation river runoff in the model namely pre-spreaded and point source option.

5.3.1 Impact of the replacement of synthetic with observed *in-situ* salinity profile assimilation in INCOIS-GODAS

It is well known from earlier studies that the TIO has strong east west gradient of sea surface salinities with low and high surface salinities in the east and west respectively. This is because the eastern parts of the Indian Ocean receives large amount of fresh waters from equatorial Pacific to the south-eastern parts of the TIO through ITF (Schott et al. (2009); and references there in), continental river runoff from the regions around the BoB (e.g. Han and McCreary (2001); Sengupta et al. (2006)), and excess amount of precipitation over evaporation in the BoB and eastern parts of the equatorial IO (e.g. Han and McCreary (2001)). It is worth mentioning here that the low salinity waters of the BoB contribute to the freshening in the regions hugging the west coast of India through narrow current systems (Chaitanya et al., 2014) and also to the south-eastern parts of the TIO through the southward moving currents at eastern boundaries of the TIO (Sengupta et al., 2006). On the other hand high salinities in the north-western parts of the TIO are helped by dominance of evaporation over precipitation, warm and saline waters from Persian Gulf and Oman, and upwelling in the regions of thermocline ridge and Somali (Han and McCreary, 2001).

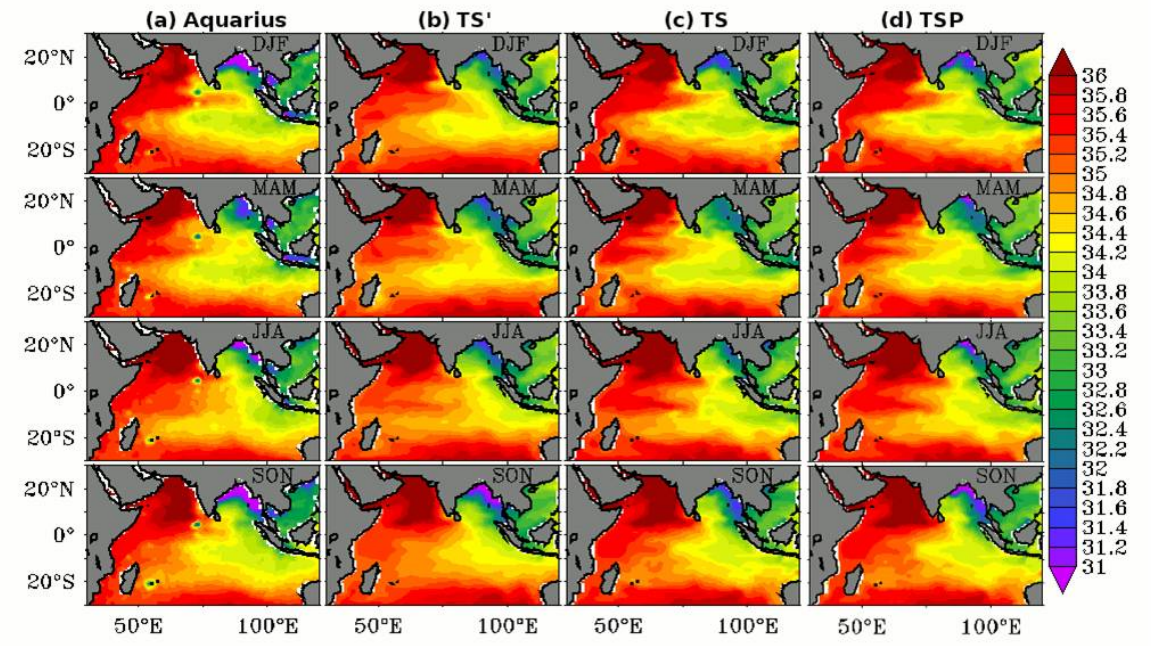

Figure 5.6: Seasonal evolution of SSS (psu) from (a) Aquarius, (b) *TS'* (c) *TS*, and (d) *TSP*. In the figure DJF, MAM, JJA, and SON represent the mean of December-January-February, March-April-May, June-July-August, and September-October-November respectively. Seasonal means are based on the data from December, 2011 to November, 2012

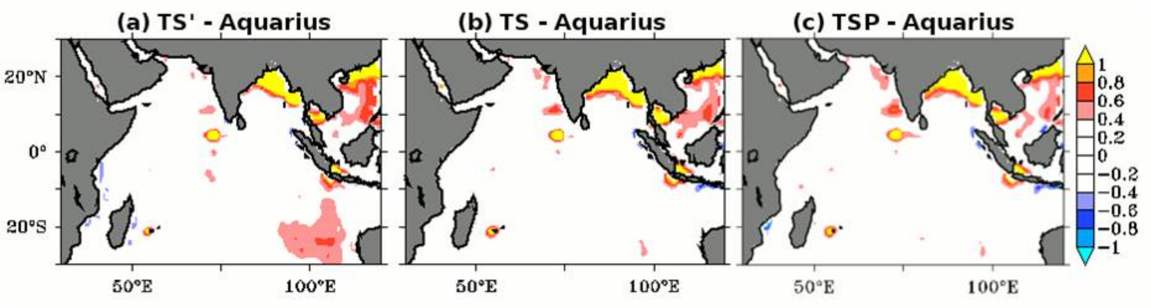

Figure 5.7: SSS bias (model-observation) in (a) *TS'* (b) *TS*, and (c) *TSP* with respect to Aquarius

Figure 5.6 shows seasonal mean patterns of SSS in the TIO from Aquarius, *TS'*, *TS*, and *TSP*. It can be inferred from the Figure 5.6 that contrasting features of SSS between eastern and western Indian Ocean are reproduced well by both

TS' and *TS* experiments. The magnitude of the SSS from *TS'* and *TS* appears to have noticeable differences with Aquarius in the BoB and also along the west coast of India. It can be observed from the Figure 5.7 that the magnitude of SSS, with respect to Aquarius, in these two experiments is overestimated, by more than 1 psu, in the northern BoB and along the west coast of India. The biases of SSS from *TS'* are large even in the south eastern parts of the TIO (0.4 to 1 psu). It appears that the discrepancies in the south-eastern parts of the TIO are significantly reduced by using observed *in-situ* salinity profiles for the assimilation. The error reduction over these regions is up-to 50% and improvements, in terms of Root Mean Square Difference (RMSD), are up to 0.3 psu (Figure 5.9). Compared to *TS'*, the variability of the SSS in the *TS* is close to the Aquarius SSS in all regions of the TIO including the northern parts of the BoB (Figure 5.8).

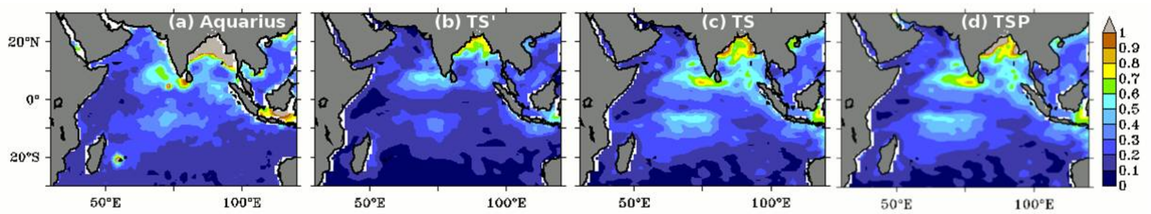

Figure 5.8: Standard deviation of SSS from (a) Aquarius, (b) *TS'* (c) *TS*, and (d) *TSP*

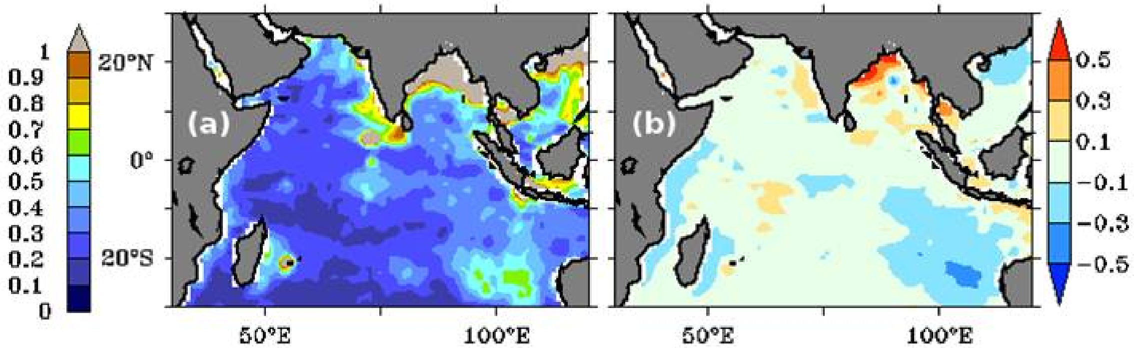

Figure 5.9: RMSD in the SSS of (a) *TS'* and (b) Difference in RMSD between *TS* and *TS'* (*TS*-*TS'*). RMSD is with respect to Aquarius SSS

Despite having such a good agreements in the variability of SSS, it is interesting to observe that the RMSDs in the northern parts of the BoB for *TS* are larger than

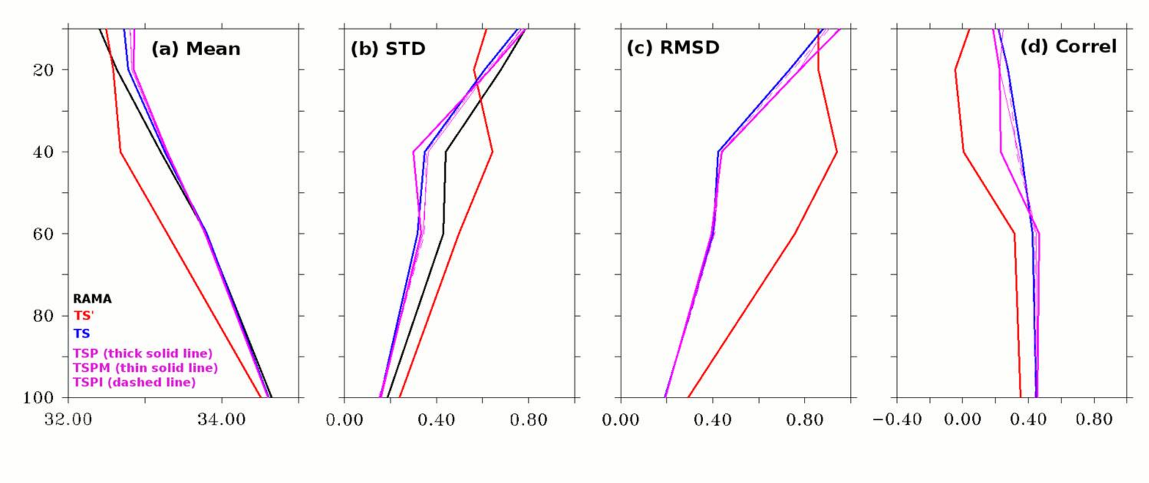

Figure 5.10: Depth-wise statistics of salinity (psu) derived from *TS'*(red), *TS* (blue), *TSP* (pink thick solid line), *TSPM* (pink thin solid line), and *TSPI* (pink dashed line) with respect to *in-situ* RAMA temperature (black) at (15°N, 90°E) location. In the figure, the panels a, b, c, d shows mean, STD, RMSD, and correlation respectively. Statistics are based on collocated daily data during 2004-2012

TS'. As indicated earlier, in general, the magnitude and variability in the northern parts of the BoB are influenced majorly by freshwater inputs from adjacent river systems (Durand et al., 2011). It is reasonable to speculate here that use of climatological SSS for relaxation as well as for the construction of synthetic salinity would have caused comparatively low SSS biases and underestimation of variability in *TS'* compared to *TS* (compare Figure 5.8a, 5.8b, and 5.8c), where observed *in-situ* salinity profiles are assimilated with no SSS relaxation. This speculation is further strengthened by the improved quality of salinity in sub-surface layers as found by comparing the salinities from *TS* and *TS'* with independent salinity measurements of RAMA buoy. For example, 50% reduction in the error with improvements, in terms of RMSD, of 0.5 psu is observed in *TS* over *TS'* for the 30-60m layer at (15°N, 90°E) (Figure 5.10). It is worth noting here that in general RMSDs are less than Standard Deviation (STD) for SSS from TS. Also, these RMSDs are comparatively large at the surface and less than 1 psu between 10-100 m depth.

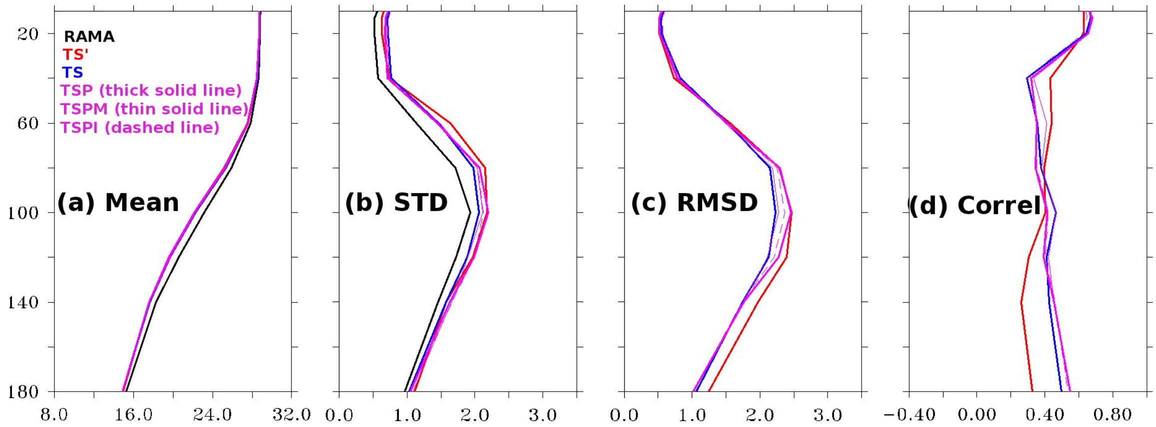

Figure 5.11: Same as Figure 5.10 except for temperature at ($8°N$, $90°E$) location

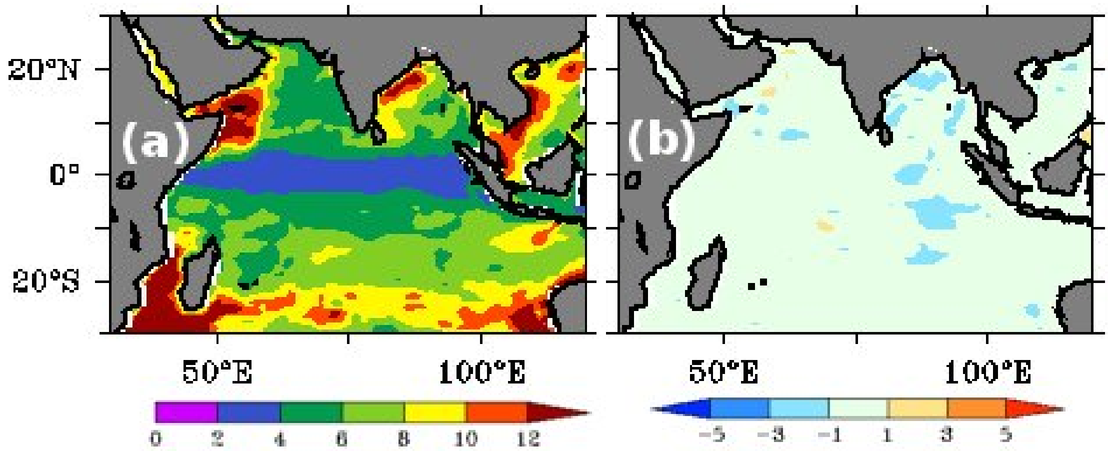

Figure 5.12: Same as Figure 5.9 except for SSHA (cm)

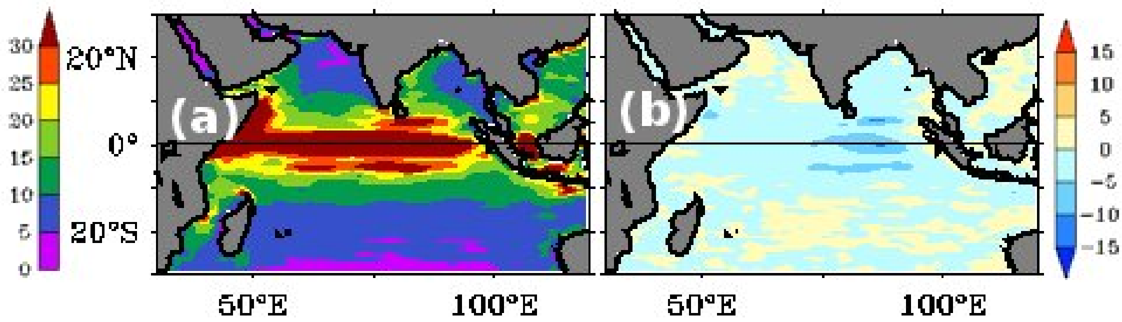

Figure 5.13: Same as Figure 5.9 except for surface current speed (cm/s)

The use of observed instead of synthetic *in-situ* salinity profiles for the assimilation reduces error for other parameters as well in some of the regions where improvements are observed in salinity. For example, at ($8°N$, $89°E$) location RMSD and correlation in 100-150 m layer is about $2.5°C$ and 0.5 respectively in *TS* whereas it is about $3°C$ and 0.2 respectively in *TS'*, which amounts an error reduction of 16% (infer from Figure 5.11). In the BoB and central parts of the BoB, the error reduction in SSHA is up-to 25% with improvements up to 3 cm (Figure 5.12). Similarly, in the eastern parts of the EIO, the difference in RMSDs of zonal surface currents between *TS'* and *TS* (*TS'*-*TS*) is about $10cm/s$, with an error reduction of ≈ 25% (Figure 5.13). These results, which are consistent with the results of Huang et al. (2008), clearly emphasize the need for the assimilation of observed *in-situ* salinity profiles.

5.3.2 Impact of river runoff

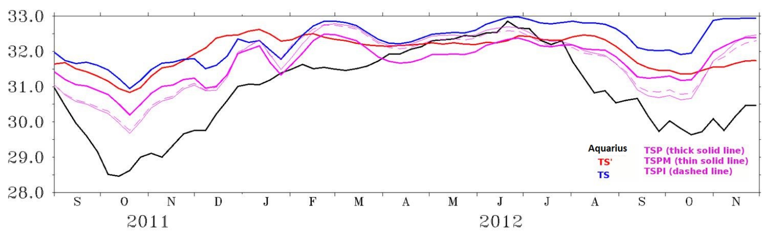

Figure 5.14: SSS averaged over the NBoB region ($12°N$-$23°N$ & $85°E$-$95°E$) from Aquarius (black), *TS'*(red), *TS* (green), *TSP* (blue), *TSPM* (thin blue line), and *TSPI* (dashed blue line)

It is interesting to note from Figures 5.6 and 5.8 that the *TSP*, where point source is used for the incorporation of river runoff in the model, yields improvements in salinity with respect to *TS*, in which pre-spreading is used for the incorporation of river runoff in the model. For example, seasonal cycle of SSS in northern parts of BoB is best captured in *TSP* compared to *TS* (Figure 5.6). It can also be verified from the Figure 5.14 that the seasonal cycle of SSS averaged over the region of North BoB (NBoB; $12°N$-$23°N$ & $85°E$-$95°E$) is well represented, with

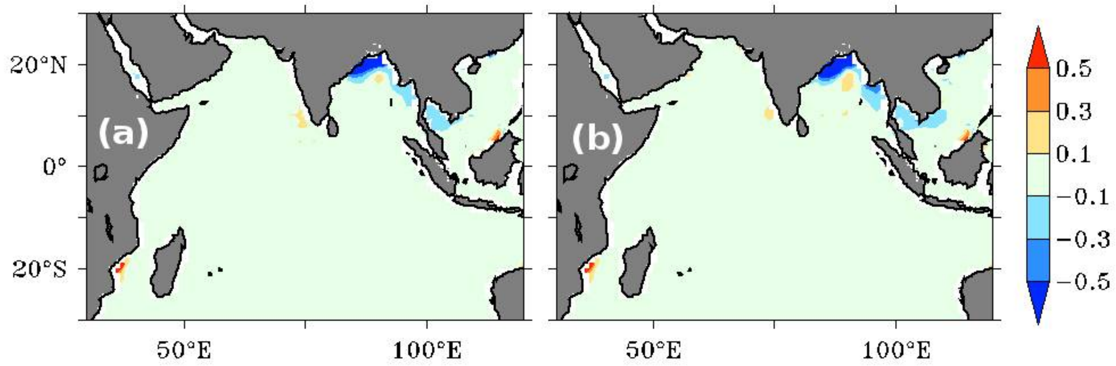

Figure 5.15: Difference in RMSD between (a) *TSP* and *TS* (*TSP*-*TS*), and (b) *TSPM* and *TS* (*TSPM*-*TS*) for SSS (psu)

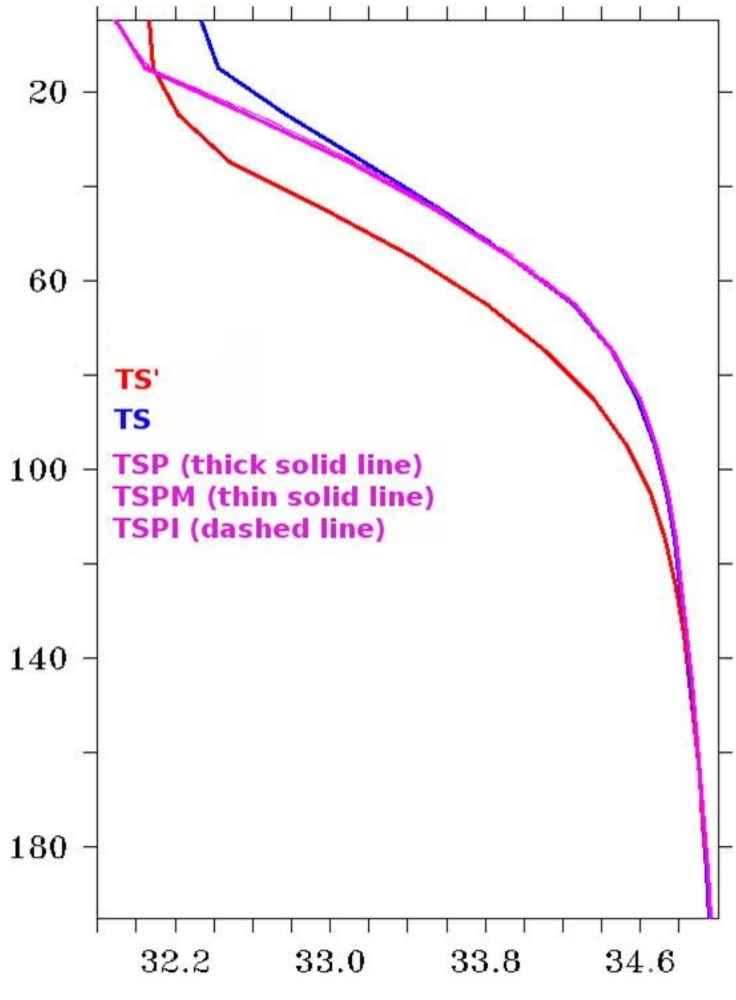

Figure 5.16: Mean salinity profile averaged for the NBoB region from Aquarius (black), *TS'*(red), *TS* (green), *TSP* (blue), *TSPM* (thin blue line), and *TSPI* (dashed blue line)

low (high) salinity waters during post-monsoon (pre-monsoon) seasons, in *TSP* compared to *TS*. The amplitude of annual cycle of SSS is relatively low in *TS* compared to Aquarius and *TSP*. In terms of RMSDs, the improvements of SSS in *TSP* with respect to *TS* reaches 0.5 psu in the northern parts of the BoB (Figure 5.15a). The mean salinity profiles averaged over the NBoB shows that there is almost 0.5 psu difference in the upper 30m between *TS* and *TSP* with no appreciable differences below 30m (Figure 5.16). The potential factors that might have lead to these interesting results are

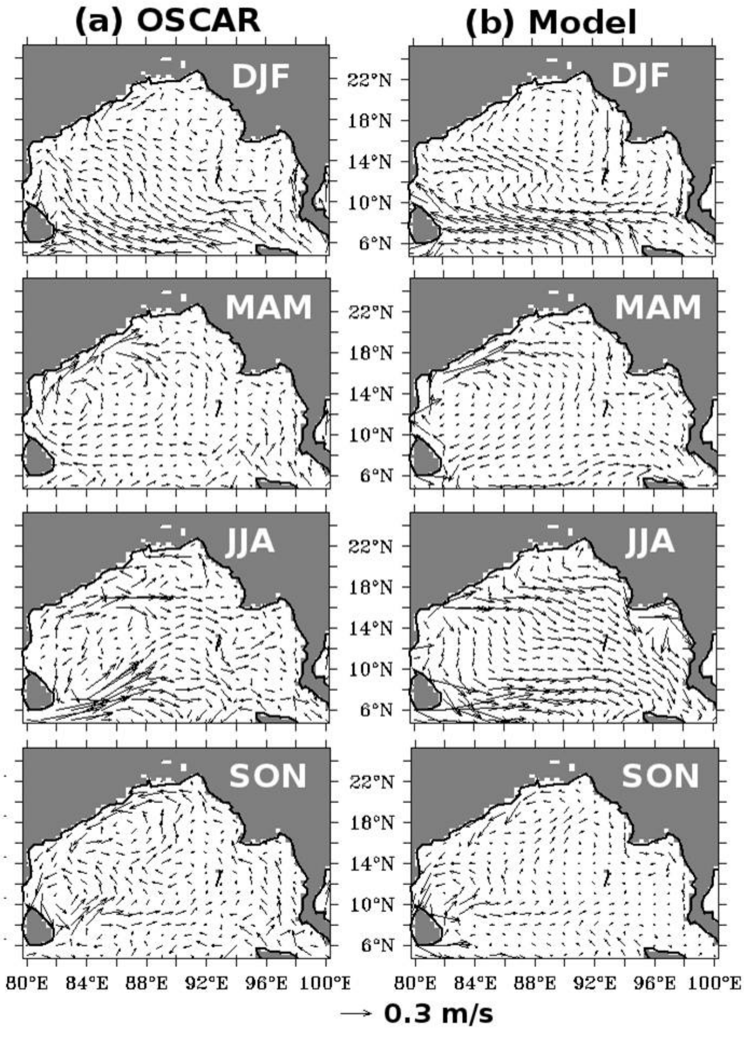

Figure 5.17: Seasonal climatology of surface currents from (a) OSCAR and (b) *TS* model experiment. Seaonal climatology is based on the data from 2004-2012

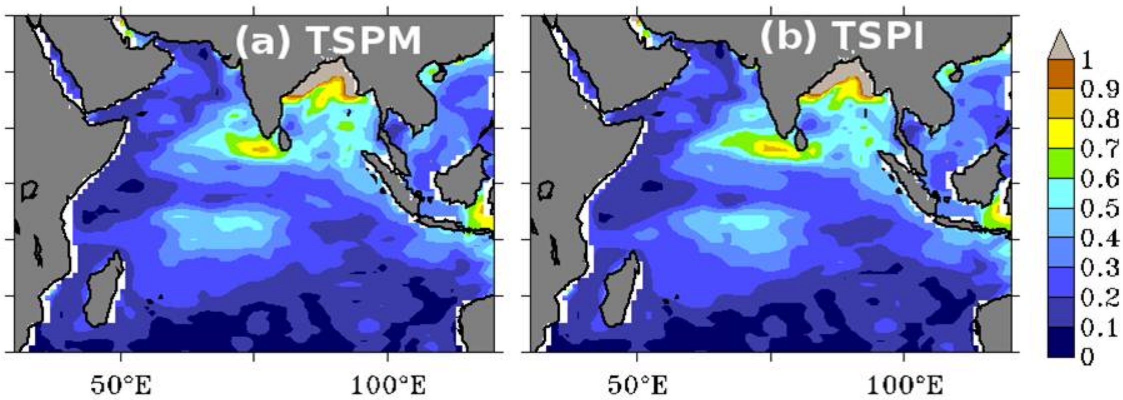

Figure 5.18: Standard deviation in SSS (psu) from (a) *TSPM*, and (b) *TSPI*

- The pre-spreading option might have caused less amount of freshwater available from the river runoff in model grid cells adjacent to river discharge regions. Although it should cause over flooding of river runoff in the interior parts of the BoB, the errors in salinity would have been suppressed due to observed salinity assimilation. In general, the impact of river runoff is mainly felt in the northern parts of the BoB as suggested by earlier studies (e.g. Durand et al. (2011); Akhil et al. (2014)). Also, availability of salinity profiles are less in the head BoB and easern parts of the BoB. These factors would have played important role to make the model to get influenced heavily on the prescribed river runoff in the northern parts.

- The ocean dynamics in the eddy permitting model might have taken care in dynamically spreading the river water flown into the model grid cell using point source option. This is supported by the Figure 5.17 where we can notice a close match of seasonal climatologies between the model simulated surface currents (climatology is derived from *TS* experiment since there is no appreciable differences between experiments in surface currents in the BoB) and satellite based surface currents. For instance the climatological features of surface currents, such as strong eastward flows in the interior BoB and south ward flows in the eastern BoB during summer monsoon, from model have close match with the OSCAR currents. Also, seasonally reversing East India Coastal Current (EICC) with southward flows during post monsoon and strong northward flows during pre-monsoon are represented by model at reasonable skill. Hence forcing a ocean model with realistic river discharges should improve the salinities in principle. Such improvements are evident from the comparisons of surface salinities between TSPM, TSPI and TSP. For example the variability of SSS is better represented in TSPM and TSPI compared to *TSP* (compare Figure 5.8 and Figure 5.18). Also, the spatial extent of SSS improvements over TS, in terms of RMSDs, is slightly large for TSPM (Figure 5.15b) compared to *TSP* (Figure 5.15a). The improvements of the salinity analysis with the use of monthly climatology corroborates the findings of earlier studies (Huang and Mehta, 2010; Durand et al., 2011). Absence of significant differences in the quality of salinity analysis between TSPI (inter-annual monthly river runoff) and TSPM (monthly climatology river runoff) experiments might be due to the absence of anomalous river runoff from Ganga+Brahmaputra during the analysis period (please infer from Figure 5.4).

Chaitanya et al. (2014) have argued that the river discharges in the BoB influence the salinity patterns along the west coast of India through narrow current systems of West India Coastal Current (WICC) and EICC. It means that the incorporation of realistic river runoff in ocean model should improve the model simulations of salinity all along the coast of India including its west coast. However, neither TSPM nor TSPI could improve the salinity analysis along the west coast of India. This may be due to the coarse resolution set up of the model as suggested by Durand et al. (2011).

5.3.3 Discussion on the erroneous patterns of SSS in the North BoB and West coast of India

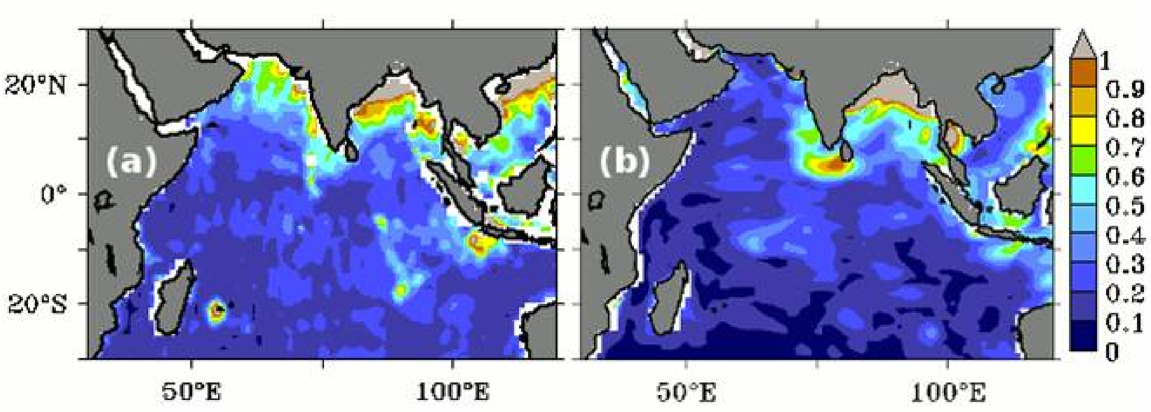

Figure 5.19: RMSD of SSS (psu) in (a) Aquarius, and (b) *TSPI* with respect to EN3V2a gridded SSS. Statistics are obtained based on monthly averaged data from September, 2011 to November, 2012

It is clear from the above results that configurations of either *TSPM* or *TSPI* offer improved ocean analysis compared to the old configuration of INCOIS-GODAS, i.e. *TS'*. It is important to remember, however, that none of the configuration could reduce SSS errors in totality either the northern BoB or along the west coast of India. It is worth mentioning here that gridded SSS data sets constructed using observations, such as the one offered by UK metoffice, the EN3V2A gridded product (Ingleby and Huddleston, 2007), also differ with the Aquarius SSS, of an order similar to that of TSPI experiment (Figure 5.19a). To gain further insights, SSS from Aquarius and TSPI are compared with EN3V2A for the Aquarius period (Figure 5.19a and 5.19b). It can be observed from the Figure 5.19 that the RMSD between the TSPI and the EN3V2A is relatively small in the areas off the west coast of India and large over most if not all of the South East Asia Sea (SEAS). Statistics using the period 2004-2012 also yield the same result. On the other hand, the RMSD between Aquarius and the EN3V2A are large along the west coast of India including the South Eastern Arabian Sea (SEAS). For both comparisons, the RMSDs are very large in the northern BoB. This indicates that the discrepancies observed in the northern BoB cannot be attributed to either the model or the observations alone. The effects of limited sampling by the Argo array and eddy activity in these regions would have contributed to these discrepancies. Not to be neglected are the difficulties of estimating SSS from Aquarius near coastlines in general (SEAS and North BoB in particular; Lagerloef et al. (2013)). Hence it is argued that the salinity analysis from TSPI offers better as much quality as other contemporary pure-observation or pure-satellite based salinity products do.

5.4 Summary

In an effort to provide better salinity analysis from INCOIS-GODAS various sensitivity experiments are conducted. The results from these experiments shed light on various aspects such as (1) the assimilation of observed *in-situ* salinity, (2) the incorporation of river-runoff. Besides being similar to the qualitative results obtained by Huang et al. (2008) on the assimilation of observed salinity instead of synthetic salinity, the quantitative results from the section 5.3.1 have provided useful insights for the assessment of the quality of salinity analysis from INCOIS-GODAS. For instance, the use of observed *in-situ* salinity profiles instead of synthetic *in-situ* salinity profiles for assimilation improves the model salinity field in a significant way particularly in the eastern parts of the TIO and BoB. The improvements in salinity of up to 0.3 psu in turn reduce errors in SSHA and currents by up to 25%. Interestingly, use of point source instead of pre-spreaded option for the incorporation of river runoff in the observed *in-situ* $T\&S$ profile assimilation enabled experiments lead to improvements in the salinity in the northern parts of the BoB especially the seasonal cycle. Improvements of salinity up to 0.5 psu are achieved within the upper 30m layer. Further improvements in salinity are also achieved with the incorporation of monthly climatology of river runoff under the point source option. However, there are no appreciable differences found in the quality of salinity analysis between the experiments with monthly climatology and inter-annual monthly river runoff. Results from the present study indicate that the configuration of either *TSPI* or *TSPM* experiments provide better ocean analysis.

Chapter 6

Evaluation of Improved Global Ocean Analysis

6.1 Introduction

An accurate representation of ocean state in space and time is important for understanding the physical and dynamical behaviour of the ocean which in-turn helps in improving the seasonal predictions of large scale systems such as Monsoon, Indian Ocean Diopole (IOD), El Nino and Southern Oscillation (ENSO), using coupled ocean atmospheric models. Considering the inputs from the previous chapters we have implemented all of the following features together to form a new configuration of INCOIS-GODAS with an objective to provide best possible ocean analysis on operational basis. The present chapter verifies the quality of ocean analysis obtained from this new configuration.

1. Assimilation of observed instead of synthetic in-situ salinity profiles.
2. Use of satellite (QSCAT or DASCAT) based gridded winds to force the ocean model instead of model (NCEP-R2) based winds.
3. Incorporation of inter-annual monthly river runoff with point source option.

4. Implementation of strong (5 day) instead of weak (30 day) relaxation time scale to bring the model SST close to observed Reynolds SST.

It is worth mentioning here that the improvements in the quality of ocean analysis offered by each of these implementations, except the 4th , is already demonstrated in the previous chapters. In the present chapter, we present the contributions from each of these implementations to the overall quality of ocean analysis in the experiment where all of these are implemented together (the *TSR* experiment; see Table 6.1 for the configuration). Section 6.2 provides a discussion on the statistical comparisons between the *TSR* and observations. It is well known that IOD event affects the rainfall over the regions covered by the Indian Ocean. It is also pointed out by earlier studies (Janakiraman et al., 2011) that ocean model in the CFS has the tendency to generate positive IOD events. It is worth mention here that the ocean model used here is similar to the ocean model used in CFS. Further, the ocean analyses generated from INCOIS-GODAS are being used in CFS, run by IITM, for improving the seasonal forecast. Hence, in the present chapter, skill of INCOIS-GODAS in capturing the IOD events is also examined for three different configurations i.e. *XA*, *TS'*, and *TSR* (see Table 6.1 for configuration of these experiments). Apart from these, we also verify *TSR* for the intra-seasonal variability of the zonal current at the equator. Section 6.3 discusses the results from these case studies. In order to demonstrate the quality of global ocean analysis, obtained from the adjudged best possible configuration of INCOIS-GODAS, the global ocean analysis is compared with the quality of ocean re-analysis from NCEP-GODAS and ECMWF-ORAS4 (ECMWF-Ocean Reanalysis-4). Section 6.4 discusses the results of this inter-comparison exercise. Summary and conclusions drawn from the results are provided in section 6.4.

Table 6.1: Configuration of experiments used in the present chapter

Experiment	Forcing	Profiles for Assimilation	River-Runoff	SST Relaxation	SSS Relaxation
XA	NCEP-R2 momentum, heat, and freshwater fluxes	No Assimilation	Annual Climatology (Spreaded)	Weak (30 day)	Weak (30 day)
TS'	NCEP-R2 momentum, heat, and freshwater fluxes	*In situ* observed Temperature and Synthetic salinity	Annual Climatology (Spreaded)	Weak (30 day)	Weak (30 day)
TS	NCEP-R2 momentum, heat, and freshwater fluxes	*In-situ* observed Temperature and observed salinity	Annual Climatology (Spreaded)	Weak (30 day)	No Relaxation
TSSR	NCEP-R2 momentum, heat, and freshwater fluxes	*In-situ* observed Temperature and observed salinity	Annual Climatology (Spreaded)	Strong (5 day)	No Relaxation
TSPI	NCEP-R2 momentum, heat, and freshwater fluxes	*In-situ* observed Temperature and observed salinity	Monthly river runoff (No Spread)	Weak (30 day)	No Relaxation
TSR	Satellite blended (3 day averaged QuikSCAT wind + DASCAT) momentum, NCEP-R2 heat, and freshwater fluxes	*In- situ* observed Temperature and observed salinity	Monthly river runoff (No Spread)	Strong (5 day)	Relaxation No Relaxation

6.2 Statistical comparisons between Improved Global Ocean Analysis and Observations

In this section, we compare the performances of *TSR* and *TS'* to realize overall improvements due to the implementation of aforementioned features altogether. Then we try to quantify the contributions of each implementation to the overall improvements in *TSR*.

6.2.1 Temperature

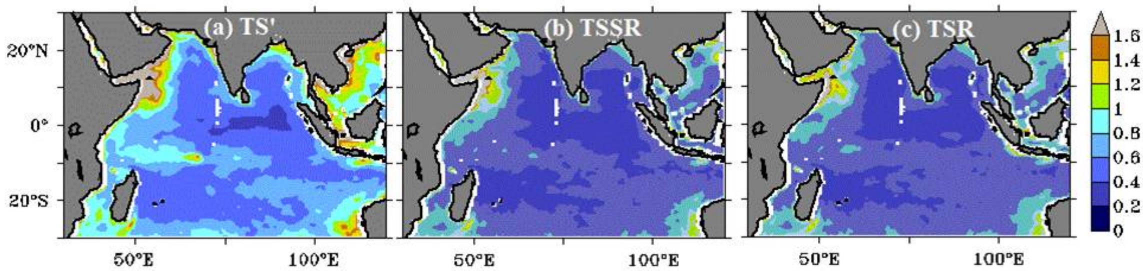

Figure 6.1: RMSDs of SST ($°C$) in (a) *TS'* (b) *TSSR* , and (c) *TSR* with respect to SST ($°C$) derived from TMIAMSRE

It is found from the comparison of SSTs from *TSR* and *TS'* with respect to SST observations from TMIAMSRE that the quality of SST is improved with *TSR*. The improvements in SST with *TSR* compared to *TS'* is as large as $0.6°C$, in terms of RMSD, in the regions such as the northern BoB, the thermocline ridge, near Somalia and offshore of western Australia (figure 6.1). These improvements are achieved due to the use of strong instead of weak SST relaxation as evident from the figure 6.1. The improvements in the sub-surface temperature in *TSR* is due to the assimilation of *in-situ* salinity profiles. For example, RMSD and correlation with respect to independent RAMA observations at ($8°N$, $89°E$) location, in 100-150m layer is about $2.5°C$ and 0.5 respectively in *TS* & *TSR*, where as it is about $3°C$ and 0.2 respectively in *TS'*. The improvements are comparatively large during fall and winter (figure 6.2f). Comparing the quality of *TSR* with *TS*

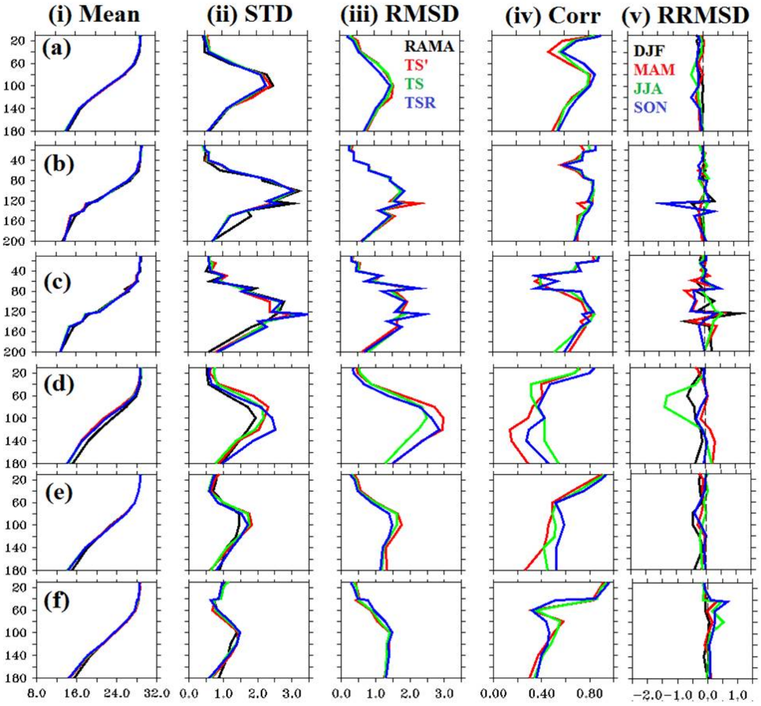

Figure 6.2: Depth-wise statistics of temperature ($^{\circ}C$) derived from *TS'*(red), *TS* (green), and *TSR* (blue) with respect to *in-situ* RAMA temperature (black) at various independent RAMA locations. (a) 1.5$^{\circ}S$, 80$^{\circ}E$, (b) 1.5$^{\circ}S$, 90$^{\circ}E$, (c) 5$^{\circ}S$, 95$^{\circ}E$, (d) 8$^{\circ}N$, 90$^{\circ}E$, (e) 12$^{\circ}N$, 90$^{\circ}E$, and (f) 15$^{\circ}N$, 90$^{\circ}E$. In the figure mean, STD, RMSD, and correlation are shown in i, ii, iii, and iv panels respectively. Statistics are based on collocated data during 2004-2012

indicates that strong relaxation degrades the quality of temperature at sub-surface layers. However, it is worth mention here that RMSDs of experiments where strong relaxation is used (*TSR*, *TSSR*) are less than observed standard deviation (Figure 6.2 and Figure 6.3).

6.2.2 Salinity

The Aquarius surface salinity data is utilized to examine the improvements of SSS in *TSR* with respect to *TS'*. It is found that the magnitude of SSS in both of the experiments is slightly overestimated in the northern parts of the BoB. Compared to the *TS'*, the SSS in *TSR* is close to Aquarius in many regions of the TIO. For example, over south-eastern parts of the TIO, the SSS bias in *TS'* is between 0.4 to 1 psu and has large spatial extent (Figure 6.4a). Further, it can be inferred

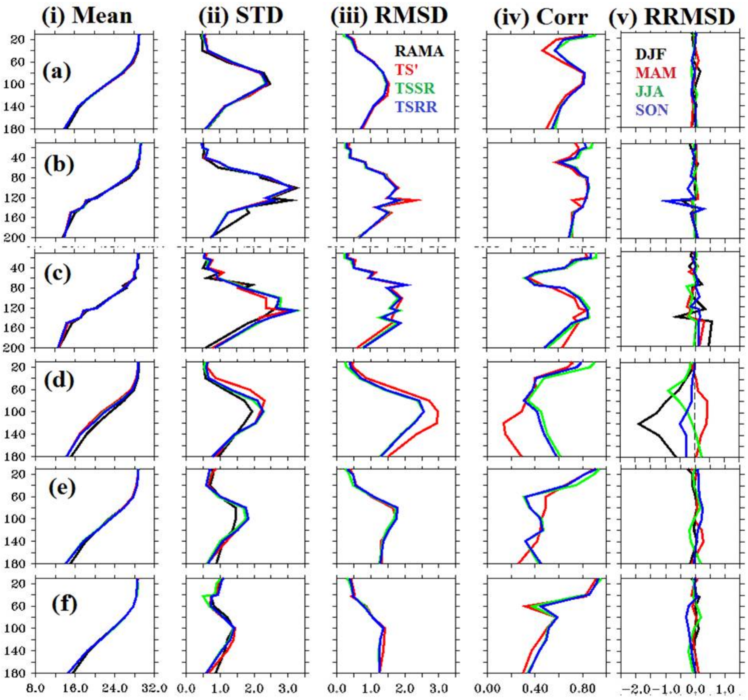

Figure 6.3: Same as Figure 6.2 except that *TS*, and *TSR* are replaced by *TSSR*, and *TSRR* respectively

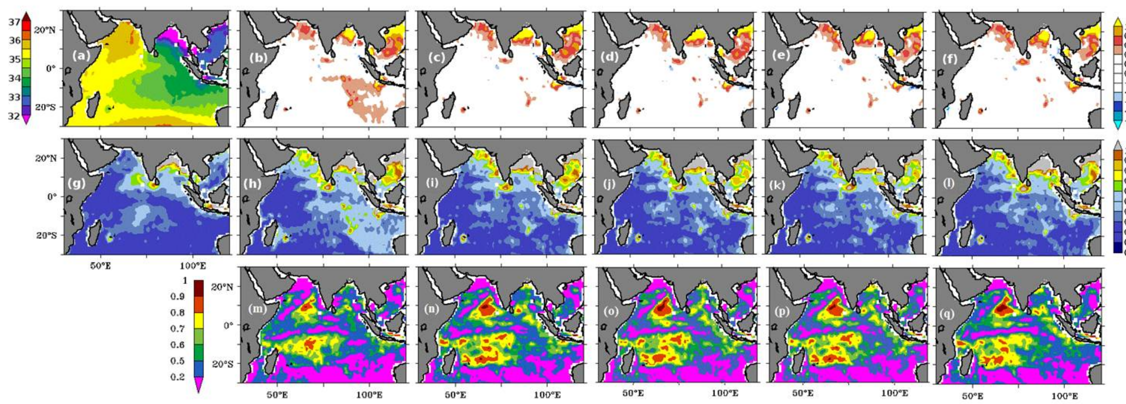

Figure 6.4: (a) Mean and (e) STD of SSS derived from Aquarius. Bias, RMSD, and correlation of SSS in *TS'*, *TS*, *TSSR*, *TSRR*, and *TSR* with respect to SSS derived from Aquarius are also shown in the figure. Panels b (g,l), c (h,m), d (i,n), e(j,o), and f (k,p) represents bias (RMSD, correlation) in *TS'*, *TS*, *TSSR*, *TSRR*, and *TSR* respectively. Statistics are obtained based on weekly data from 01^{st} September, 2011 to 30^{th} November, 2012

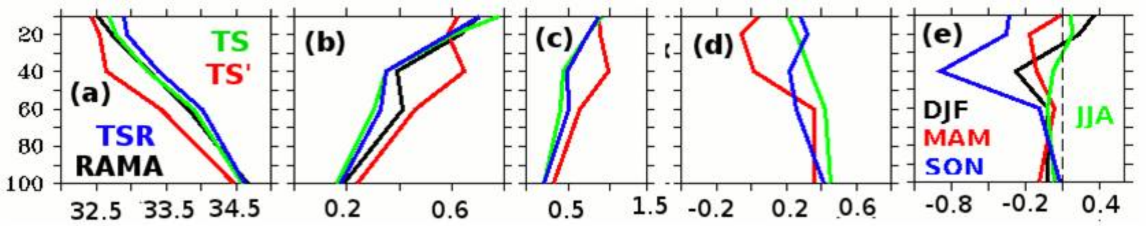

Figure 6.5: Same as Figure 6.2 except for salinity (psu) shown only for 15°N, 90°E. Other locations are avoided from the Figure as STD and RMSD for all other regions observed to be very less (less than 0.5 psu)

from the Figure 6.4b that the variability is underestimated and RMSD is larger than STD. The improvements in SSS, in terms of RMSD, over these regions are up to 0.3 psu in *TSR* over *TS'*. Depth wise comparison of salinity with respect to independent RAMA observation also suggests that *TSR* is better than *TS'* for sub-surface layers as well. The sub-surface improvements are large in the northern parts of the BoB with improvements amounting up to 0.5 psu. For example, the difference in RMSD between *TS'* and *TSR* (*TS'*-*TSR*) is greater than 0.5 psu at 15°N&90°E (Figure 6.5). The improvements in TSR are large, especially at 50m depth. It can be inferred from the Figures 6.4 and 6.5 that these improvements are majorly due to the assimilation of observed salinity instead of synthetic salinity for the assimilation. It is worth mentioning here that the incorporation of river runoff and satellite wind forcing have also contributed for improvements of salinity especially in the head BoB. The improvements in the BoB due to the incorporation of river runoff are upto 0.5 psu with in the upper 30m layer as noted in chapter 5.

6.2.3 Sea Surface Height Anomaly

Figure 6.6 show RMSD and correlation of SSHA by various experiments with respect to merged SSHA from altimeters. It can be inferred from the Figure 6.6 that there are noticeable improvements of SSHA with *TSR* over *TS'* configuration. The use of *in-situ* salinity instead of synthetic salinity brings this improvement in SSHA by up to 3 cm, particularly in the BoB and central parts of the south IO.

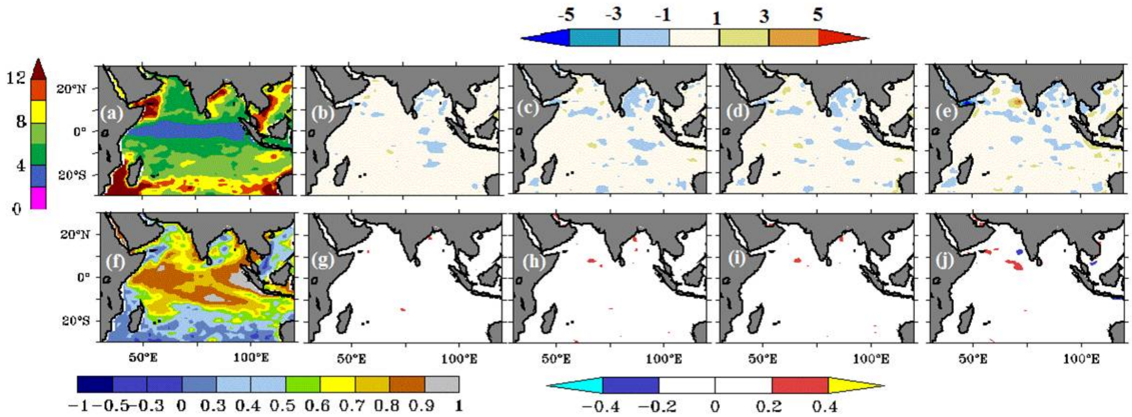

Figure 6.6: Statistics of model derived SSHA with respect to Altimeter derived SSHAs and reference experiments. Panels a and f show RMSD (cm) and correlation respectively between SSHAs derived from Altimeter and *TS'* Relative RMSD (relative correlation) in *TS*, *TSSR*, *TSRR*, and *TSR* with respect to *TS'*(ex: *TS-TS'* is shown in b, c, d, and e (g, h, i, and j) respectively

The use of satellite based wind instead of NCEP-R2 wind improves model SSHA further over regions such as near the thermocline ridge (Figure 6.6) where Ekman pumping may play an important role. It is interesting to observe that neither strong SST relaxation nor incorporation of inter-annual monthly river runoff could contribute further to the overall improvements on the quality of the SSHA in *TSR* (Figure 6.6).

6.2.4 Currents

Ocean currents are the principal agents for transferring heat, water mass properties, and various other trace materials. When we compare model currents from *TSR* and *TS'* with respect to observations, it is observed that although, the current speed is slightly over-estimated in the model experiments, the mean structures are well captured in all but a few locales. In general, surface currents from *TS'* show a westward current anomaly during the southwest monsoon season along the central equator, as noticed in chapter 3. In general RMSEs are large in the equatorial IO (EIO) than elsewhere in the tropical IO. For example, at the equa-

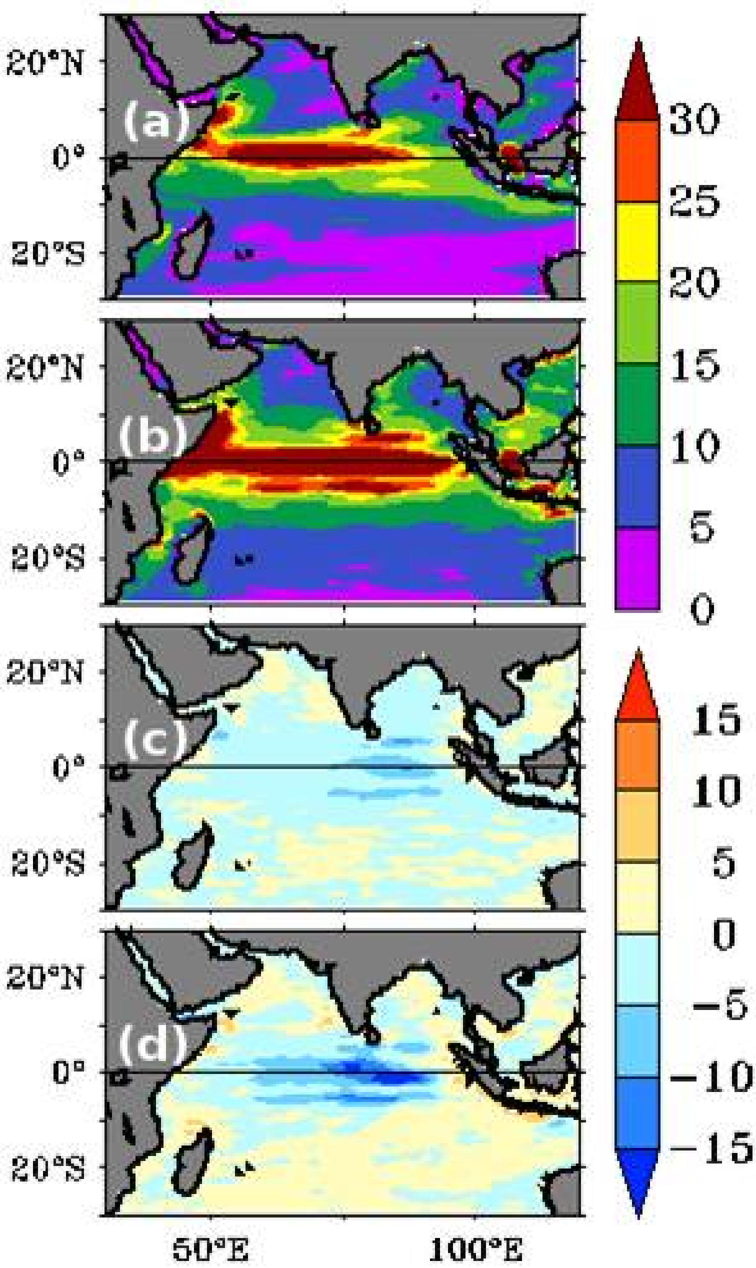

Figure 6.7: (a) STD derived from OSCAR (observed) zonal surface current (cm/s). (b) RMSD of zonal surface current (upper 30m averaged) in *TS'* with respect to zonal surface current derived from OSCAR. Relative RMSD (RRMSD) in *TS*, and *TSR* with respect to *TS'* is shown in panels c, and d respectively

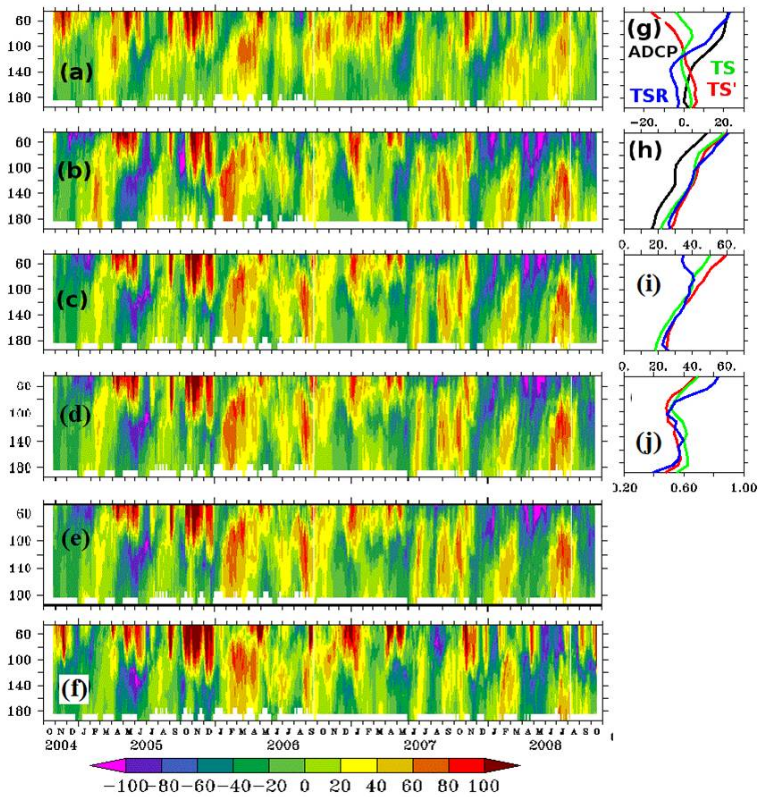

Figure 6.8: Depth time section of zonal current (cm/s) at $Equator$, 80.5°E derived from (a) ADCP, (b) *TS'* (c) *TS*, (d) *TSSR*, (e) *TSRR*, and (f) *TSR*. Depth-wise statistics such as mean, STD, RMSD and correlation, estimated with respect to ADCP, are shown in the figures in the panels (h), (i), (j), and (k) respectively. In the panels (h) to (k), ADCP, *TS'*, *TS*, and *TSR* are represented in black, red, green, and blue colour respectively

tor, the RMSD between currents derived from *TS'* and OSCAR is greater than 30cm/s while it is less than 15cm/s in other regions (Figure 6.7b). Depth-wise comparison of currents with ADCP at two equatorial locations (80.5°E&Eq, and 90°E&Eq) suggest that *TS'* has difficulty in capturing intra-seasonal variations such as eastward jets during spring and fall followed by weak west-ward currents (Wyrtki, 1973; Masumoto et al., 2005), east-ward flowing monsoon jets (Senan et al., 2003), and west-ward (east-ward) subsurface flow in October-December and May-June (January-February) (Masumoto et al., 2005), in a realistic way. For example, eastward jets during September-December, 2005 and 2008 (Figure 6.8a), are reversed in *TS'* (Figure 6.8b). In general, zonal currents in *TS'* are biased low by $30cm/s$, variability is overestimated by $5-10cm/s$ and RMSDs (correlations) are between $40-50cm/s$ (0.4-0.6) and are large (small) at the surface compared to the deeper layers. The large differences found in *TS'* on the equator are reduced significantly with *TSR* configuration. It is worth mention here that neither strong SST relaxation nor the inter-annual river runoff could yield visible improvements in the surface currents, indicating insignificant contributions to the improvements of currents with *TSR* from these two implementations. The improvements of currents in *TSR* is majorly due to the use of satellite instead of model based winds as evident from Figure 6.7 and 6.8. Also, the use of observed salinity for assimilation has contributed positively to the improvements of currents in *TSR*. For example, the difference in RMSDs of zonal surface currents between *TS'* and *TS* (*TS'*-*TS*) is about $10cm/s$ in the eastern parts of the EIO, while the difference between *TS'* and *TSR* (*TS'*-*TSR*) is as much as $30cm/s$ in the EIO (Figure 6.8). These results indicate that not only wind, but salinity assimilation can improve the surface and sub-surface currents.

From the above discussions, it is clear that ocean analysis obtained from TSR is best among all the experiments. Thus in the following section we use ocean analysis from *TSR* to verify how good INCOIS-GODAS able to re-produce inter-annual (IOD) and intra-seasonal variability of zonal surface currents at equator.

6.3 Intra-seasonal and inter-annual variability

An important question with regard to the *TSR* is whether it has the ability to reproduce the intra-seasonal variability in the Indian Ocean. Zonal currents in the EIO show a substantial intra-seasonal variability (30-90 days) which arises due to local wind anomalies and the remote effects of wind acting through Rossby and Kelvin waves at intra-seasonal time scales (McPhaden, 1982; Reppin et al., 1999; Masumoto et al., 2005; Han and McCreary, 2001; Han, 2005; Sengupta et al.,

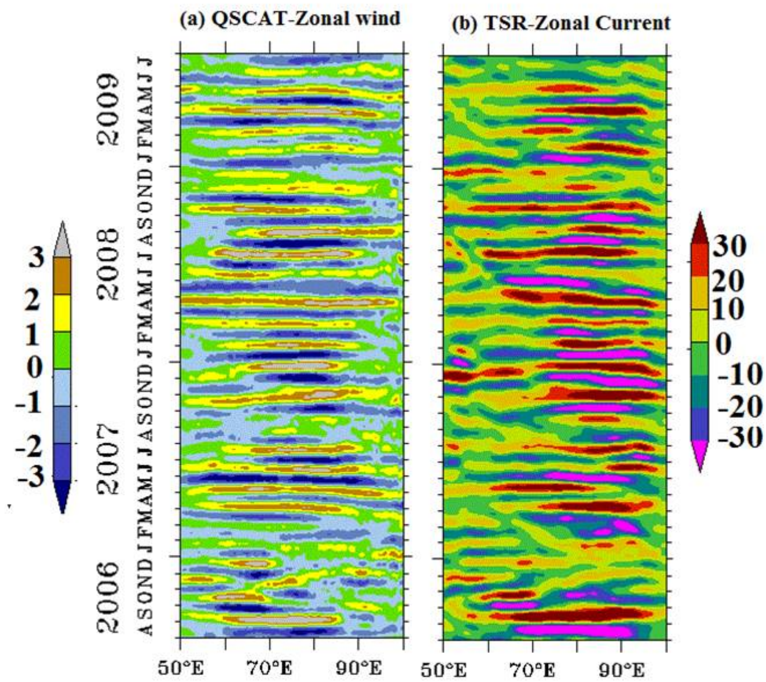

Figure 6.9: Temporal evolution of band-pass filtered (30-90 days) (a) QuikSCAT zonal wind (m/s) , surface zonal current (cm/s) obtained from (b) TSR in the equatorial Indian Ocean

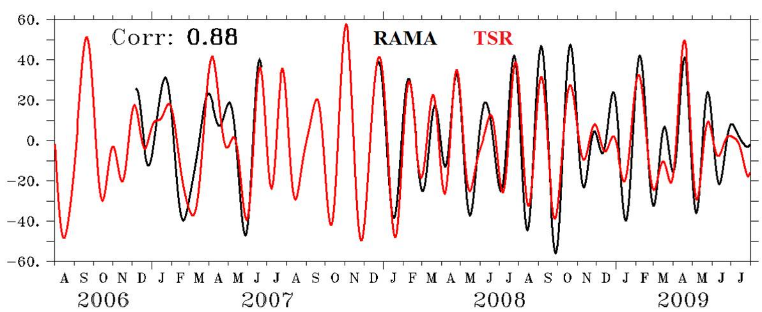

Figure 6.10: Time series of band pass filtered (30-90 days) zonal surface currents (cm/s) derived from RAMA (black line), and TSR (green line) at 0°, 90°E

2007; Iskandar and McPhaden, 2011). The 30-70 day oscillation in the zonal surface currents in the EIO arises as a response to the local wind anomalies at similar time-scales (Sengupta et al., 2007; Iskandar and McPhaden, 2011). The ability of the *TSR* in capturing these variations is illustrated in Figures 6.9 and 6.10. The Figure 6.9 shows the temporal evolution of band-pass filtered (30-90 days) QuikSCAT zonal wind stress (a), surface zonal currents obtained from the *TSR* (b) in the EIO. Time series of band-pass filtered (30-90 days) zonal surface currents derived from RAMA, and *TSR* at (Eq, $90°E$) is shown in the Figure 6.10. The intra-seasonal modulation of the zonal currents in response to intra-seasonal variations in wind stress along the equator can be clearly seen in Figures 6.9a, 6.9b, and 6.10c. Comparisons of band-pass filtered (30-90 day) zonal surface currents from *TSR* is in excellent agreement with *in-situ* observations (Figure 6.10) with high correlation (0.88).

The Indian Ocean Dipole (IOD) or zonal mode is one of the major modes of inter-annual climate variability in the Indian Ocean (Saji et al., 1999; Webster et al., 1999). It has been argued that the IOD significantly modulates global climate conditions in addition to conditions in the Indian Ocean region (e.g., Saji and Yamagata (2003)). Capturing the phase and amplitude of the IOD signature in any ocean model is important, especially if the model is intended for use in initializing a coupled ocean-atmospheric model for seasonal monsoon predictions (e.g., Janakiraman et al. (2011); Lee Drbohlav and Krishnamurthy (2010)).

A fundamental characteristic of the IOD is its apparent phase-locking to the seasonal cycle, with the peak strength of the IOD event tending to occur during October-November (Saji et al., 1999). A strong positive IOD event occurred during 2006. In this section, we examine the skill of *TSR* in simulating the observed oceanic conditions (SST anomaly, SSHA and surface current) associated with the peak phase of the IOD (October-November) event of 2006 (Figure 6.11a and 6.11b). A positive IOD event is characterized by cooler (warmer) than nor-

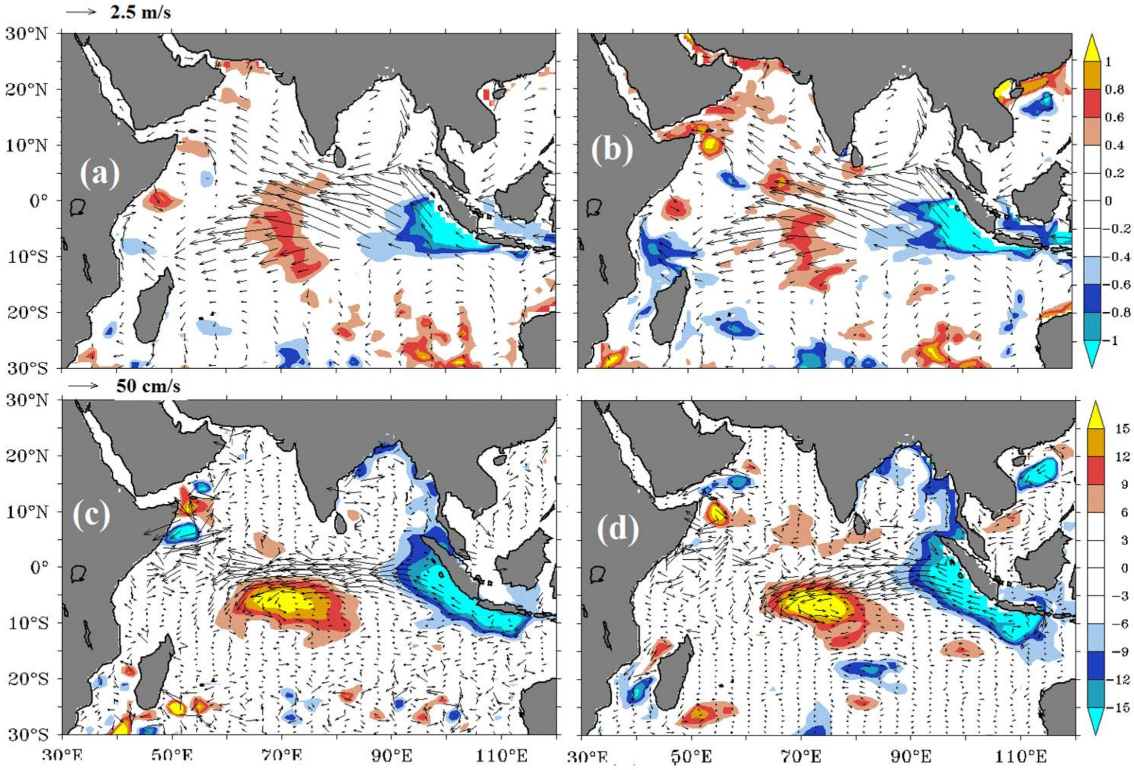

Figure 6.11: (Top panel) SSTA ($°C$, shaded) obtained from (a) TMIAMSRE and (b) TSR overlaid with wind vector anomaly (m/s) obtained from (b) QuikSCAT. (Bottom panel) SSHA (cm, shaded) obtained from (c) AVISO and (d) *TSR* overlaid with current vector anomaly (cm/s) obtained from (c) OSCAR and (d) TSR. All field are averaged during October-November, 2006

mal SST and enhanced (suppressed) convection in the tropical eastern (western) Indian Ocean and an easterly wind anomaly in the EIO (Saji et al., 1999; Vinayachandran et al., 2007). As seen in Figure 6.11a, *TSR* reproduces the well known dipole structure (SST anomaly) during the peak phase of IOD. The magnitude of cool (warm) SST anomaly in the east (west) of EIO and its spatial coverage shows a good agreement with observation. However, *TSR* shows pocket of warm (cold) bias in the Arabian Sea (west of Madagascar) contrary to observation.

The anomalous easterly winds over the central and eastern EIO (Figure 6.11a and 6.11b) associated with a positive IOD event can also modulate the SSHA and current variability in the EIO. As shown by earlier studies (Vinayachandran et al., 2007; Cai et al., 2009), anomalous easterly winds, associated with a positive IOD event in 2006, triggered anomalous upwelling Kelvin waves propagating eastward along the eastern EIO and poleward along the eastern boundary of the BoB. Likewise, there were downwelling off-equatorial Rossby waves in the western EIO (around 70°E). The signature of these Kelvin (Rossby) waves, which is clearly seen as negative (positive) SSHA anomalies, is reproduced by the TSR with good spatial correspondence. However, the northern expression of the off-equatorial maxima is relatively stronger in the model as compared to altimeter observations.

During the fall, the zonal current (the Wyrtki jet) in the EIO normally flows eastward (Wyrtki, 1973). It has been reported that the Wyrtki jet weakens or reverses direction during positive dipole years due to local forcing of the anomalous easterly wind in the EIO (e.g., Vinayachandran et al. (2007); Gnanaseelan et al. (2012)). The reversal of Wyrtki jet associated with the IOD event of 2006 is successfully reproduced by the model with good temporal correspondence.

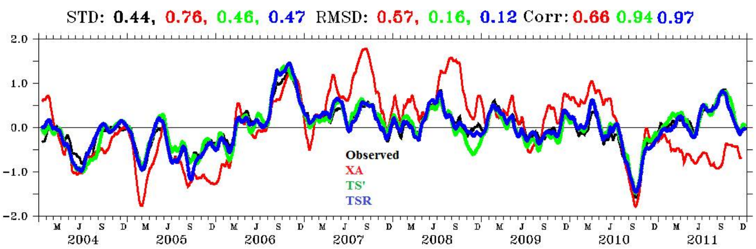

Figure 6.12: Time series of Dipole mode index (DMI), which is defined as the difference between SST anomalies (obtained by removing monthly climatology) of south eastern IO box (90°E-100°E & 10°S-$Equator$) and western box (50°E-70°E & 10°S-10°N), derived from TMIAMSRE (observed, black), XA (red), TS'(green), and TSR (blue) experiments. Units are in °C. Statistics such as STD, RMSD, and correlation are also shown at the top

Earlier studies have shown that occurrence of IOD can be defined by a simple index called Dipole Mode Index (DMI) which is defined as the difference in SST anomaly between tropical western IO (50°E-70°E, 10°S-10°N) and the south-eastern IO (90°E-100°E, 10°S-Eq) (Saji et al., 1999). Due to the reasons summarized in the introduction section with regard to the results found by Janakiraman et al. (2011) on the positive biases of IOD in CFS, in this section we examine the

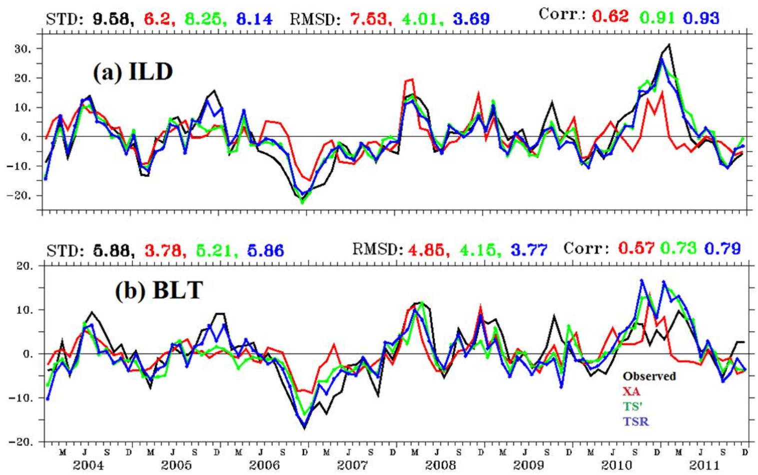

Figure 6.13: South-eastern IO box ($90°E$-$100°E$ & $10°S$-$Equator$) averaged anomalies (obtained by removing monthly climatology) of (a) Isothermal Layer Depth (ILD), and (b) Barrier Layer Thickness (BLT), derived from TMIAMSRE (observed, black), *XA* (red), *TS'*(green), and *TSR* (blue) experiments. Units are in meters. Statistics such as STD, RMSD, and correlation are shown at the top of each panel

skill of (i) *XA*, (ii) *TS'* and (iii) *TSR* (refer Table 6.1) in capturing DMI. Figure 6.12 shows the time series of DMI obtained from TMI-AMSRE, *XA*, *TS'*, and *TSR*. It can be inferred from the figure that though XA does show the sign of the DMI realistically, it has overestimations in the magnitude. However, assimilation experiments does simulate DMI accurately both in sign as well as magnitude. The correlation between the observed and assimilation experiment's DMI exceeds 0.9. Further analysis on IOD characteristics is done using Figure 6.13. Figure 6.13 shows the time series, averaged over the south-eastern IO box, of ILD (a) and BLT (b) anomalies derived from EN3V2a gridded temperature and salinities (black), *XA* (red), *TS'* (green), and *TSR* (blue). Typical character of positive (negative) IOD event during 2006 (2010) can be seen from the figure where ILD shoals (deepens) by about 20m during 2006 (2010) and also help reducing (increasing) the barrier layer thickness which is crucial to promote (demote) entrainment. Figure further indicates better skill of *TSR* in capturing these features of IOD by showing correlations in BLT (ILD) of 0.79 (0.93) over *TS'* and *XA* where correlations found to be 0.73 (0.91) and 0.57 (0.62) respectively. Though there seems to be some issues in the BLT magnitude during the 2010 negative IOD event in all the experiments, the sign is captured realistically well in all the experiments. It is also evident from the figure that BLT in *XA* during 2006 positive IOD event is not reduced as much as in the observation. However, the BLT reductions in assimilation experiments during 2006 are close to observation. In a nutshell, the results indicate that ocean analysis generated from assimilation experiments of INCOIS-GODAS is suitable for studying inter-annual variability in the Indian ocean, both dynamic and thermo-dynamic.

6.4 Inter-comparison of improved INCOIS-GODAS Global Ocean Analysis with NCEP-GODAS, ECMWF-ORAS4

In this section the quality of improved global ocean analysis obtained with the *TSR* configuration of INCOIS-GODAS is compared with other ocean re-analysis from the state-of-the-art operational ocean data assimilation models of NCEP-GODAS, and ECMWF-ORAS4 (European Centre for Medium range Weather Forecast- Ocean Reanalysis-4). This is done to demonstrate and understand the level of accuracy offered by improved ocean analysis from INCOIS-GODAS. The selection of NCEP-GODAS and ECMWF-ORAS4 is due to the following facts

- There are numerous similarities between INCOIS-GODAS and NCEP-GODAS especially in the implementation of assimilation technique except some differences outlined in Table 6.2.

- The quality of ocean analysis from ECMWF-ORAS4 is reported to be significantly improved compared to the older versions of the ocean re-analysis from the same operational center (Balmaseda et al., 2013). Major factors contributed to the improvements is due to better ocean model, reduction of assimilation shocks by implementing parallel adjustments to all prognostic variables while performing assimilation.

Hence if the quality of ocean analysis from INCOIS-GODAS is on par with the quality of the other two systems, we can regard the INCOIS-GODAS is fit for the use of research. This exercise is also useful in adjudging the INCOIS-GODAS suitable for conducting Observation System Experiments, an important application of data assimilation systems to understand the value of ocean observing systems. For this inter-comparison exercise, we have considered monthly averaged analysis of NCEP-GODAS and ECMWF-ORAS4 for the period 2004-2009. This is because, as of now the ocean re-analysis from ECMWF-ORAS4 as monthly averaged fields are updated up to the end of 2009 only (from 2010 the analysis is based on real time assimilation systems which may be less accurate compared to re-analysis).

Before performing inter-comparison, it is worth examining some major differences amongst each of the ocean data assimilation models considered in this study. These major differences are summarized in Table 6.2. Apart from the background models, there are differences in these models as far as the parameters that are being assimilated. ECMWF-ORAS4 assimilates many parameters (SSH, SST, temperature and salinity profiles) from various sources such as SSHA measurements from satellite altimeters, satellite and in-situ based measurements of SST, depth wise profiles of *in-situ* temperature and salinity measurements taken from Argo, tropical moorings, XBTs etc. NCEP-GODAS also assimilates as many parameters as ECMWF-ORAS4 does except that the salinity profiles used for assimilation are of synthetic/artificial estimated from the local temperature profile. This is done mainly to conserve water-mass properties. In the case of INCOIS-GODAS there is no assimilation of SSHA, the INCOIS-GODAS does assimilate depth-wise profile of in-situ temperature and salinity measurements from various sources (such as

Table 6.2: Summary of the configuration of ocean data assimilation systems used for the inter-comparison study

	ECMWF-ORAS4	**NCEP-GODAS**	**INCOIS-GODAS**
Ocean Model	NEMO V3.0	MOM V3	MOM-V4.0
Assimilation Scheme	NEMOVAR in its 3D-VAR FGAT mode	3D-VAR	3D-VAR
SST relaxation	Model SST is strongly relaxed to Reynolds SST	Model SST is strongly relaxed to Reynolds SST	Model SST is strongly relaxed to Reynolds SST
Forcing Fields	Atmospheric fluxes from ERA-40 reanalysis	NCEP-R2 atmospheric fluxes	NCEP-R2 atmospheric fluxes
Assimilation of Temperature Profiles	Yes. Observations from XBT corrected EN3 profiles are utilized	Yes. Observations are collected from USGODAE Monterey Data Server and the NODCs World Ocean Database (WOD)	Yes. Observations are collected from USGODAE Monterey Data Server and the NODCs World Ocean Database (WOD)
Assimilation of Salinity Profiles	Yes. Observations from XBT corrected EN3 profiles are utilized	Artificial salinities derived from local temperature profiles are used for assimilation	Observations are collected from USGODAE Monterey Data Server and the NODCs World Ocean Database (WOD)
Altimeter SSHA assimilation	Yes	Yes	No
Reference(s)	Balmaseda et al. (2013)	Behringer (2007)	present study
Information on Ocean Analysis	`http://www.ecmwf.int/products/forecasts/d/charts/oras4/reanalysis`	`http://www.cpc.ncep.noaa.gov/products/GODAS`	`www.incois.gov.in/portal/GODAS`

GTS, WOD05, USGODAE). Also, it uses satellite based SST to correct model SST similar to that implemented in other two models.

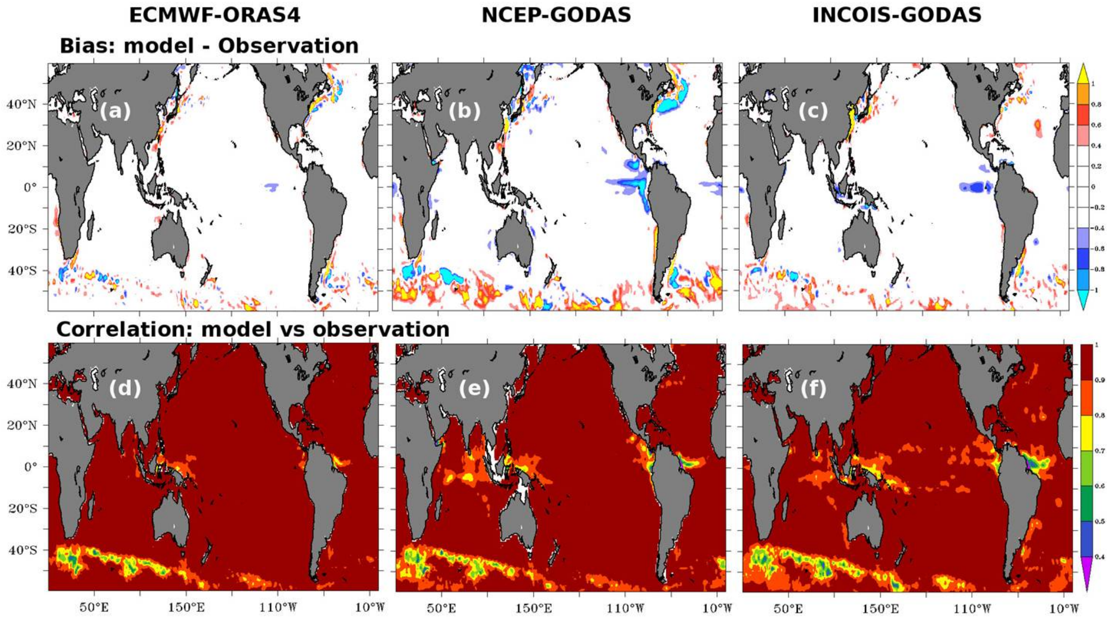

Figure 6.14: Bias (model-Observation; top panels; a, b, and c) and correlation (bottom panels; d, e, and f) between model and observation for SST analysis ($°C$) from ECMWF-ORAS4 (a & d), NCEP-GODAS (b & e), and INCOIS-GODAS (c & f). Monthly averaged SST of OISST data set is used as observation

In order to verify the overall skill of ECMWF-ORAS4, NCEP-GODAS, and INCOIS-GODAS in simulating SST and SSS features, we have used Reynolds SST and SSS from the gridded product of EN3V2a. Mean biases and correlations in the simulated SST (SSS) from each of these models with respect to OISST (EN3V2a) are shown in Figure 6.14 (Figure 6.15). It can be inferred from the Figure 6.14 that there is a large spatial resemblance amongst the SSTs simulated by models as far as the regional patterns of bias and correlations of SST are concerned. For example, all the models have comparatively large bias and low correlations in the Southern Ocean. The SST biases are also large in the regions of western boundary currents in the Pacific and the Atlantic Oceans. It is interesting to note that SSS from INCOIS-GODAS has excellent agreement with the observation unlike the NCEP-GODAS. Compared to INCOIS-GODAS and ECMWF-ORAS4, SSS from

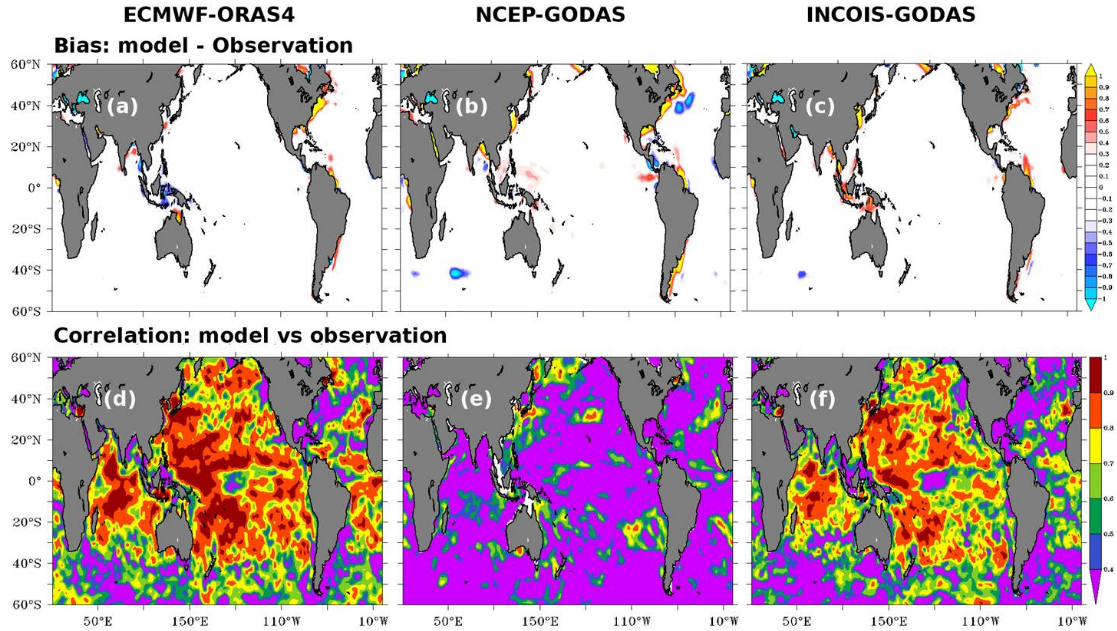

Figure 6.15: Same as Figure 6.14 except that for SSS analysis (psu)

NCEP-GODAS has large biases and low correlations with respect to observation based EN3V2a. Compared to other, ECMWF-ORAS4 has low biases and large correlations for both SST as well as SSS. Further, the skill of INCOIS-GODAS is close to the skill of ECMWF-ORAS4 than from NCEP-GODAS.

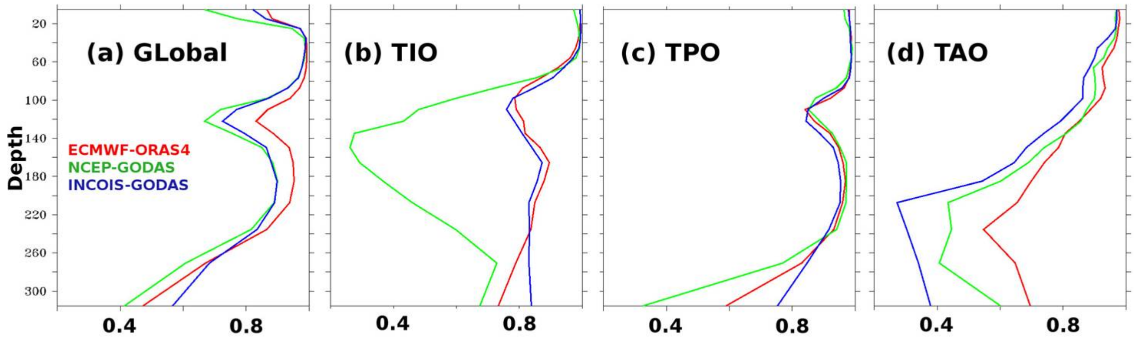

Figure 6.16: Depth-wise correlations between model and observations for region averaged temperature. The regions considered are (a) Global (60°S-60°N & all longitudes), (b) Tropical Indian Ocean (TIO; 30°E-120°E & 30°S-30°N), (c) Tropical Pacific Ocean (TPO; 130°E-80°W & 30°S-30°N), and (d) Tropical Atlantic Ocean (TAO; 60°W-10°E & 30°S-30°N). Monthly averaged gridded data from EN3V2a is used as an observation. In the figure correlations between ECMWF-ORAS4 and EN3V2a, NCEP-GODAS and EN3V2a, and INCOIS-GODAS and EN3V2a are represented in red, green, and blue colored lines respectively

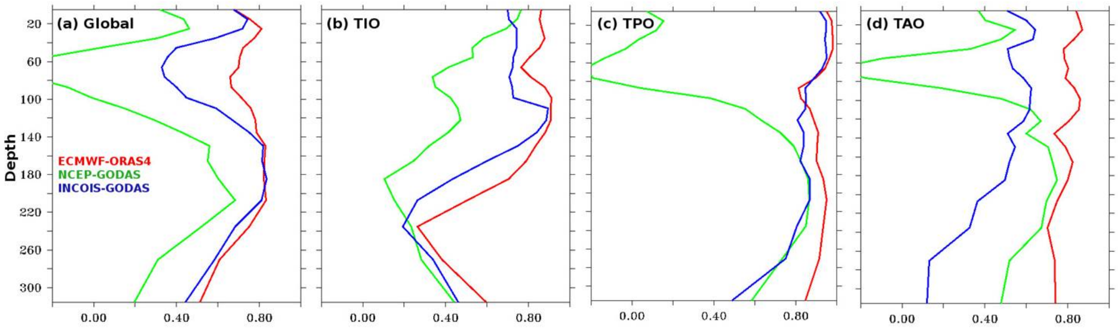

Figure 6.17: Same as figure 6.16 but for salinity (psu)

Comparison of depth-wise correlations of regional averaged temperature and salinity estimated for each model with respect to EN3V2a for different regions is shown in Figures 6.16 and 6.17. It can be inferred from these figures that even at sub-surface levels the skill of INCOIS-GODAS is good and close to ECMWF-ORAS4 than to NCEP-GODAS except for the Tropical Atlantic Ocean. The skill appears to be less in this Tropical Atlantic Ocean especially in the sub-surface layers for all models. It is worth noting here that there are significant correlation differences for temperature (salinity) between NCEP-GODAS and INCOIS-GODAS especially in the Tropical Indian Ocean (Tropical Pacific Ocean). One of the potential reasons for the better quality of INCOIS-GODAS temperature and salinity could be the assimilation of observed salinity in INCOIS-GODAS compared to the synthetic salinity assimilation in NCEP-GODAS.

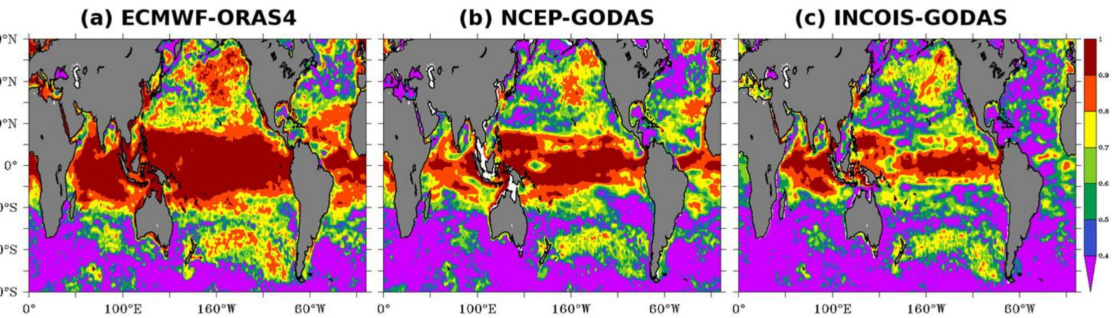

Figure 6.18: SSHA Correlation between (a) ECMWF-ORAS4 and observation, (b) NCEP-GODAS and observation, and (c) INCOIS-GODAS and observation. Monthly averages of merged altimeter SSHA data is used as observation

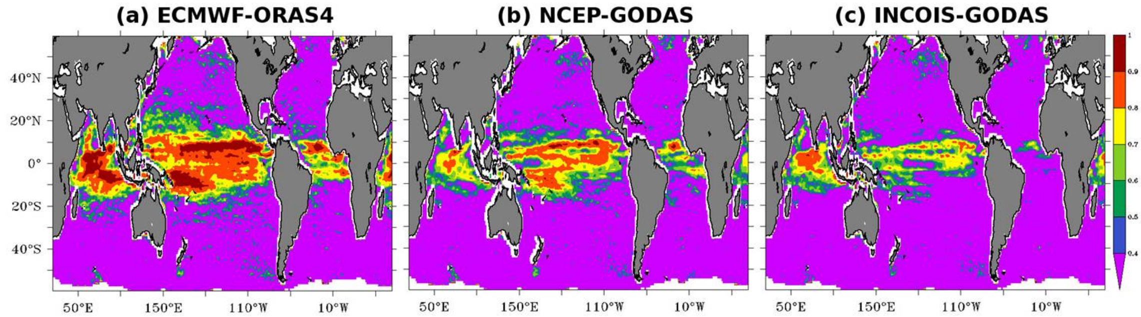

Figure 6.19: Correlation in Zonal Surface currents (cm/s) between (a) ECMWF-ORAS4 and observation, (b) NCEP-GODAS and observation, and (c) INCOIS-GODAS and observation. Monthly averages of OSCAR surface current data is used as observation. Upper 30m averaged zonal current from model is represented as surface current

Turning our attention to examine the skill of each model in representing the variations in SSH, a parameter which is regarded as the integrated response of the total water column, we can understand that the spatial patterns of the model skill are almost similar to one another except in the Tropical Atlantic Ocean. For example, there is a great deal of differences in the correlation patterns amongst the models in the Tropical Atlantic Ocean as can be noticed from Figure 6.18. In general, widespread SSHA correlations are observed for ECMWF-ORAS4. The spatial extent of large correlations and also the magnitude of correlations for INCOIS-GODAS appear to be little less compared to the other two models. The fact that the other two models, i.e. ECMWF-ORAS4 and NCEP-GODAS, assimilates altimeter SSHA and the absence of the SSHA assimilation in INCOIS-GODAS naturally explains comparatively less correlations in INCOIS-GODAS than the other two models. Examining the quality of ocean currents from these models with respect to Ocean Surface Current Analysis-Realtime (OSCAR) data indicates that the SSHA assimilation improves the currents as well in the tropical regions. For instance, it can be observed from the Figures 6.18 and 6.19 that the spatial patterns of correlations for zonal surface currents (Figure 6.19) of a model are more or less similar to their corresponding spatial patterns of correlations for SSH (Figure 6.18). This result is understandable as the assimilation of SSH in general improves model geostrophy, hence the currents. It is important to notice, however, that despite the absence of the SSHA assimilation, INCOIS-GODAS does reasonably well to capture currents at surface as well as in sub-surface layers, which are evident from the correlation patterns of surface currents (Figure 6.19) and depth-time series plots of equatorial zonal currents (Figures 6.20 and 6.21). Also, the magnitude of correlations of SSHA and surface currents for INCOIS-GODAS over most of the regions is still comparable to other two models.

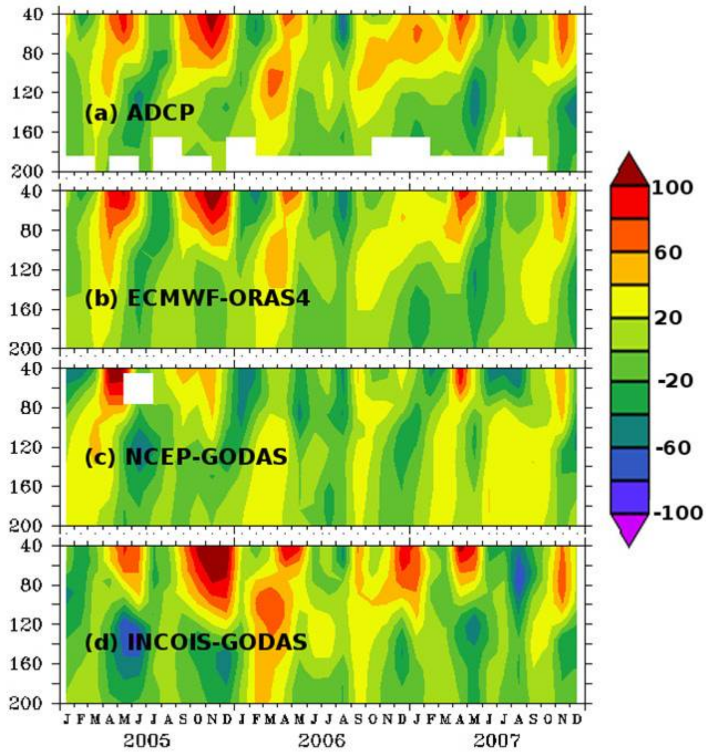

Figure 6.20: Depth-time sections of zonal currents (cm/s) at (80.5°E, Eq) location derived from (a) Observation (Accoustic Doppler Current Profiler, ADCP), (b) ECMWF-ORAS4, (c) NCEP-GODAS, and (d) INCOIS-GODAS

The results from the inter-comparison discussed in this section arguably suggest that the quality of ocean analysis from INCOIS-GODAS is on par with the other two state-of-the-art ocean data assimilation systems. This in turn suggests that the INCOIS-GODAS can be utilized to conduct OSEs to know the impact of *in-situ* ocean observing systems on ocean analysis in the current scenario.

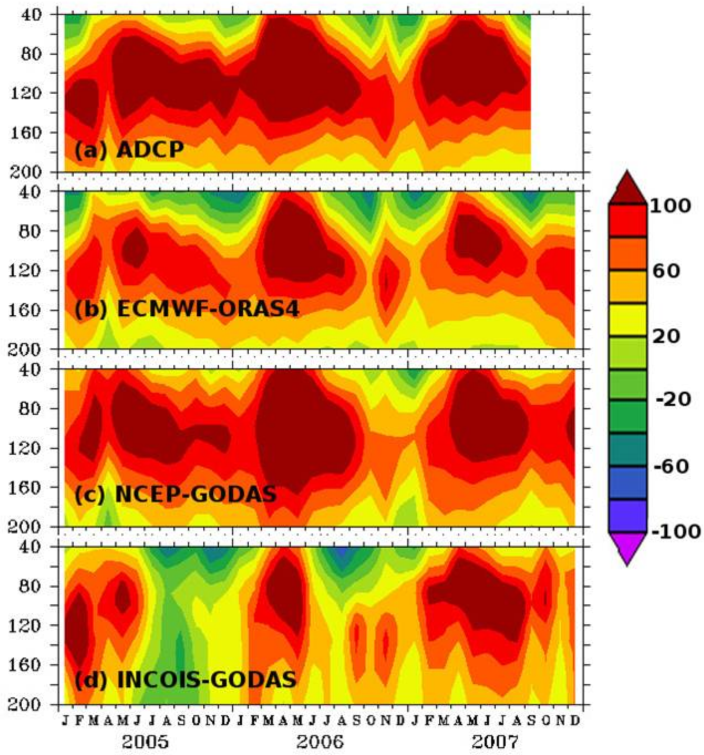

Figure 6.21: Same as Figure 6.20 but at ($140°W$, Eq) location

6.5 Summary and conclusions

In order to provide improved global ocean analysis from INCOIS-GODAS, the configuration of *TS'* is upgraded to *TSR* by incorporating many additions discussed in the previous chapters. The improvements in the quality of ocean analysis obtained with the new configuration (*TSR*) over the old configuration (*TS'*) are examined by elucidating the effective contributions from different choices. It is found that strong relaxation to satellite based SST helps to bring model SST close to observed SSTs. These improvements, in terms of RMSDs, are as large as $0.6°C$ in the regions such as the northern BoB and the thermocline ridge region. The assimilation of observed salinity profiles instead of synthetic salinity profiles improve model salinity in a significant way particularly in the eastern parts of the IO and the BoB. The improvements in salinity of up to 0.3 psu in turn improve SSHA and currents by up-to $3cm$ and $10cm/s$ respectively. Comparing the results of currents from the present Chapter with the results of currents from Chapter 3, 4 indicates that not only wind improves the surface and sub-surface currents, but also the salinity assimilation. It is observed that use of monthly river-runoff does not bring significant changes in the quality of the ocean analysis except in the northern most BoB where improvements in the salinity field found to be between $0 - 0.5psu$. Further analysis is carried out on IOD and intra-seasonal variability in the zonal current to understand the skill of TSR in capturing intra-seasonal and inter-annual features. The results indicate that these features are reproduced with *TSR* at excellent skill. In order to examine whether the accuracy of global ocean analysis from the *TSR* meets the level of research quality ocean re-analysis offered from other state-of-the-art ocean assimilation models, an inter-comparison study is carried out. The results indicate that despite the absence of altimeter assimilation in INCOIS-GODAS, the quality of global ocean analysis from TSR of INCOIS-GODAS is on par with NCEP-GODAS and ECMWF-ORAS4. In fact the quality of global ocean analysis obtained from *TSR* configuration of INCOIS-GODAS is better than NCEP-GODAS and close to ECMWF-ORAS4.

Chapter 7

Impact of in-situ Global Ocean Observing systems

7.1 Introduction

Continual evaluations on the design and credibility of each component of the Global Ocean Observing System (GOOS) are crucial for the efficient management and utilization of funds. Such evaluations can be done using ocean data assimilation systems by conducting Observation System Experiments (OSEs), in which the impact of an observing system is assessed by carrying out a reference experiment, where observations from all available sources are used for assimilation, and then use ocean analysis from this reference experiment to compare the performance of a similar experiment where observations from the corresponding network are excluded for assimilation (e.g. Oke and Schiller (2007)). Earlier studies have indicated that though there exists redundancy in the observations in some regions, each component of the GOOS brings unique contributions to the overall skill of model forecasts and analysis (Balmaseda et al., 2007; Vidard et al., 2007; Oke and Schiller, 2007; Huang et al., 2008; Balmaseda et al., 2009) particularly for the meso-scale circulations (Oke and Schiller, 2007). Most of these studies were carried out using sparse/inhomogeneous observations (before 2006). For example, Balmaseda et al. (2009) assessed the relative importance of Argo, altimeter and moorings for the period 2001-2006 during which Argo was highly inhomogeneous over the Indian Ocean. Their study indicated that the evaluation of observation systems should be done after reaching well-matured stage so that the chances for misinterpreting results from OSEs due to faulty observations are less.

The last decade has witnessed significant improvements in the spatial and temporal coverage of ocean observations, particularly from profiling floats (majorly from Argo project) and tropical moorings except a decline of moorings in tropical Pacific Ocean during recent years. Significant efforts were also put to remove biases in the ocean observing systems (e.g. Ingleby and Huddleston (2007); Wijffels et al. (2008). Motivated by these factors Fujii Y (2015) and Xue (2015) have conducted multi-model based OSEs to evaluate the values of TAO moorings relative to other observing platforms. However, their studies are limited to tropical Pacific Ocean. In the present study, we examine the impact of moored buoy, profiling floats, and ship-based components of GOOS in the Indian and the Pacific Ocean using INCOIS-GODAS for the recent observation rich period 2004-2011. We don't analyze results from OSEs for Atlantic due to low skill scores of state-of-the-art ocean models in this region (please refer to last chapter on inter-comparison of ocean analysis). The Southern and Northern Oceans are also excluded from the analysis because the assimilation is being performed only between "$60°S$ - $63°N$". Apart from demonstrating the capabilities of INCOIS-GODAS, the present OSE study can also benefit the policy makers involved in the design and maintenance of the GOOS. This chapter is organized in four sections. As indicated earlier, we have designed some special experiments for conducting OSEs. Configuration of these model experiments and methodology followed are available in section 7.2. Results and discussions followed by summary are provided in sections 7.3 and 7.4 respectively.

7.2 Configuration of model experiments and Methodology

The results discussed in the last chapter support that the INCOIS-GODAS is suitable for conducting OSEs in the Indian Ocean and the Pacific Ocean. Hence, in this chapter for the present study, we use the same configuration of INCOIS-GODAS as that of *TSR* discussed in the last chapter, except for SST relaxation. Turning off SST relaxation for the present exercise offers an advantage to have an independent source of SST for comparisons while assessing the impact. It is worth mentioning here that the results presented in this chapter on OSEs do not seem to be dependent on the choice of SST relaxation (figures not shown).

In the present OSE study, the "XBT corrected" temperature and salinity profiles from the UK Met Office Ensemble (EN) quality controlled version-2a (EN2a; Ingleby and Huddleston (2007); Wijffels et al. (2008)) were used for assimilation. This data set was chosen due to its rich collection of *in-situ* temperature and salinity profiles (acquired from various projects, i.e. WOD05, GTSPP, Argo, and ASBO), subjected to rigorous quality checks (Ingleby and Huddleston, 2007). We have considered delayed mode and high quality profiles - inferred from position QC and profile QC, but discarded profiles with large vertical data gap. Further, profiles within $0.5°(\approx 50km)$ radius of three RAMA buoys at ($1.5°S$, $80.5°E$), ($1.5°S$, $90°E$), and ($12°N$, $90°E$) locations, shown as black dots in Figure 7.1, were not used so that they could be used as independent observations for validation of OSE runs. These three locations were selected since there were some redundancy in profiles from the existing moored buoy network - all of the three selected locations are surrounded by other moored buoy observations within $3°$ ($\approx 330km$) radius- and (2) considering the local importance of the region. Spatial distributions of locations of resultant temperature profiles available for assimilation during 2004-2011 from moored buoy, profiling floats, and ship-based components of GOOS

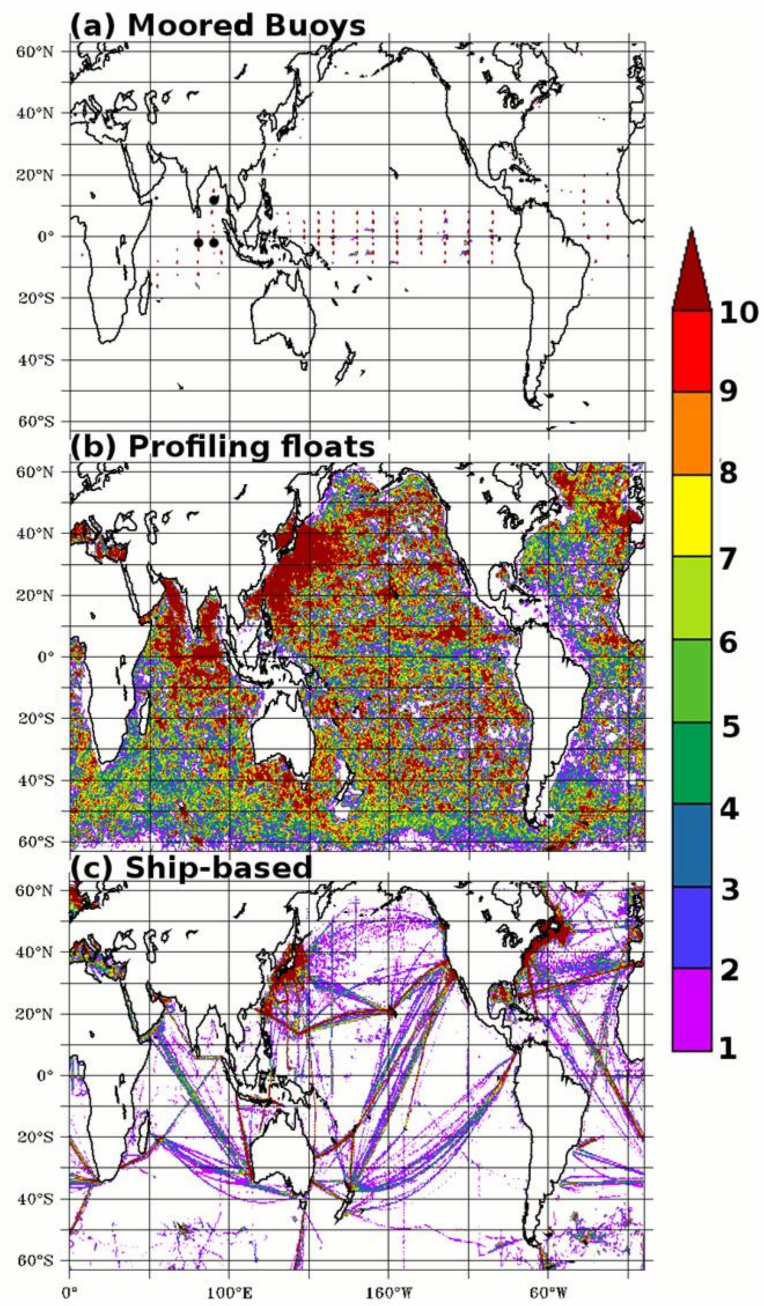

Figure 7.1: Distribution of temperature profiles available for assimilation from (a) Moored buoy, (b) Profiling floats, and (c) Ship-based platforms. The color bar indicates the number of profiles available in $0.5° \times 0.5°$ grid box for the whole 2004-2011 period. Black dots on (a) indicates observation locations withheld for assimilation

Table 7.1: Configuration of experiments used in the present study

Experiment	Profiles for Assimilation
REF	*in-situ* observed temperature and observed salinity profiles from all components of GOOS
XBU	*in-situ* observed temperature and observed salinity profiles from all components of GOOS except moored buoy (TAO/PIRATA/TRITON/RAMA) network
XPR	*in-situ* observed temperature and observed salinity profiles from all components of GOOS except profiling floats (Argo) network
XSH	*in-situ* observed temperature and observed salinity profiles from all components of GOOS except ship-based network
PRF	*in-situ* observed Temperature and observed salinity profiles from profiling floats (Argo)
BU	*in-situ* observed Temperature and observed salinity profiles from moored buoy (TAO/PIRATA/TRITON/RAMA) network
XA	No assimilation

are shown in Figure 7.1. One of the important steps in conducting OSEs is to rightly distinguish the observation networks of interest. We have used profile IDs and various other things for distinguishing the observation network in EN2a. It is clear from the figure that the criteria we used effectively distinguish observations of each ocean observation network under study.

To meet the objectives of the present study, analysis is carried out using outputs from various experiments for the Indian Ocean and the Pacific Ocean. All of these experiments use NCEP-R2 (National Centre for Environmental Prediction Reanalysis-Version 2) radiation, freshwater, and momentum fluxes for forcing the model and without using any relaxation for Sea Surface Temperature (SST) and Sea Surface Salinity (SSS). Details about the configuration of experiments are summarized in Table 7.1. One can infer the value of a particular network in the presence (absence) of other network by comparing the performance of corresponding with-holded (assimilated) experiment with the performance of *REF* (*XA*). For example, the value of profiling floats in the presence (absence) of other networks can be understood by comparing the performance of *XPR* (*PR*) with *REF* (*XA*). Results discussed in the present study in section 7.3 are mainly based on this kind of comparisons. It is worth mentioning here that the quality of ocean analysis obtained from *REF* (*XA*) is similar to the quality of ocean analysis offered by *TS* experiment.

7.3 Results and Discussion

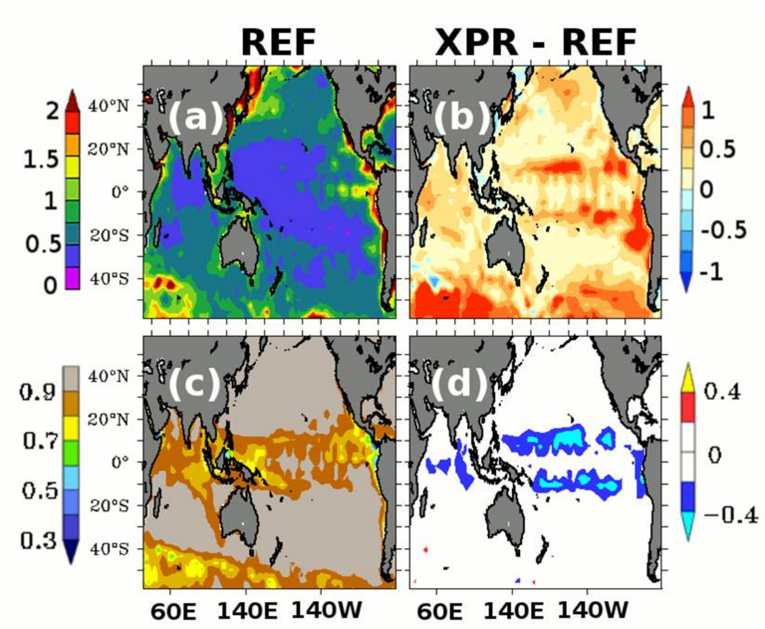

Figure 7.2: (a) Root Mean Square Difference (RMSD), and (c) correlation of SST (°C), computed with respect to observed SST, for *REF*. Difference in RMSD (correlation) between *REF* and *XPR* (*XPR* - *REF*) is shown in b (d)

Investigations based on OSEs (*REF*, *XBU*, *XPR*, and *XSH*) reveal that the mean and variability of SST derived from all of the experiments except *XPR* (in which observations from profiling floats were avoided for assimilation) compare well with the observed SST. The SST variability is overestimated in *XPR*. It can be

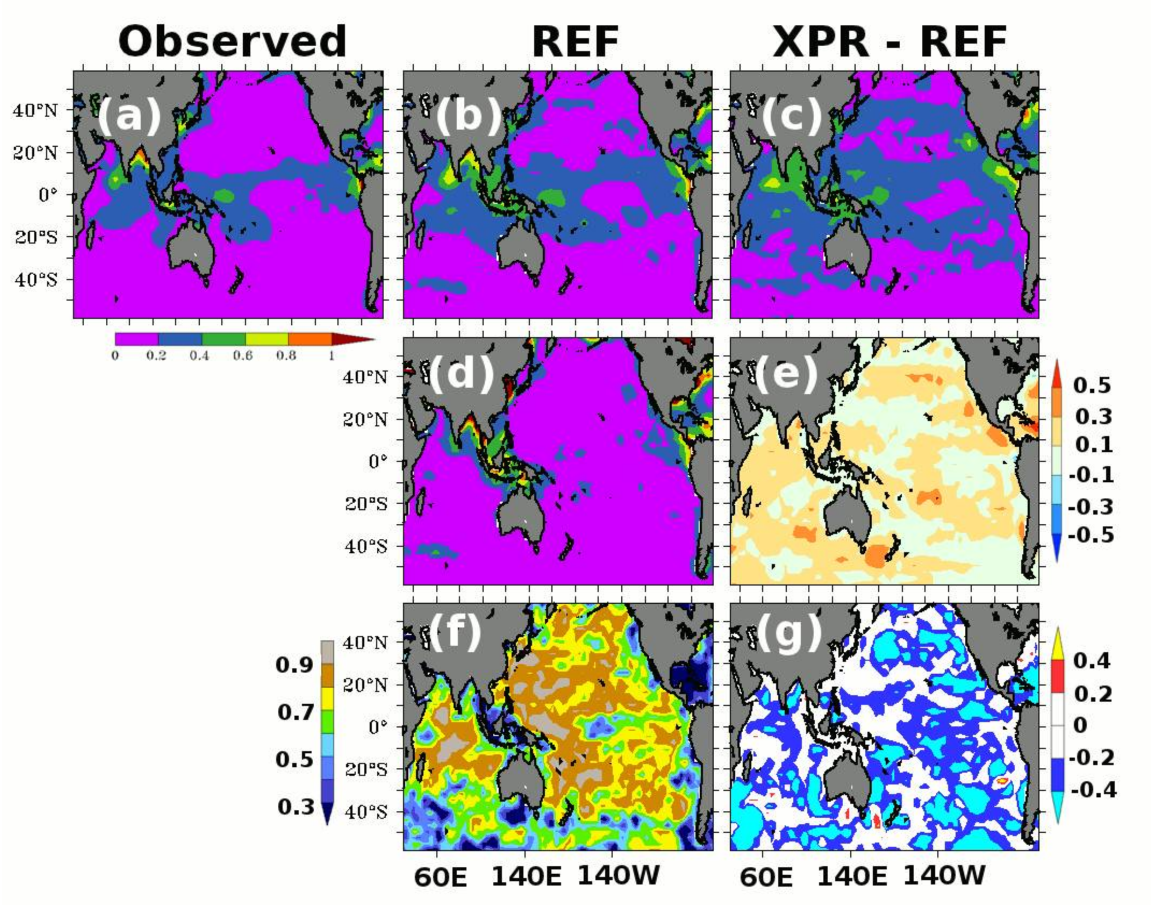

Figure 7.3: Standard deviation (STD) of SSS (psu) derived from (a) EN3V2a, (b) *REF*, and (c) *XPR*. RMSD and correlation, computed using SSS of EN3V2a, for *REF* are shown in d and f respectively. Difference in RMSD (correlation) between *REF* and *XPR* (*XPR*-*REF*) is shown in e (f)

noticed from the Figure 7.2 that quality of SST in *XPR* experiment is significantly degraded from *REF*. The degradations are large (reaching $1°C$ in RMSD) in the southern ocean. This is expected since the observations from profiling floats forms the major source for observation coverage in this region. It is interesting to observe that large degradations are also found in the tropical Pacific Ocean despite the good coverage of moored buoys in this tropical Pacific Ocean. Correlation between the SSTs of OISST and *XPR* over these regions is also poor. We suspect that this is linked to the negative impact of moored buoy, which we are going to discuss later. It can be inferred from the Figure 7.3 that the performance of *XPR* is poor for SSS also, compared to the performance of *REF*. For example, SSS variability is under-estimated (over-estimated) in the northern parts of the Bay of Bengal and over-estimated (sub-tropical latitudes of Pacific Ocean) in *XPR*. Degradations of *XPR* from *REF* in the quality of SSS in these regions are between 0.3-0.5 in terms of RMSD.

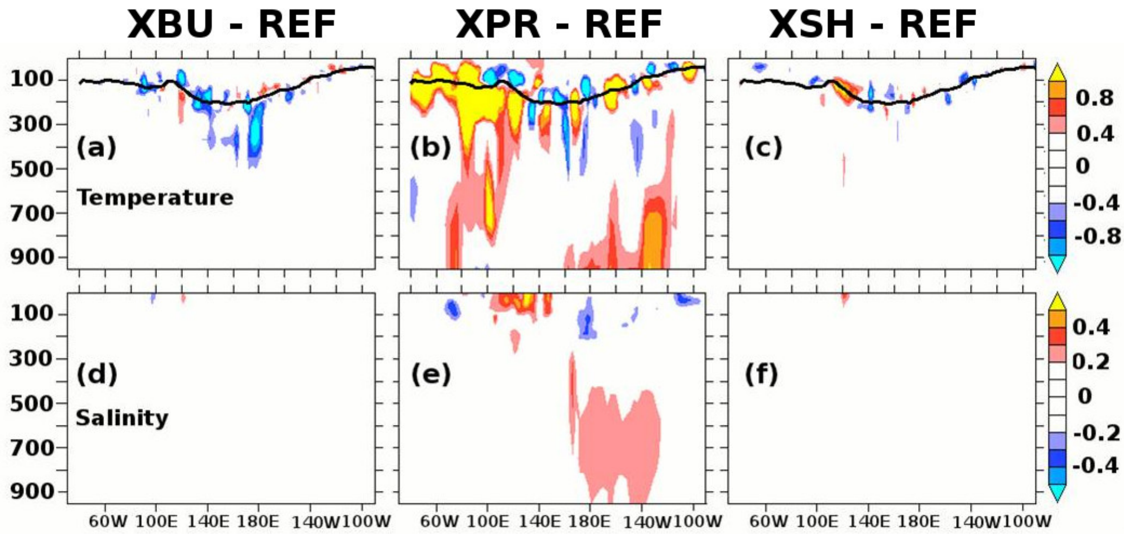

Figure 7.4: Depth-Longitude section of temperature (°C; top panels; a, b, and c) and salinity (psu; bottom panels; d, e, and f) differences between *XBU* and *REF* (a & d), *XPR* and *REF* (b & e), and *XSH* and *REF* (c & f). Temperature and salinity was averaged for month of October in 2008 and for the latitude section of "10°S - 10°N" before plotting the differences

Changes in the simulation of temperature and salinity analysis at sub-surface layers with the exclusion of a particular network are demonstrated in Figure 7.4. The top (bottom) panels of Figure 7.4 show the depth-longitude section of the difference across the "10°S to 10°N" averaged temperature (salinity) for a month of April, 2008. It can be observed from the figure that the temperature and salinity differences occurs in and around the thermocline layer with the exclusion of either moored buoy or ship-based observations. With the exclusion of $T\&S$ observations from profiling floats the temperature and salinity differences are found in all most all layers in the Pacific whereas the differences are limited to 200m in the Indian Ocean. In order to understand whether these differences contributes to positive or negative impact of the particular network of interest, we have compared tempera-

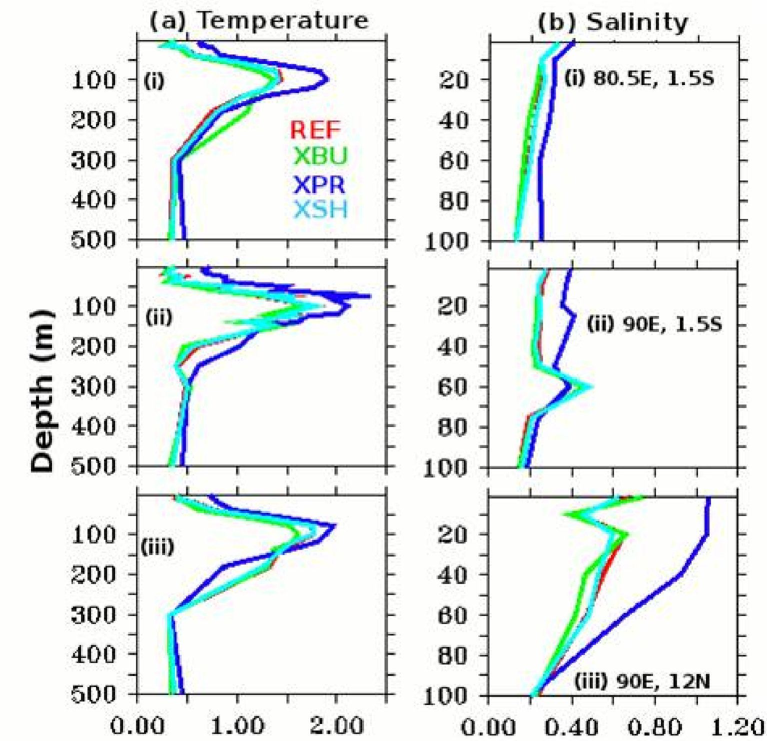

Figure 7.5: Depth wise RMSD of (a) temperature (°C) and (b) salinity (psu) with respect to RAMA at three different independent (with held) locations. (i) (1.5°S, 80.5°E), (ii) (1.5°S, 90°E), and (iii) (12°N, 90°E). In the figure Observation, *REF*, *XBU*, *XPR*, and *XSH* are indicated in red, green, blue, and sky blue respectively

ture and salinity profiles with respect to fore-mentioned independent temperature and salinity measurements from RAMA profiles (Figure 7.5). The comparison suggests that the exclusion of profiling floats degrades the quality of temperature (salinity) by up to 27% (66%) in the upper 100m layer (Figure 7.5). In the case of XBU and XSH, the changes in the quality of temperature and salinity, with respect to REF, are not noticeable through statistical comparisons (Figure 7.5). It is worth to note from Figure 7.5 that RMSD is as large as 2°C in temperature for all experiments, including REF, in the sub-surface layers owing mainly to the well-known rich variability (due to high vertical gradients) within the thermocline layer. Thus it is tough to account contributions from the thermocline layer to the overall credibility of an observation system, if the assessments are based on temperature measurements alone. This can be accomplished to some degree, however, by performing statistical comparisons of Sea Surface Height Anomaly (SSHA) using altimeter observations, as variations of temperature and salinity in the entire column is mostly represented by SSHA. For example, a temperature increase of $1°C$ in the thermocline layer of 100m thick increases sea level by $\approx 4.5cm$.

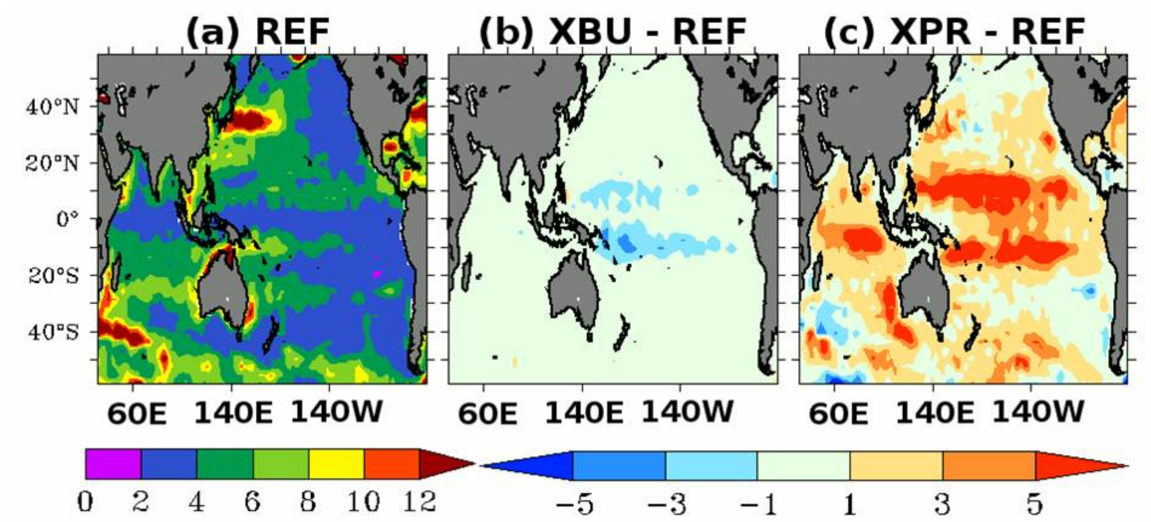

Figure 7.6: (a) RMSD of SSHA (cm), with respect to Altimeter based SSHA, for *REF*. Difference in RMSD (correlation) between *XBU* and *REF* (*XBU-REF*), and *XPR* and *REF* (*XPR-REF*) is shown in b and c respectively

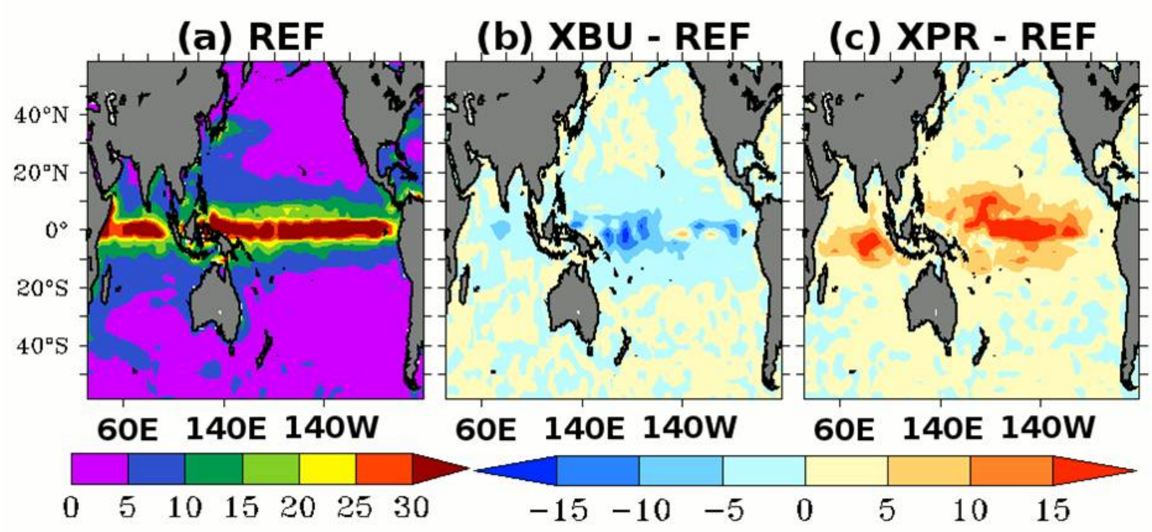

Figure 7.7: Same as Figure 7.6 but for zonal surface current (cm/s)

Examination of the changes, in the quality of non-assimilated parameters (SSHA and currents), of XPR from REF, also emphasizes the importance of as-

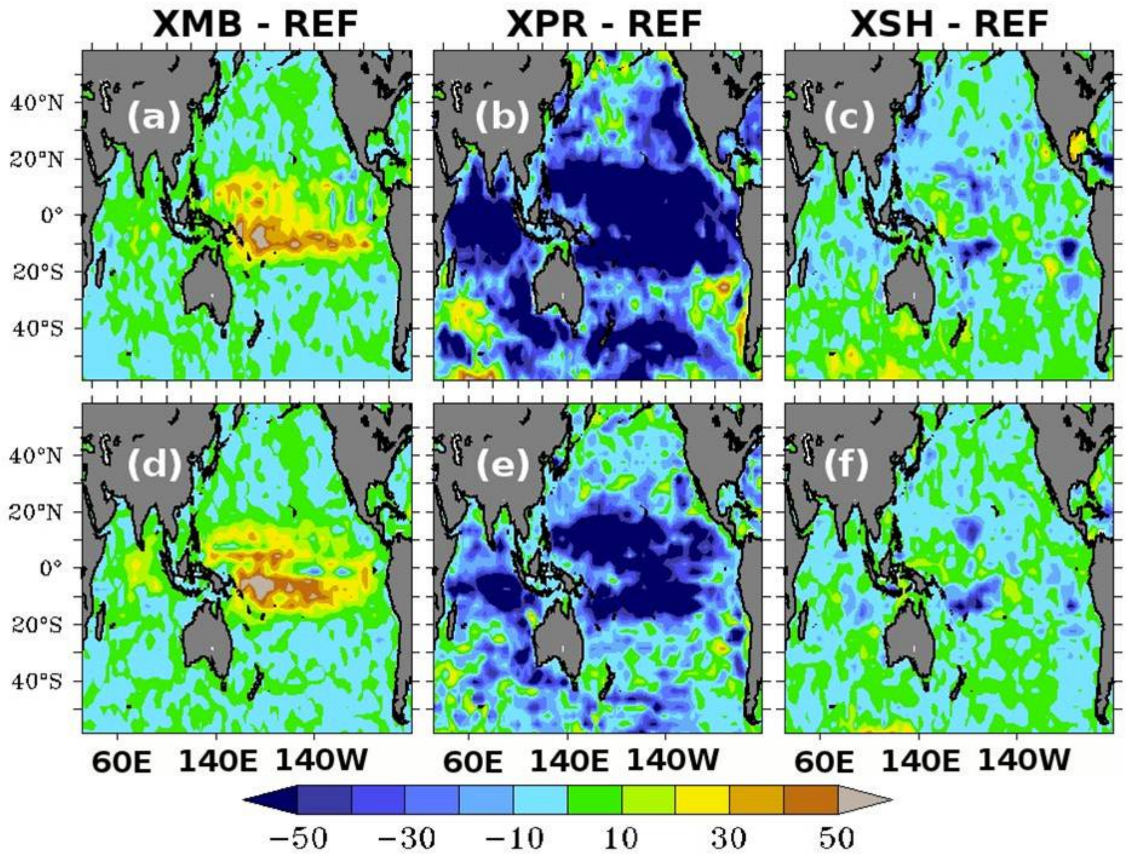

Figure 7.8: Percent degradation of SSHA (top panels; a, b, and c) and Zonal Surface currents (bottom panels; d, e, and f) for *XMB* (a & d), *XPR* (b & e), and *XSH* (c & f)

similation of observations from profiling floats. For instance, quality of SSHA is degraded in XPR from REF, by about 5 cm (percent degradation of more than 100%) in the tropical regions (Figure 7.6). The quality degradation in zonal surface currents near the equator reaches $10cm/s$ (Figure 7.7). Although not as large as profiling floats and not so significant exclusion of T&S profiles from ship-based network also degrades the quality of SSHA and currents especially in the Pacific Ocean. The percent degradations reach 30% for each of these parameters of SSHA and zonal surface currents (Figure 7.8). Relatively less impact of ship-based network in the Indian Ocean compared to the Pacific is understandable as the coverage from ship-based network is much better in the Pacific than in the Indian Ocean (Figure 7.1). Despite having a good spatial coverage in the tropical latitudes, observations from moored buoy could not yield significant impact on the quality of either SSHA or currents, when the other networks are being used. SSHA results corroborate the results from multi-model OSE study carried out by Xue (2015). Interestingly exclusion of observations from moored buoy improves SSHA by 3-5 cm (up to 50% improvements) and currents by 5-10cm/s (up to 50% improvements) in the tropical Pacific (Figures 7.6, 7.7, and 7.8). Similar results are even observed for sub-surface currents. Figure 7.9 shows depth-wise correlations of zonal currents between ADCP and from model experiments at (Eq, 80.5°E) and (Eq, 140°W). It can be clearly noticed from these two figures that while the exclusion of $T\&S$ observations from either profiling floats or ship-based degrades the correlations, improved correlations are noticed with the exclusion of $T\&S$ observations from moored buoys.

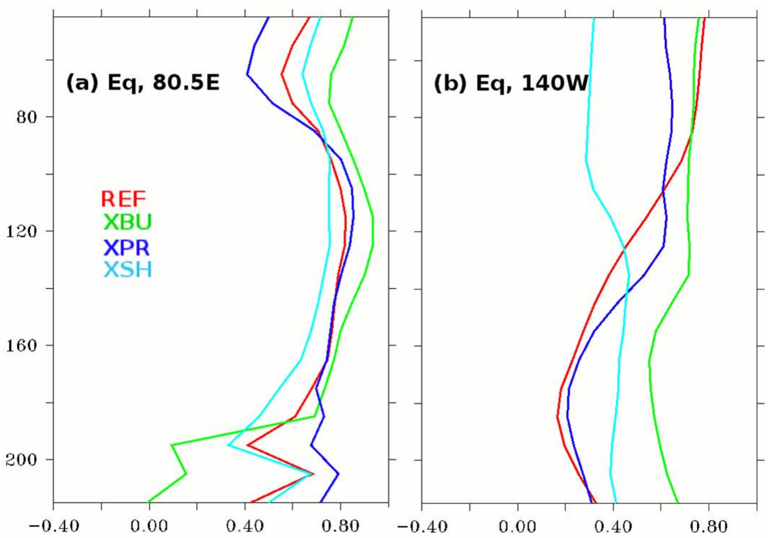

Figure 7.9: Depth-time sections of zonal currents (cm/s) at (140°W, Eq) location derived from (a) Observation (Accoustic Doppler Current Profiler, ADCP), (b) *REF*, (c) *XBU*, (d) *XPR*, and (e) *XSH*

7.3.1 Discussion on the negative impact of Moored Buoy

From the above results, it is surprising to note that exclusion of moored buoy observations for assimilation improves the quality of SSHA and ocean currents in the tropical Pacific. It is worth noting here that such a negative impact of moored buoy (particularly SSHA and currents) is even observed for multi-model OSEs of Xue (2015) as can be inferred from their comparison figures of "noMoor" and "ALL". These results in-turn question the capabilities of state-of-the-art assimilation systems in taking full advantage of the moored buoy observations. In this context, we discuss some potential factors that would have been responsible for the observed negative impact of moored buoys in the following two sections.

7.3.1.1 Vertical resolution of Moored Buoy

One of the major differences between moored buoy and other observational networks that are being studied in the present work is the vertical resolution. In general, both profiling floats and ship-based networks have vertical resolution of 10 m or even higher and available up-to at-least 700 m. Compared to these two networks moored buoys have low vertical resolution. Typical vertical levels at which temperature measurements are taken from moored buoy are "1, 5 10, 20,40, 60, 80, 100, 120, 140, 180, 300, and 500" in the tropical Indian Ocean, and "1, 25, 50, 75, 100, 125, 150, 200, 250, 300, 500, and 700" in the tropical Pacific Ocean. For salinity, measurements are available from surface to 140 m depth. Poor vertical resolution can introduce large interpolation errors in the temperature and salinity profiles for assimilation. This is demonstrated in Figure 7.10 using monthly averages of temperature and salinity analysis from ECMWF-ORAS4 during 2004-2009. In the Figure 7.10, we have shown spatial distribution of accumulated interpolation errors of temperature for the above two typical level selections of moored buoy measurements. It can be observed from the figure that the estimated accumulated errors of interpolation are small (RMS error is within $0.2°C$; Figure 7.10a) in the tropical Indian Ocean and large in the western parts of the tropical Pacific Ocean (RMS error reaches $0.5°C$; Figure 7.10b). In general interpolation errors are small for salinity.

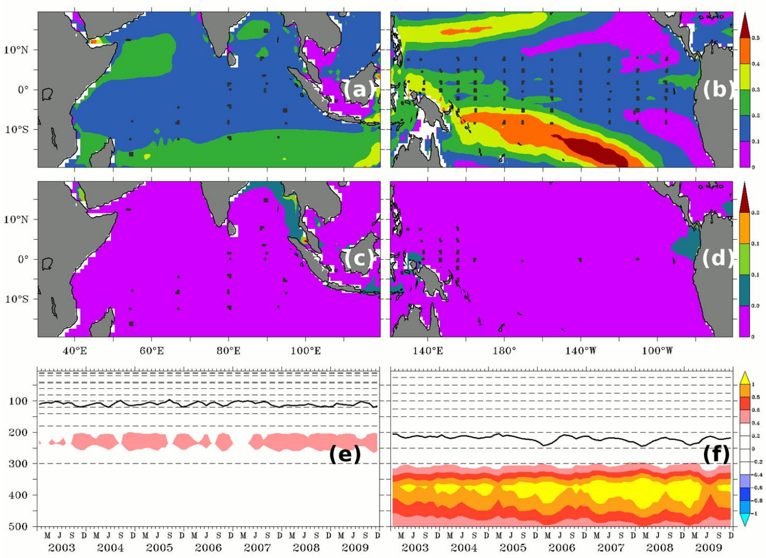

Figure 7.10: Spatial distribution RMS of estimated linear interpolation errors for temperature (a & b) and salinity (c & d) due to selected vertical resolutions in the Indian (a & c) and Pacific Oceans (b & d). Locations at which the temperature and salinity measurements are available from moored buoys are represented in the respective panels as filled circles. The panels $e\&f$ shows the typical levels of moored buoy (dashed lines) in the Indian (e) and Pacific Ocean (f) along with depth-time distribution of linear interpolation errors for temperature ($^{\circ}C$) corresponding to the region covered by (e) $75^{\circ}E$-$85^{\circ}E$ & $10^{\circ}S$-$20^{\circ}S$, and (f) $175^{\circ}E$-$175^{\circ}W$ & $5^{\circ}S$-$15^{\circ}S$. Panels e and f also shows corresponding depth of $20^{\circ}C$ isotherm (thick solid line). These interpolation errors are estimated by using ECMWF-ORAS4 temperature analysis which is available on $\approx 10m$ resolution in the vertical direction. The model data is used to first sample the ocean for temperature at discrete levels determined by typical vertical resolution of moored buoy around the corresponding location (typical levels of moored buoy are shown in the figure as dashed lines). Then this sampled data is used to re-sample the temperature at vertical levels of model. The difference between the re-sampled data and the original model data (synthetic data - model data) gives the error due to linear interpolation

Comparison of the Figure 7.10 with Figure 7.6b indicates that there is some contribution from interpolation errors to the observed negative impact of moored buoy. For instance, region of south-western parts of the equatorial Pacific (130°E -160°W & 10°S - 0°N), where we noticed large negative impact of moored buoy (Figure 7.6b) on SST and SSHA, is also the region with large interpolation errors (Figure 7.10b). Also, the region of tropical Indian Ocean where we did not notice negative impact of moored buoy (Figure 7.6b) is the region with very small interpolation errors (Figure 7.10a). Based on these realizations, it can be speculated that the absence of positive impact of moored buoys on SSHA in the Pacific Ocean and the Indian Oceans would have been the result of counteraction of the interpolation errors due to poor vertical resolution of buoys. This speculation is further supported by the following result. The equatorial section of the Pacific Ocean, which is well surrounded by moored buoys, has shown positive impact for SST but no impact (neither positive nor negative) for SSHA, suggesting that there is some issue at deeper layers. In fact interpolation errors are in general large in the sub-surface layers due to the degraded vertical resolution as shown in the Figure 7.10e. More convincing results with regard to vertical resolution may be obtained with dedicated experiments using assimilation systems, which clearly deserve to be reported as a separate study.

7.3.1.2 Spatial coverage of moored buoys

It appears from the Figure 7.6 and Figure 7.10 that interpolation error alone is not the player responsible for negative impact of moored buoy. This is because in the Pacific Ocean negative impact of moored buoy on SSHA with westward intensification (Figure 7.6b) is noticed around the spatial boundaries of moored buoy coverage irrespective of the magnitude of interpolation error (Figure 7.6). It is important to understand that updates of density field at the boundaries of assimilation can have adverse effects on SSHA gradients, which lead to artificial

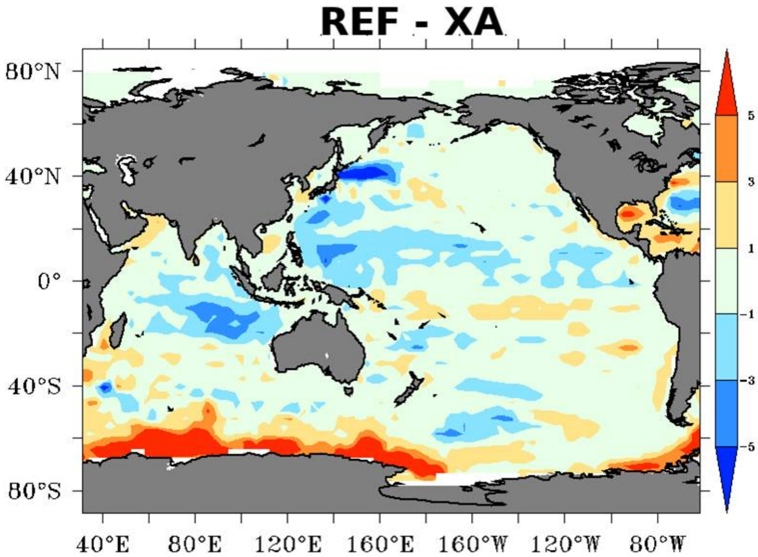

Figure 7.11: Difference in RMSD for SSHA (cm) between *REF* and *XA* (*REF*-*XA*). RMSD is with respect to merged altimeter SSHA

baroclinic instabilities. These instabilities at boundaries of assimilation which are difficult to handle can contribute to the effective growth of the error. The error growth at local scales subsequently carries to eastward and/or westward by planetary waves such as Rossby and Kelvin wave depending on the latitude and lateral boundaries of error growth occurrence regions. The verification of the growth of such errors around the boundaries of assimilation can be done by examining the quality of ocean analysis around the boundary of assimilation (i.e. 60°) in any of the experiment conducted in the present study. For example, while we notice positive impact of profiling floats north of the $60°S$, the southern boundary of the assimilation, negative impact is observed south of this latitude (Figure 7.11). In the tropical Pacific and the Indian Ocean, the number of temperature and salinity profiles from profiling floats and ship-based platforms are far less than the number of observations from moored buoys. This means that even we assimilate observations from all networks, it is like assimilating observations from moored buoy only in the tropical regions. This can open chances for the growth of instabilities along the boundaries of moored buoy network (here onwards virtual boundary of assimilation).

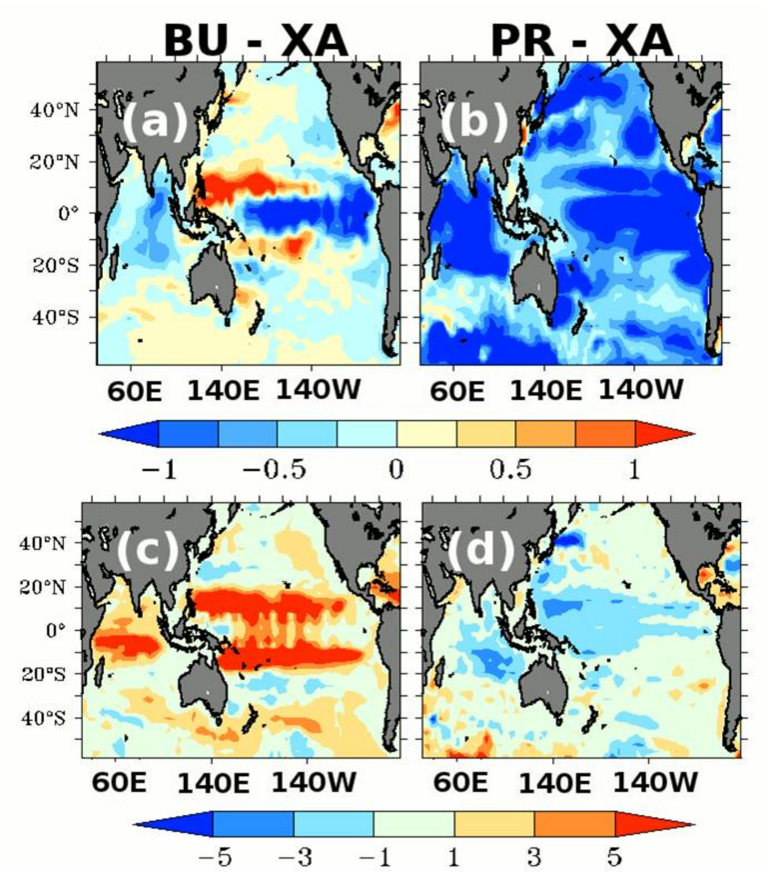

Figure 7.12: Difference in RMSDs of SST (°C; a,and b) and SSHA (psu; c and d) between BU and XA ($BU - XA$), and PR and XA ($PR - XA$)

In-order to better understand the spatial structures of the degradations offered by moored buoy at its spatial boundaries, we have conducted some more experiments namely, *PR*, *BU*, and *XA* (see Table 7.1 for description of these experiments). Results from these special experiments (*PR*, *BU* and *XA*) reveals that the assimilation of temperature and salinity observations from any observation network improves SST analysis significantly in the regions covered by the respective network consistent with the earlier studies (Balmaseda et al., 2007; Vidard et al., 2007; Huang et al., 2008; Balmaseda et al., 2009). However, degradations in SST are observed along the spatial boundaries of a particular network (Figure 7.12a, 7.12b). Such a situation is particularly prominent for moored buoy network in the tropical Pacific Ocean due to the discontinuity of measurements towards poleward from 10°. For example, improvements are observed within 10°S-10°N of tropical Pacific but degradations with west ward extension are observed around the boundaries of the 10°N and 10°S. The degradations of SST around the moored buoy network in the tropical Indian Ocean (coverage extends up to 16°S) are comparatively less than the Pacific Ocean (coverage is mainly upto 8°S). This could be due to the relatively fast and less dissipation rates of instabilities (e.g. Rossby wave) at lower latitudes than at higher latitudes. When we consider SSHA for the comparison of BU and XA, the affect of both virtual boundary and interpolation errors comes into picture (Figure 7.12c, 7.12d). Hence the degradations in BU with respect to XA seem to be everywhere within the spatial coverage area of moored buoys and particularly large along the virtual boundary of assimilation created by moored buoys (Figure 7.12c). As we have good vertical resolution and homogeneous spatial coverage from profiling floats we could mainly witness positive impact of this platform except around the boundaries of assimilation (e.g. 60°S; Figure 7.12d).

From the above paragraph it is clear that the present spatial coverage of moored buoy offers degradations in SST and SSHA around its spatial boundaries. It is important to understand that the degradations at the virtual boundary of assimilation associated with the moored buoy become large when there is no coverage from other network (comparison of BU and XA) and they gets suppressed when there is some coverage from other network (Figure 7.11). Combining the results from this virtual boundary of moored buoy with the results from the vertical resolution of moored buoy suggests that the negative impact of moored buoy noted in OSEs in the tropical Pacific ocean are contributed by both poor vertical resolution and insufficient spatial coverage of moored buoy with the major contribution from the later. The reason for the absence of negative impact of moored buoy in the Indian Ocean might be due to both low interpolation errors and the extended spatial coverage of moored buoys in the tropical Indian Ocean with respect to the coverage of moored buoys in the tropical Pacific. The extended coverage of moored buoy is important because the propagation speed of the instabilities generated at the virtual boundary depends on the latitude (Rossby wave moves faster near Equator and slower near poles). Since the propagation speed of the instability is less at higher latitudes, there are more chances for the suppression of the error, because by the time the error grows there will be counter action from the other less-frequent observation network (e.g. profiling floats with its 10 day cycle) due to the availability of observation from it.

7.4 Summary

Observation System Experiments are conducted using INCOIS-GODAS for the period 2004-2011 to know the impact of temperature and salinity observations of moored buoy, profiling floats and ship-based network on the quality of the Indian Ocean and the Pacific Ocean analysis. Observations from profiling floats played crucial role in obtaining good quality ocean analysis from INCOIS-GODAS corroborating the findings of earlier studies in which the importance of Argo (major contributor for profiling floats) was emphasized (Balmaseda et al., 2007; Huang et al., 2008). Also, observations from ship-based platform complement the observations from profiling floats. It appears from the present study that, in the Pacific and the Indian Ocean, current set up of moored buoy network do not add significant value in improving the quality of ocean analysis. Although the near homogeneous coverage of profiling float network appear to be major factor for the absence of positive impact of moored buoy, further analysis indicates that there are few more issues that are worth to be attended. Extended coverage with improved vertical resolution appears to be crucial for delivering best quality ocean analysis from INCOIS-GODAS.

The present study provides an overall idea on the impact of each *in-situ* observation system and the core-results from the present study appear to be in-line with other multi-model studies. We emphasize here that the results be tested thoroughly for all the time and space scales before further conclusions can be drawn regarding redundancies and requirements in the observing systems. The results from this study does not mean that moored buoy network is not important since here we test only the impact of temperature and salinity observations for the seasonal timescales and above. High frequency observations (daily) from moored buoys may provide better impact in diurnal scale and intra-seasonal scale. Further, the marine meteorological variables measured from moored buoy will provide additional input to atmospheric model.

Chapter 8

End Notes and Future Scope

8.1 Summary and Conclusions

The demand for an accurate global ocean analysis is high in the recent period. This is mainly because they offer dynamically consistent spatial and temporally complete products, which is necessary for use in coupled ocean-atmospheric models and also to understand the ocean process in detail. Recently, a new version of GODAS has been developed at the NCEP, to increase the understanding and predictive capability of the oceans role in future climate change scenarios. This new system, which can assimilate *in-situ* temperature and salinity profiles, is part of the new CFSR at NCEP (Saha et al., 2010). The same CFS system is setup at IITM, Pune under "National Monsoon Mission" by Ministry of Earth Sciences (MoES), Government of India to provide seasonal forecasts of monsoon. The initial condition for the coupled model require global ocean analysis. The ocean data assimilation component of the CFS system, GODAS, is set up at INCOIS (INCOIS-GODAS) with an objective to provide (1) accurate ocean initial conditions for the CFS, run at IITM, and (2) research quality ocean analysis products for new in-sights. Such an accurate and research quality global ocean analysis is thought to improve seasonal forecasts of monsoon generated from CFS by IITM. These products are also thought to aid in better understanding the physical and dynamical state of the ocean (temperature, salinity, currents and sea level) over a range of spatio-temporal scales especially in the tropical Indian Ocean.

The present study carried out various experiments towards finding an optimal configuration for providing accurate global ocean analysis from INCOIS-GODAS. We evaluate the ocean analysis from each of these experiments to arrive at a best possible configuration to provide ocean analysis on operational basis. We start off by first examining the impact of using temperature and synthetic salinity for assimilation in INCOIS-GODAS, and sensitivity of the assimilation system to momentum forcing by using model based NCEP2 (*TS'*-experiment) and satellite based QuikSCAT winds (*QTS'*-experiment) (chapter 3). The analysis was carried out for the tropical Indian Ocean during the period January, 2004-october, 2009.

Verifying the model SST fields with observations reveals that the model with assimilation improves (*TS'* and *QTS'*) SST field by 1°C compared to the model without assimilation (*XA*). The RMSD between the SSTs of the assimilation experiments and observations are smaller than 0.5°C in the TIO, except over the few localized regions such as near Somali, thermocline ridge. Notable improvements (0.2-0.4 psu) are also observed in salinity analysis upon assimilation compared to assimilation-free run. Discrepancies in SSS, in terms of RMSDs, are less than 0.5 psu over most of the regions in the TIO with the *TS'*. However, discrepancies were still large in the north BoB and SEAS in *TS'* compared to observations. The difference in the SSHA derived from the assimilation experiments and the altimetry observations was generally less than ±3 cm over most of the TIO. The RMSD between SSHA estimated from assimilation experiments and altimeter measurements were relatively small in the EIO, and large in those regions affected by small scale eddies such as along the Somalia coast, in the western BoB and in the southern Indian Ocean (> 5 cm). Comparing the performances of three experiments, *XA*, *TS'*, and *QTS'*, reveals that the assimilation of temperature and synthetic salinity improves the quality of the ocean analysis significantly except for currents near the equator. The degradation of the equatorial currents as a consequence of the assimilation, is a common feature in most of the assimilation systems as well (Burgers et al., 2002; Bell et al., 2004; Balmaseda et al., 2007; Balmaseda and Anderson, 2009). Use of satellite based QuikSCAT instead of model based NCEP2 winds appears to improve currents, especially at equator, which is in agreement with earlier studies (Sengupta et al., 2007). The analysis carried out in this chapter helped to identify various issues in the INCOIS-GODAS with *TS'* configuration. Some of these issues are fixed with the assimilation of observed salinity and inclusion of monthly varying river discharge. These results are discussed in chapter 5.

As part of the present work, evaluation of ASCAT based gridded wind (DASCAT) product was performed in the tropical Indian Ocean using *in-situ* RAMA winds, QuikSCAT based gridded (QSCAT) winds and also using INCOIS-GODAS (chapter 4). This was done to qualify DASCAT wind as a successor to QuikSCAT wind for use in the operational assimilation system, INCOIS-GODAS, owing to (1) the well known degraded performance of model based NCEP2 winds compared to satellite blended winds and (2) non-availability of QuikSCAT winds after November, 2009. The analysis was carried out in the TIO during the period 01^{st} April, 2009 to 30^{th} October, 2009. Comparison of DASCAT wind with QSCAT shows that, even though both QSCAT and DASCAT have a strong spatial correspondence, the mean wind speed is underestimated in DASCAT (by up-to $1m/s$) with respect to QSCAT. The discrepancies between DASCAT and QSCAT winds are comparatively large over the eastern parts of the north Indian Ocean (with biases and RMSDs of greater than $2m/s$ and $1.5m/s$ respectively). We also find a strong spatial coherence between the number of rainy days and the differences between these two wind products. Further, analysis of the source of these discrepancies is performed in terms of different wind speed and rain regimes using *in-situ* wind speed from the RAMA buoy. This analysis clearly showed that the accuracy of QSCAT winds have wind speed dependence and does not compare well under low wind speed conditions ($< 4m/s$). DASCAT, on the other hand, shows no significant change in accuracy with wind speed. Rainfall significantly influences the QSCAT wind product: wind speed estimates are biased high, particularly for winds weaker than $10m/s$. The DASCAT product compares well with *in-situ* RAMA observations even in rainy conditions. It was found, from the sensitivity experiments using assimilation system, the INCIOS-GODAS, that the quality of current analysis from DTS is slightly better than *QTS(TS)* in the TIO except (including) near equatorial regions. It appears that lack of rich small scale variations in the wind field of DASCAT due to over smoothness lead to poor representation of current field in the EIO especially during inter-monsoon period. The study from this chapter 4 carries an important message that small discrepancies in the wind field along the equator could produce significantly large discrepancies in current analysis along the equator in assimilation systems. The results further suggests that though DTS performance is poorer than QTS in capturing surface currents realistically, it is still a better thing to replace NCEP2 winds with DASCAT wind forcing in INCOIS-GODAS.

In chapter 5, we have discussed on the improvements in salinity analysis brought by implementing observed *in-situ* salinity profile assimilation and using monthly river discharge forcing for the INCOIS-GODAS. Experiments were conducted for the period 2004-2012. Analysis was carried out for the TIO. Assessments were done by mainly comparing model SSS with respect to satellite based Aquarius gridded SSS and independent *in-situ* salinity measurements from RAMA. It is found that the use of observed *in-situ* salinity profiles instead of synthetic *in-situ* salinity profiles for assimilation improves the model salinity field in a significant way particularly in the eastern parts of the TIO and BoB. The improvements in salinity were up to 0.3 psu which in turn reduced errors in SSHA and currents by up to 25%. Interestingly, use of point source instead of pre-spreaded option for the incorporation of river runoff in the observed *in-situ* T & S profile assimilation enabled experiments lead to improvements in the salinity in the northern parts of the BoB, especially the seasonal cycle. Improvements of salinity up to 0.5 psu were achieved within the upper 30 m layer. Further improvements in salinity were also achieved with the incorporation of monthly climatology of river runoff under the point source option. However, there were no appreciable differences found in the quality of salinity analysis between the experiments with monthly climatology and inter-annual monthly river runoff. Results from the chapter 5 qualify the use of observed *in-situ* salinity profile assimilation and monthly river discharge as a forcing in the INCOIS-GODAS for operational purposes.

The knowledge gained from Chapters 3, 4 and 5, an IGOA (Improved Global Ocean Analysis) was prepared by implementing (1) Assimilation of observed salinity instead of synthetic salinity, (2) inter-annual monthly river runoff, (3) strong relaxation of model SST towards observations, and (4) replace NCEP2 winds with QSCAT+DASCAT winds. Results suggest that the strong SST relaxation help to reduce errors in model SST beyond the improvements achieved with the assimilation of observed *in-situ* T & S profiles, particularly in regions such as northern parts of BoB, thermocline ridge where SST plays important role in air-sea interaction process. Discussion on the quality of this IGOA was presented in Chapter 6. The quality is assessed by first performing statistical comparisons with respect to observations, performing case studies, and finally by comparing the quality of this IGOA with respect to other global ocean re-analysis. The following two paragraphs provide a brief summary of the results obtained from these comparisons.

Statistical comparisons of temperature and salinity analysis of the IGOA with respect to independent RAMA measurements indicates that RMSDs are less than observed standard deviations in any given depth. Spatial comparison of SSHA with respect to satellite based altimeter SSHA also shows that the RMSDs and correlations in most of the regions in the TIO are within the acceptable ranges. Although there appears to have degradations in the quality of ocean currents in the IGOA compared to outputs from free model runs, all the important circulation features are captured at reasonable skill in the IGOA. Analysis further indicates that the IGOA reproduces the ocean phenomena associated with the IOD and intra-seasonal variability with a reasonable skill.

In order to understand the status of the quality of IGOA amongst the contemporary global ocean analysis produced by various operational centres across the world, an inter-comparison study was carried out. In this inter-comparison study the performance of IGOA from INCOIS-GODAS was compared with respect to the global ocean re-analysis from NCEP-GODAS and ECMWF-ORAS4. Results from the inter-comparison exercise suggest that despite the absence of altimeter sea level assimilation in INCOIS-GODAS, the quality of IGOA obtained from the INCOIS-GODAS is on par with the global ocean re-analysis from NCEP-GODAS and ECMWF-ORAS4. In fact, the quality of IGOA is better than NCEP-GODAS and close to ECMWF-ORAS4.

Results discussed in the present study clearly indicate that IGOA from INCOIS-GODAS is at research quality, fulfilling objectives set for the present study to a large extent. In fact, during the year 2013, the INCOIS-GODAS is operationalized at INCOIS to provide global ocean analysis on near real time. The present study formed the backbone for this new service from INCOIS. The configuration used for this operational INCOIS-GODAS is close to the one used for obtaining IGOA. At present, the new operational system of INCOIS-GODAS provides real time ocean analysis using NCMRWF atmospheric fluxes, monthly varying river discharge forcing, real time QC'ed temperature and salinity profiles, and real time Reynolds SST.

Motivated by the results from the inter-comparison study using INCOIS-GODAS, we have carried out OSEs, an important exercise and application of assimilation systems, to understand the value of global ocean observation platforms. Results from these OSEs are discussed in chapter 7. The OSEs were conducted for the period 2004-2011 to know the impact of *in-situ* temperature and salinity observations of moored buoy, profiling floats and ship-based network on the quality of global ocean analysis. Results indicated that observations of T & S from profiling floats play crucial role in obtaining good quality global ocean analysis from INCOIS-GODAS, corroborating the findings of earlier studies in which the importance of Argo (major contributor for profiling floats) was emphasized (Balmaseda et al., 2007; Huang et al., 2008). Also, measurements of T & S from ship-based platform complement the observations from profiling floats. It appeared from this OSE study that in the Pacific and the Indian Ocean, current set up of moored buoy network do not add significant value in improving the quality of ocean analysis. Although the near homogeneous coverage of profiling float network appear to be major factor for the absence of positive impact of moored buoy, further analysis indicates that there are few more issues that are worth to be attended. Extended coverage with improved vertical resolution appears to be crucial for delivering best quality ocean analysis from INCOIS-GODAS.

8.2 Scope for the future work

Though we have made a significant progress with the present study towards meeting the objective to provide research quality global ocean analysis, there is a lot of scope for future work to improve the global ocean analysis. Out of many things we identified, below are few.

- It is found that there are issues with the present INCOIS-GODAS coarse resolution set up in capturing meso scale eddy activity especially at higher latitudes. Increasing the model resolution or SSHA assimilation might help bringing model simulations close to observations.

- Assimilation of temperature and salinity degrades the quality of currents near the equator. The quality can be improved by implementing the method suggested by Burgers et al. (2002)- in which balanced updates are made for velocity field- in the present assimilation system i.e., the INCOIS-GODAS.

- It is well known that there are significant errors in the NCEP2 heat flux, which will contribute to errors in the model SST (Sun et al., 2003; Swain et al., 2009; McPhaden et al., 2009b). Forcing the model with the recently developed heat flux data, the OA flux (Yu and Weller, 2007), which have better accuracy, may provide better oceanic conditions.

- Recently new version of MOM, the MOM-5, is released which has the capability to simulate non-Boussinesq fluids. It has various impressive physical parameterization schemes as well, targeted to improve the ocean simulations. Upgrading from MOM-4 to MOM-5 in INCOIS-GODAS might provide better simulations for global sea level, especially the steric component.

- There are various assimilation schemes being implemented for ocean models in the recent period, out of which Ensemble Kalman Filters (EnKF) are one. Evolution of error variance in EnKF, in principle, is more physical as it involves model. Currently INCOIS-GODAS uses 3D-VAR assimilation scheme with background error covariance evolved from the previous analysis. It is worth to implement EKF in INCOIS-GODAS and then compare the results with the 3D-VAR setup.

8.3 Dissemination of global ocean analysis through LAS of INCOIS

The IGOA obtained from INCOIS-GODAS is made available for research purposes through INCOIS- Live access server (`http://las.incois.gov.in`). This data is

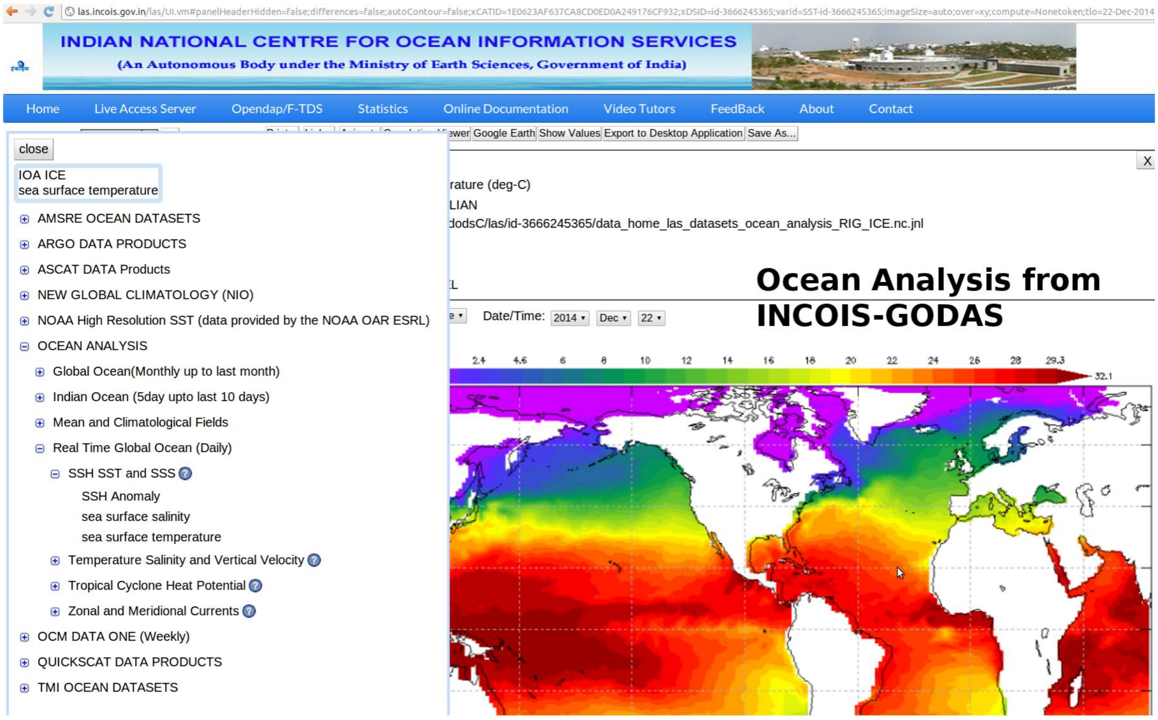

Figure 8.1: Screenshot demonstrating the visualization capabilities of INCOIS Live Access server

available from the 2004 onwards under the directory of "ocean analysis" under "choose data set" and gets updated every day with latest analysis of -2^{nd} day. The LAS makes it relatively easy to create basic graphics and to download subsets of the data. We also offer OpeNDAP, formerly known as DODS (Distributed Oceanographic Data Server). The Figure 8.1 shows a screen shot, which gives an overview of the visualization capabilities of LAS for ocean analysis products.

Bibliography

Agarwal, N., R. Sharma, S. K. Basu, A. Sarkar, and V. K. Agarwal, 2007: Evaluation of relative performance of quikscat and ncep re-analysis winds through simulations by an ogcm. *Deep Sea Research Part I: Oceanographic Research Papers*, **54 (8)**, 1311–1328.

Akhil, V., et al., 2014: A modeling study of the processes of surface salinity seasonal cycle in the bay of bengal. *Journal of Geophysical Research: Oceans*.

Anderson, E., et al., 1998: The ecmwf implementation of three-dimensional variational assimilation (3d-var). iii: Experimental results. *Quarterly journal of the Royal Meteorological Society*, **124 (550)**, 1831–1860.

AVISO, 2008: Ssalto/duacs user handbook:(m) sla and (m) adt near-real time and delayed time products.

Baehr, J., S. Cunnningham, H. Haak, P. Heimbach, T. Kanzow, and J. Marotzke, 2009: Observed and simulated estimates of the meridional overturning circulation at 26.5 degrees n in the atlantic.

Balmaseda, M. and D. Anderson, 2009: Impact of initialization strategies and observations on seasonal forecast skill. *Geophysical Research Letters*, **36 (1)**.

Balmaseda, M., D. Anderson, and A. Vidard, 2007: Impact of argo on analyses of the global ocean. *Geophysical Research Letters*, **34 (16)**.

Balmaseda, M. A., K. Mogensen, and A. T. Weaver, 2013: Evaluation of the ecmwf ocean reanalysis system oras4. *Quarterly Journal of the Royal Meteorological Society*, **139 (674)**, 1132–1161.

Balmaseda, M. A., et al., 2009: Ocean initialization for seasonal forecasts. *Oceanography*, **22 (3)**, 154.

Behringer, D. and Y. Xue, 2004: Evaluation of the global ocean data assimilation system at ncep: The pacific ocean. *Proc. Eighth Symp. on Integrated Observing and Assimilation Systems for Atmosphere, Oceans, and Land Surface.*

Behringer, D. W., 2007: 3.3 the global ocean data assimilation system (godas) at ncep.

Behringer, D. W., M. Ji, and A. Leetmaa, 1998: An improved coupled model for enso prediction and implications for ocean initialization. part i: The ocean data assimilation system. *Monthly Weather Review*, **126 (4)**, 1013–1021.

Bell, M. J., M. Martin, and N. Nichols, 2004: Assimilation of data into an ocean model with systematic errors near the equator. *Quarterly Journal of the Royal Meteorological Society*, **130 (598)**, 873–893.

Bentamy, A. and D. C. Fillon, 2012: Gridded surface wind fields from metop/ascat measurements. *International Journal of Remote Sensing*, **33 (6)**, 1729–1754.

Bentamy, A., Y. Quilfen, and P. Flament, 2002: Scatterometer wind fields: A new release over the decade 1991-2001. *Canadian journal of remote sensing*, **28 (3)**, 431–449.

Bonjean, F. and G. S. Lagerloef, 2002: Diagnostic model and analysis of the surface currents in the tropical pacific ocean. *Journal of Physical Oceanography*, **32 (10)**, 2938–2954.

Bouttier, F. and P. Courtier, 2002: Data assimilation concepts and methods march 1999. *Meteorological training course lecture series. ECMWF.*

Bryan, K. and L. Lewis, 1979: A water mass model of the world ocean. *Journal of Geophysical Research: Oceans (1978–2012)*, **84 (C5)**, 2503–2517.

Bubnov, V., 1994: Climatic zonal pressure in the equatorial zone of the indian ocean. *Oceanology of the Russian Academy of Sciences*, **33 (4)**, 414–420.

Burgers, G., M. A. Balmaseda, F. C. Vossepoel, G. J. van Oldenborgh, and P. J. van Leeuwen, 2002: Balanced ocean-data assimilation near the equator. *Journal of physical oceanography*, **32 (9)**, 2509–2519.

Cai, W., A. Pan, D. Roemmich, T. Cowan, and X. Guo, 2009: Argo profiles a rare occurrence of three consecutive positive indian ocean dipole events, 2006–2008. *Geophysical research letters*, **36 (8)**.

Carton, J. A. and A. Santorelli, 2008: Global decadal upper-ocean heat content as viewed in nine analyses. *Journal of Climate*, **21 (22)**, 6015–6035.

Cazes-Boezio, G., D. Menemenlis, and C. R. Mechoso, 2008: Impact of ecco ocean-state estimates on the initialization of seasonal climate forecasts. *Journal of Climate*, **21 (9)**, 1929–1947.

Chaitanya, A., et al., 2014: Salinity measurements collected by fishermen reveal a river in the sea flowing along the east coast of india. *Bulletin of the American Meteorological Society*.

Chakraborty, A., R. Sharma, R. Kumar, and S. Basu, 2014: An ogcm assessment of blended oscat winds. *Journal of Geophysical Research: Oceans*, **119 (1)**, 173–186.

Chamarthi, S., P. S. Ram, and L. Josyula, 2008: Effect of river discharge on bay of bengal circulation. *Marine Geodesy*, **31 (3)**, 160–168.

Chelton, D. B., M. G. Schlax, M. H. Freilich, and R. F. Milliff, 2004: Satellite measurements reveal persistent small-scale features in ocean winds. *Science*, **303 (5660)**, 978–983.

Conkright, M. E., R. A. Locarnini, H. E. Garcia, T. D. O'Brien, T. P. Boyer, C. Stephens, and J. I. Antonov, 2002: *World Ocean Atlas 2001: Objective analyses, data statistics, and figures: CD-ROM documentation*. US Department of Commerce, National Oceanic and Atmospheric Administration, National Oceanographic Data Center, Ocean Climate Laboratory.

Cushman Roisin, B. and J.-M. Beckers, 2011: *Introduction to geophysical fluid dynamics: physical and numerical aspects*, Vol. 101. Academic Press.

Dai, A., T. Qian, K. E. Trenberth, and J. D. Milliman, 2009: Changes in continental freshwater discharge from 1948 to 2004. *Journal of Climate*, **22 (10)**, 2773–2792.

Dai, A. and K. E. Trenberth, 2002: Estimates of freshwater discharge from continents: Latitudinal and seasonal variations. *Journal of hydrometeorology*, **3 (6)**, 660–687.

Davis, R. E., 2005: Intermediate-depth circulation of the indian and south pacific oceans measured by autonomous floats. *Journal of physical oceanography*, **35 (5)**, 683–707.

de Boyer Montégut, C., J. Mignot, A. Lazar, and S. Cravatte, 2007: Control of salinity on the mixed layer depth in the world ocean: 1. general description. *Journal of Geophysical Research: Oceans (1978–2012)*, **112 (C6)**.

De Mey, P. and M. Benkiran, 2002: A multivariate reduced-order optimal interpolation method and its application to the mediterranean basin-scale circulation. *Ocean Forecasting*, Springer, 281–305.

Demirov, E., N. Pinardi, C. Fratianni, M. Tonani, L. Giacomelli, and P. D. Mey, 1999: Assimilation scheme of the mediterranean forecasting system: operational implementation. *Annales Geophysicae*, Copernicus GmbH, Vol. 21, 189–204.

Derber, J. and A. Rosati, 1989: A global oceanic data assimilation system. *Journal of Physical Oceanography*, **19 (9)**, 1333–1347.

Dohan, K. and N. Maximenko, 2010: Monitoring ocean currents with satellite sensors. *Oceanography*, **23 (4)**, 94.

Dong, C. and L.-Y. Oey, 2005: Sensitivity of coastal currents near point conception to forcing by three different winds: Ecmwf, coamps, and blended ssm/i-ecmwf-buoy winds. *Journal of physical oceanography*, **35 (7)**, 1229–1244.

Durand, F., F. Papa, A. Rahman, and S. K. Bala, 2011: Impact of ganges–brahmaputra interannual discharge variations on bay of bengal salinity and temperature during 1992–1999 period. *Journal of earth system science*, **120 (5)**, 859–872.

Durran, D. R., 1999: *Numerical methods for wave equations in geophysical fluid dynamics*. 32, Springer.

Fairall, C., E. F. Bradley, J. Hare, A. Grachev, and J. Edson, 2003: Bulk parameterization of air-sea fluxes: Updates and verification for the coare algorithm. *Journal of climate*, **16 (4)**, 571–591.

Fernandez, D. E., X. Zhang, J. Carswell, D. McLaughlin, P. Chang, L. Connor, P. G. Black, and F. D. Marks, 2003: Hurricane wind and rain measurements using a dual polarized c/ku-band airborne radar profiler. *Geoscience and Remote Sensing Symposium, 2003. IGARSS'03. Proceedings. 2003 IEEE International*, IEEE, Vol. 2, 1247–1248.

Foltz, G. R., J. Vialard, B. Praveen Kumar, and M. J. McPhaden, 2010: Seasonal mixed layer heat balance of the southwestern tropical indian ocean*. *Journal of Climate*, **23 (4)**, 947–965.

Francis, P. and S. Gadgil, 2009: The aberrant behaviour of the indian monsoon in june 2009. *Current science*, **97 (9)**, 1291–1295.

Freeland, H. J., et al., 2010: Argo-a decade of progress. *OceanObs 09: Sustained Ocean Observations and Information for Society (Vol. 2), Venice, Italy, 21-25 September 2009*.

Fujii Y, X. Y. S. A. L. T. B. M. R. E. M. S. B. G. A. O. C. B. M. M. O. P. S. G. Y. X., Cummings J, 2015: Evaluation of the tropical pacific observing system from the ocean data assimilation perspective. *Submitted to Q J R MeteorolSoc*.

Gadgil, S. and J. Srinivasan, 2011: Seasonal prediction of the indian monsoon. *Current Science*, **100 (3)**, 343–353.

Gent, P. R. and J. C. Mcwilliams, 1990: Isopycnal mixing in ocean circulation models. *Journal of Physical Oceanography*, **20 (1)**, 150–155.

Gent, P. R., J. Willebrand, T. J. McDougall, and J. C. McWilliams, 1995: Parameterizing eddy-induced tracer transports in ocean circulation models. *Journal of Physical Ocenography*, **25 (4)**, 463–474.

Gill, A. E., 1982: *Atmosphere-Ocean dynamics*, Vol. 30. Academic press.

Girishkumar, M., M. Ravichandran, and W. Han, 2013: Observed intraseasonal thermocline variability in the bay of bengal. *Journal of Geophysical Research: Oceans*, **118 (7)**, 3336–3349.

Girishkumar, M., M. Ravichandran, M. McPhaden, and R. Rao, 2011: Intraseasonal variability in barrier layer thickness in the south central bay of bengal. *Journal of Geophysical Research: Oceans (1978–2012)*, **116 (C3)**.

Gnanaseelan, C., A. Deshpande, and M. J. McPhaden, 2012: Impact of indian ocean dipole and el niño/southern oscillation wind-forcing on the wyrtki jets. *Journal of Geophysical Research: Oceans (1978–2012)*, **117 (C8)**.

Goswami, B. N. and D. Sengupta, 2003: A note on the deficiency of ncep/ncar reanalysis surface winds over the equatorial indian ocean. *Journal of Geophysical Research: Oceans (1978–2012)*, **108 (C4)**.

Griffies, S. M., 2004: *Fundamentals of ocean climate models*, Vol. 518. Princeton University Press Princeton.

Griffies, S. M., A. Gnanadesikan, R. C. Pacanowski, V. D. Larichev, J. K. Dukowicz, and R. D. Smith, 1998: Isoneutral diffusion in az-coordinate ocean model. *Journal of Physical Oceanography*, **28 (5)**, 805–830.

Griffies, S. M. and R. W. Hallberg, 2000: Biharmonic friction with a smagorinsky-like viscosity for use in large-scale eddy-permitting ocean models. *Monthly Weather Review*, **128 (8)**, 2935–2946.

Griffies, S. M., et al., 2000: Developments in ocean climate modelling. *Ocean Modelling*, **2 (3)**, 123–192.

Haines, K., J. Blower, J.-P. Dr'e court, C. Liu, A. Vidard, I. Astin, and X. Zhou, 2006: Salinity assimilation using s (t): Covariance relationships. *Monthly weather review*, **134 (3)**, 759–771.

Haltiner, G. J. and R. T. Williams, 1980: *Numerical prediction and dynamic meteorology*, Vol. 2. Wiley New York.

Han, W., 2005: Origins and dynamics of the 90-day and 30-60-day variations in the equatorial indian ocean. *Journal of physical oceanography*, **35 (5)**, 708–728.

Han, W. and J. P. McCreary, 2001: Modeling salinity distributions in the indian ocean. *Journal of Geophysical Research: Oceans (1978–2012)*, **106 (C1)**, 859–877.

Han, W., J. P. McCreary, and K. E. Kohler, 2001: Influence of precipitation minus evaporation and bay of bengal rivers on dynamics, thermodynamics, and mixed layer physics in the upper indian ocean. *Journal of Geophysical Research: Oceans (1978–2012)*, **106 (C4)**, 6895–6916.

Hastenrath, S. and L. Greischar, 1991: The monsoonal current regimes of the tropical indian ocean: Observed surface flow fields and their geostrophic and wind-driven components. *Journal of Geophysical Research: Oceans (1978–2012)*, **96 (C7)**, 12 619–12 633.

Hoteit, I., B. Cornuelle, V. Thierry, and D. Stammer, 2008: Impact of resolution and optimized ecco forcing on simulations of the tropical pacific. *Journal of Atmospheric and Oceanic Technology*, **25 (1)**, 131–147.

Howden, S. D. and R. Murtugudde, 2001: Effects of river inputs into the bay of bengal. *Journal of Geophysical Research: Oceans (1978–2012)*, **106 (C9)**, 19 825–19 843.

Huang, B. and V. M. Mehta, 2010: Influences of freshwater from major rivers on global ocean circulation and temperatures in the mit ocean general circulation model. *Advances in Atmospheric Sciences*, **27 (3)**, 455–468.

Huang, B., Y. Xue, and D. W. Behringer, 2008: Impacts of argo salinity in ncep global ocean data assimilation system: the tropical indian ocean. *Journal of Geophysical Research: Oceans (1978–2012)*, **113 (C8)**.

Huang, B., Y. Xue, A. Kumar, and D. W. Behringer, 2012: Amoc variations in 1979–2008 simulated by ncep operational ocean data assimilation system. *Climate dynamics*, **38 (3-4)**, 513–525.

Huang, B., Y. Xue, D. Zhang, A. Kumar, and M. J. McPhaden, 2010: The ncep godas ocean analysis of the tropical pacific mixed layer heat budget on seasonal to interannual time scales. *Journal of Climate*, **23 (18)**, 4901–4925.

Ingleby, B. and M. Huddleston, 2007: Quality control of ocean temperature and salinity profileshistorical and real-time data. *Journal of Marine Systems*, **65 (1)**, 158–175.

Iskandar, I., W. Mardiansyah, Y. Masumoto, and T. Yamagata, 2005: Intraseasonal kelvin waves along the southern coast of sumatra and java. *Journal of Geophysical Research: Oceans (1978–2012)*, **110 (C4)**.

Iskandar, I., Y. Masumoto, and K. Mizuno, 2009: Subsurface equatorial zonal current in the eastern indian ocean. *Journal of Geophysical Research: Oceans (1978–2012)*, **114 (C6)**.

Iskandar, I. and M. J. McPhaden, 2011: Dynamics of wind-forced intraseasonal zonal current variations in the equatorial indian ocean. *Journal of Geophysical Research: Oceans (1978–2012)*, **116 (C6)**.

Jamet, C. and H. Loisel, 2009: Data assimilation methods. *Surface Ocean-Lower Atmosphere Processes*, 303–317.

Janakiraman, S., M. Ved, R. N. Laveti, P. Yadav, and S. Gadgil, 2011: Prediction of the indian summer monsoon rainfall using a state-of-the-art coupled ocean-atmosphere model. *Current Science (Bangalore)*, **100 (3)**, 354–362.

Jiang, C., L. Thompson, and K. A. Kelly, 2008: Equatorial influence of quikscat winds in an isopycnal ocean model compared to ncep2 winds. *Ocean Modelling*, **24 (1)**, 65–71.

Johnson, E. S., F. Bonjean, G. S. Lagerloef, J. T. Gunn, and G. T. Mitchum, 2007: Validation and error analysis of oscar sea surface currents. *Journal of Atmospheric and Oceanic Technology*, **24 (4)**, 688–701.

Joseph, P., K. Sooraj, C. Babu, and T. Sabin, 2005: A cold pool in the bay of bengal and its interaction with the active-break cycle of the monsoon. *Clivar Exchanges*, **34 (10)**, 3.

Joseph, S., A. J. Wallcraft, T. G. Jensen, M. Ravichandran, S. Shenoi, and S. Nayak, 2012: Weakening of spring wyrtki jets in the indian ocean during 2006–2011. *Journal of Geophysical Research: Oceans (1978–2012)*, **117 (C4)**.

Kamenkovich, I. V. and E. Sarachik, 2004: Reducing errors in temperature and salinity in an ocean model forced by restoring boundary conditions*. *Journal of physical oceanography*, **34 (8)**, 1856–1869.

Kanamitsu, M., W. Ebisuzaki, J. Woollen, S.-K. Yang, J. Hnilo, M. Fiorino, and G. Potter, 2002: Ncep-doe amip-ii reanalysis (r-2). *Bulletin of the American Meteorological Society*, **83 (11)**, 1631–1643.

Kang, I.-S. and J.-S. Kug, 2000: An el-nino prediction system using an intermediate ocean and a statistical atmosphere. *Geophysical research letters*, **27 (8)**, 1167–1170.

Killworth, P. D., D. A. Smeed, and A. G. Nurser, 2000: The effects on ocean models of relaxation toward observations at the surface. *Journal of physical oceanography*, **30 (1)**, 160–174.

Kumar, B. P., J. Vialard, M. Lengaigne, V. Murty, and M. McPhaden, 2012: Tropflux: air-sea fluxes for the global tropical oceansdescription and evaluation. *Climate dynamics*, **38 (7-8)**, 1521–1543.

Kurian, J. and P. Vinayachandran, 2007: Mechanisms of formation of the arabian sea mini warm pool in a high-resolution ocean general circulation model. *Journal of Geophysical Research: Oceans (1978–2012)*, **112 (C5)**.

Lagerloef, G., et al., 2013: Aquarius salinity validation analysis (data version 2.0). aquarius project document aq-014-ps-0016. *Available online a t http://aquarius. umaine. edu/docs/AQ-014-PS-0016_AquariusSa linityDataValidationAnalysis_DatasetVersion2. 0. pdf*, 36.

Large, W. G., J. C. McWilliams, and S. C. Doney, 1994: Oceanic vertical mixing: A review and a model with a nonlocal boundary layer parameterization. *Reviews of Geophysics*, **32 (4)**, 363–403.

Large, W. G. and S. G. Yeager, 2004: *Diurnal to decadal global forcing for ocean and sea-ice models: the data sets and flux climatologies*. National Center for Atmospheric Research.

LaViolette, P. E., 1967: Temperature, salinity, and density of the world's seas: Bay of bengal and andaman sea. Tech. rep., DTIC Document.

Lee Drbohlav, H.-K. and V. Krishnamurthy, 2010: Spatial structure, forecast errors, and predictability of the south asian monsoon in cfs monthly retrospective forecasts. *Journal of Climate*, **23 (18)**, 4750–4769.

Li, L. Y. Y.-Q. S., J. and W. Dong-Xiao, 2012: Temperature inversion in the bay of bengal prior to the summer monsoon onsets in 2010 and 2011. *Atmospheric and Oceanic Science Letters*, **5 (4)**, 290294.

Maes, C. and D. Behringer, 2000: Using satellite-derived sea level and temperature profiles for determining the salinity variability: A new approach. *Journal of Geophysical Research: Oceans (1978–2012)*, **105 (C4)**, 8537–8547.

Martin, M., A. Hines, and M. Bell, 2007: Data assimilation in the foam operational short-range ocean forecasting system: A description of the scheme and its impact. *Quarterly Journal of the Royal Meteorological Society*, **133 (625)**, 981–995.

Masumoto, Y., H. Hase, Y. Kuroda, H. Matsuura, and K. Takeuchi, 2005: Intraseasonal variability in the upper layer currents observed in the eastern equatorial indian ocean. *Geophysical research letters*, **32 (2)**.

Masumoto, Y. and G. Meyers, 1998: Forced rossby waves in the southern tropical indian ocean. *Journal of Geophysical Research: Oceans (1978–2012)*, **103 (C12)**, 27 589–27 602.

McPhaden, M., 1982: Variability in the central equatorial indian-ocean,. 2. oceanic heat and turbulent energy balances. *Journal of Marine Research*, **40 (2)**, 403–419.

McPhaden, M. J., 1993: Toga-tao and the 1991–93 el niño-southern oscillation event. *Oceanography*, **6 (2)**, 36–44.

McPhaden, M. J., et al., 2009a: Ocean-atmosphere interactions during cyclone nargis. *Eos, Transactions American Geophysical Union*, **90 (7)**, 53–54.

McPhaden, M. J., et al., 2009b: Rama: The research moored array for african–asian–australian monsoon analysis and prediction.

Mears, C., D. K. Smith, and F. J. Wentz, 2001: Comparison of special sensor microwave imager and buoy-measured wind speeds from 1987 to 1997. *Journal of Geophysical Research: Oceans (1978–2012)*, **106 (C6)**, 11 719–11 729.

Megann, A. and A. New, 2001: The effects of resolution and viscosity in an isopycnic-coordinate model of the equatorial pacific. *Journal of physical oceanography*, **31 (8)**, 1993–2018.

Momin, I. M., N. Agarwal, R. Sharma, S. Basu, and V. K. Agarwal, 2010: Impact of satellite-derived precipitation on simulated sea-surface salinity in the tropical indian ocean. *Geoscience and Remote Sensing Letters, IEEE*, **7 (4)**, 650–654.

Morel, A. and D. Antoine, 1994: Heating rate within the upper ocean in relation to its bio-optical state. *Journal of Physical Oceanography*, **24 (7)**, 1652–1665.

Murray, R. J., 1996: Explicit generation of orthogonal grids for ocean models. *Journal of Computational Physics*, **126 (2)**, 251–273.

Murtugudde, R. and A. J. Busalacchi, 1998: Salinity effects in a tropical ocean model. *Journal of Geophysical Research: Oceans (1978–2012)*, **103 (C2)**, 3283–3300.

Nanjundiah, R., 2009: A quick look into assessment of forecasts for the indian summer monsoon rainfall in 2009. *CAOS Report, CAOS, IISc, Bangalore.*

Oke, P. R. and A. Schiller, 2007: Impact of argo, sst, and altimeter data on an eddy-resolving ocean reanalysis. *Geophysical research letters*, **34 (19)**.

Panel, C.-G. I. O., 2006: Coauthors, 2006: Understanding the role of the indian ocean in the climate systemimplementation plan for sustained observations. *WCRP Informal Rep*, **5**.

Papa, F., S. K. Bala, R. K. Pandey, F. Durand, V. Gopalakrishna, A. Rahman, and W. B. Rossow, 2012: Ganga-brahmaputra river discharge from jason-2 radar altimetry: An update to the long-term satellite-derived estimates of continental freshwater forcing flux into the bay of bengal. *Journal of Geophysical Research: Oceans (1978–2012)*, **117 (C11)**.

Papa, F., F. Durand, W. B. Rossow, A. Rahman, and S. K. Bala, 2010: Satellite altimeter-derived monthly discharge of the ganga-brahmaputra river and its seasonal to interannual variations from 1993 to 2008. *Journal of Geophysical Research: Oceans (1978–2012)*, **115 (C12)**.

Peixdto, J. P. and A. H. Oort, 1992: Physics of climate. *American institute of physics, New York*.

Prasanna Kumar, S., P. Muraleedharan, T. Prasad, M. Gauns, N. Ramaiah, S. De Souza, S. Sardesai, and M. Madhupratap, 2002: Why is the bay of bengal less productive during summer monsoon compared to the arabian sea? *Geophysical Research Letters*, **29 (24)**, 88–1.

Quilfen, Y., B. Chapron, F. Collard, and D. Vandemark, 2004: Relationship between ers scatterometer measurement and integrated wind and wave parameters. *Journal of Atmospheric and Oceanic Technology*, **21 (2)**, 368–373.

Rajeevan, M. and L. Sridhar, 2008: Inter-annual relationship between atlantic sea surface temperature anomalies and indian summer monsoon. *Geophysical Research Letters*, **35 (21)**.

Rao, R., G. Kumar, M. Ravichandran, A. Rao, V. Gopalakrishna, and P. Thadathil, 2010: Interannual variability of kelvin wave propagation in the wave guides of the equatorial indian ocean, the coastal bay of bengal and the southeastern arabian sea during 1993–2006. *Deep Sea Research Part I: Oceanographic Research Papers*, **57 (1)**, 1–13.

Rao, R., G. Kumar, M. Ravichandran, B. Samala, and G. Anitha, 2006: Observed intraseasonal variability of mini-cold pool off the southern tip of india and its intrusion into the south central bay of bengal during summer monsoon season. *Geophysical research letters*, **33 (15)**.

Rao, R. and R. Sivakumar, 1999: On the possible mechanisms of the evolution of a mini-warm pool during the pre-summer monsoon season and the genesis of onset vortex in the south-eastern arabian sea. *Quarterly Journal of the Royal Meteorological Society*, **125 (555)**, 787–809.

Rao, R. and R. Sivakumar, 2003: Seasonal variability of sea surface salinity and salt budget of the mixed layer of the north indian ocean. *Journal of Geophysical Research: Oceans (1978–2012)*, **108 (C1)**, 9–1.

Reppin, J., F. A. Schott, J. Fischer, and D. Quadfasel, 1999: Equatorial currents and transports in the upper central indian ocean: Annual cycle and interannual variability. *Journal of Geophysical Research: Oceans (1978–2012)*, **104 (C7)**, 15 495–15 514.

Reynolds, R. W., T. M. Smith, C. Liu, D. B. Chelton, K. S. Casey, and M. G. Schlax, 2007: Daily high-resolution-blended analyses for sea surface temperature. *Journal of Climate*, **20 (22)**, 5473–5496.

Ridgway, K. and J. Dunn, 2007: Observational evidence for a southern hemisphere oceanic supergyre. *Geophysical Research Letters*, **34 (13)**.

Robinson, A. R. and P. F. Lermusiaux, 2000: Overview of data assimilation. *Harvard reports in physical/interdisciplinary ocean science*, **62**, 1–13.

Saha, S., et al., 2010: The ncep climate forecast system reanalysis. *Bulletin of the American Meteorological Society*, **91 (8)**, 1015–1057.

Saji, N., B. N. Goswami, P. Vinayachandran, and T. Yamagata, 1999: A dipole mode in the tropical indian ocean. *Nature*, **401 (6751)**, 360–363.

Saji, N. and T. Yamagata, 2003: Possible impacts of indian ocean dipole mode events on global climate. *Climate Research*, **25 (2)**, 151–169.

Sakova, I. V., G. Meyers, and R. Coleman, 2006: Interannual variability in the indian ocean using altimeter and ix1-expendable bathy-thermograph (xbt) data: Does the 18-month signal exist? *Geophysical research letters*, **33 (20)**.

Satheesan, K., A. Sarkar, A. Parekh, M. R. Kumar, and Y. Kuroda, 2007: Comparison of wind data from quikscat and buoys in the indian ocean. *International Journal of Remote Sensing*, **28 (10)**, 2375–2382.

Schott, F. A., S.-P. Xie, and J. P. McCreary, 2009: Indian ocean circulation and climate variability. *Reviews of Geophysics*, **47 (1)**.

Senan, R., D. Sengupta, and B. N. Goswami, 2003: Intraseasonal monsoon jets in the equatorial indian ocean. *Geophysical research letters*, **30 (14)**.

Sengupta, D., G. Bharath Raj, and S. Shenoi, 2006: Surface freshwater from bay of bengal runoff and indonesian throughflow in the tropical indian ocean. *Geophysical research letters*, **33 (22)**.

Sengupta, D., B. R. Goddalehundi, and D. Anitha, 2008: Cyclone-induced mixing does not cool sst in the post-monsoon north bay of bengal. *Atmospheric Science Letters*, **9 (1)**, 1–6.

Sengupta, D., R. Senan, B. N. Goswami, and J. Vialard, 2007: Intraseasonal variability of equatorial indian ocean zonal currents. *Journal of Climate*, **20 (13)**, 3036–3055.

Seo, H., S.-P. Xie, R. Murtugudde, M. Jochum, and A. J. Miller, 2009: Seasonal effects of indian ocean freshwater forcing in a regional coupled model*. *Journal of Climate*, **22 (24)**, 6577–6596.

Servain, J., A. J. Busalacchi, M. J. McPhaden, A. D. Moura, G. Reverdin, M. Vianna, and S. E. Zebiak, 1998: A pilot research moored array in the tropical atlantic (pirata). *Bulletin of the American Meteorological Society*, **79 (10)**, 2019–2031.

Shankar, D., S. Shetye, and P. Joseph, 2007: Link between convection and meridional gradient of sea surface temperature in the bay of bengal. *Journal of Earth System Science*, **116 (5)**, 385–406.

Shankar, D., P. Vinayachandran, and A. Unnikrishnan, 2002: The monsoon currents in the north indian ocean. *Progress in Oceanography*, **52 (1)**, 63–120.

Sharma, R., N. Agarwal, S. Basu, and V. K. Agarwal, 2007: Impact of satellite-derived forcings on numerical ocean model simulations and study of sea surface salinity variations in the indian ocean. *Journal of climate*, **20 (5)**, 871–890.

Sharma, R., B. Mankad, N. Agarwal, R. Kumar, and S. Basu, 2012: An assessment of two different satellite-derived precipitation products in relation to simulation of sea surface salinity in the tropical indian ocean. *Journal of Geophysical Research: Oceans (1978–2012)*, **117 (C7)**.

Shenoi, S., D. Shankar, and S. Shetye, 1999: On the sea surface temperature high in the lakshadweep sea before the onset of the southwest monsoon. *Journal of Geophysical Research: Oceans (1978–2012)*, **104 (C7)**, 15 703–15 712.

Shenoi, S., D. Shankar, and S. Shetye, 2002: Differences in heat budgets of the near-surface arabian sea and bay of bengal: Implications for the summer monsoon. *Journal of Geophysical Research: Oceans (1978–2012)*, **107 (C6)**, 5–1.

Sikhakolli, R., R. Sharma, S. Basu, B. Gohil, A. Sarkar, and K. Prasad, 2013: Evaluation of oscar ocean surface current product in the tropical indian ocean using in situ data. *Journal of Earth System Science*, **122 (1)**, 187–199.

Smith, G., K. Haines, T. Kanzow, and S. Cunningham, 2010: Impact of hydrographic data assimilation on the modelled atlantic meridional overturning circulation. *Ocean Science*, **6 (3)**, 761–774.

Sparnocchia, S., N. Pinardi, and E. Demirov, 1999: Multivariate empirical orthogonal function analysis of the upper thermocline structure of the mediterranean sea from observations and model simulations. *Annales Geophysicae*, Copernicus GmbH, Vol. 21, 167–187.

Speich, S., B. Blanke, and W. Cai, 2007: Atlantic meridional overturning circulation and the southern hemisphere supergyre. *Geophysical Research Letters*, **34 (23)**.

Speich, S., B. Blanke, P. De Vries, S. Drijfhout, K. Do's, A. Ganachaud, and R. Marsh, 2002: Tasman leakage: A new route in the global ocean conveyor belt. *Geophysical Research Letters*, **29 (10)**, 55–1.

Sprintall, J. and M. Tomczak, 1992: Evidence of the barrier layer in the surface layer of the tropics. *Journal of Geophysical Research: Oceans (1978–2012)*, **97 (C5)**, 7305–7316.

Stommel, H., 1960: Wind-drift near the equator. *Deep Sea Research (1953)*, **6**, 298–302.

Sun, B., L. Yu, and R. A. Weller, 2003: Comparisons of surface meteorology and turbulent heat fluxes over the atlantic: Nwp model analyses versus moored buoy observations*. *Journal of climate*, **16 (4)**, 679–695.

Swain, D., S. Rahman, and M. Ravichandran, 2009: Comparison of ncep turbulent heat fluxes with in situ observations over the south-eastern arabian sea. *Meteorology and atmospheric physics*, **104 (3-4)**, 163–175.

Tournadre, J. and Y. Quilfen, 2003: Impact of rain cell on scatterometer data: 1. theory and modeling. *Journal of Geophysical Research: Oceans (1978–2012)*, **108 (C7)**.

Troccoli, A. and K. Haines, 1999: Use of the temperature-salinity relation in a data assimilation context. *Journal of Atmospheric and Oceanic Technology*, **16 (12)**, 2011–2025.

Troccoli, A., et al., 2002: Salinity adjustments in the presence of temperature data assimilation. *Monthly Weather Review*, **130 (1)**, 89–102.

Uppala, S. M., et al., 2005: The era-40 re-analysis. *Quarterly Journal of the Royal Meteorological Society*, **131 (612)**, 2961–3012.

Vecchi, G. A. and D. Harrison, 2002: Monsoon breaks and subseasonal sea surface temperature variability in the bay of bengal*. *Journal of climate*, **15 (12)**, 1485–1493.

Vialard, J., S. Shenoi, J. McCreary, D. Shankar, F. Durand, V. Fernando, and S. Shetye, 2009: Intraseasonal response of the northern indian ocean coastal waveguide to the madden-julian oscillation. *Geophysical Research Letters*, **36 (14)**.

Vialard, J., A. Weaver, D. Anderson, and P. Delecluse, 2003: Three-and four-dimensional variational assimilation with a general circulation model of the tropical pacific ocean. part ii: Physical validation. *Monthly Weather Review*, **131 (7)**, 1379–1395.

Vidard, A., D. L. Anderson, and M. Balmaseda, 2007: Impact of ocean observation systems on ocean analysis and seasonal forecasts. *Monthly weather review*, **135 (2)**, 409–429.

Vinayachandran, P., J. Kurian, and C. Neema, 2007: Indian ocean response to anomalous conditions in 2006. *Geophysical Research Letters*, **34 (15)**.

Vinayachandran, P., Y. Masumoto, T. Mikawa, and T. Yamagata, 1999: Intrusion of the southwest monsoon current into the bay of bengal. *Journal of Geophysical Research: Oceans (1978–2012)*, **104 (C5)**, 11 077–11 085.

Vinayachandran, P. and R. S. Nanjundiah, 2009: Indian ocean sea surface salinity variations in a coupled model. *Climate dynamics*, **33 (2-3)**, 245–263.

Vinayachandran, P., C. Neema, S. Mathew, and R. Remya, 2012: Mechanisms of summer intraseasonal sea surface temperature oscillations in the bay of bengal. *Journal of Geophysical Research: Oceans (1978–2012)*, **117 (C1)**.

Weaver, A., J. Vialard, and D. Anderson, 2003: Three-and four-dimensional variational assimilation with a general circulation model of the tropical pacific ocean. part i: Formulation, internal diagnostics, and consistency checks. *Monthly Weather Review*, **131 (7)**, 1360–1378.

Webster, P. J., A. M. Moore, J. P. Loschnigg, and R. R. Leben, 1999: Coupled ocean–atmosphere dynamics in the indian ocean during 1997–98. *Nature*, **401 (6751)**, 356–360.

Wentz, F. J., D. K. Smith, C. A. Mears, and C. L. Gentemann, 2001: Advanced algorithms for quikscat and seawinds/amsr. *Geoscience and Remote Sensing Symposium, 2001. IGARSS'01. IEEE 2001 International*, IEEE, Vol. 3, 1079–1081.

Wijffels, S. E., J. Willis, C. M. Domingues, P. Barker, N. J. White, A. Gronell, K. Ridgway, and J. A. Church, 2008: Changing expendable bathythermograph fall rates and their impact on estimates of thermosteric sea level rise. *Journal of Climate*, **21 (21)**, 5657–5672.

Wyrtki, K., 1973: An equatorial jet in the indian ocean. *Science*, **181 (4096)**, 262–264.

Xue, C. W. X. Y. D. B. A. K. G. V. A. R., Y., 2015: Evaluation of tropical pacific observing systems using ncep and gfdl ocean data assimilation systems. *submitted to Climate Dynamics*.

Yu, L., 2003: Variability of the depth of the 20 c isotherm along 6 n in the bay of bengal: Its response to remote and local forcing and its relation to satellite ssh variability. *Deep Sea Research Part II: Topical Studies in Oceanography*, **50 (12)**, 2285–2304.

Yu, L. and M. J. McPhaden, 2011: Ocean preconditioning of cyclone nargis in the bay of bengal: Interaction between rossby waves, surface fresh waters, and sea surface temperatures*. *Journal of Physical Oceanography*, **41 (9)**, 1741–1755.

Yu, L. and R. A. Weller, 2007: Objectively analyzed air-sea heat fluxes for the global ice-free oceans (1981-2005).

Yu, Z. and J. McCreary, 2004: Assessing precipitation products in the indian ocean using an ocean model. *Journal of Geophysical Research: Oceans (1978–2012)*, **109 (C5)**.

Appendices

Appendix A

Derivation of Primitive Equations

This section provides a brief overview on how primitive equations are derived from basic laws of physics. The information provided in these sections are borrowed from various sources (e.g. Griffies et al. (2000), `www.meted.ucar.edu`, `www.oc.nps.ed`, Cushman Roisin and Beckers (2011), Griffies (2004)) and thus the reader is advised to go through these sources for a detailed information.

A.1 Equations governing Geophysical fluid motions

According to Newton's second law of motion, i.e., mass times acceleration equals to force, acceleration of a fluid parcel on the rotating earth can be expressed as a resultant of pressure gradient, Coriolis, gravitational, and frictional forces. Expressing this conservation law of momentum in mathematical terms yields three sets of equations for velocity.

$$x : \rho(\frac{du}{dt} + f_* w - fv) = -\frac{\partial p}{\partial x} + \frac{\partial \tau^{xx}}{\partial x} + \frac{\partial \tau^{xy}}{\partial y} + \frac{\partial \tau^{xz}}{\partial z} \tag{A.1}$$

$$y : \rho(\frac{dv}{dt} + fu) = -\frac{\partial p}{\partial y} + \frac{\partial \tau^{xy}}{\partial x} + \frac{\partial \tau^{yy}}{\partial y} + \frac{\partial \tau^{yz}}{\partial z} \tag{A.2}$$

$$z : \rho(\frac{dw}{dt} + f_* u) = -\frac{\partial p}{\partial z} - \rho g + \frac{\partial \tau^{xz}}{\partial x} + \frac{\partial \tau^{yz}}{\partial y} + \frac{\partial \tau^{zz}}{\partial z} \tag{A.3}$$

where x, y and z axes are directed eastward, northward and upward, respectively, $f = 2\omega \sin\varphi$ is the Coriolis parameter with ω and φ representing angular velocity and latitude respectively, $f_* = 2\omega\cos\varphi$ the reciprocal Coriolis parameter, ρ density, p pressure, g the gravitational acceleration, and τ terms represent the normal and shear stresses due to friction. Because the acceleration in a fluid is not counted as the rate of change in velocity at a fixed location but as the change in velocity of a fluid particle as it moves along with the flow, the time derivatives in the acceleration components, $\frac{du}{dt}$, $\frac{dv}{dt}$, and $\frac{dw}{dt}$, consists of both the local time rate of change and the so-called advective terms:

$$\frac{d}{dt} = \frac{\partial}{\partial t} + u\frac{\partial}{\partial x} + v\frac{\partial}{\partial y} + w\frac{\partial}{\partial z} \tag{A.4}$$

This derivative is called the material derivative. Equations A.1, through A.3 are called Navier-Stokes equations and can be viewed as three equations providing three velocity components, u, v, and w. These equations contain two more unknowns, namely, the pressure p and density ρ, emphasizing the need to have additional equations for obtaining solution. Utilization of the law of conservation of mass (equation A.5), equation of state (equation A.6), the law of conservation of energy (equation A.7), and salt budget (equation A.8), shown below, to the above system of Navier-Stokes equations enable us to obtain solutions, although they introduce two more unknowns.

$$Continuity equation : \frac{\partial \rho}{\partial t} + \frac{\partial}{\partial x}(\rho u) + \frac{\partial}{\partial y}(\rho v) + \frac{\partial}{\partial z}(\rho w) = 0 \tag{A.5}$$

$$Equation of state : \rho = \rho_0[1 - \alpha(T - T_0) + \beta(S - S_0)] \tag{A.6}$$

$$Equation for temperature : Q = \frac{k_T}{\rho}\nabla^2 T \tag{A.7}$$

$$Equation for Salinity : \frac{dS}{dt} = k_S \nabla^2 S \tag{A.8}$$

In these equations, T is the temperature (in $°C$ or Kelvin) and S the salinity (in practical salinity unit “psu”). The constants ρ_0, T_0, and S_0 are reference values of density, temperature, and salinity respectively, whereas α is the coefficient of thermal expansion and β is called, by anology, the coefficient of saline contraction. Typical seawater values are $\rho_0 = 1028 kg/m^3, T_0 = 10°C = 283K, S_0 = 35, \alpha = 1.7 \times 10^{-4} K^{-1}$, and $\beta = 7.6 \times 10^{-4}$. Q is the rate of heat gain, k_T the thermal conductivity of the fluid, and k_S the coefficient of salt diffusion, which plays a role analogous to the heat diffusion k_T. Laplace operator ∇^2 is defined as sum of double derivatives: $\nabla^2 = \frac{\partial^2}{\partial x^2} + \frac{\partial^2}{\partial y^2} + \frac{\partial^2}{\partial z^2}$

It is worth mentioning here about how the equations A.5 to A.8 have arrived. The continuity equation A.5 is obtained after implementing mass conservation. That is, any imbalance between convergence and divergence in the three spatial directions must create a local compression or expansion of the fluid. The equation of state A.6 is obtained by considering the incompressible nature of the ocean water. Because for most applications, as can be found in "Gill (1982)-Appendix 3", the density of the seawater is independent of pressure and linearly dependent upon both temperature (warmer waters are lighter) and salinity (saltier waters are denser).

The equation governing temperature A.7 is obtained from conservation of energy- the internal energy gained by a parcel of matter is equal to the heat it receives minus the mechanical work it performs- after assuming no internal heat sources in the ocean.

Equation for salinity A.8 is obtained from the salt budget. For a detailed derivation of these equations, reader may go through chapter 3 of Cushman Roisin and Beckers (2011).

Although the above equations are established after using numerous simplifying approximations, they are still too complicated for the purpose of geophysical fluid dynamics. Additional simplifications can be obtained by so-called Hydrostatic approximation, Shallo-ocean approximation, Boussinesq approximation, without appreciable loss of accuracy.

A.1.1 Hydrostatic Approximation

Pressure is a force per unit area acting on a fluid parcel. Pressure at a point within a fluid at rest in a gravitational field is given by the weight of the fluid above the point per unit horizontal cross-sectional area. Hence, the vertical pressure gradient is given by the buoyancy. This situation constitutes the hydrostatic balance. When the fluid is in motion, vertical pressure gradients are also affected by vertical accelerations and friction. However, for many geophysically relevant fluid motions, the dominant balance in the vertical momentum equation remains the hydrostatic balance. That means in the equation (A.3) only the vertical pressure gradient ($-\frac{\partial p}{\partial z}$) and vertical gravity ($-\rho g$) term are important and all other terms can be neglected. This gives us a following equation traditionally called as Hydrostatic equation.

$\frac{\partial p}{\partial z} = -g\rho$

The hydrostatic approximation simplifies the computation of pressure. In addition to this the hydrostatic approximation filters out sound waves, which are three-dimensional pressure fluctuations. There remains, however, a strictly horizontal acoustic mode known as the Lamb wave that is not filtered by the hydrostatic approximation. The Lamb wave propagates at the speed of sound, yet has small energy and may be dissipated by numerical effects. For studies aiming to simulate motions with large vertical accelerations and relatively small horizontal scales, such as those occurring in convective regions, the hydrostatic approximation can be an unacceptable limitation.

A.1.2 Shallow ocean approximation

Relative to the earth's radius, the ocean is a shallow layer of fluid moving in an approximately spherical geometry. When measuring the distance between two points within the ocean, one must use a metric tensor. The metric tensor components are generally functions of the latitudinal, longitudinal, and radial position within the ocean. Recognizing the huge scale separation between the depth of the ocean fluid and the radius of the earth, the shallow ocean approximation drops the radial dependence of the metric tensor components. Upon doing so, it sets the radius to a constant.

A.1.3 Boussinesq approximation

In most geophysical systems, the fluid density varies, but not greatly, around a mean value. Even in estuaries where fresh river waters (Salinity =0 psu) ultimately turn into salty seawaters (salinity = 34.7 psu), the relative density difference is less than 3%. These realizations which allow the replacement of actual density ρ by its reference value ρ_0 everywhere except in-front of the gravitational acceleration and in the energy equation lead to a very useful approximation, the Boussinesq approximation.

Boussinesq approximation makes conservation of mass to become conservation of volume. The approximation also eliminates sound waves, which rely on compressibility for their propagation. The Boussinesq approximation has been commonly used in ocean climate models due to the near incompressibility of ocean fluid parcels, and thus the near conservation of volume maintained by the these parcels. Like any approximate description, a Boussinesq fluid has its limitations. Most notably for climate purposes, a Boussinesq fluid does not render an accurate computation of the sea level height. The reason is that it does not incorporate fluctuations in the depth averaged density field. Such Steric effects are not incorporated into volume conserving kinematics.

After applying these shallow-ocean, hydrostatic and Boussinesq approximations to the aforementioned system of equations (Navier-Stokes equations A.1,A.2,A.3, Continuity equation A.5, Equation of state A.6, Equation of temperature A.7 and Equation of salinity A.8), and considering Reynolds stresses (introduced by the fluctuations from the mean field of the flow) a set of seven equations for the seven variables u (zonal velocity), v (meridional velocity), w (vertical velocity), p (hydrostatic pressure), T (temperature), S (salinity), and ρ (density), as shown in the introductory chapter of the thesis, can be obtained. These are called primitive equations. These are the cornerstone of geophysical fluid dynamics and thus are starting point for most of the ocean models.

Appendix B

Spatial and Temporal Staggering of model grids

This section provides brief information on the arrangement of commonly used spatial and temporal grids for the effective discretization of primitive equations. The information provided in these sections are borrowed from various sources (e.g. Griffies et al. (2000), Cushman Roisin and Beckers (2011), Griffies (2004)). Thus the reader is advised to go through these sources for a detailed information.

B.1 Spatial staggering: Arakawa grids

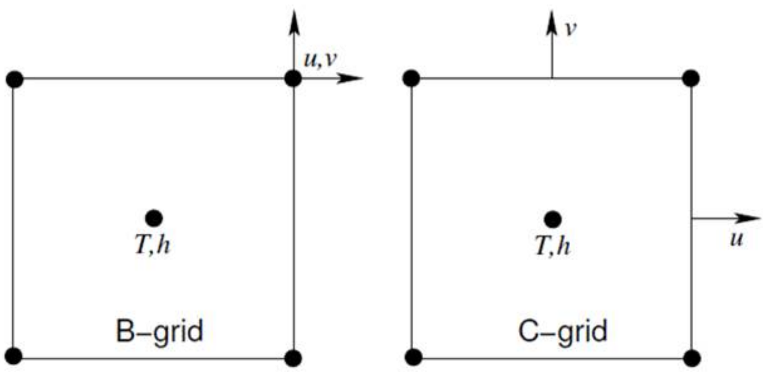

Figure B.1: Schematic of the placement of model variables on the staggered horizontal Arakawa B- and C-grids. These are the two grids most commonly used in ocean climate models. T refers to tracer and density, u refers to the zonal velocity component, v refers to the meridional velocity component, and h refers to layer thickness (as appears in isopycnal models) as well as the free surface height η. The figure is reproduced from Griffies (2004)

Primitive equations used in ocean models contain more than one prognostic variable. In particular, the Boussinesq system contains two horizontal velocity components, a multitude of tracers, and the free surface height. Vertical velocity, density, and pressure are diagnosed. The non-Boussinesq system in Z-models also has a prognostic equation for density via the mass continuity equation. Given the many variables to be time stepped or diagnosed, Arakawa and co-workers characterized a set of horizontal grids, commonly known as Arakawa grids, to arrange the fields spatially. The most common Arakawa grids used in ocean models are B- and C-grids (shown in Figure B.1). In the B-grid momentum components (u and v) are located together on what will be called the *momentum or velocity grid.* Sea level, temperature, salinity and an arbitrary number of tracers are located together on what will be called the *mass or temperature grid.* C-grid is same as that of B- except that the velocity grid is splitted into two. The zonal component (u) falls on the interface between *mass* cells in the zonal direction. Similarly for the meridional component (v) falls on the interface between *mass* cells in the meridional direction. The B- and C-grids have somewhat complementary properties, with some arguing for the relevance of the C grid as the model grid resolution is refined, and the B grid for coarser resolutions.

B.2 Three and two-time level time stepping schemes

Just as one must consider where to place fields discretely in space, it is also necessary to consider what time to evaluate the fields. As spatial grid staggering, it is possible to consider temporal grid staggering, where the prognostic variables are not all co-located in time (see section 3.1.2 of Durran (1999)). In general, there are many time stepping schemes used in ocean models, with some model mixing schemes depending on what part of the equations is being considered. For example, the invicid dynamics is often time stepped using *three time level* - the *leap-frog scheme*, whereby the time tendency $\frac{\partial \phi}{\partial t}$ is approximated as $2\Delta t \frac{\partial \phi}{\partial t} \approx \phi(t + \Delta t) - \phi(t - \Delta t)$ and the inviscid forcing terms are evaluated at the intermediate time t. This approach is accurate to second order in the discrete time step Δt. The dissipative parts of the ocean equations, such as friction and diffusion, are unstable using a *leap-frog* scheme (e.g. Haltiner and Williams (1980)). Consequently, alternatives must be considered, with a *two-time level scheme* common. For the case of leap-frog inviscid dynamics, dissipative forcing terms are evaluated at the lagged time step $t - \Delta t$ rather than the intermediate step t. Although it is still relatively popular, there are well known problems with the leap-frog approach to the inviscid dynamics which necessitate the introduction of time filters (e.g. Robert-Asselin time filter) to remove a spurious mode that can cause numerical instability. More discussion on time stepping schemes can be found in Chapter 12 of Griffies (2004).

Appendix C

Commonly used parametrization schemes for OGCMs

This section provides brief information on commonly used parameterization schemes in OGCMs to account processes such as horizontal and vertical mixing, friction. The majority of the information provided in these sections are borrowed from Griffies et al. (2000). Thus the reader is advised to go through this paper for a detailed information on numerical ocean models.

C.1 Mixing schemes for surface mixed layer

The surface mixed layer is that part of the upper ocean which directly interacts with the overlying atmosphere and sea ice. Accurate surface boundary layer models (for the atmosphere as well as the ocean) are thought to be crucial for coupled ocean-atmosphere models to converge to a realistic mean climate state, and to accurately simulate the variability about this mean state. The hydrostatic approximation necessitates the use of a parameterization of vertical overturning processes. A perfect surface mixed layer parameterization for ocean models must simulate mixing driven by wind stirring at the surface, unstable buoyancy forcing, current shear instability, advection of turbulence, and non-local mixing such as the penetration of dense plumes into a stratified fluid and breaking internal gravity waves. All the present mixed layer parameterizations assume one-dimensional physics in the vertical, using empirical constants and further parameterizations to represent the three-dimensional structure of the sub-grid-scale processes. The parameterizations are of two basic kinds: the bulk mixed layer models and continuous models. Bulk models assume that the surface mixed layer is fully turbulent and so velocity and tracers in the model are uniform over the mixed layer depth;

continuous models allow for vertical structure. The bulk mixed layer models are deficient in some of the requirements described earlier that are desirable for a perfect mixed layer model. Large et al. (1994) introduced to the ocean modelling community the *K-Profile Parameterization (KPP)* scheme. This development effort was designed to create mixing scheme that accounts for all important process, including non-local mixing, and that will perform well on relatively coarse vertical grid. This approach can be summarized by the equation for vertical diapycnal transport of a tracer or velocity component Φ

$$\frac{\partial \Phi}{\partial t} = \frac{\partial}{\partial z}(k\frac{\partial \Phi}{\partial z} - \gamma) \tag{C.1}$$

Where k is a space-time dependent vertical diffusivity, and γ is a non-local transport term. k is large in regions of small Richardson number to account for shear instability, it reduces to the internal wave background of roughly $0.1 - 0.2cm^2/s$ in the ocean interior, and it allows for double diffusive type effects which can locally result in different salinity and temperature diffusivities. Large diffusivities and viscosities in the surface mixed layer result from surface wind stirring and unstable surface boundary forcing. The non-local term is novel, as it aims to parameterize non-local (or non-diffusive) processes in the surface mixed layer which are well known from large-eddy simulations.

C.2 Parameterization of mesoscale eddies

Motivated by the property of baroclinic instability to adiabatically feed off the available potential energy (APE) in the mean flow, GM90 (Gent and Mcwilliams (1990) and Gent et al. (1995)) suggested a form for such a sink in coarse resolution models. In Z-models, the sink takes the form of a divergence-free eddy-induced velocity field V^*. As proposed by Gent et al. (1995), the GM90 eddy-induced velocity is given by

$$V^* = -\frac{\partial}{\partial z}(kS) + Z^\wedge \nabla.(kS) \tag{C.2}$$

Where k is diffusivity and $S = -\frac{\nabla \rho}{(\partial \rho / \partial z)}$ the projection of the neutral slope into the two horizontal direction.

When advecting tracers, this eddy-induced velocity is added to the model's resolved scale velocity V to produce a divergence-free effective transport velocity $V^\wedge = V + V^*$. Griffies et al. (1998) suggested an alternative form of the GM90, in which the eddy induced velocity V^* is represented in terms of its vector stream function. The result is a transformation of the GM90 advective tracer flux into a skew tracer flux. It has been found that the combination of isopycnal diffusion plus GM90 skew-diffusion is generally much more efficient and numerically accurate to realize than the alternative isopycnal diffusion plus GM90 eddy-advection approach.

C.3 Horizontal Momentum Friction

Ocean models require frictional dissipation in-order to suppress instabilities such as those associated with the grid Reynolds number, to provide a vorticity sink at western boundaries, and to generally suppress power at unresolved scales. Frictional dissipation can be included as a physical parameterization of the effect of unresolved scales on the resolved scales. There are many viscocity schemes developed for ocean models out of which *Smagorinsky viscosity scheme* is the one most popular. The *Smagorinsky viscosity* is a function of the local horizontal rate of deformation times the local grid spacing

$A_{smag} = (C\Delta/\phi)^2 \det D$

Where C is a dimensionless scaling parameter, Δ a measure of the local grid spacing, and $D^2 = D_T^2 + D_S^2$ is the squared horizontal deformation rate. In Cartesian co-ordinates, the horizontal tension $D_T = u_x - u_y$ and the horizontal shearing strain $D_S = u_x + u_y$.

The *Smagorinsky viscosity* is enhanced in regions of large horizontal shear, such as near boundaries, and reduced in quiescent regions, such as the ocean interior, as well as regions of smaller grid spacing, such as near poles. Typically this approach produces enough viscosity in those regions with vigorous currents, yet it can have a tendency to under-dissipate in the more quiet regions. The overall strength of the *Smagorinsky viscosity* is set via a single non-dimensional number C, and this parameter is empirically determined in ocean models. One advantage of this approach is that upon setting C for one model resolution, it is typically appropriate when resolution is changed.

Appendix D

List of Publications

D.1 Publications related to thesis

- Ravichandran, M., Behringer, D., **Sivareddy, S.,** Girishkumar, M. S., Chacko, N., and Harikumar, R. (2013). Evaluation of the global ocean data assimilation system at INCOIS: The tropical Indian Ocean. *Ocean Modelling*, 69, 123-135.

- **Sivareddy, S.,** Ravichandran, M., and Girishkumar, M. S. (2013). Evaluation of ASCAT-Based Daily Gridded Winds in the Tropical Indian Ocean. *Journal of Atmospheric and Oceanic Technology*, 30(7), 1371-1381.

- **Sivareddy, S.,** Ravichandran, M., Girishkumar, M. S., and Prasad, K.V.S.R. (2015). Assessing the impact of various wind forcing on INCOIS-GODAS simulated ocean currents in the Equatorial Indian Ocean. *Ocean Dynamics*, in press, DOI: 10.1007/s10236-015-0870-6

- **Sivareddy, S.,** Ravichandran, M., Fabien Durand, Fabrice Papa, and KVSR Prasad. (2015). Impact of salinity observations and river runoff on salinity in Global Ocean Data Assimilation System configured at INCOIS: the Tropical Indian Ocean. *Climate Dynamics*, Under Review

D.2 Other Publications

- Vijay Pottapinjara, M.S.Girishkumar, **Sivareddy, S.,**, M.Ravichandrana, and R.Murtugudde, (2015), Relation between the upper ocean heat content in the equatorial Atlantic during boreal spring and the Indian summer monsoon rainfall during June-September, *International Journal of Climatology*, in press.